Studies of the Crab Nebula and Pulsar at TeV Energies

John Kildea

Supervised by Prof. David J. Fegan

Physics Department,
University College Dublin

November 2002

Abstract

The work described in this thesis concerns a search for pulsed emission from the Crab pulsar in the energy regime from ∼100 GeV to ∼2 TeV. The observations used in the search were taken with the Whipple 10 m γ-ray telescope, located in Southern Arizona. Pulsed emission from the Crab pulsar has been detected across a wide range of energies, from radio waves to GeV γ-rays. No reliable pulsed detections have been reported at TeV energies, although steady unpulsed emission is observed and believed to originate in the Crab supernova remnant, a plerion, which surrounds the pulsar.

Whipple Crab nebula/pulsar data was examined for periodicity after two independent γ-ray selection techniques, the Supercuts and Kernel analyses, were applied. Both techniques utilise the imaging atmospheric Čerenkov technique and both were optimised to select the maximum number of γ-ray events from the Crab dataset, with maximum statistical significance. Temporal analysis of the selected γ-ray events involved barycentering their arrival times, as recorded using a GPS clock at the Whipple observatory, and calculating the associated Crab pulsar rotation phase.

Neither selection method yielded γ-ray events which indicated evidence of statistically significant pulsed γ-ray emission from the Crab pulsar. Accordingly, upper limits for pulsed emission were estimated at different energies and compared with previous results and the models for pulsed γ-ray emission

Abstract

Tá and obair leirithe sa tráchtas seo ag baint le cuardach radaíocht buillte ón réal-builte Crab sa régiún fuinneamh ó ∼100 GeV go dtí ∼2 TeV. Bhí na breathnóireachta úsaideatha sa cuardach tógtha leis an teileascóp 10 m Whipple atá suite í Arizona theas. Bhí radaíocht buillte as an Crab tógtha faoi ndeara fós fein trasna réimse fairsing fuinneamh ó radaíocht raidió go dtí radaíocht GeV. Ní raibh tuairiscí bleachtaireachaí buillte tógtha raimh go húdarásach ag fuineamh TeV, cé go raibh radaíochtaí seasta breathnaighte agus meastar gurb as an Crab supernova remnant thar timpeall an real-buillte ás a dtagann sé.

Bhí na sonraí Crab scrúdaithe le haghaidh radaíocht buillte tar éis na h-anaílisí neamhspleach Supercuts agus Kernel usaidthe. Bhí an IACT úsaidthe leis an dá anailísí agus bhí said araon feabthasaithe chun an úimhir is mó do γ-ray íomhanna a thabhairt amach leis an méid is mó statistic felith. San anailís temporal bhí amanna na γ-ray, mar atá said cláraithe le clog GPS san réadlann Whipple, cuirthe trí próiseas barycentering agus an phase rotlách ríomhiathe.

Níor thug ceachtaracht modh acu aon fianaise do statistic felith de radaíocht buillte ón Crab pulsar. De réir sin, bhí teoranta uachtarach dón radaíocht buillte meastaithe ag fuinneamh eagsula agus curtha í gcomparáid le teorthaí a bhí riomhaithe ríomhe seo, agus le na módhanna don radaíocht buillte γ-ray.

To My Parents

Acknowledgements

The completion of this thesis would not be possible but for the assistance and generosity of a large number of people. My supervisor Prof. Dave Fegan has been a tremendous ally over the past few years, particularly during the writing of this thesis when his support and encouragement were invaluable. I would like to express my gratitude to the staff of the Physics department at UCD, to Prof. Fegan, Prof. Peter Mitchell and Prof. Gerry O'Sullivan for their support as Departmental heads; to Peggy Curran and Marian Hanson for their assistance in all things bureaucratic; and to Catherine Casey–the guardian angel of the astrophysics lab–who provided valuable support, encouragement, and general bonheur during my studies. John Quinn, Ann Breslin and Barry McKernan have been very supportive members of the High Energy Astrophysics group.

My introduction to the field of γ-ray astronomy was enthusiastically facilitated by Michael Cawley, whose assistance during my first year in UCD and during my first visit to Arizona is very much appreciated. I am very grateful to Trevor Weekes for affording me the opportunity to spend time at the Whipple observatory and for his generous support during my visits. Many other members of the VERITAS collaboration have volunteered their expertise at various stages throughout my work, both in Arizona and in Dublin, to assist and support; I am very fortunate to have worked as part of such a fantastic team.

In the preparation of this thesis several people have taken the time to read and correct my work. Their assistance has been very useful; any errors which may remain are mine alone. Apart from Dave Fegan, who spent many weekends in the company of these pages, Trevor Weekes, Stephen Gammell, Colin Hogg and John Crater read through various chapters.

My interest in physics and astrophysics stems from the excellent teaching of John Conaty at St. Macartan's College in Monaghan, whilst the late John Earnshaw at the Queen's University of Belfast introduced me to the field of cosmic ray research. I am lucky to have stumbled upon such enthusiastic and articulate educators.

During my time with the High Energy Astrophysics research group at UCD I have shared resources with a wonderful bunch of people. To those grad-students who showed me the ropes and patiently endured my incessant questioning I am very grateful. These include Conor Masterson, JoJo Boyle, Michael Carson, Shane Dunlea, and Deirdre Horan. I would also like to express my gratitude to Stephen Gammell, Colin Hogg, Paul Hughes, Daithí "Madspoon" O'Caoimh, Deborah O'Connell, Bevin Power-Mooney, Alan Shealy and Sandra Spillane for their support and friendship during my

studies.

Beyond the realm of γ-ray astrophysics many people have provided support and friendship during the last four years. I am grateful to my flatmates and friends Phil Bradley, Alaska John Crater, Paul Duggan, Donal Gallagher, Maeve Gaynor, Kramer and George, Yvette Giblin, Deirdre Horan, Tim Jefferson, Kevin "K-man" Kelleher, Deirdre Kilbane, Nora Kingston, Sheile McBreen, Craig McKelton, Dave O'Reilly, Liz O'Toole, Catherine Phillips, Tabatha Schellenger and Kim Scullion.

Finally, I'd like to thank my brother David for his valuable support over the past year, and my parents and family who have always been there for me and have supported my education from the very beginning.

Contents

List of Figures

List of Tables

Chapter 1

Introduction

The last century witnessed great advances in all areas of astronomical research. Our understanding of the origin and evolution of the Universe has been enhanced by numerous exciting developments, in observational astronomy from radio to γ-ray energies, in astroparticle physics, in cosmology, and in the technologies which drive and are driven by astronomical endeavour. γ-ray astronomy remains a relatively new addition to the realm of astronomical exploration; the oldest science. Nonetheless, in the final decade of the last century observational γ-ray astronomy, nourished by the efforts of its early workers, matured into a serious purveyor of astrophysical insight. Today we view astrophysical research, not as a set of independent entities at different wavelengths, but as a composite of intertwined efforts providing a rich and coherent picture of nature beyond the Earth.

Research described in this thesis is mainly concerned with a search for pulsed TeV emission from the Crab pulsar using data recorded by the Whipple 10 m telescope. At present two main models exist which attempt to explain pulsed γ-ray emission from pulsars. The polar cap model contends that pulsed γ-rays are produced near the pulsar's polar cap in a region of strong magnetic field, while the outer gap model argues that they are produced in a vacuum gap far out in the pulsar's magnetosphere where the magnetic field is much weaker. The two models predict conflicting consequences for pulsed TeV detections: the polar cap pulsed spectrum cuts off super-exponentially at just a few GeV, whereas the outer gap spectrum cuts off more gradually, with possible outer gap emission extending to $\sim$1 TeV albeit at a very low flux level. Since no reliable ground-based detections of pulsed emission from the Crab pulsar exist above $\sim$100 GeV, although steady emission above this energy from the Crab nebula is well established, and since observations of pulsed emission by the EGRET space-telescope extend only to $\sim$10 GeV, the

Crab's pulsed emission cut-off must lie somewhere in between. The possibility of detecting pulsed TeV-scale emission, and thereby settling the model issue, provided the impetus behind this work.

In chapter 2 the astrophysics of relevance to pulsars is discussing in detail; the field of γ-ray astronomy is presently reviewed.

1.1 The Non-thermal Universe – An Introduction

Our concept of the Universe is derived from that part of it we passively observe from Earth. As such, until relatively recently we were limited to visions of a relatively quiet optical Universe comprising mainly thermal production processes. Today, with astronomical research thriving at all wavelengths, we are no longer so confined and we can perceive a more exotic extreme Universe of which violent non-thermal processes play a major part. On the stage of the non-thermal Universe there are a variety of important characters. These include Galactic objects such as pulsar-powered systems (isolated pulsars, plerions, and pulsars with binary companions) and shell-type supernova remnants. The extra-galactic catalog contains objects such as active galactic nuclei and γ-ray bursts. There is also a class of unidentified objects from which non-thermal emission has been observed, albeit with poor angular resolution. A brief introduction to pulsars, supernova remnants and active galactic nuclei is provided here.

1.1.1 Pulsars

Pulsars were an accidental discovery. The first recorded pulsar, PSR 1919+21, was serendipitously observed by Jocelyn Bell on 6 August 1967, as a strange periodic signal at right ascension $19^h\ 19^m$. Bell was working at the time as a astrophysics graduate student, under the direction of Anthony Hewish at the University of Cambridge. Hewish's group were studying radio scintillation phenomena in interplanetary plasma and radio signals from quasi stellar objects using a dipole array, and it was amongst the radio data that Bell noticed the curious periodic signal. The publication of this observation (Hewish et al., 1968) demonstrated that the source was beyond the solar system and postulated several explanations for its origin. Ultimately, it was shown that the pulsed emission must arise from a rotating neutron star. The term "pulsar" (pulsating star) was coined by a science correspondent for the London *Daily Telegraph*. Today pulsars are designated by the prefix "PSR"

(*Pulsating Source of Radio*) followed by their right ascension and declination. For example the Crab pulsar is PSR 0531+21.

The present catalog of radio pulsars extends to more than 1400 isolated objects. Figure 1.1 shows the distribution of pulsars in galactic coordinates and demonstrates quite clearly that they mainly populate the disk of the Galaxy. Indeed, all but eight of the known pulsars reside within the Milky Way; the eight missing residing in the Magellanic Clouds. Pulsar distances can be estimated using Dispersion Measure; a quantity that relates the delay between arrival times of radio pulses of different frequencies to distance. Pulsar periods are observed to increase in regular fashion with typical slowdown rates, $\dot{P} \approx 10^{-15}$ seconds per second. Pulsar age, τ, can be estimated from the slowdown rate and pulse period as:

$$\tau = \frac{P}{2\dot{P}} \tag{1.1}$$

Assuming that the rotational slowdown is caused by the release of electromagnetic dipole radiation the pulsar magnetic field can also be estimated (see section 2.6.3 for full discussion).

The contemporaneous pulsar list embraces a myriad of objects, with pulsars of several different varieties; pulsars in binary systems, single isolated pulsars and millisecond pulsars. It is generally agreed that pulsars are formed as the spinning cores of collapsed massive stars that explode as supernovae (see chapter 2). Binary pulsars are formed after one star in a binary system explodes. Since most stars in the Galaxy are members of binary or multiple star systems, one would expect pulsars to also exist in such systems. On the contrary, the vast majority ($\sim$95%) of pulsars are observed as single isolated objects. The discrepancy can be accounted for by the high probability of disruption of the binary system caused by the supernova explosion. Disruption results in stellar separation so that the spinning neutron star becomes a single isolated pulsar, similar to one formed by the collapse of a single isolated progenitor star.

Those binary systems which remain intact after the supernova explosion are distinguished by their X-ray emission. X-rays originate in such systems as a result of matter accreted from the large companion onto the degenerate neutron star. Millisecond pulsars are identified by their millisecond spin periods (close to the minimum period possible without neutron star breakup) and their very small, stable slowdown rates ($\dot{P} \approx 10^{-18}$ seconds per second). The majority of millisecond pulsars are observed in binary systems and are believed to have spun-down over time, and then recycled or spun-up as a result of long-term accretion from the larger binary companion.

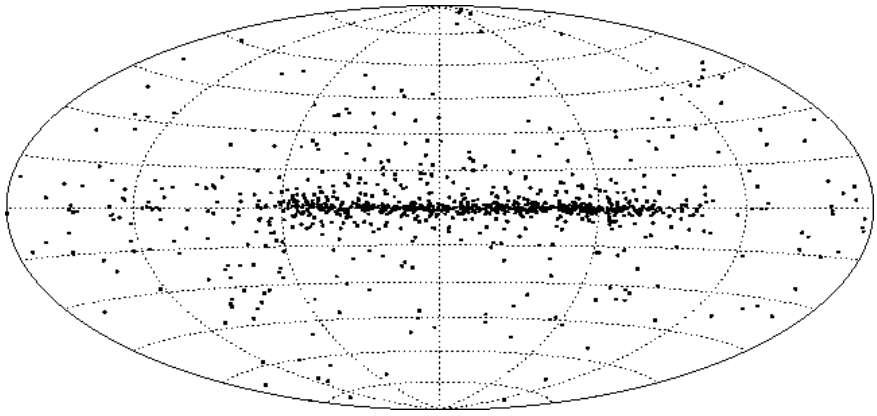

Figure 1.1: The Galactic distribution of radio pulsars. Figure from: Lorimer (2001).

Of interest to γ-ray astronomers are the rotation-powered single isolated pulsars, in which relativistic particle acceleration is an important mechanism (see section 2.7). The EGRET telescope (section 1.2.1 below) produced no evidence for γ-ray emission from X-ray binaries (Jones et al., 1997) and no reliable X-ray binary detections have been confirmed at TeV energies, although several early unconfirmed claims were made using first-generation Čerenkov detectors. A recent survey of pulsars in binary systems using the Whipple 10 m telescope (Hall et al., 2002) indicated no evidence of detectable TeV emission from any of the objects studied.

1.1.2 Supernova Remnants

Supernova Remnants (SNRs) are formed as expanding shells of gas and dust thrown out by supernova explosions. They are considered very efficient particle accelerators and are believed (although not yet proven) to be the source of Galactic cosmic rays. There are three main types of SNR, shell-type, plerions and composite, although the classification is not strict. Shklovsky (1953) first connected SNRs with non-thermal emission by suggesting the optical continuum emission of the Crab nebula might be due to synchrotron emission from relativistic electrons. Today synchrotron emission from the Crab and other SNRs is well established and TeV emission from SNRs (see TeV Catalog below) can be explained by the synchrotron inverse-Compton process of Gould (1965). Although EGRET did not detect any emission from SNRs, there is some evidence in EGRET data for high-energy γ-ray emission from at least five radio bright SNRs (Sturner and Dermer, 1995; Esposito et al., 1996). A more complete discussion of TeV γ-ray emission from SNRs

is provided in section 2.4.

1.1.3 Active Galactic Nuclei

Active Galactic Nuclei (AGN) are galaxies in which a compact nucleus may outshine the rest of the galaxy by a factor of as much as 1000. About 3% of all galaxies have active nuclei, with a multitude of different forms possible, depending on their orientations towards the observer. Active galaxies have distinct observational characteristics which set them apart from "ordinary" galaxies. In particular they exhibit bright nuclei and show broadened optical emission lines instead of absorption lines. Their short-time scale variability, down to days or less, also sets them apart as "active". The AGN class is today generally defined to include Radio Galaxies, Quasars, Quasi-stellar Objects (QSOs) and Blazars.

In an attempt to unify the many diverse AGN phenomena, Urry and Padovani (1995) developed what is now widely accepted as the standard AGN model: a supermassive black hole at the centre of the galaxy, accreting matter from its immediate environment to form an accretion disk and a thick torus. Blazars are a relatively rare type of radio loud AGN, orientated such that the viewing angle is small and the jet is the most obvious feature. BL Lacerate (BL Lac) objects are blazars which exhibit emission lines, and Flat Spectrum Radio Quasars (FSRQs) are blazars which do not. BL Lacs and FSRQs have been detected at energies above 10 MeV, with TeV emission detected almost exclusively from the BL Lacs. The Third EGRET catalog (Hartman et al., 1999) contains a list of over 60 FSRQs detected above 100 MeV, while the TeV catalog as it now stands (see below) contains 4 confirmed BL Lac objects, including: Markarian 421 (Punch et al., 1992), Markarian 501 (Quinn et al., 1996), H1426+428 (Horan et al., 2002; Aharonian et al., 2002) and 1ES 1959 (Holder et al., 2002; Konopelko et al., 2002). Despite these detections no model for γ-ray production in AGN is yet generally accepted.

In their own right AGN are fascinating objects for γ-ray study and despite the observational gains of recent years much remains to be learned regarding their structure and γ-ray emission. As cosmologically distant sources they are also valuable tools for studies of the intergalactic infrared background.

1.2 γ-ray Observatories – An Overview

γ-ray telescopes can be divided into two broad categories: space-based instruments which directly detect γ-rays and ground-based telescopes which rely on indirect detection techniques. The division is not arbitrary; rather it

is imposed by nature. Electromagnetic radiation of energy greater than 10 eV is effectively precluded by the atmosphere from reaching the Earth's surface. Hence, satellite telescopes are required. From ∼100 GeV to ∼50 TeV, however, a "γ-ray window" exists. This window is provided by the Čerenkov radiation produced in the interaction of a primary γ-ray in the upper atmosphere. An overview is provided here of recent, current, and up-and-coming, space- and ground-based γ-ray telescopes which operate at energies above ∼20 MeV.

1.2.1 Space-based γ-ray Observatories

CGRO The Compton Gamma Ray Observatory (Figure 1.2) was launched on April 5 1991 and hailed the coming of age of γ-ray astronomy. This very successful mission remained in orbit until June 2000 and yielded a wealth of information regarding cosmic γ-ray sources. CGRO carried four scientific instruments into space; each designed to operate simultaneously and cooperatively to cover the γ-ray energy range from 15 keV to 30 GeV:

- **BATSE:** The Burst and Transient Source Experiment was the all-sky monitor onboard the CGRO and was designed for the detection of γ-ray bursts and solar flares, in the energy range 20 keV to 1.9 MeV. Figure 1.3 shows the Galactic distribution of all γ-ray bursts detected by BATSE. The isotropic distribution was unexpected and is regarded as one of BATSE's great achievements (Paciesas et al., 1999).

- **OSSE:** The Orientated Scintillator Spectrometer Experiment was designed to undertake spectral observations in the 0.05–10 MeV energy range.

- **COMPTEL:** The imaging Compton Telescope was designed for sky mapping and operated in the energy range 1–30 MeV.

- **EGRET:** Of greatest interest to TeV γ-ray astrophysicists, the Energetic Gamma Ray Experiment Telescope was sensitive to photons in the energy range from 20 MeV to ∼30 GeV. It was the highest energy instrument on the CGRO and remains the highest energy detector thus far launched into space. Since EGRET observations are of relevance to the present work, it is described in more detail below.

EGRET (Thompson et al., 1995; Hartman et al., 1999) operated with good angular resolution (5.8° at 100 MeV, 0.5°at 10 GeV), low background, and a wide field of view (0.5 sr), across its full dynamic energy range. It operated as a pair-telescope (see section 3.2) and utilised a spark chamber

Figure 1.2: The Compton Gamma Ray Observatory. From: http://cossc.gsfc.nasa.gov/images/epo/gallery/cgro/index.html.

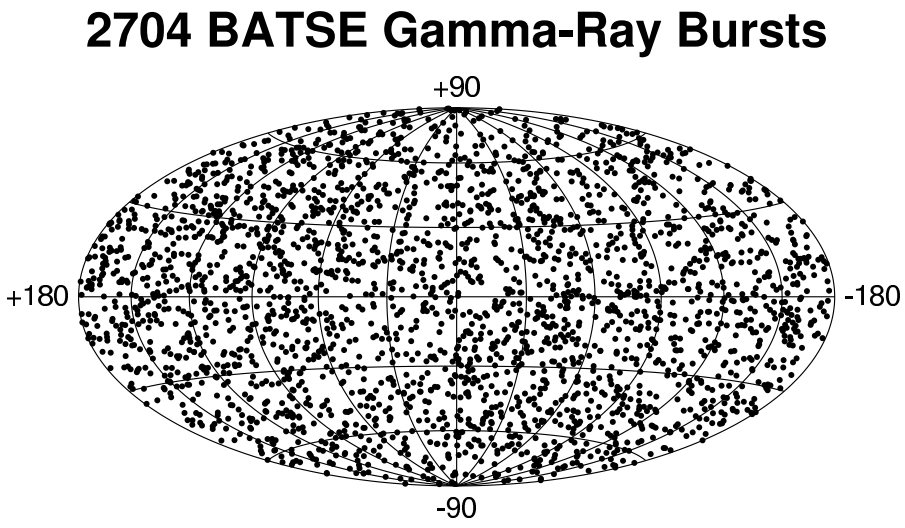

Figure 1.3: The distribution of γ-ray bursts detected by BATSE, in Galactic coordinates (Paciesas et al., 1999).

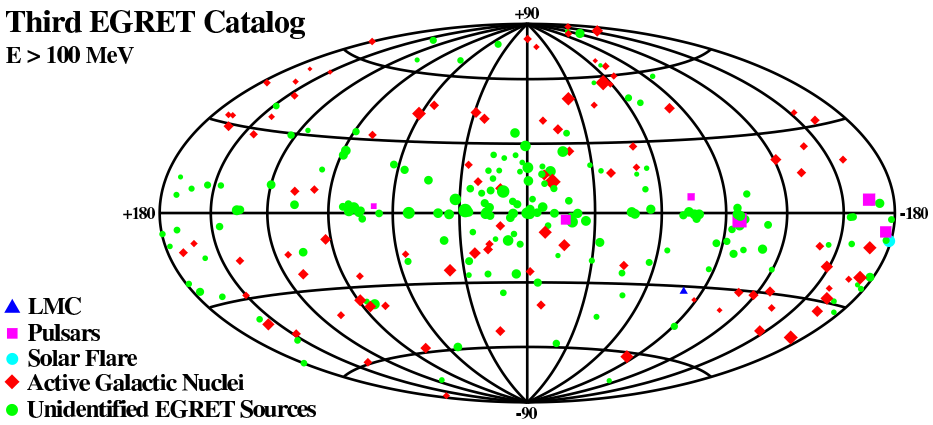

Figure 1.4: The third EGRET catalog all-sky map, in Galactic coordinates (Hartman et al., 1999).

as its particle detector. Prior to the launch of EGRET, the quasar 3C273 was the only known extragalactic source of high-energy γ-rays. One of the great successes of EGRET was its detection of 93 extragalactic sources (66 reliable, 27 marginal), mostly blazar AGN. It also identified 6 γ-ray pulsars above $\sim$5 GeV, detected γ-rays from the Large Magellanic Cloud, prolonged GeV emission from solar flares and γ-ray bursts, and provided a list of $\sim$170 unidentified objects. Figure 1.4 shows, in Galactic coordinates, the location and type of all sources listed in the third EGRET catalog Hartman et al. (1999).

AGILE The Astro-rivelatore Gamma a Immagini LEggero (Light Imaging Detector for Gamma-ray Astronomy) (Tavani et al., 2001; Barbiellini et al., 2001) is due for launch by the Italian Space Agency in 2003. It incorporates an innovative design, combining hard X-ray and γ-ray detectors, and will detect and image photons in the 20 MeV–50 GeV and 10–40 keV bands. AGILE will carry three instruments:

- **GRID:** The Gamma-Ray Imaging Detector will have sensitivity in the energy range $\sim$30 MeV to $\sim$50 GeV and is characterised by very short deadtime ($\lesssim$100 μs) and a large field-of-view ($\sim$0.5 sr).
- **MC:** The Mini-Calorimeter will detect and collect events independently of GRID and will be sensitive in the 0.3–300 MeV range. It will primarily observe transient events such as γ-ray bursts.
- **Super-AGILE:** The Super-AGILE detector will undertake simultaneous hard X-ray observations of γ-ray sources.

GLAST The Gamma-ray Large Area Space Telescope (Gehrels and Michelson, 1999) is the next generation of γ-ray space telescope. Its principle design will be the same as EGRET but it will replace the spark chamber with solid state detectors, and improve on EGRET's sensitivity and energy range. GLAST will comprise two parts: the Large Area Telescope (LAT) and the Gamma-Ray Burst Monitor (GRM). The LAT is the main instrument, with GRM acting as a simple, wide field, low-energy detector which will alert GLAST to the occurrence of a γ-ray burst. GLAST is designed by an international collaboration and is due for launch by NASA in 2006. With an energy range extending from 20 MeV to $\sim$300 GeV GLAST will complement the next generation of ground-based γ-ray telescopes.

A comparison of the mission parameters of EGRET, GLAST and AGILE is provided in table 1.1.

1.2.2 Ground-based γ-ray Observatories

At very high energies (>30 GeV) γ-ray astronomical observations are possible using ground-based telescopes. Ground-based γ-ray astronomy was born in 1958 with the realisation (Morrison, 1958) that γ-ray initiated air showers should be detectable at ground-level by the Čerenkov radiation they emit. Many ground-based γ-ray telescopes were built in the 1960s to detect atmospheric Čerenkov radiation from γ-rays but the first statistically significant results were not realised until 1989 (Weekes et al., 1989).

Very high energy astronomy (in the 300 GeV to 50 TeV energy domain) is accomplished using the Imaging Atmospheric Čerenkov Technique (see section 3.8). IACT systems focus the Čerenkov light from γ-ray air showers onto an array of photomultiplier tubes and identify γ-ray initiated showers by means of their characteristic shape and orientation within the detector's field-of-view. Major recent advances in the IACT include the use of high resolution cameras (for example the CAT 600-pixel camera) and the construction of large IACT systems such as VERITAS, H.E.S.S., CANGAROO and MAGIC. A summary of recent, current and future IACT telescopes is provided in table 1.2.

1.3 The TeV Catalog

Ong (2002) reviews the current state of very high energy γ-ray astronomy. Table 1.3 summarises the current list of confirmed and unconfirmed TeV source detections. A map of their Galactic coordinates is provided in Figure

Parameter	EGRET	AGILE	GLAST
Energy Range	20 MeV to 30 GeV	30 MeV to 50 GeV	20 MeV to 300 GeV
Energy Resolution ($\frac{\Delta E}{E}$)	0.1	1	0.1
Effective Area (peak)	1500 cm^2	700 cm^2	12000 cm^2
Field-of-view	0.5 sr	$\sim$3 sr	2.5 sr
Angular Resolution	5.8° @ 100 MeV	4.7° @100 MeV	$\sim$3.5° @ 100 MeV
	0.5° @ 10 GeV	0.2° @ 10 GeV	$\sim$0.1° @ 10 GeV
Sensitivity (>100MeV)	10^{-7} $cm^{-2}s^{-1}$	$5\times10^{-8}cm^{-2}s^{-1}$	$\sim2\times10^{-9}$ $cm^{-2}s^{-1}$
Mass	1810 kg	60 kg	2000 kg
Lifetime	1991–1997	2003–2005	2006–2010

Table 1.1: A comparison of the mission parameters of the EGRET, AGILE and GLAST γ-ray space telescopes. From Gehrels and The GLAST Collaboration (2001).

Group	Location	No. Telescopes	Aperature	Camera Pixels	Threshold (TeV)
		Current			
Whipple	Arizona, USA	1	10 m	490	0.25
Crimea	Crimea	2	2.4 m (×6)	37	1.0
		No longer operating			
SHALON	Tien Shen, Russia	1	4 m	244	1.0
HEGRA	La Palma, Spain	5	3 m	271	0.5
CAT	French Pyrenées	1	3 m	600	0.25
Durham	Narrabri, Australia	3	7 m	109	0.25
TACTIC	Mount Abu, India	1	10 m	348	0.3
Seven Telescope Array	Utah, USA	7	2 m	256	0.5
		Under Construction			
H.E.S.S.	Namibia	4	12 m	960	0.05
VERITAS	Arizona, USA	7	10 m	499	0.05
CANGAROO	Woomera, Australia	4	10 m	512	0.05
MAGIC	La Palma, Spain	1	17 m	>800	0.03
		Proposed			
5@5	Undecided	5	20 m	1000	0.005

Table 1.2: Current, recent, and up-and-coming γ-ray research groups which utilise the IACT. Adapted from Catanese and Whipple Collaboration (1999).

1.5. As it now stands there are six confirmed sources of TeV γ-rays, and six unconfirmed detections. With the advent of the H.E.S.S., VERITAS and CANGAROO IACT arrays and the development of the large MAGIC telescope this number is expected to increase significantly over the next few years.

1.4 Thesis Overview

The scientific quest summarised in this thesis concerns the search for pulsed TeV emission from the Crab pulsar using data recorded at the Whipple 10 m telescope. The astrophysics of γ-ray emission from pulsars is developed in detail in chapter 2. Chapter 3 discusses the physics of the imaging atmospheric Čerenkov technique and is followed by a detailed description of the specifics of detecting γ-rays using the Whipple 10 m telescope. All associated data analyses methodologies are reviewed in chapters 4 and 5 respectively. The analysis of astrophysical time series data, as applied in this work, is detailed in chapter 6 with the final chapter presenting the results and conclusions of the search for pulsed TeV emission from the Crab pulsar.

Source	Type	Energy	Flux	Significance
		Galactic		
Crab Nebula [a]	Plerion	0.3 TeV	1.26×10^{-10} cm^{-2} s^{-1}	Confirmed
PSR1706 [b]	Plerion	1.0 TeV	0.38 Crab	Confirmed
Vela [c]	Plerion	2.5 TeV	0.54 Crab	5.8σ
SN1006 [d]	Shell	1.7 TeV	0.48 Crab	8.0σ
RXJ1713 [e]	Shell	2.0 TeV	0.40 Crab	5.0σ
Cassiopeia A [f]	Shell	0.5 TeV		4.7σ
Centaurus X-3 [g]	Binary	0.4 TeV	0.24 Crab	6.5σ
		Extragalactic		
Markarian 421 [h]	HBL	0.5 TeV	*	Confirmed
Markarian 501 [i]	HBL	0.3 TeV	*	Confirmed
1ES2344 [j]	HBL	0.3 TeV	0.11 Crab	3.7σ
PKS2155 [k]	HBL	0.3 TeV	0.48 Crab	6.8σ
1ES1959 [l]	HBL	0.9 TeV	*	Confirmed
3C66A [m]	LBL	0.9 TeV	1.2 Crab	5.0σ
1H1426 [n]	HBL	0.4 TeV		Confirmed

[a] Whipple (Weekes et al., 1989)
[b] CANGAROO (Kifune et al., 1995)
[c] CANGAROO (Yoshikoshi et al., 1997)
[d] CANGAROO (Tanimori et al., 1998)
[e] CANGAROO (Muraishi et al., 1999)
[f] HEGRA (Puehlhofer et al., 1999)
[g] Durham (Chadwick et al., 1998)
[h] Whipple (Punch et al., 1992)
[i] Whipple (Quinn et al., 1996)
[j] Whipple (Catanese et al., 1998)
[k] Durham (Chadwick et al., 1999)
[l] Seven Telescope Array (Nishiyama et al., 1999)
[m] Crimea (Neshpor et al., 1998)
[n] Whipple (Horan et al., 2002)

* Variable sources

Table 1.3: The TeV catalog as it currently stands.

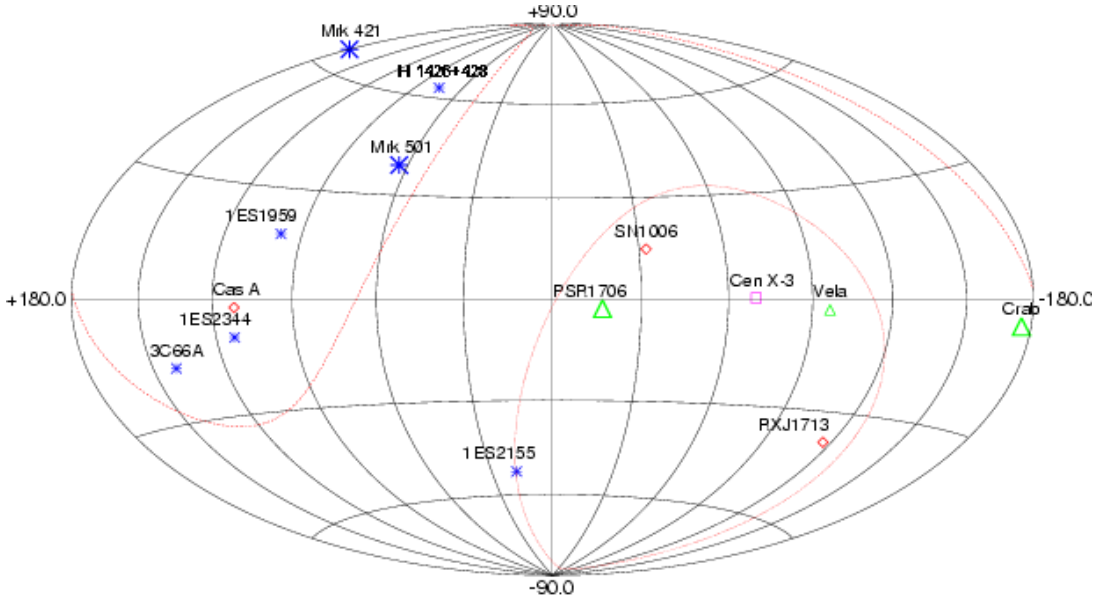

Figure 1.5: Map of the TeV sky in Galactic coordinates showing three plerions (triangles), three shell-type supernova remnants (diamonds), one X-ray binary (square) and seven AGN (asterisks) – The dotted curve shows the dividing line for sources visible from northern hemisphere observatories (above a declination of -30°) and the dashed lines show the approximate cut-off for southern hemisphere observatories (declination +30°).

Chapter 2

Astrophysical γ-ray Production in Supernova Remnants and Pulsars

2.1 Introduction

As described in the last chapter, pulsar physics is a relatively new science. Since their discovery by Jocelyn Bell and Anthony Hewish, however, we have learned a great deal about these fascinating objects. Nevertheless the picture is not clear and our observations are incomplete. Although there exists a large volume of low energy pulsar data, high-energy observations are somewhat lacking. Still, with the realisation of low energy solar tower γ-ray observatories, the advent of the next generation of ground-based γ-ray detectors, and the anticipated launch of the AGILE and GLAST satellites, the field of high-energy pulsar astronomy has never seemed so promising. What makes the subject interesting is the existence of well developed, competing, pulsar models, with contradictory predictions for high-energy observations. In particular, the two most popular models, the polar cap and outer gap models, predict conflicting consequences for γ-ray observations above $\sim$10 GeV. Since no pulsar emission has been observed by ground-based TeV-scale detectors above $\sim$100 GeV, and since EGRET has only been able to observe with good significance up to $\sim$10 GeV, a pulsed emission cut-off must lie somewhere in between. Work with current detectors, can provide constraining upper limits and help the refine models, while the next generation of detectors will conclusively provide the missing data.

This chapter provides an overview of the most popular models for high-energy pulsar emission, along with the physics of stellar evolution, supernova explo-

sions and supernova remnants, with which pulsars are intrinsically connected.

2.2 Stellar Evolution, Supernovae Explosions and Pulsar Formation

In general, the stars which populate the night sky are stable. By fusing lighter elements into heavier ones, in thermonuclear reactions, they radiate, and it is radiation pressure which sustains them. Without this pressure they would succumb to gravity and implode. Indeed, on rare occasions they do just that. For large stars the result is catastrophic; the stellar core collapses into a dense ultra-compact object, off which the outer layers violently rebound, in a *supernova* explosion. Hundreds of years later the results may still be seen. The collapsed core if it survives is a *neutron star*, and it may spin rapidly as a *pulsar* for centuries, periodically emitting brief pulses of non-thermal radiation. The outer layers become a *supernova remnant* and continue their expansion into space until they become indistinguishable from it. Not all Supernovae give rise to neutron stars; for example the supernova remnant Cassiopeia A is not associated with a neutron star or pulsar.

2.2.1 Initial Evolution

The detailed process of stellar formation remains, as yet, poorly understood. Nevertheless, the basic theme is clear: A star is formed out of the gravitational collapse of a cloud of interstellar gas and dust. As the cloud collapses it heats up, converting gravitational potential energy into thermal and radiative energy. Eventually, the collapsed matter reaches the ignition temperature for the thermonuclear fusion of hydrogen, and radiative energy prevents further collapse. At this point a stable star is born. Initial stellar evolution may be categorised in terms of three main stages: collapse, ignition and stabilisation.

2.2.2 The Hertzsprung-Russell Diagram

The Hertzsprung-Russell (H-R) diagram is a graph displaying, for any sample of stars, the relationship between their temperature and luminosity. It was first plotted, independently, by Ejnar Hertzsprung and Henry Norris Russell around 1913. In the context of stellar evolution it is an extremely valuable tool. By examining a star's position on a typical H-R diagram, its current stage of evolution may easily be inferred. As shown in Figure 2.1, there are several distinct regions on a H-R diagram. Newly ignited stars, burning hydrogen in their cores, reside along the *Main Sequence*. Eventually, as their

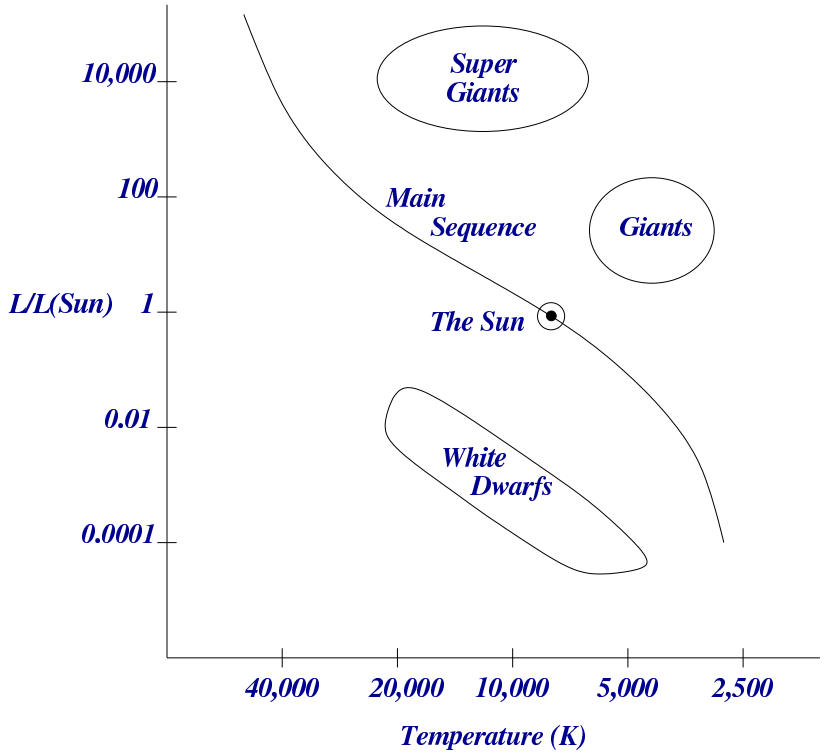

Figure 2.1: Sketch of a typical Hertzsprung-Russell diagram, showing the *Main Sequence*, *Giant*, *Supergiant*, and *White Dwarf* branches (L refers to stellar luminosity).

supply of hydrogen is used up, they undergo significant internal changes and move away from the main sequence into the *Giant* and *Supergiant* branches. Further evolution results in them moving down the diagram, below the main sequence, to end their days as white dwarfs. As described below, the post main sequence evolution of a particular star depends primarily on its mass.

2.2.3 Post-Main Sequence Evolution

Low Mass Stars ($\lesssim 8\ M_\odot$)

When a low mass star exhausts the supply of hydrogen in its core, it contracts under gravity, heats up, and ultimately burns helium. While helium burns in the core, the outer regions continue to burn hydrogen, causing the star to increase in luminosity and move up the H-R diagram, from the *Main Sequence* to the *Giant Branch*.

Eventually, the supply of helium expires and a carbon core develops, surrounded by a layer of burning helium. At this stage the radiation pressure

is enormous and the star exceeds its *Eddington limit* (the Eddington limit is a limit on the luminosity to mass ratio of a stable thermonuclear star. As a result, the outer layers are blown off to form a planetary nebula, leaving the carbon core behind. Without a power source, the core lacks the radiative pressure needed to withstand gravitational collapse, and implodes under its own weight. At some point, however, collapse is halted, as the collapsing matter becomes sufficiently dense that electron degeneracy pressure provides a balance against gravity. Stability only holds, however, if the core's mass is less than the *Chandrasekhar* limit (the Chandrasekhar limit is the upper mass limit for white dwarf stars). For low mass stars the *Chandrasekhar* limit is not easily exceeded and the core cools in the *White Dwarf* branch of the H-R diagram. Eventually, after tens of millions of years, it cools to a point where it can no longer be observed, and disappears as a black dwarf.

High Mass Stars ($\gtrsim$ 8 $M_\odot$)

The initial *Main Sequence* evolution of high mass stars is similar to that of their low mass relatives, i.e. hydrogen is converted to helium and helium to carbon, as the star moves up to the *Giant Branch*. However, high mass stars do not easily exceed their *Eddington limits*, and so continue to undergo thermonuclear reactions long after their core's supply of helium is depleted. In these post-helium reactions, lighter elements are fused to form heavier ones, and a layered burning structure forms around the core. A limit is reached, however, when pure iron—the most tightly bound element—develops. Although the presence of iron prevents further nuclear fusion in the core, fusion of lighter elements continues unabated in the surrounding layers. Consequently, the core gains mass and ultimately reaches the *Chandrasekhar* limit, at which point gravitational pressure exceeds electron degeneracy pressure, and core collapse recommences. Gravitational collapse inevitably causes the core's temperature to rise and, at $\sim$6 $\times 10^9$ K, photodisintegration of iron into helium occurs

$$^{56}Fe + \gamma \rightarrow 13\,^4He + 4n$$

The newly formed helium atoms then further disintegrate into protons and neutrons

$$^4He \rightarrow 2p + 2n$$

The protons, in turn, combine with ambient electrons to form neutrons, thereby adding to the already plentiful neutron population

$$p^+ + e^- \rightarrow n + \nu$$

Eventually, the neutrons provide a degeneracy pressure which prevents further gravitational collapse. At this stage, however, the outer layers continue falling inwards, and in so doing gain thermal energy. Since they still have sufficient fuel for nucleosynthesis, they eventually rebound in a massive explosion, off the dense degenerate core. The result is a huge shock wave that moves radially out from the core and pushes into the ISM. The surviving degenerate core is extremely dense, with typical mass M $\approx$ 1.4 $M_\odot$ and radius R $\approx$ 15 km.

This type of explosive rebound is known as a type II supernova, the surviving core is referred to as a neutron star (it resides in the *Neutron Star* branch of the H-R diagram, well below the *Main Sequence*) and the shock front is called a supernova remnant. The Crab nebula, for instance, is the supernova remnant formed by the supernova of 1054, and the Crab pulsar is the resultant neutron star.

2.3 Mechanisms for Astrophysical γ-ray Production

Before discussing in detail the emission of γ-rays from supernova remnants and pulsars, it is useful to provide a general overview of the main mechanisms involved in astrophysical γ-ray production. Although thermal emission mechanisms can explain virtually all terrestrial radiation sources, such mechanisms cannot produce photons as energetic as γ-rays. Thus, more powerful non-thermal processes are required.

In general, astrophysical γ-rays are produced in particle interactions at sites of extreme acceleration. In the context of this work the main acceleration sites include the electromagnetic potential drop induced by a highly magnetised neutron star, and the shock wave blasting into the ISM after a supernova explosion. The main γ-ray production mechanisms, which pertain to all acceleration sites, are discussed here.

2.3.1 Cyclotron Radiation

The simplest accelerated motion of a charged particle in a magnetic field is non-relativistic gyration around and along a field line. The *Larmor* radius with which the particle gyrates is due to a balance between the *Lorentz* force

of the magnetic field and the centrifugal repulsion of the orbiting particle. In the process, circularly polarised or linearly polarised waves are observed radiating from the charged particle, depending on the orientation of the observer to the magnetic field direction.

2.3.2 Synchrotron Radiation

When the speed of a charged particle gyrating in a magnetic field approaches the speed of light, its cyclotron radiation changes to synchrotron radiation and becomes beamed in the forward direction. Synchrotron radiation is the main non-thermal emission process in astrophysics and was originally observed in betatron experiments on Earth. It is of great importance in TeV astrophysics as it is thought to play a critical role in the indirect production of TeV photons, through the synchrotron self-Compton process (see section 2.3.5 below). As shown in Fig 2.2, the instantaneous beam of synchrotron radiation is a narrow cone in the forward direction, of opening angle $\alpha \lesssim \gamma^{-1}$, where γ is the particle's Lorentz factor. This narrow cone of radiation is due to aberration of the electron's dipole radiation by its relativistic motion. As the charged particle (generally an electron) spirals around the magnetic field line, the observer sees a pulse of radiation each time it passes through his line-of-sight. The pulse is strongly polarised and appears in the form of a continuum frequency spectrum, with maximum frequency depending on the particle's energy and the strength of the magnetic field. The frequency spectrum for an astrophysical plasma is broadened compared to that for as single electron, as radiation from astrophysical plasmas originates from a population of electrons with a spread of energies and with different magnetic field orientations. Nevertheless, synchrotron radiation from astrophysical sources (e.g. from the Crab nebula) is clearly identifiable, due to its high degree of polarisation and continuum spectrum.

2.3.3 Curvature Radiation

In a strong magnetic field ($\sim 10^{12}$ G) an electron's motion may be damped by synchrotron radiation and so constrained to closely follow a magnetic field line (Figure 2.3), such that the curvature of the field line itself causes the electron to radiate. The frequency spectrum for curvature radiation is similar to that for synchrotron radiation and depends on the energy of the electron, the magnetic field strength and the curvature of the magnetic field line.

Both synchrotron and curvature radiation are very important processes for photon production in pulsars and supernova remnants.

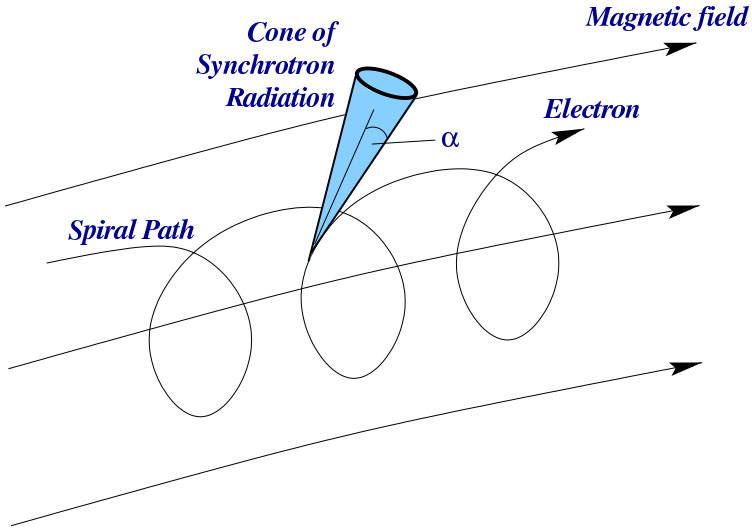

Figure 2.2: Synchrotron radiation is emitted by a relativistic electron as it spirals along a magnetic field line. Shown here is an instantaneous cone of synchrotron radiation with opening angle α, emitted at a tangent to the electron's trajectory.

2.3.4 Relativistic Electron Bremsstrahlung

Bremsstrahlung is the emission of continuum radiation from charged particles decelerating in an electric field (see section 3.3.1 for details regarding bremsstrahlung in extensive air showers). In astrophysical plasmas relativistic electron-nucleon bremsstrahlung is most important, although electron-electron and nucleon-electron bremsstrahlung processes also exist. In the context of TeV supernovae and pulsar astrophysics bremsstrahlung is not a major process. However, for studies of diffuse Galactic emission it is very important, particularly in the energy range < 200 MeV.

2.3.5 Inverse-Compton Scattering

Inverse-Compton Scattering is the process by which low energy photons gain energy by interacting with electrons of much higher energy (Figure 2.4). As a consequence the electrons loose some of their energy. In TeV γ-ray astronomy inverse-Compton scattering is an extremely important mechanism. In particular, the so-called synchrotron self-Compton process, whereby low energy synchrotron photons are up-scattered by the same population of electrons from which they originate, is believed to contribute significantly to TeV γ-ray emission from supernova remnants and active galactic nuclei.

The cross section for inverse-Compton scattering is approximated by the

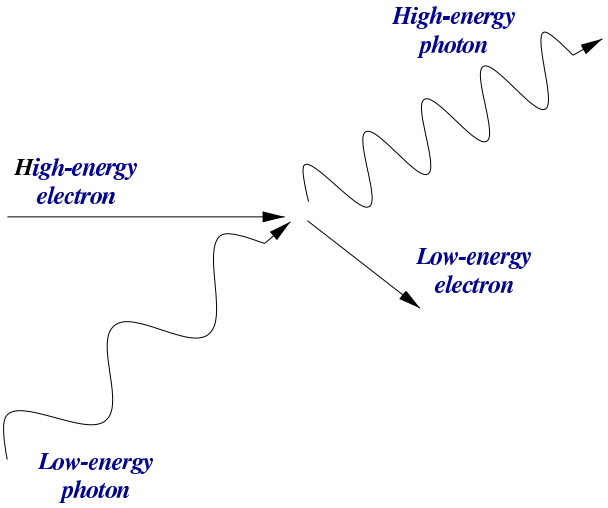

Figure 2.4: Inverse-Compton scattering: A low energy photon is up-scattered to a higher energy by a high-energy electron, which loses energy in the process.

$$\pi^0 \rightarrow \gamma + \gamma$$

while the charged pions decay into muons and neutrinos. The identification of γ-rays that originate in neutral pion decay was one of the original objectives of TeV astronomy. To date, no positive identifications have been made, although the hadronic interpretation of a recent supernova remnant detection at TeV energies is in dispute (see section 2.4.4).

2.4 Supernova Remnants

After a star explodes as a supernova, a shock wave expands rapidly outwards, from the point of ignition, and sweeps up any interstellar gas and dust in its path. As a result, the gas and dust becomes hot and ionised and moves with the shock to form an observable bubble-like structure known as a Supernova Remnant (SNR). Most SNRs appear circular in shape and are limb brightened, suggestive of a hollow spherical structure, Figure 2.5. Initially the mass of the swept-up interstellar material is negligible compared to the ejected stellar envelope, and the SNR expands unhindered with uniform velocity (of the order of 10,000 km s^{-1}). This first stage is referred to as the "free expansion" stage. Over time ($\sim$200 years) expansion decelerates and the SNR enters a phase of adiabatic expansion known as the "Sedov

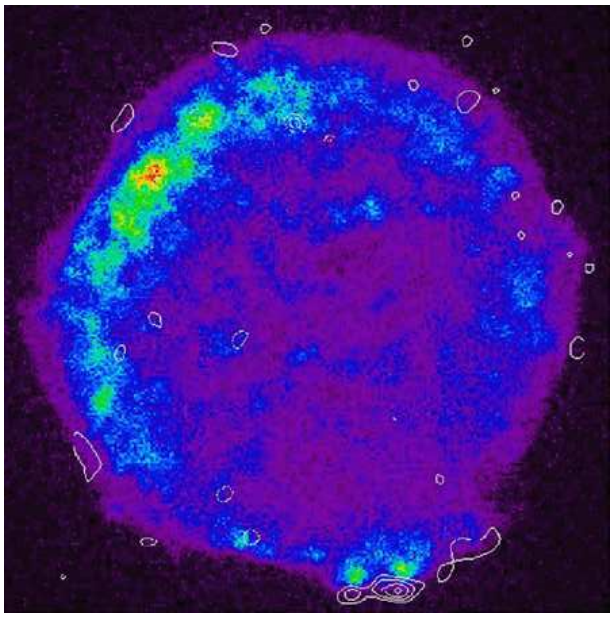

Figure 2.5: The Tycho supernova remnant: limb brightening is evident in this image, and suggests a hollow spherical structure.

phase". At this stage the mass of the swept-up interstellar material is large compared to the mass of the ejecta. However, the energy radiated by the SNR is still small compared to the kinetic energy of its constituents, and therefore, the rate of expansion depends mainly on the initial kinetic energy of the supernova explosion and on the density of the local ISM. Eventually the SNR reaches its final phase, "the radiative phase". At this point most of the internal energy is lost by radiation and the expanding shell coasts through interstellar space until (after about 1000 years) it becomes indistinguishable from the surrounding medium. There are three basic types of SNR, as detailed below.

2.4.1 Shell-Type SNRs

Shell-type SNRs have a distinctive shell-like structure from which most of their observed emission originates. They are formed by the simple expansion of the supernova shock wave and the heating up of the interstellar gas and dust which it encounters. Examples include the Tycho SNR and the Cygnus Loop. An X-ray image of the Cygnus loop is presented in Figure 2.6. Shell type SNRs comprise more than 80% of all known SNRs. The first detection of TeV emission from a shell-type SNR, SN 1006, was reported by Tanimori et al. (1998). Since then two other TeV detections have been reported,

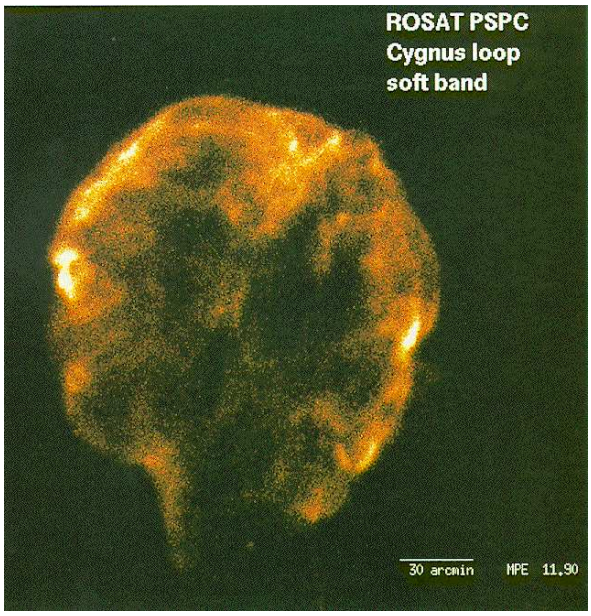

Figure 2.6: The Cygnus Loop: an example of a shell-type supernova remnant.

RXJ 1713.7-3946 (Muraishi et al., 1999) and Cas A (Aharonian et al., 2001). Buckley et al. (1998) and Lessard et al. (1999) provide a list of upper limits for SNR detections based on observations made with the Whipple γ-ray telescope.

2.4.2 Plerions

Plerions (also known as Pulsar Wind Nebulae) are SNRs which resemble the Crab nebula. They are roughly spherical in shape and have a filled central region, which generally hosts a pulsar (Weiler, 1978). The name plerion, which means "full" in Greek, was considered appropriate for this type of SNR as emission (mainly synchrotron radiation) is observed from all parts of the remnant, with most intense emission originating towards the centre. Due to the intrinsically short lifetimes of the synchrotron radiating energetic electrons, it is clear that there must be a steady supply of electrons in order to maintain the observed synchrotron luminosity. It was first proposed by Pacini and Salvati (1973) that the filled interior is continuously replenished by the conversion of the energy outflow from the pulsar into magnetic energy and relativistic particles. The total energy of the plerion is, therefore, determined by a balance between the pulsar's relativistic wind, and energy losses from the radiation and expansion of its of relativistic particles. More specific details regarding the Crab plerion, which is the prototype object for this type of

SNR, are provided in section 2.9.

2.4.3 Composite SNRs

Composite SNRs are a cross between shell-type SNRs and plerions. They have the appearance of shell-like, shock-treated hot gas, but with a small central synchrotron nebula. Depending on which part of the spectrum they are viewed in, they appear more shell-like or plerionic. The Vela SNR is considered an example of a composite SNR. It contains a central pulsar with a small 1' diameter synchrotron nebula, that appears not unlike a plerion at TeV γ-ray energies (Yoshikoshi et al., 1997).

2.4.4 γ-ray Production in Supernova Remnants

High-energy γ-ray emission from SNRs is thought to originate in interactions between the energetic particles of the remnant with surrounding interstellar material, ambient photons and magnetic fields. As detailed below, four major processes are believed to contribute to the γ-ray flux, namely synchrotron emission by electrons in the SNR magnetic field, inverse-Compton scattering of ambient synchrotron and thermal photons, relativistic electron bremsstrahlung, and neutral pion production and decay. The first three mechanisms involve electrons, of which two populations are expected: primary electrons directly accelerated in the SNR shock, and secondary electrons and positrons produced via the decay of charged pions that are created in pp and $p\alpha$ collisions (Iyudin and Kanbach, 2001). The contribution of secondary electrons to the bremsstrahlung, inverse-Compton and synchrotron processes, however, is expected to be negligible and so may be neglected. The fourth mechanism involves hadrons and its clear identification in SNRs would have very significant consequences for theories of the SNR origin of galactic cosmic rays.

The Synchrotron-Compton Component

First discussions of the synchrotron-Compton component of γ-ray production in SNRs were given by Gould (1965) and Rieke and Weekes (1969). Hillas et al. (1998) used the observed synchrotron spectrum of the Crab nebula, from radio waves to 10^9 eV γ-rays, to deduce the energy spectrum of relativistic electrons which give rise, through inverse-Compton scattering, to the observed TeV flux. The observed synchrotron spectrum, together with the thermal radiation spectrum, and the deduced electron spectra for assumed magnetic field strengths of 10, 20, and 40 nT, are presented in Figure 2.7.

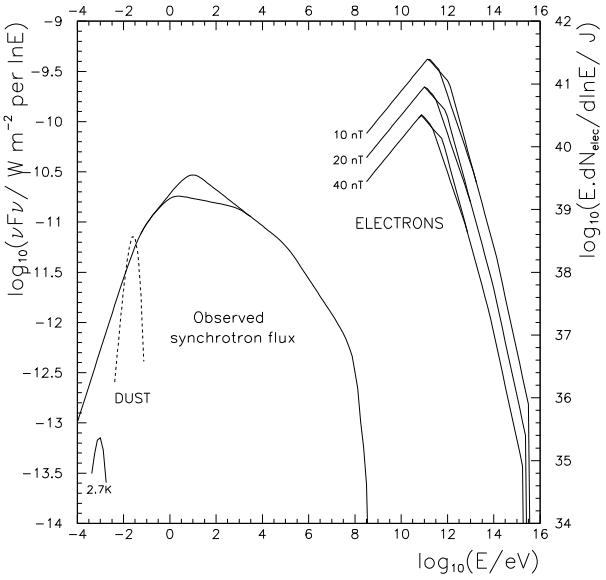

Figure 2.7: The Crab synchrotron spectrum together with the deduced energy spectrum for electrons, for various values of the modelled magnetic field strength, taken from Hillas et al. (1998).

Using an estimated size of the photon source, Hillas et al. converted the observed synchrotron and thermal spectra into a spectrum of "target photon" densities. The inverse-Compton spectrum for up-scattering of the ($\sim$75%) ambient synchrotron IR photons, and the ($\sim$ 25%) thermal photons from dust, was then calculated for a variety of magnetic field strengths. By comparing the calculated spectra with the true observed TeV spectrum (Figure 2.8), Hillas et al. showed convincingly that TeV γ-rays may be produced in SNRs via the inverse-Compton mechanism. Furthermore they deduced the magnetic field strength of the region within the Crab nebula responsible for X-ray and TeV emission to be $\approx$16 nT.

Of the five other SNRs detected at TeV energies (see table 1.3 and Figure 1.4), emission from two of them, Vela and SN 1006, may also be explained as a composite of a synchrotron and an inverse-Compton component emitted by a population of accelerated electrons. Detected TeV fluxes from another two, Cas A and PSR 1706-44, are not strong enough to constrain the emission mechanisms, while the mechanism behind non-thermal emission from RX J1713.7-3846 remains in dispute (see below).

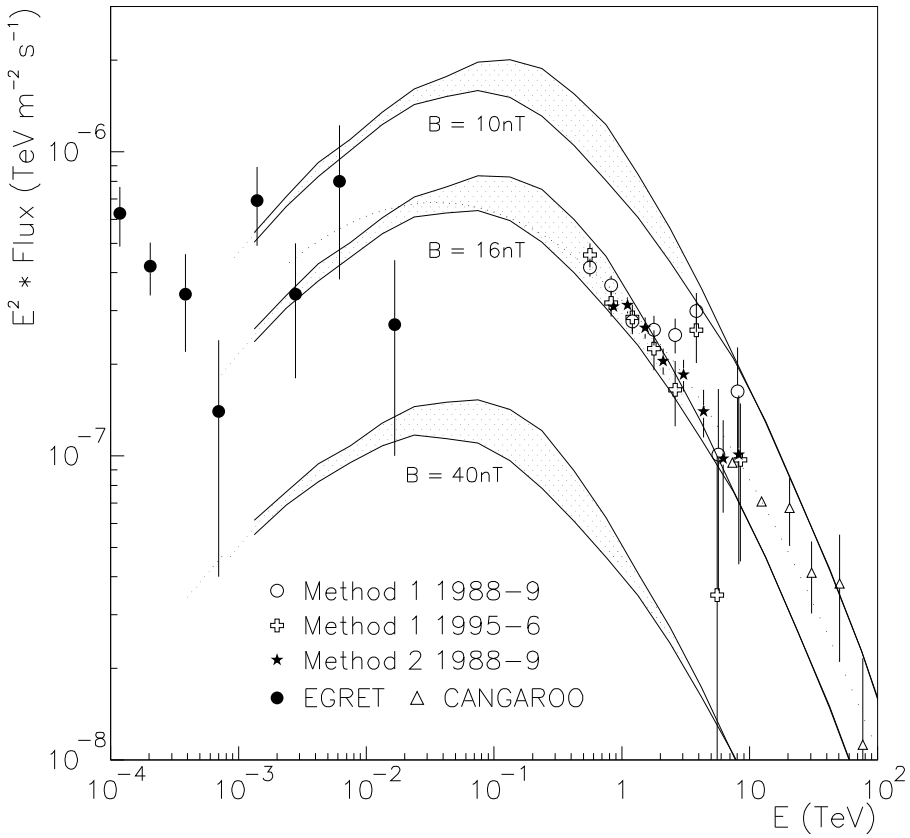

Figure 2.8: TeV spectra of the Crab nebula from 1988/89 and 1995/96 Whipple datasets using two independent analysis methods, compared with spectrum points from the EGRET and CANGAROO experiments, and with the predicted inverse-Compton spectrum for three different magnetic fields strengths - the dotted curve shows the parabolic fit to the data in logE. After Hillas et al. (1998).

The Bremsstrahlung Component

In their calculations, Hillas et al. (1998) ignored the contribution of bremsstrahlung of relativistic electrons to the overall γ-ray flux. It was shown, however, by Aharonian and Atoyan (1995) that the flux of bremsstrahlung radiation produced in the Crab nebula filaments could play a significant role in the 1–100 GeV domain. Given the 500 GeV lower threshold quoted by Hillas et al., such a bremsstrahlung component would, in any case, have no effect on their data.

The Neutral Pion Component

Several authors, for example Dorfi (1991) and Drury et al. (1994) have studied γ-ray emission from SNRs due to π^0 decay. Using calculations of particle acceleration they have studied pion production via ion-ion collisions (see section 2.3.6), to estimate the associated γ-ray flux. Their work has shown that γ-ray emission, attributable to neutral pions, should peak in the Sedov phase and then fall off slowly during the remainder of a SNR's lifetime. The γ-ray luminosity around 100 MeV, due to π^0 decay, is expected to be rather low, and therefore difficult to detect. The flux above $\sim$100 GeV though, was predicted to be well above the sensitivity of atmospheric Čerenkov telescopes. It was pointed out that this high-energy flux should be detectable, because the expected hard flux ($\alpha \sim 4$) from SNRs should stand out against a softer ISM background.

A recent publication by the CANGAROO collaboration (Enomoto et al., 2002) reports a detection of TeV γ-rays from the SNR RX J1713.7-3846, at the 14.3 σ level. They claim that their data, and an EGRET upper limit from a nearby unidentified source RX J1714-3857 (Hartman et al., 1999), is best fitted by a model which produces γ-rays via neutral pion decay, and present their results as evidence for cosmic proton acceleration in SNRs. This claim has been strongly disputed, however, by Reimer and Pohl (2002), who use the complete EGRET dataset for the nearby source, to show that the GeV flux required by π^0 decay models, significantly exceeds the EGRET measurements. As a means of settling this debate, Alvarez-Muñiz and Halzen (2002) propose that a detection of neutrinos from this source, attributable to the decay of charged pions which are created alongside the neutral pions, could unequivocally distinguish between hadronic and leptonic emission mechanisms. Furthermore, they estimate the associated high-energy neutrino flux for RX J1713.7-3846 and other TeV sources.

Given the importance of TeV observations of SNRs in the cosmic ray origin debate, and their usefulness in elucidating γ-ray emission mechanisms,

there is little doubt that such observations will form a significant part of future observing programs with the next generation of ground-based γ-ray instruments.

2.5 Pulsars – An Overview

Pulsars (so-called because of their pulsed emission, as observed on Earth) are rapidly rotating, highly magnetised, neutron stars, which produce polarised non-thermal emission by converting rotational energy into dipole radiation. The generally accepted model for pulsar emission is the light-house model, whereby the observed photons are emitted at one particular point on the pulsar and, therefore, only seen when that point rotates into an observer's field-of-view. For a given pulsar, the observed pulse period (typically of the order of P $\approx$ 1 s) repeats with a very high degree of accuracy, down to 10^{-15} (Kundt, 2001), placing pulsars amongst the most accurate clocks available to mankind.

To date, more than 1400 pulsars have been observed at radio energies. About 50 of these are seen in X-rays, but only 6 have been detected by EGRET above $\gtrsim$ 5 GeV. No pulsed emission from pulsars has been detected by Atmospheric Čerenkov telescopes, although several non-statistically significant reports were published in the 1980s. At present, two main models attempt to explain high-energy pulsed emission from pulsars. The polar cap model contends that high-energy photons are produced near the pulsar's polar cap, whereas the outer gap model argues that they are produced in a vacuum gap, far out in the magnetosphere. The two models predict conflicting consequences for TeV-scale detections and so are extremely important in the impetus which they provide for observations at TeV energies. Further details are provided in section 2.7. Recent reviews include Konopelko et al. (2002) and Harding (2001).

2.6 Pulsar Characteristics

2.6.1 Pulsar – Neutron Star Relationship

In their discovery publication, made using data from the Cambridge dipole array, Hewish et al. (1968), postulated two possible explanations for pulsars. Both theories contended that pulsed emission arises from very compact celestial objects, most likely white dwarfs. The first assumed stellar oscillation as the origin, while the second argued for rapid stellar rotation.

Periodic behaviour in astrophysics may generally be attributed to either oscillation, orbital motion around another object, or rotation of a celestial object. As the first pulsars detected by Hewish et al. displayed short periods, of the order of $\sim$1 s, oscillation was soon ruled out—based on the analysis of Melzer and Thorne (1966) who showed that a white dwarf could not radially oscillate with a period of less than $\sim$8 s. It was also clear that orbital motion of a satellite around a white dwarf star could not produce the stable emission observed by the Cambridge team (Pacini and Salpeter, 1968). Stellar rotation, therefore, appeared to be the only reasonable explanation, and after the discovery of the Crab pulsar, with a period of 33 ms (Staelin and Reifenstein, 1968), it was clear that a only an extremely compact neutron star could sustain such rapid rotation without fragmenting.

2.6.2 Rapid Rotation

The origin of a pulsar's rapid rotation may easily be explained using a simple conservation of angular momentum argument. If $L_s = I\omega_s$, and $L_{NS} = I\omega_{NS}$, are the angular momenta of the progenitor and neutron stars, respectively, where I and ω represent their moments of inertia and angular frequency respectively, then, if conservation of angular momentum holds during stellar collapse, the following argument should hold true

$$L_s = L_{NS}$$

$$\Rightarrow \frac{I_{NS}}{I_s} = \frac{\omega_s}{\omega_{NS}}$$

Since the angular frequency ω, of a star with period P, is equal to $2\pi/P$; then

$$\frac{I_{NS}}{I_s} = \frac{P_{NS}}{P_s}$$

and since the moment of inertia I, goes as R^2, where R is the stellar radius; the neutron star is born with a period

$$P_{NS} \simeq P_s \left(\frac{R_{NS}}{R_s}\right)^2$$

For a characteristic neutron star radius of $R_{NS} \sim 10^4$ m, and a progenitor star with a typical radius of $R_s \sim 10^9$ m, rotating with a period of the

order of a few weeks ($P_s \sim 10^6$ s), this yields an expected rotation period P_{NS}, for the neutron star of the order of 0.1 ms. In reality, of course, this is a rather simplified calculation, as the system would naturally lose some angular momentum. Nonetheless, it demonstrates that pulsar periods of the correct magnitude may be obtained by simply considering the star's original rotation.

2.6.3 High Magnetic Field Strength

All pulsars, thus far observed, have been shown to be slowing down. If the slowdown is due to the transformation of rotational energy into another form of energy, then the rate of rotational energy loss may be expressed as

$$\dot{E} = \frac{d}{dt}\left(\frac{1}{2}I\omega^2\right) = -4\pi^2\left(\frac{I\dot{P}}{P^3}\right) \tag{2.1}$$

where $\dot{E}$ is the rate of rotational energy loss, and ω,I, and P, retain their previous meanings. Ostriker and Gunn (1969) estimated that the a neutron star would emit magnetic dipole radiation with a power given by

$$\dot{E} \simeq \frac{2}{3}\left(\frac{B^2R^6\omega^4}{c^3}\right) \tag{2.2}$$

where B corresponds to the surface magnetic field of the neutron star. Assuming that the dipole radiation is the cause of the rotational slowdown, then B can be determined by equating equation 2.1 with equation 2.2. The resultant expression for the surface magnetic field is thus

$$B \simeq 3.2 \times 10^{19}\sqrt{P\dot{P}} \quad \text{Gauss} \tag{2.3}$$

where P is the pulsar period in seconds and $\dot{P}$ is the period derivative (unitless). For a typical pulsar this yields a surface magnetic field of the order of 10^{12} Gauss. At first glance this may seem rather strong. However, its validity can easily be established by considering a simple conservation of magnetic flux argument during progenitor stellar collapse. Since, during collapse, the star may be treated as an almost superconductor, and if the magnetic flux $\Phi \propto BR^2$, is conserved, such that $\Phi_p = \Phi_{NS}$, then

$$B_pR_p^2 = B_{NS}R_{NS}^2$$

$$\Rightarrow B_{NS} = B_p \left(\frac{R_p}{R_{NS}} \right)^2 \tag{2.4}$$

For a typical progenitor star with radius $R_p \sim 10^9$ m, and magnetic field $B_p \sim 100$ Gauss, collapsing into a neutron star of radius $R_{NS} \sim 10^4$ cm, this yields a neutron star magnetic field of magnitude $B_{NS} \sim 10^{12}$ Gauss. So, clearly the estimate of equation 2.3 is not as unreasonable at it may at first seem.

2.7 Models of Pulsar γ-ray Emission

With a wealth of data available from EGRET detected γ-ray pulsars (see section 2.8) and with TeV observations yielding only pulsed upper limits (Hall et al., 2001), many models explaining and predicting pulsar high-energy emission that were proposed in the pre-EGRET era have evolved in the context of new results. The two most popular models under investigation include the polar cap model and the outer gap model. Both have their origins in early models of pulsar magnetospheres and both seem to adequately explain current GeV observations and TeV upper limits. It is in their predictions for future observations that they are separated, and it is these observations that form prime targets for the next generation of γ-ray detectors. In the following sections the original pulsar magnetosphere model is outlined, followed by details of the two main emission models.

2.7.1 The Standard Magnetosphere Model

The electrodynamics of isolated, magnetised, rotating neutron stars, as outlined in the seminal paper of Goldreich and Julian (1969), forms the linchpin of pulsar emission models. In their paper, Goldreich and Julian develop the pulsar spinning neutron star relationship, proposed by Gold (1968) and Pacini (1967), and argue that a pulsar's magnetosphere must contain charged particles, pulled from the neutron star's surface. Their reasoning, as summarised here, is based on the accepted notion of a neutron star as a unipolar conductor.

Far above its surface, the magnetic field of a neutron star may be treated as one due to a magnetic dipole within the star (Figure 2.9). This being the case, a classical electrodynamics treatment, for a magnetic field B, rotating with angular velocity ω, yields an electric field E, in the form

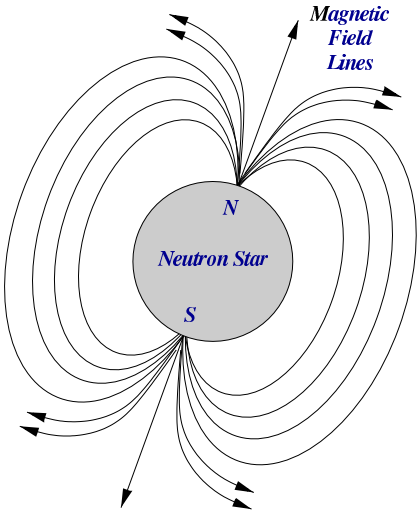

Figure 2.9: Far above the a neutron star's surface its magnetic field may be treated as a due to a magnetic dipole within the star.

$$E = -\frac{(\omega \times r) \times B}{c} \tag{2.5}$$

Thus, the positive and negative charges inside the star experience Lorentz forces in opposite directions, and move to redistribute themselves in such a way that their electric fields counterbalance the magnetic forces. Accordingly, no permanent currents flow in the stellar interior, and $E \cdot B = 0$. For the case of a vacuum magnetosphere, Goldreich and Julian show that outside the star $E \cdot B \neq 0$; and they contend that since the value of $E \cdot B$ must change continuously, from its interior value of zero to its non-zero exterior value, a huge electrostatic force must exist at the stellar surface. Furthermore, they argue that such a force acts along the direction of the magnetic field and that it overwhelms the component of the gravitational force in the same direction, causing plasma to be drawn out into the magnetosphere. In essence, they prove that a vacuum magnetosphere cannot exist.

Assuming that the pulsar can supply enough charged particles to fill its magnetosphere, and ignoring the effects of magnetospheric currents and their associated magnetic fields, the charged density, ρ_c, above the neutron star is given by

$$\rho_c = \frac{1}{4\pi}\nabla \cdot E = -\frac{1}{2\pi c}\,\frac{\omega \cdot B}{1 - |\omega \times r/c|^2} \tag{2.6}$$

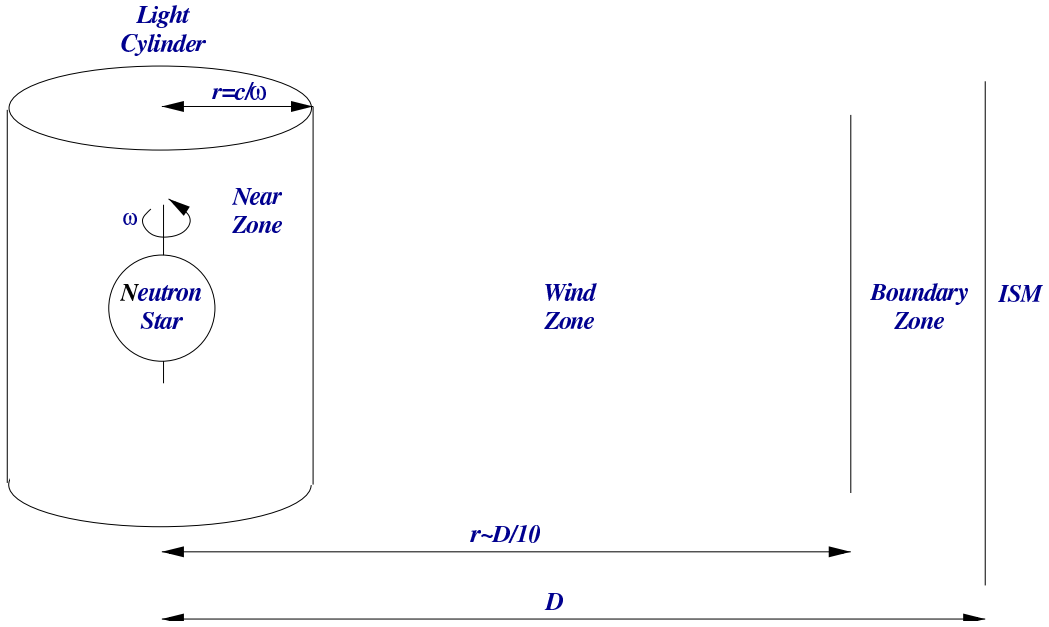

Figure 2.10: The various regions around a rotating neutron star, as defined by Goldreich and Julian (1969).

This is known as the Goldreich-Julian density.

The various regions around the rotating neutron star which were defined by Goldreich and Julian, are presented in Figure 2.10. The *light-cylinder* is a boundary, at a distance of $r_{LC} = c/\omega$ from the axis of rotation, inside which an observer may happily co-rotate with the star. Beyond the light-cylinder an observer would need to exceed the speed of light in order to co-rotate, and accordingly, is precluded from doing so. The region inside the light-cylinder is known as the *near zone*. The *boundary zone begins* at a distance $r \sim D/10$, (where D is the distance from the neutron star to the ISM) and extends to the ISM. The *wind zone*, then, is the remaining region, between the neutron star and the boundary zone.

Charged particle motions in the near and wind zones may be thought of as sliding along magnetic field lines which co-rotate with the pulsar. This is as a result of the large magnitude of the magnetic-energy density, compared to the particle kinetic-energy density, and the fact that the magnetic field lines are almost equipotential. Field lines crossing the light-cylinder are compelled to deposit their charged particles in the wind zone and so leave behind a charge deficit, in so-called charge depleted gaps, in the near zone. In the Goldreich and Julian model, where the rotation and magnetic dipole axes are aligned (aligned rotator), electrons slide out along field lines above

the poles, while protons escape along open field lines near the equator. The surfaces of zero charge density ($\rho_c = 0$), separating the electron and proton lines, are determined by the condition that the star suffers no net charge loss.

The aforementioned charge depleted gaps develop above the *polar caps*, and in supposed *outer gaps* in the region between the zero charge density surfaces and the last closed magnetic field lines close to the light-cylinder (see Figures 2.11 and 2.15). These gaps are of fundamental importance for emission models, as within them the electrostatic potential of the rotating dipole is not balanced by charged particles, and so is free to accelerate any available particles to high energies—sufficient to generate non-thermal radiation. The two main emission models, the Polar Cap model and the Outer Gap model, discussed below, develop the physics of charge acceleration and photon emission within the polar caps and outer gaps, respectively, and offer predictions for high-energy observations.

2.7.2 The Polar Cap Model

Polar cap models have their roots in the early work of Sturrock (1971) and Ruderman and Sutherland (1975) who built upon the Goldreich and Julian magnetosphere model, and advanced the notion of particle acceleration and radiation near the neutron star surface, in the vicinity of the magnetic poles. Sturrock predicted the existence of a strong electric potential normal to the polar cap, sufficient to rip charged particles from the surface and accelerate them along magnetic field lines. Subsequent curvature radiation and pair production cascades were then used to explain observed radio emissions. Ruderman and Sutherland improved on Sturrock's model and proposed the existence of a vacuum gap and potential drop—of the order of 10^{12} V—above the poles, in which charged particles are accelerated to high energies and create Sturrock-type curvature-cascades. Harding (1981) and Daugherty and Harding (1982) provided the first detailed models of high-energy emission and set the scene for modern γ-ray models. After some introductory definitions, the early work and recent developments in polar cap theory are presented here.

Polar Cap Definitions

The edge of the polar cap is defined by the last closed magnetic field lines—or the field lines which just touch the light cylinder, see Figure 2.11. Thus, since in spherical polar coordinates, dipolar field lines obey the equation

$$r^{-1} sin^2\theta = constant$$

the angular radius of the polar cap is given by

$$\theta_{PC} \simeq \sqrt{\frac{r}{r_L C}} = \sqrt{\frac{\omega r}{c}} \tag{2.7}$$

and, assuming $r \ll r_{LC}$, the radius of the polar cap is

$$r_{PC} \simeq r\theta_{PC} \simeq \sqrt{\frac{\omega r^3}{c}}$$

The number of relativistic particles per second (known as the Goldreich-Julian current) flowing from the polar cap, of area $A_{PC} \sim \pi r^2 r_{PC}$, can be estimated as

$$N_{PC}\cdot \simeq A_{PC} \cdot n_{GJ} \cdot c \cdot e^{-1} \simeq \frac{\omega^2 r^3 B_s}{2ec}$$

where B_S is the surface magnetic field. For the Crab pulsar, Sturrock arrived at a value of $\sim 10^{38}$ s^{-1}. Using equation 2.5 and 2.7 the maximum potential difference between the centre and the edge of the polar cap is

$$\triangle\Phi = \int E \cdot ds \simeq \frac{\omega^3 r^3 B_s}{2c^2}. \tag{2.8}$$

For the Crab pulsar this implies a polar cap potential drop of $\triangle\Phi \simeq 2 \times 10^{16}$ V.

Model of Sturrock (1971)

In order to explain the observed radio emission from pulsars[1], Sturrock (1971) argued that the Goldreich and Julian assumption of parallel dipole and rotation axes, needed to be relaxed. Such a modification does not lead to a drastic change in polar cap physics, but rather helps explain the presence of interpulses in the observed lightcurves. By assuming that the electric field above the polar caps is radial for heights $h < r_{PC}$, and transverse for heights $h > r_{PC}$, the Sturrock model provides for a potential normal to the polar cap surface, with a maximum essentially equivalent to the potential difference between the centre and the edge of the polar cap (equation 2.8). This

[1]In 1971, only the Crab pulsar had been observed at frequencies greater than a few hundred megahertz.

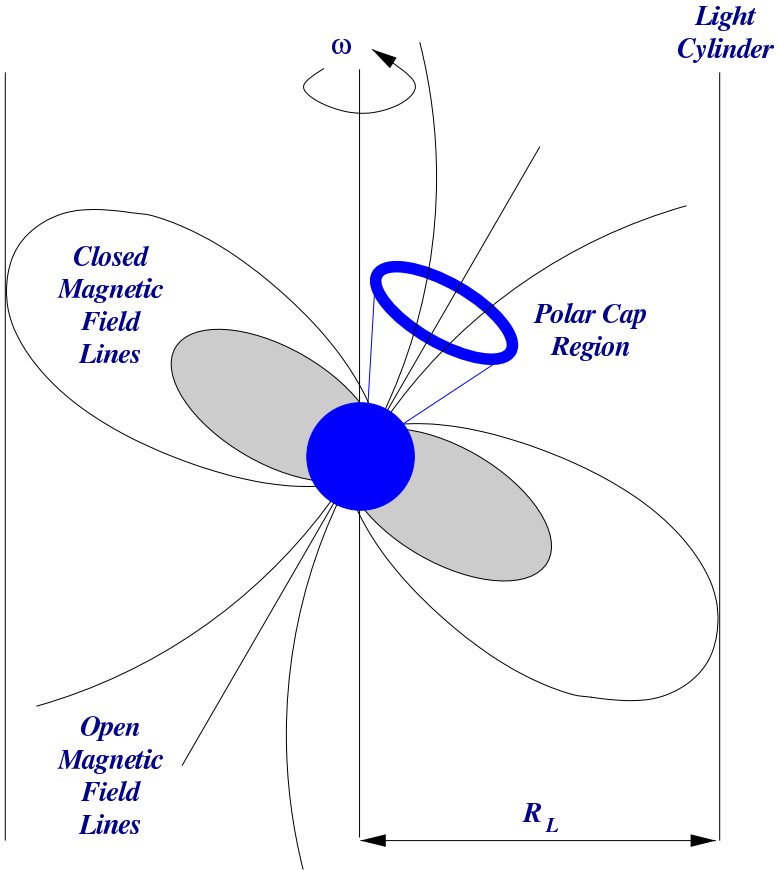

Figure 2.11: The various regions around a rotating neutron star, as defined by Goldreich and Julian (1969).

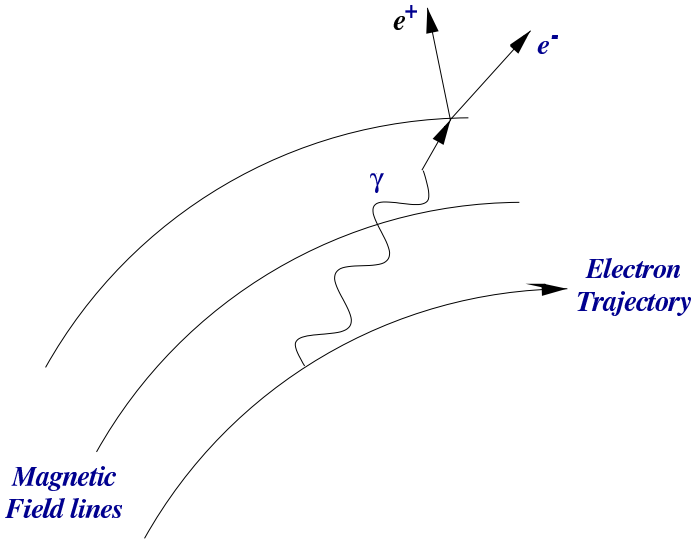

Figure 2.12: Curvature radiated photons, are compelled to cross neighbouring field lines and, therefore, are likely to pair produce into electron-positron pairs.

potential drop is sufficient to pull electrons from the stellar surface and accelerate them along magnetic field lines. Since the field lines are curved, and because the electrons have an assumed negligible transverse kinetic-energy, the electrons move along curved orbits at relativistic velocities and radiate curvature radiation.

A crucial point in the Sturrock model is that the curvature radiated photons create electron-positron pairs by interacting with the surrounding magnetic field lines. Pair production occurs because the curvature photons travel in straight lines and so necessarily cross nearby magnetic field lines, see Fig 2.12. As an example Sturrock showed that for a photon with energy $\sim 10^{10}$ eV, pair production takes place when the magnetic field component transverse to the photon's direction of motion is of the order of 10^9 G; well below estimated pulsar magnetic fields of $\sim 10^{12}$ G. The pair produced charged particles, in turn, emit curvature or synchrotron radiation of their own, thereby creating a pair-production cascade which may explain radio frequency observations.

Model of Ruderman and Sutherland (1975)

Ruderman and Sutherland (1975) expanded on the Sturrock model and attempted to reconcile some of its problems. In particular they addressed the difficulty of maintaining a force-free ($E \cdot B = 0$) condition everywhere as the

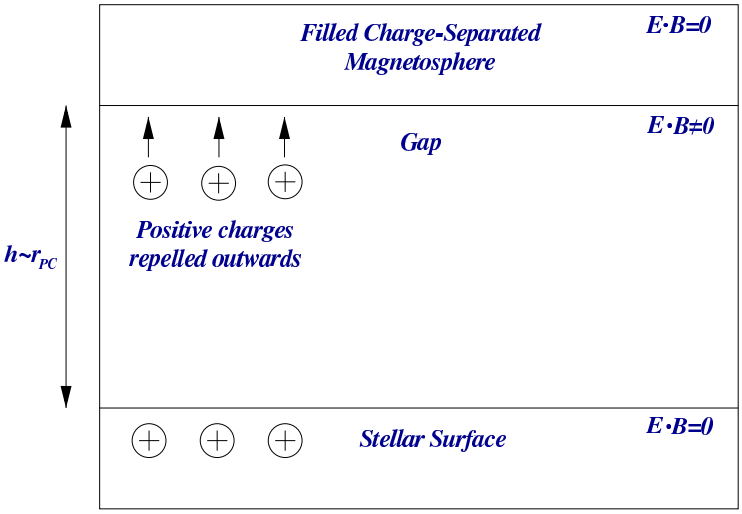

Figure 2.13: In the model of Ruderman and Sutherland (1975) positive ions, due to their higher binding energy, remain on the neutron star surface and repel positive charges in the magnetosphere outwards, thereby creating a vacuum gap in which $E \cdot B \neq 0$.

charge density moves along divergent magnetic field lines. They pointed out that a reasonable expectation for the composition of the neutron star surface is a layer of ^{52}Fe. Thus, given the high binding energy of iron, they showed that positive ions are not expected to be ripped from the stellar surface, as envisaged by Sturrock (1971) and Goldreich and Julian (1969). Instead, the ions remain behind and form an effective repellent for positive charges in the magnetosphere. This repulsion leads to the formation of vacuum gaps above the polar caps, which grow relativistically until they attain a maximum height of $h \sim r_{PC}$, (see Figure 2.13).

Above the vacuum gap, the filled, charged-separated magnetosphere co-rotates with the pulsar, as in the Goldreich and Julian model, with $E \cdot B = 0$. Inside the gaps, however, $E \cdot B \neq 0$, and a potential difference of $\sim 10^{12}$ V exists between the base and the top. The gap is impermanent and so continuously breaks down due to the production of electron positron pairs (so-called *sparking*), with the positrons accelerated out along the open field lines and the electrons pulled back towards the stellar surface. According to Ruderman and Sutherland, this charged particle motion gives rise to the curvature radiation induced pair cascade, and radio emission envisaged by Sturrock (1971). They also point out that although particle acceleration only occurs within the vacuum gap, curvature radiation may persist beyond it, as the particles continue to follow curved dipolar field lines.

The major contribution of Ruderman and Sutherland to modern pulsar physics was the introduction of the vacuum gap, in which $E \cdot B \neq 0$, and in which charged particles may easily be accelerated. Their anticipation of a potential difference of $\sim 10^{12}$ V was challenged, however, when it was pointed out that the reverse flow of electrons to the stellar surface gives rise to electromagnetic showers in a surface layer approximately 10 radiation lengths in depth (Jones, 1981), and that subsequent photonuclear interactions reduce the mean atomic number to $Z < 26$. Jones (1985) found that the cohesive energies for $Z < 26$ nuclei in the presence of strong pulsar magnetic fields ($\sim 10^{12}$ G) are insufficient to bear the polar cap potential of Ruderman and Sutherland. Nevertheless, subsequent polar cap models have predicted potential drops comparable to or greater than, that of Ruderman and Sutherland, for example Arons (1983), Daugherty and Harding (1982) and Muslimov and Tsygan (1992).

Polar Cap Models of Harding (1981) and Daugherty and Harding (1982)

Harding (1981) assumed that pulsed γ-ray emission above 100 MeV arises from curvature radiated photons, produced above the polar cap, that escape the pulsar magnetosphere. The most important attenuation mechanism, preventing all photons from escaping, was assumed to be the magnetic-induced pair production envisaged by Sturrock (1971), which becomes important around 500 MeV. Harding pointed out that the presence of the electric field increases the pair production rate above what it would be for just a pure magnetic field, and so concluded that high-energy γ-rays are more severely attenuated in short period pulsars, for which the rotation induced electric field is higher. The model ignored the primary particle acceleration mechanism and used just a monoenergetic beam of primary particles to radiate curvature photons. The production of synchrotron radiation from secondary particles, was also ignored, although pair production attenuation was a prime consideration. Harding's results agreed qualitatively with γ-ray pulse profiles for the Crab and Vela pulsars, as observed by *COS B*.

In their collaborative effort, Daugherty and Harding (1982) fine-tuned the numerical simulations of Harding (1981). They presented a Monte Carlo method for simulating the electromagnetic cascades produced by primary electrons. In a significant deviation from Harding's previous method, they traced in detail, not alone the curvature radiation of the primary electrons, but also their subsequent electron positron pairs and the quantised synchrotron radiation produced by the pairs. Two separate methods were used to provide the energy for the primary electrons. The first method simply

initiated the electrons with a particular energy at a particular height above the polar cap, while the second method assiduously accelerated each particle from the stellar surface using an acceleration model of the type proposed by Ruderman and Sutherland (1975). Final results revealed no significant differences between the two methods.

The Daugherty and Harding simulations predicted a sharp high-energy cut-off of the γ-ray spectrum, around a few GeV. This cut-off is due to a balance between the decreasing optical depth of the magnetosphere at high energies (higher energy photons are more likely to pair produce in the magnetic field), and the low curvature radiation contribution generated further out in the magnetosphere, where the magnetic field is lower and radii of curvature of the field lines greater. They also predicted that the pulse profiles observed in the γ-ray regime should be consistent across all wavelengths, since the γ-rays and the coherent low energy photons have their origins in the same population of accelerated primary electrons.

Modern Polar Cap Models

Modern polar cap models are essentially refined versions of those developed by Sturrock (1971), Ruderman and Sutherland (1975) and Daugherty and Harding (1982). Major deviations include the introduction of a single polar cap, aligned rotator model (Sturner and Dermer, 1994; Daugherty and Harding, 1994), the provision for thermal emission of charged particles from the neutron star surface (Becker and Truemper, 1997), and allowances for inverse Compton up-scattering of photons to γ-ray energies (Sturner and Dermer, 1994).

The single polar cap aligned rotator concept was introduced by Sturner and Dermer (1994), in their polar cap model which relied upon inverse Compton scattering of optical and soft X-rays near the polar cap (see below). It was then developed by Daugherty and Harding (1994) who used it to explain the possibility of double-peaked pulse profiles, from a hollow beam of curvature radiated γ-rays emanating from a single polar cap. With reference to Fig 2.14, their model may be outlined as follows:

- A hollow cone of curvature radiation is naturally expected from a polar cap, due to the straightening out of magnetic field lines towards the cap centre. This "straightening out" renders it increasingly difficult for curvature radiation to occur, thereby reducing emission from the cap centre.

- For a nearly aligned rotator, in which the magnetic and rotation axes are almost parallel ($\alpha \ll 1$), an observer situated at angle ξ to the

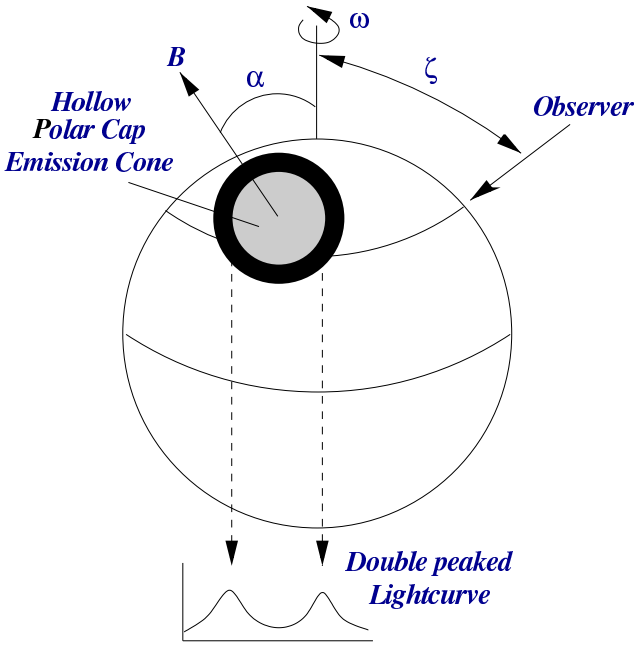

Figure 2.14: Origin of the double peaked lightcurve from a single, nearly aligned rotator: according to the concept developed by Daugherty and Harding (1994) an observer located at angle ξ to the rotation axis will observe two peaks of emission from a polar cap hollow cone of emission, as the edges of the cone pass through his field of view.

rotational axis, will observe two peaks of emission, R_1 and R_2 from the hollow beam as it passes.

Daugherty and Harding argue that this model readily reproduces the $\sim$0.4 phase separation between γ-ray pulses, observed in lightcurves for the Crab, Vela and Geminga. In a subsequent analysis (Daugherty and Harding, 1996) they explained interpeak emission as arising from pair cascades in the polar cap interior, while still maintaining the enhanced rim emission process.

Sturner and Dermer (1994) advocated an alternative mechanism to the conventional curvature radiation pair cascade scenario, for the production of γ-ray emission. They showed that magnetic Compton scattering, of optical and soft X-ray photons in the magnetosphere, could reproduce some of the observed γ-ray spectra and pulse profiles. Primary electrons, with energies which would otherwise not produce curvature radiation, may nevertheless, create pair cascades by first up-scattering ambient photons to γ-ray energies. The inverse Compton model, however, has difficulty producing cascades at heights extending to several stellar radii above the neutron star, due to the

decreasing flux of ambient soft photons with altitude and, accordingly, cannot properly reproduce widely separated double-peaked profiles.

In general modern polar cap models resemble in many ways the original frameworks proposed by early theoreticians in the field. They vary in the details of acceleration above the neutron star surface, in the method by which particles are released from the surface, and in the extent to which inverse-Compton and curvature radiation contribute to the observed spectral characteristics. A crucial common prediction is the severe attenuation, and consequent super exponential spectral cut-off above a few GeV (Nel and de Jager, 1995; de Jager et al., 2001)—due to pair creation in the strong magnetic field close to the pulsar's surface. Outer gap models avoid this cut-off, by producing γ-rays in vacuum gaps much further out in the magnetosphere, where the magnetic field strength, and hence the pair production rate, is lower.

2.7.3 The Outer Gap Model

The outer gap model, was originally developed by Cheng, Ho and Ruderman (1986a,b) and later refined by other workers, e.g. Romani (1996). It serves as an alternative model for high-energy pulsar emission, in which γ-rays are produced in vacuum gaps of the outer magnetosphere. Although it is based on an assumption that vacuum gaps in the outer magnetosphere *may* exist rather than *should* exist, it warrants serious consideration due to its success in reproducing high-energy (GeV-scale) observations. An inevitable consequence of γ-ray production in the outer magnetosphere, where the magnetic field is weaker, is that high-energy photons suffer less magnetic pair-production attenutation. Thus, the outer gap model allows for high-energy (TeV-scale) emission, which should be observable by ground-based air Čerenkov experiments.

Outer Gap Model of Cheng, Ho and Ruderman (1986a,b)

Just as the polar cap model is built upon the basic assumptions of the standard model, so too is the outer gap model of Cheng, Ho and Ruderman (1986a,b) (hereafter CHR). Referring to the expression for the Goldreich and Julian charge density (equation 2.6), it is clear that there should exist null surfaces (defined by $\omega \cdot B = 0$), along which there is no net charge (ie $\rho_c = 0$). A null surface, therefore, separates regions of positive and negative charge within the magnetosphere, as shown in Fig 2.15. With the null surfaces defined, there are two key assumptions of the CHR model:

1. The return current to the neutron star flows along the null surfaces.

2. If a hypothetically frozen charge-separated magnetosphere full of plasma were suddenly unfrozen, so that its charged particles could move freely, then charges of one particular sign beyond the null surfaces will move outwards. CHR developed their model on the assumption that negative charges move out.

Since charged particles cannot cross the null surface ($\rho_c = 0$), the flow of negative charges outwards leaves behind a region of depleted negative charge. This region then acts electrostatically as a region of effective positive charge, with respect to the surrounding magnetosphere. Consequently, positive charges on the stellar side of the null surface are repelled away, towards the neutron star, and a vacuum gap is created. According to CHR, if left uninterrupted, the vacuum gap would grow until the maximum potential drop allowed by the standard model (equation 2.8) develops.

Unlike previous studies which investigated vacuum gaps in the outer magnetosphere (e.g. Michel (1979)), the CHR model limits gap growth by pair production. Inside a gap $E \cdot B \neq 0$, so charged particles from the return current to the neutron star, which enter and leave the gap, are accelerated along the curved magnetic field lines while inside the gap. As they traverse the gap they emit γ-rays due to synchro-curvature radiation or inverse Compton scattering of soft ambient photons. For an extended gap the newly created γ-rays may pair-produce through collisions with the soft photon background ($\gamma + \gamma \rightarrow e^+ + e^-$). If sufficient γ-ray production is sustained then enough electrons and positrons may be created to replenish the gap and limit its growth. The result, CHR maintain, is the formation of a long slab gap along a magnetic field line.

The gap's exact position in the magnetosphere is determined by the requirement that it must persist and that it should not self-destruct. In order to exist, the gap cannot end in a region where $\rho_c = 0$, as charges from that region would immediately flow inwards and destroy it. As such, it must end on a null surface. However, both ends cannot end on a null surface or charged particles would be trapped within, and the gap would quench itself by pair production. Accordingly, the only stable solution is a gap with one end on a null surface and the other end on the light cylinder, where the charges can easily escape. Since gaps outside the light cylinder may provide enough plasma to quench themselves and each other (the probability for pair production increases further out in the magnetosphere), while gaps inside the light cylinder can only limit themselves, it is further required that gaps form only along the last closed magnetic field lines, inside the light cylinder (Figure

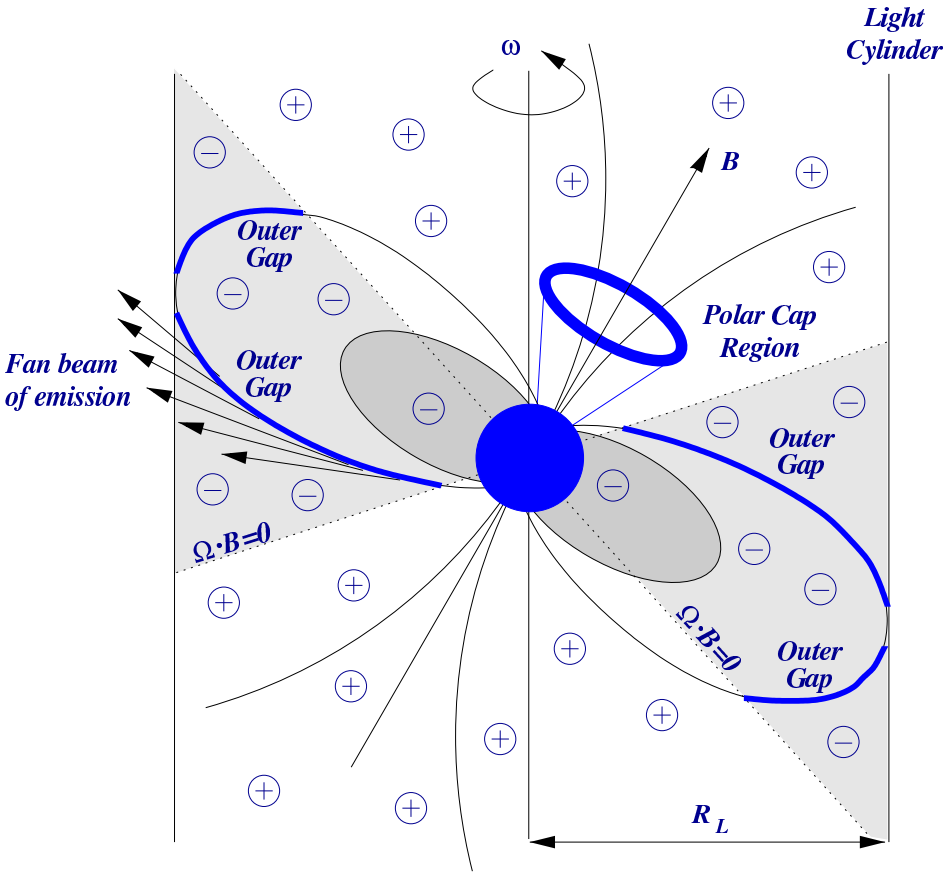

Figure 2.15: Charge separated pulsar magnetosphere according to the outer gap model, showing outer gaps, charge separation, null surfaces ($\Omega \cdot B = 0$), and the polar cap cone of emission from figure 2.11. Slab outer gaps form along the last closed magnetic field lines between the null surfaces and the light cylinder and give rise to fan shape emission beams.

2.15). CHR argue that only two outer gaps of significance can form, the two longer gaps in Figure 2.15. They contend that (1) the two more powerful longer gaps can produce enough γ-rays and electron-positron pairs to quench their smaller counterparts and (2) the the smaller gaps must be thicker than longer in order to sustain themselves. Furthermore, since the smaller gaps are closer to the light cylinder, any emission they do create will suffer severe aberration due to the light cylinder, and therefore may not be observable in any case.

In the CHR model, high-energy γ-ray emission arises as a result of curvature radiation of accelerated charged particles, within the two main gaps. Since electrons and positrons are accelerated in opposite directions, two fan beams of emission (one forward and one backward) form tangential to the last closed field lines, Figure 2.15. Additionally, because the gaps are symmetrically positioned relative to the neutron star, the beam from one gap will be emitted parallel to the beam from the other. Hence, a single observer will record two beams for each stellar rotation, as long as his viewing angle with respect to the pulsar spin axis does not fall outside the fan emission angle θ_0.

By predicting two parallel beams, the outer gap model naturally reproduces the observed double peaked γ-ray phase profiles of the Crab and Vela pulsars. The phase separation between the two pulses is determined, in the CHR model, by a combination of time-of-flight delay for the beam on the far side of the magnetosphere, aberration of the emitted beam directions, and bending of magnetic field lines near the light cylinder, due to retardation and plasma loading. Primary charged particle acceleration in the outer gaps can produce emission from optical to γ-ray wavelengths.

For young Crab-type pulsars, which have small curvature radii, curvature radiation of GeV photons from primary particles accelerated within the outer gaps, forms the main component of the observed γ-ray emission. This helps to explain the observed soft γ-ray spectrum from the Crab pulsar. For Vela-type pulsars with harder spectra, CHR propose that inverse-Compton scattering, of the primary electrons with ambient IR photons, acts as the primary mechanism by which the charged particles emit high-energy γ-rays. In fact, their work predicts a significant TeV flux for curvature emission from Vela-like objects. Although CHR concede that their model cannot reproduce the observed low energy radio emission, they indicate that a combined emission mechanism involving elements of both the polar cap and outer gap models may provide an explanation.

Modern Outer Gap Models

Modern outer gap models attempt to modify the original CHR scenario to better fit the observed patterns of emission in EGRET detected pulsars. In particular the predicted TeV flux for Vela-like pulsars, from inverse-Compton scattering, which exceeds the observed upper limits (Nel et al., 1993) by several orders of magnitude, has been revised. To address the problem, Cheng (1994) proposed another gap mechanism whereby thermal X-rays from the neutron star surface interact with the primary γ-rays to produce pairs. The thermal X-rays take the place of the (unobserved) ambient IR photons, proposed in the original model. All Vela-type outer gap models subsequent to Cheng (1994) adopt this thermal X-ray scenario.

By assuming emission from outer gaps associated with just one pole, as opposed to both poles as in the original CHR model, modern outer gap models can more successfully account for observed lightcurves (e.g. Romani and Yadigaroglu (1995)). These models also better account for low energy radio and optical emission, while maintaining the essential pair production and gap formation mechanisms outlined in the original model.

In general, the high-energy cut-offs for outer gap models are much higher and more gradual than those for polar cap models, due to the more modest magnetic field strength in the outer magnetosphere. Limiting factors at high-energies are, therefore, determined mainly by photon-photon pair production and the available accelerating potential. Indeed, modern outer gap studies of Romani (1996) and Hirotani (2001) suggest a very high-energy pulsed signal, due to inverse-Compton scattering, at about 1 TeV. Although the pulsed flux is predicted to be less than 1% of the pulsed GeV flux, it is nevertheless an attractive target for observations with current and future ground-based γ-ray detectors.

2.7.4 Other Models

There are several other models, besides the popular polar cap and outer gap models, which attempt to explain high-energy pulsar emission. Examples include a scenario in which γ-ray emission originates near the light cylinder (Lyubarskii, 1996), a model in which high-energy photons are generated in vacuum fields in the magnetosphere (Higgins and Henriksen, 1997), and a neutron star wind model (Kirk et al., 2002).

2.7.5 Pulsar Models: A Summary

Polar cap models by their nature—γ-ray production in a region of high magnetic field strength near the pulsar surface—predict sharp cut-offs (super exponential) in the γ-ray flux above a few GeV. Outer gap models, by producing γ-rays further out in the magnetosphere, experience a milder magnetic field strength and, therefore, predict higher energy, more gradual cut-offs (simple exponential), dependent on photon-photon pair production and the electron accelerating potential. As such, the polar cap and outer gap models predict contradictory results for observations above a few GeV. Unambiguous detection of TeV γ-rays from an object would therefore usefully assist in distinguishing between the models.

2.8 Observations of Pulsars above ~100 MeV

The launch of *SAS2* on November 15, 1972 marked the beginning of high-energy pulsar astronomy. Although its unexpectedly short, seven month, lifetime severely limited its potential, it nonetheless provided the first positive high-energy detections of the Crab and Vela pulsars and identified the object which became known as Geminga (Kniffen et al., 1974; Thompson et al., 1975).

The next orbiting γ-ray satellite, *COS B*, launched on August 9, 1975, with a much longer lifetime of almost seven years, provided a wealth of information regarding the γ-ray sky. With regard to compact objects, its success was mixed. On one hand, it managed to detect the Crab and Vela pulsars with enhanced temporal and spectral sensitivity. On the other hand, although it detected more than twenty new γ-ray point sources, primarily along the galactic plane (Hermsen W. et al., 1977; Hermsen, 1980; Swanenburg et al., 1981; Mayer-Hasselwander and Simpson, 1990) its imperfect angular resolution meant these objects were never associated with any pulsed radio sources.

Things improved significantly, however, with the launch of the EGRET instrument on board the CGRO on April 5, 1991. EGRET provided for high-significance detections of six objects above ~5 GeV, and set significant upper limits for about 40 other radio pulsars. Those detected above ~5 GeV include the Crab, Vela, Geminga, PSR B1509-58, PSR B1706-44 and PSR B1055-52. For a full review of EGRET pulsar observations see Thompson (2001). Additionally, three radio pulsars (PSR B1046-58, PSR B0656+14 and PSR J0218+4243) were identified as low-significance possible detections.

The six EGRET detected pulsars all share a common feature—they ex-

hibit double peaked lightcurves (Thompson, 2001). Explanations for their γ-ray emission must, therefore, account for this. For example, as outlined earlier, modern polar cap models envisage a hollow cone of γ-ray emission which when observed from Earth appears as two distinct peaks.

In general, the EGRET pulsars have high magnetic field strengths ($\sim 10^{12}$ G) and relatively young ages ($\sim 10^3$ years). Consistent with expectations for high-energy γ-ray production (see section 2.7) they also have high estimated voltages along their open field lines. Interestingly, in the highest EGRET energy range ($\gtrsim$5 GeV) each of the detected pulsars is dominated by one of the two pulses seen at lower energies. Except for PSR B1706-44, it is the trailing pulse which dominates. In fact, the subordinate pulse is only visible due to EGRET's very low background and may, therefore, be extremely difficult to detect by detectors which suffer from large backgrounds. This observation clearly has implications for current single-instrument ground-based detectors, which suffer an insidious background at lower energies, and indicates a difficulty in observing double-peaked emission.

Apart from Geminga, which appears to be radio quiet, the high-energy γ-ray pulsars have all been observed at radio wavelengths. In general the γ-ray lightcurves do not resemble their radio counterparts. The Crab is a notable exception, as it maintains its pulse profile across all detected energies (more details are presented in section 2.9).

The spectral energy distributions for the six high-energy pulsars peak in the hard X-ray or γ-ray domains. For example the Crab peaks around 100 keV while PSR B1951+32 peaks above 10 GeV. In all cases there is a fall off at higher energies and the upper limits provided by ground-based telescopes are about an order of magnitude below the peak γ-ray luminosity.

Clearly, the upper end of the EGRET energy range currently represents the highest energy of pulsed detections and marks the beginning of unknown and exciting territory. This region is, accordingly, prime target for upcoming space and ground based detectors, such as AGILE, GLAST, VERITAS and H.E.S.S., with interesting results anticipated.

2.9 The Crab Nebula and Pulsar

The Crab complex (NGC 1952 or Messier 1), in the constellation of Taurus, is one of the most extensively studied objects in all astrophysics. Its birth, as a type II supernova, was recorded by early Chinese and Native American astronomers on July 4, A.D. 1054, during which time it was visible in daylight for several weeks (Clark and Stephenson, 1977). In 1791 the British

astronomer John Bevis rediscovered it, and it was subsequently named the "Crab nebula" by William Parsons, third Earl of Rosse, sometime around 1850. In modern times the Crab has formed the basis for many exciting astrophysical discoveries, over a broad range of energies. For example, it was the first object identified as an SNR, the first SNR connected with a central pulsar, and the first pulsar observed at optical, X-ray and γ-ray wavelengths. Indeed, its discovery as a GeV and TeV emitter, in 1971 (Browning et al., 1971) and in 1989 (Weekes et al., 1989) respectively, opened up the field of high-energy γ-ray astronomy. Today, it remains an extremely important object in high-energy astrophysics and is routinely observed as the standard candle at TeV energies. Multi-wavelength images of the Crab nebula are presented in Figure 2.16.

The Crab complex comprises three main components. The *Crab pulsar* at the centre is the remnant neutron star which survived the supernova explosion. It provides a relativistic wind of particles that feeds the *Crab synchrotron nebula* with a steady supply of plasma (de Jager and Harding, 1992; Atoyan and Aharonian, 1996; de Jager et al., 1996). Towards the outer edge of the synchrotron nebula resides a cage-like *composite of filaments*, which consist of stellar ejecta from the supernova itself. These filaments effectively confine the expanding nebula, which in turn accelerates the filaments. Although easily separable in the energy range from radio wavelengths to X-rays, the Crab pulsar and nebula are indistinguishable in γ-rays. This is due to the insufficient angular resolution of current γ-ray telescopes. Hence, all γ-ray observations pertain to the complex as a whole. In general though, it is believed that the observed pulsed emission must originate at the pulsar, while the unpulsed emission (ordinarily referred to as DC emission) arises in the nebula.

Unpulsed Emission

A high-energy inverse-Compton component of the Crab nebula synchrotron emission was predicted by Gould (1965), with strongest γ-ray emission expected in the 0.1–1 TeV range. A variety of experiments attempted to detect this component with mixed, often contradictory, results. For an overview of the early work see the introduction of Weekes et al. (1989). The breakthrough came in 1989 with the detection, by the Whipple collaboration, of a TeV signal (> 0.7 TeV) at the 9 σ level, using the imaging atmospheric Čerenkov technique (Weekes et al., 1989). This result represented a milestone in the development of high-energy γ-ray astronomy and was the first detection of any source with such a high level of statistical significance. Since then the Crab has been detected at TeV energies by at least 13 other groups,

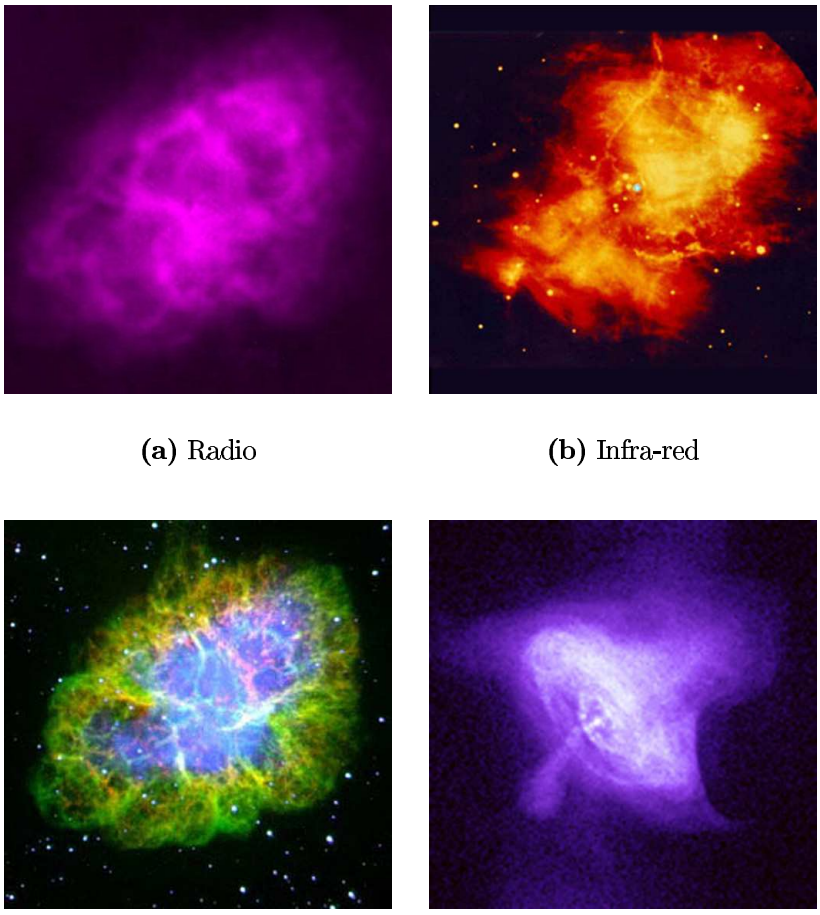

(a) Radio

(b) Infra-red

(c) Optical

(d) X-ray

Figure 2.16: Multi-wavelength images of the Crab complex.

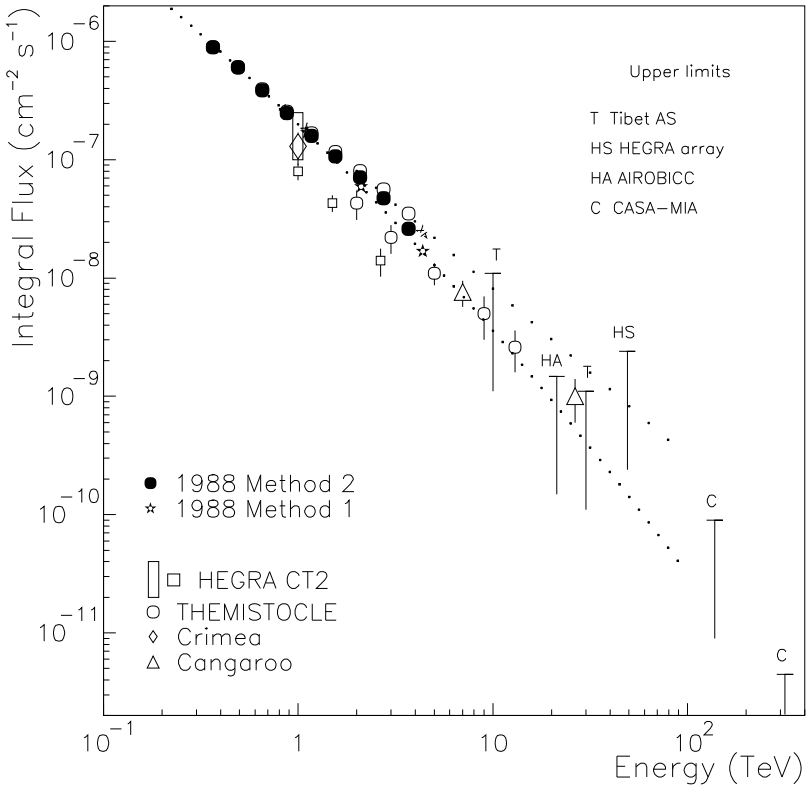

Figure 2.17: Integral spectrum for the Crab nebula in the TeV regime. From Hillas et al. (1998). See also Aharonian et al. (2000).

using ground-based techniques. The Crab's TeV energy spectrum is now well determined, with good agreement between the different groups (Hillas et al., 1998; Aharonian et al., 2000). The Crab integral spectrum is shown in Fig 2.17. Details regarding the determination of this spectrum and its interpretation are given above in section 2.4.4.

Pulsed Emission

Soon after the Crab pulsar (PSR B0531+21) was detected, at radio wavelengths in 1968 (Staelin and Reifenstein, 1968), it became clear that it was unique among the known radio pulsars. Rotating with a period of 33.4 ms, it was the fastest known pulsar at that time and the first pulsar confirmed to be decelerating (Richards and Comella, 1969). Amongst detected γ-ray pulsars the Crab is special, in that it maintains its pulse profile across all wavelengths (i.e. from radio waves to GeV γ-rays), see Figure 2.18. Accordingly, pulsar models which attempt to explain emission from the Crab must ac-

count for this alignment, presumably due to photons of different wavelengths originating from the same place in the pulsar's magnetosphere.

Pulsed γ-ray emission from the Crab, in the energy range 1 MeV to 1 GeV was established in the 1970s and 1980s by a number of balloon (Browning et al., 1971; Albats et al., 1972; Kinzer et al., 1973; McBreen et al., 1973; Parlier et al., 1973) and satellite (Thompson et al., 1977; Bennett et al., 1977; Clear et al., 1987) experiments. The EGRET γ-ray detector on board the CGRO was used to successfully study pulsed emission from the Crab at energies from 100 MeV to $\sim$10 GeV (Nolan et al., 1993; Ramanamurthy et al., 1995; Fierro et al., 1998) during the 1990s. Over the EGRET energy range, the Crab's pulsed component dominates the total observed emission. The observations also indicate a softening of the pulsed spectrum around 1 GeV, and hint at a hardening of the unpulsed component compared to the pulsed above $\sim$1 GeV. Although so-called *Giant Pulses* have been observed from the Crab pulsar in radio waves (Heiles et al., 1970; Staelin and Sutton, 1970) no evidence was found for any correlated increase in γ-ray emission at EGRET energies (Fierro, 1995).

The TeV observations, thus far reported, may be divided into two categories: those which report pulsed emission (albeit with low statistical significance) and those which report just upper limits. Table 2.9 provides a summary of the reported TeV observations. In general positive detections were reported from observations made using the first generation of non-imaging atmospheric Čerenkov telescopes. With one or two exceptions (e.g. Acharya et al. (1992)) only upper limits have been reported since the first statistically significant DC Crab detection using a second generation detector.

Detections	
Author	**Comment**
Grindlay (1972)	Persistent
Jennings et al. (1974)	
Grindlay et al. (1976)	Persistent
Porter et al. (1976)	
Erickson et al. (1976)	Episodic
Vishwanath (1982)	
Gibson et al. (1982)	Episodic
Dowthwaite et al. (1984)	Persistent
Turner et al. (1985)	
Bhat et al. (1986)	Episodic
Acharya et al. (1992)	Episodic

Non-detections/Upper-limits		
Author	**Upper Limit** (cm^{-2} s^{-1})	**Energy** (TeV)
Helmken et al. (1973)		
Weekes et al. (1989)		
Vacanti et al. (1991)	7.0×10^{-12}	>0.4
Goret et al. (1993)		
Sapru et al. (1996)		
Gillanders et al. (1997)		
Borione et al. (1997)		
Aharonian et al. (1999)	5.7% of DC	<1.0
	3.3% of DC	>1.0
Musqère (1999)		
Lessard et al. (2000)	4.8×10^{-12}	>0.25
Oser et al. (2001)	5.5% of DC	> 0.19
Vishwanath et al. (2001)		
de Naurois et al. (2002)	12.0% of DC	>0.06

Table 2.1: Summary of various publications reporting detections and non-detections/upper-limits for pulsed TeV emission from the Crab pulsar.

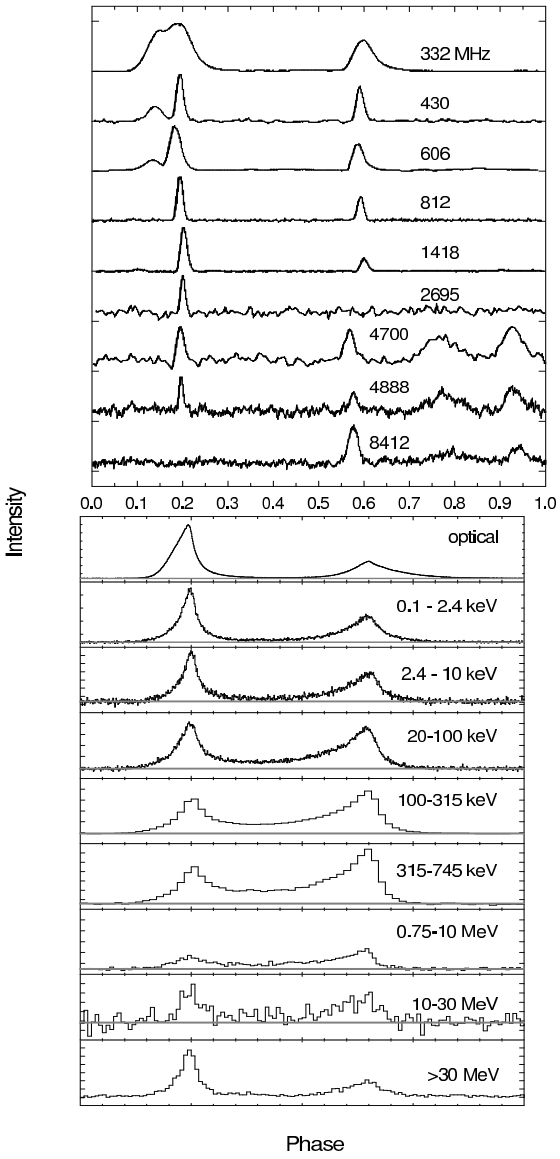

Figure 2.18: Multi-wavelength lightcurves for the Crab pulsar, in the radio range (top, Moffett and Hankins 1996) and at high energies (bottom, Kuiper et al. 2001). From Kanbach (2002).

Recent TeV-scale observations have attempted to constrain the Polar Cap and Outer Gap models (see section 2.7 above) and are beginning to create difficulties for some Outer Gap models, which predict pulsed high-energy emission as high as $\sim$50 GeV. Nevertheless, since the Outer Gap predicted fluxes are very low, the observed upper limits are well within expectation and consequently offer no real discrimination between the models. What is really required are good upper limits or a pulsed detection just above the upper end of the EGRET domain. Until recently the lowest energy TeV-scale measurements were those reported by Lessard et al. (2000) at $\sim$250 GeV. Recent publications by the STACEE and CELESTE solar-tower observatories have reported new upper limits at even lower energies of $\sim$190 GeV (Oser et al., 2001) and $\sim$60 GeV (de Naurois et al., 2002) respectively. Since only upper limits above $\sim$100 GeV have been reported by current γ-ray telescopes, and since Crab DC emission is firmly established by these instruments, the pulsed γ-ray cut-off must lie somewhere in the region 10 GeV to $\sim$200 GeV. Although future instruments such as GLAST and VERITAS will no doubt provide the solution, it is, nevertheless, worthwhile to attempt to improve on the upper limits currently available by improving the available detection and analysis techniques. This thesis work is one such endeavour.

Chapter 3

Detecting Cosmic γ-rays

3.1 Introduction

The atmosphere is a thin gaseous envelope which surrounds our delicate planet. Apart from providing the air that we breathe and the weather systems which sustain us, it acts as an important shield against the harmful and unremitting flux of solar and cosmic radiation. For γ-ray astronomers, however, the atmosphere is both a hinderance and a help. It is a hinderance insofar as it precludes direct ground-based detection of extra-terrestrial γ-rays; while it is a help in that it may be used for their indirect identification.

Atmospheric absorption of cosmic γ-rays necessitates placing γ-ray telescopes onboard satellites in space, beyond the atmospheric shield. GLAST, for example, will directly detect γ-rays as they pass through its solid-state detector (see section 3.2). Space-based astronomical detectors unfortunately, are generally compact devices with limited collection areas. Due to the decrease in γ-ray flux with increasing energy, this inauspicious size limitation imposes an effective upper limit of about 100 GeV on the detection of high energy photons. It is fortuitous though that also at about 100 GeV the signature of atmospheric γ-ray absorption becomes detectable at sea level.

Incoming high energy γ-rays can produce cascades of charged particles, called Extensive Air Showers (EAS), in the upper atmosphere which develop rapidly towards the Earth's surface. It is the observation of these EAS which enables the indirect ground-based detection of γ-rays. At energies from about 100 GeV to 50 TeV EAS are detected by means of the visible Čerenkov radiation they produce on traversing the upper atmosphere, using Atmospheric Čerenkov Telescopes. At much higher energies (>50 TeV) the cascade of charged particles may penetrate deep enough into the atmosphere to allow detection using high altitude particle detectors such as those in the Tibet Air

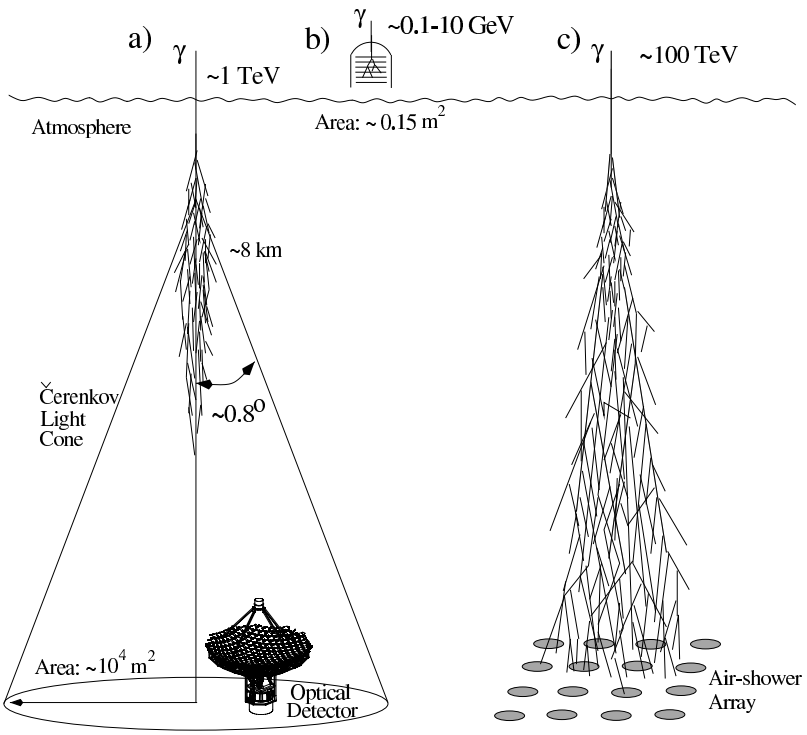

Figure 3.1: Three methods for detecting cosmic γ-rays (a) the atmospheric Čerenkov technique, (b) space-based detectors, (c) high altitude air-shower arrays.

Shower array. Figures 3.1 and 3.2 illustrate the three methods for detecting cosmic γ-rays and the energy ranges involved. In this chapter the direct and indirect detection of astrophysical γ-rays is discussed with emphasis on indirect detection using the Imaging Atmospheric Čerenkov Technique, upon which this thesis work is based.

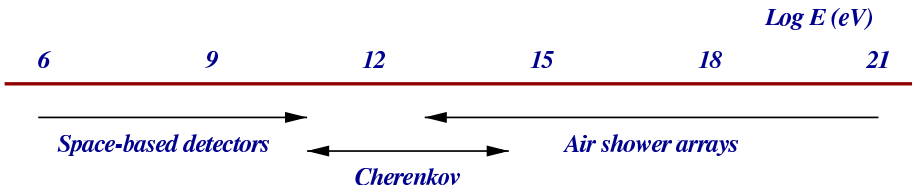

Figure 3.2: Energy ranges for current γ-ray detection techniques.

3.2 Space-Based Detection of Cosmic γ-rays

Pair-production of an electron and a positron is the principal interaction of γ-ray photons with matter above 10 MeV. In the process the electron and positron take up the direction, energy, and polarisation of the instigating photon. Immediate identification of electrons and positrons originating from cosmic γ-rays is therefore, an obvious detection technique for γ-ray astronomy. However, since the radiation length for γ-ray pair-production in air is $\sim$37 g cm^{-2}, and since the Earth's atmosphere has a thickness of $\sim$1000 g cm^{-2}, the direct and immediate identification of cosmic γ-ray pair-production, within a detector, is precluded at the Earth's surface.

Space-based detectors, however, can easily and unambiguously detect the electron and positron pair produced by a primary γ-ray. Their main obstacle, therefore, lies in rejecting the overwhelming flux of background charged cosmic ray particles—which leave signatures not unlike those of γ-rays. Accordingly the main components of satellite γ-ray detectors are:

1. **An anti-coincidence shield** to detect and reject charged cosmic ray particles which are incident at the detector. Anti-coincidence shields normally comprise a thin sheet of scintillator material coupled to photomultiplier tubes, surrounding the main detector.

2. **A tracking detector** to record the tracks of electrons and positrons, enabling reconstruction of the photon's arrival direction. The Large Area Telescope on GLAST, for example, will employ several layers of silicon strip detectors to track electrons and positrons. The EGRET experiment used spark chambers for the same purpose.

3. **A calorimeter** to absorb the electromagnetic particles and record their total energy. This recorded energy may then be used to reconstruct the energy of the incident photon. A hodoscopic arrangement of cesium iodide bars will be used for this purpose on the LAT of GLAST.

The layout of a typical space-based γ-ray telescope, including the three main components, listed above, is presented in Figure 3.3. A γ-ray is identified in such an instrument when: (1) no signal is observed in the anti-coincidence shield, (2) two or more tracks originate from the same position in the tracking detector and (3) an electromagnetic shower is absorbed in the calorimeter. Once a γ-ray photon has been identified, the spatial information recorded in the tracking detector and the size of the shower in the calorimeter, are used to determine its direction and energy.

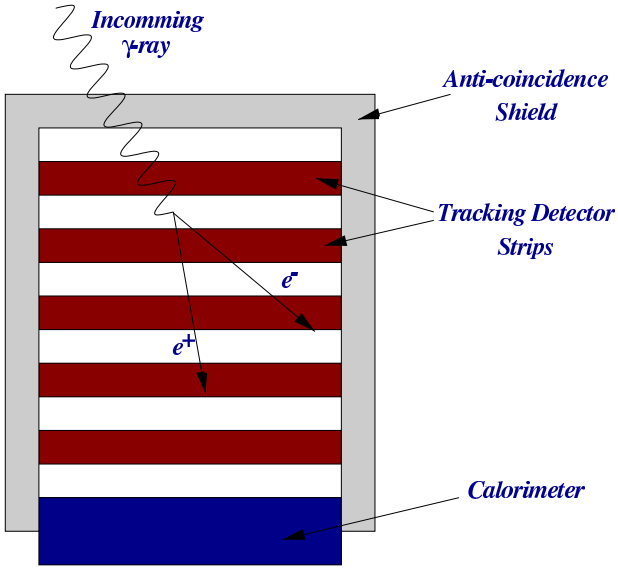

Figure 3.3: Sketch of a typical detector layout for a space-based γ-ray telescope.

Space-based instruments can have an energy resolution of about 10%, an angular resolution of about 3° at 100 MeV, and field-of-view of 20°-40° half-angle. Unfortunately, however, the restricted collection areas imposed by current space-technology are a severe limiting factor for γ-ray observations, especially considering the rapid decrease in γ-ray flux with increasing energy. The effective collection area of EGRET, for instance, was just 1500 cm^2. Although GLAST will have a much greater effective area, at 8000 cm^2, it is still tiny compared to what may be achieved by ground-based Čerenkov instruments at slightly higher energies. Notwithstanding this unfortunate limitation at higher energies, space-based γ-ray detectors remain very valuable facilities for γ-ray observations (see Hoffman et al. (1999), Catanese and Weekes (1999) or Ong (1998) for recent reviews).

3.3 Interactions with the Earth's Atmosphere – γ-rays and Hadrons

On entering the Earth's atmosphere a primary cosmic ray nucleus or γ-ray will interact with atmospheric nuclei, and trigger a cascade of secondary cosmic ray particles and photons which fall as a group towards the Earth's surface. A sufficiently energetic primary may initiate a self-propagating cascade that may contain several thousand secondary particles, spread over an area of the order 10^5 m^2 at ground-level. Hence, such cascades are called

Extensive Air Showers. They were discovered by Pierre Auger in 1938 and are occasionally also referred to as Auger Showers.

EAS detected at ground-level may be used to build up a picture of the instigating primary, including details of its energy and direction of origin. The vast majority of EAS are initiated by cosmic ray nuclei and comprise three distinct, but superimposed, components: nucleonic, muonic and electromagnetic. γ-ray EAS, on the other hand, are generally distinguished by their predominantly electromagnetic nature. In order to identify a γ-ray induced shower and measure the primary photon energy, it is first necessary to extract its signal from the overwhelming hadronic background and then classify it with reference to the known properties of γ-ray showers. Accordingly, an in depth knowledge of the development of both hadronic and γ-ray showers is required for the successful ground-based detection of cosmic γ-rays.

3.3.1 γ-ray Induced EAS

γ-ray EAS are initiated when an incoming primary γ-ray passes close to the nucleus of an atmospheric atom and pair produces. Pair production (Figure 3.4(a)) is the production of an electron-positron pair from a single photon. In the process momentum must be conserved; hence the presence of another body, such as a nucleus, is required, to take up some of the momentum. The cross section for pair-production of a sufficiently energetic ($h\nu \gg 2m_e c^2$) photon is independent of energy. Thus, for the ultra-relativistic case of an air shower the radiation length for pair-production has a value of $\approx$37.7 g cm^{-2}, which means that γ-ray induced cascades are initiated high in the upper atmosphere (total atmospheric depth $\approx$1000 g cm^{-2}).

As illustrated in Figure 3.5, the secondary electron and secondary positron (collectively referred to as secondary electrons) may themselves further interact with other ambient nuclei, via bremsstrahlung (Figure 3.4(b)), giving rise to more γ-rays, which may in turn pair-produce into additional secondary electrons. The cross-section for bremsstrahlung is very similar to that for pair-production, owing to the similarity of the two processes. As such, the pair-production and bremsstrahlung branching process may repeat itself many times down through the depth of the atmosphere, while sufficient ($\sim$ 83 MeV) energy is available.

Initially the electromagnetic cascade grows exponentially, and reaches a maximum of the order of 10^3 particles (for a 1 TeV γ-ray). For all but the very highest energy γ-rays, shower maximum is reached well above the Earth's surface.

After shower maximum has occurred, Compton scattering (Figure 3.4(c)) takes over from pair-production as the main process for photon dissipation,

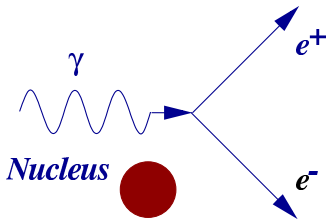

(a) Pair Production.

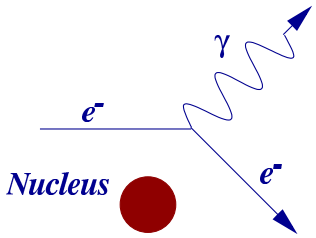

(b) Bremsstrahlung.

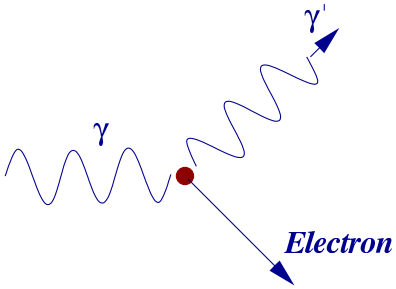

(c) Compton Scattering.

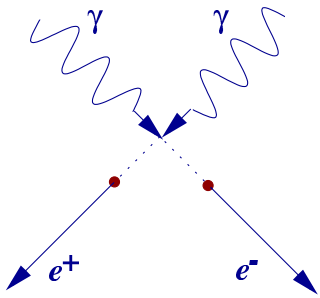

(d) Annihilation.

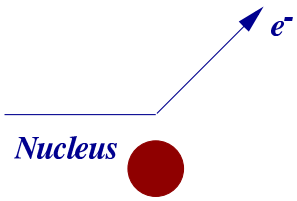

(e) Coulomb Scattering.

Figure 3.4: Air shower interactions.

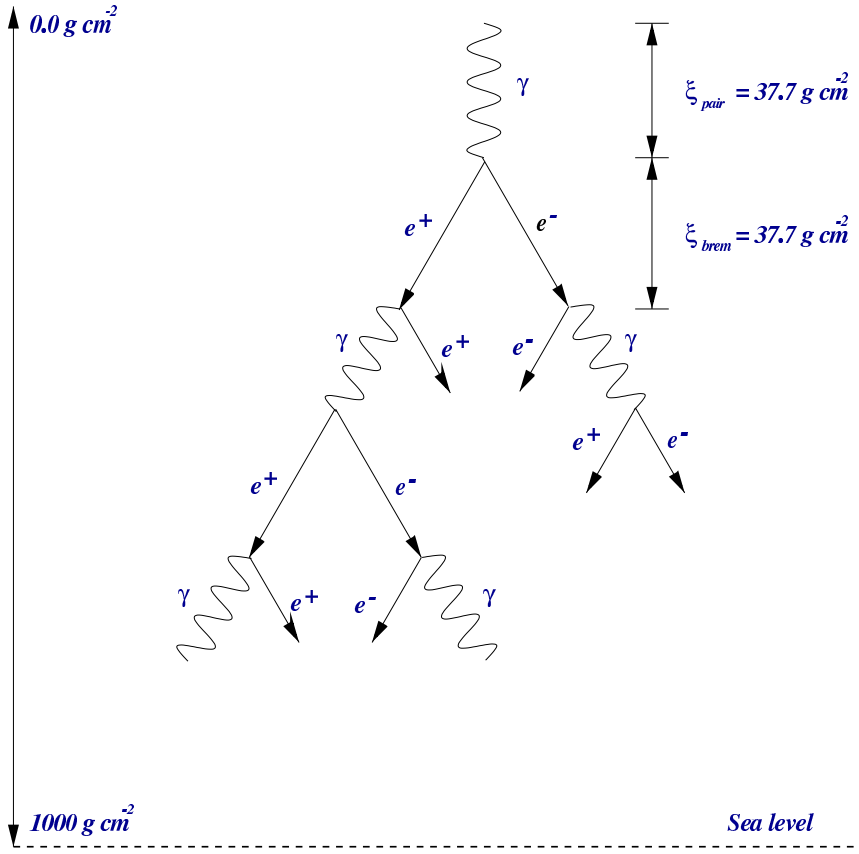

Figure 3.5: γ-ray induced electromagnetic cascade.

and the electrons begin to lose their energy through ionisation rather than through bremsstrahlung. Thus the shower can no longer self-propagate and begins to abate (Cranshaw, 1963). As described in section 3.5.2, Čerenkov radiation is emitted from the secondary electrons until their energies fall below a threshold of 21 MeV. This means that the shower continues to emit Čerenkov light after shower maximum. The cross section for annihilation of secondary positrons (Figure 3.4(d)), with ambient atmospheric electrons does not become important until the individual positron energies reach 0.5 MeV ($\sim m_0c^2$). Annihilation may, therefore, be neglected in the context of particles which emit Čerenkov radiation, but must be accounted for when considering the number of particles which reach ground-level.

Although there is a possibility of muon production in γ-ray induced cascades, through photo-nuclear interactions, the probability is 10^{-4} times that of pair-production. This being the case, γ-ray induced cascades may be considered predominantly electromagnetic in nature and, therefore (as a consequence of the low transverse momentum of the secondary electrons), strongly beamed along the direction of the primary γ-ray. In spite of this forward beaming, the shower may spread out over considerable area (typically 3×10^4 m^2), due in large part to Coulomb scattering (Figure 3.4(e)) of the secondary electrons. As a result, γ-ray induced EAS may cover an area much wider than the physical size of a ground-based detector and any detector lying inside the spread of the EAS should be able to detect it. This large effective collection area is the main advantage of ground-based detection techniques, over space-based techniques, for observing the low flux of high energy γ-rays.

3.3.2 Hadron Induced EAS

Primary charged cosmic ray particles (mainly protons, but also some heavier elements) incident on the Earth's atmosphere, interact with atmospheric atoms, through collisions, to form hadronic EAS. Two types of collision may occur: ionising collisions with atomic electrons, and nuclear collisions with atomic nuclei. The energy transferred in an ionising collision is very small ($\sim$30 eV), as it depends mainly on the electronic binding energy of the target atom, and not on the energy of the projectile cosmic ray. The scattering angle of an ionising collision is similarly insignificant and does not contribute to the lateral development of a hadron-induced air shower. Accordingly, in the context of ground-based γ-ray astronomy the effect of ionising collisions on the primary hadron may be neglected. Nuclear collisions, although less frequent, play a much more substantial part in the development of hadronic EAS and are therefore important considerations for ground-based γ-ray astronomy.

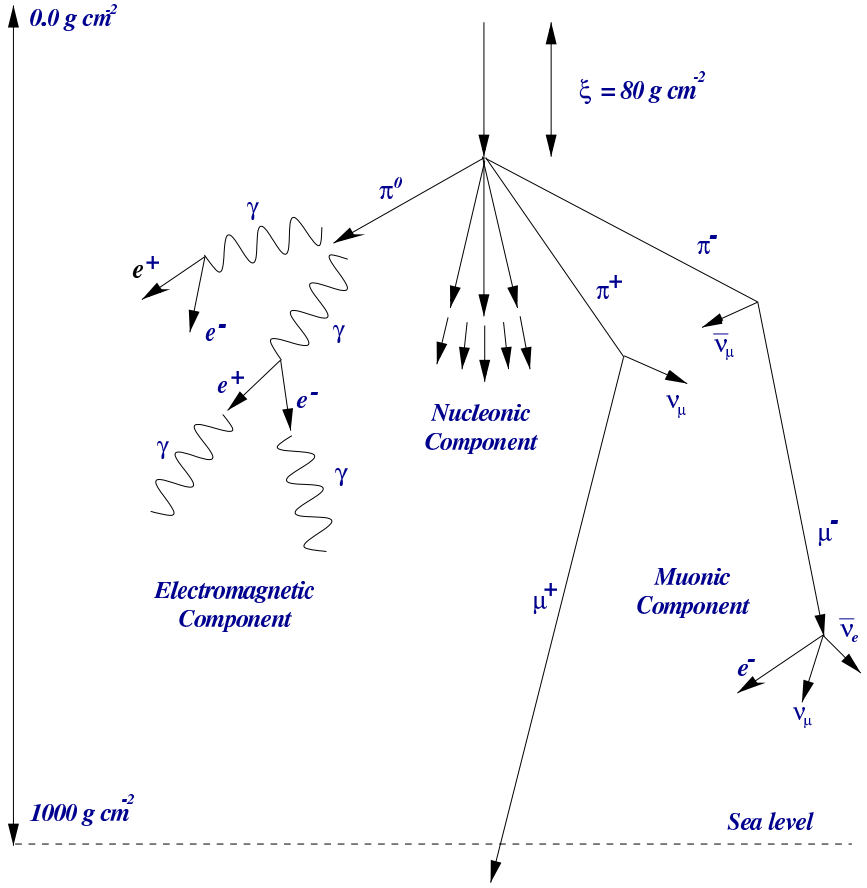

Figure 3.6: Hadron induced extensive air shower, containing three distinct components; electromagnetic, nucleonic and muonic.

The mean free path for a proton in air is $\approx$80 g cm^{-2} (Wilson, 1976), which means that initial hadronic interactions take place much deeper in the atmosphere than initial γ-ray interactions. This is an important difference between γ-ray and hadronic air showers, as it impacts on the number of particles which reach sea level, and hence on the UV content of the Čerenkov photons which are detected (see section 3.7).

On interacting with the nucleus of an atmospheric atom, the primary hadron loses a considerable amount of its initial energy. It may, nevertheless, retain sufficient energy to undergo several more nuclear interactions before its behaviour is significantly altered. In each collision several target nucleons may become detached and move off independently, to undergo nuclear interactions of their own, in a manner not unlike that of the primary hadron.

In this way, a retinue of nucleons propagates downwards through the atmosphere with a combined kinetic energy completely dependent on the initial primary particle. This cascade is referred to as the "nucleonic component" of a hadronic air shower, and is distinguished by its lack of lateral spread and strong directionality along the initial trajectory of interaction.

If the energies of the primary proton or its daughter nucleons are greater than ~1 GeV, mesons (in particular charged and neutral pions) may be produced in the nuclear interactions. Pions are strongly interacting, although short-lived, and may interact with atmospheric nuclei to produce further pions. The charged pions decay into muons, to form the muonic component of the shower, and the neutral pions decay into photons to form the electromagnetic component. The following decay mechanisms are obeyed:

$$\pi^0 \rightarrow 2\gamma \qquad \text{lifetime} \sim 0.83 \times 10^{-16} \text{ seconds}$$

$$\pi^+ \rightarrow \mu^+ + \nu_\mu \qquad \text{lifetime} \sim 2.6 \times 10^{-8} \text{ seconds}$$

$$\pi^- \rightarrow \mu^- + \overline{\nu}_\mu \qquad \text{lifetime} \sim 2.6 \times 10^{-8} \text{ seconds}$$

The muons are very weakly interacting and so play no further part in developing the air shower. They eventually decay into electrons via the following decay processes:

$$\mu^+ \rightarrow e^+ + \overline{\nu}_\mu + \nu_e \qquad \text{lifetime} \sim 2.2 \times 10^{-6} \text{ seconds}$$

$$\mu^- \rightarrow e^- + \nu_\mu + \overline{\nu}_e \qquad \text{lifetime} \sim 2.2 \times 10^{-6} \text{ seconds}$$

Due to their relatively long lifetimes and their relativistic velocities, muons may persist until ground level (their lifetimes are sufficiently spread by the Lorentz contraction) where they form an insidious background for the observation of γ-rays, using isolated ground-based detectors (section 5.8).

Each nuclear interaction in the nucleonic component feeds muons into the muonic component and electrons into the electromagnetic component. Thus the muonic and electronic components are continuously replenished while the nucleons propagate. The electromagnetic component is also self-replenishing, not unlike a γ-ray induced cascade, and so ultimately dominates the air shower and acquires the largest portion of its total energy. Figure 3.6 is an illustration of the three main components of a hadron-induced extensive air showers. Hadron-induced showers are generally less compact and uniform than the purely electromagnetic showers from γ-rays. This is due to their tripartite development and to the large transverse momentum of their constituent particles–in particular pions, as a result of the large opening angles of

pion interactions. Hence, hadrons and γ-rays leave very different signatures in ground-based detectors, enabling discrimination between them.

3.4 Detecting Extensive Air Showers – An Overview

Air shower detectors at ground-level, may be divided into two broad categories: those whose *primary* function is to detect hadronic EAS, and those whose *primary* function is to detect γ-ray EAS. Hadronic cosmic rays, by virtue of their electronic charge, arrive isotropically at the top of the Earth's atmosphere. Detectors designed to detect mainly hadron-induced EAS, are therefore, sensitive to showers from all directions simultaneously. γ-rays, on the other hand, do not arrive isotropically at the Earth, but preserve their initial direction, as prescribed by the source. In order to exploit this direction, dedicated γ-ray detectors are, ordinarily, pointed instruments, with narrow fields of view. Notwithstanding the above, hadron detectors may be used to identify point sources of γ-rays, and γ-ray detectors are sensitive to a background of hadronic EAS falling within their fields of view. This section provides a brief overview of the various detection techniques used to observe both hadronic and γ-ray EAS, with reference to a few topical projects.

3.4.1 Hadronic Air Shower Detectors

The generic method used to detect hadronic EAS is to use an array of particle detectors spread over an area of the Earth's surface. The KASCADE experiment in Karlsruhe, Germany (Klages et al., 1997), for example, simultaneously detects all three components of hadron-induced air showers between 5×10^{14} eV and 10^{17} eV, using an array of 252 particle detectors spread over 40,000 m^2 at ground-level (Figure 3.7). In the experiment liquid scintillator detectors are sensitive to the electromagnetic component; plastic scintillator detectors mounted below iron/lead shielding are sensitive to the muonic component; while a finely segmented central calorimeter comprising ionisation chambers tracks the hadronic and high-energy muonic (>2.4 GeV) component. Muon tracks are additionally observed using streamer tubes in an underground tunnel. Other notable experiments employing ground based detectors, to detect hadronic showers, include the AGASA project in Japan which utlises scintillator detectors, and the Pierre Auger observatory in Argentina which uses an array of water-Čerenkov detectors to detect ultra-high energy cosmic rays.

Figure 3.7: Part of the KASCADE air shower array, in Karlsruhe, Germany.

The HiRes experiment in Utah makes use of a very different technique to observe air showers as they traverse the atmosphere. The technique exploits the luminescence of nitrogen atoms, which are ionised and excited by the passage of charged particles in an air shower. The luminescence occurs in the 300–400 nm band and is detected using an array of photomultiplier tubes, on clear, moonless nights. The technique is known as "air fluorescence" and works well for EAS produced by primary particles with energies above $\sim 3 \times 10^{17}$ eV. The Pierre Auger observatory also utilises this technique, in addition to its water-Čerenkov detectors, in order to provide improved accuracy in the measurement of arrival directions and energies of the highest energy cosmic rays.

A further ambitious use of the air fluorescence technique is proposed for the EUSO and OWL experiments, scheduled for ∼2010. They will observe air fluorescence from high Earth-orbit satellites.

3.4.2 γ-ray Air Shower Detectors

An air shower produced by a cosmic γ-ray may be detected by means of the Čerenkov light emitted from its constituent electrons or, if the energy of the instigating photon is sufficiently high, by the signature of the electrons themselves in a high-altitude air shower array. Čerenkov detectors for ground-based γ-ray astronomy fit into two broad categories: imaging detectors, such as the Whipple telescope, or non-imaging wavefront sampling detectors, such as STACEE and CELESTE. Both types of detector ultise Čerenkov radiation from air showers in a straightforward manner. Imaging telescopes record Čerenkov images from the direction of an expected point source, and subsequently use a moment-fitting analysis to reject background hadronic signals. Wavefront sampling experiments measure the arrival times of Čerenkov photons at an array of detectors and use the temporal spread to identify those events which originated in the direction of the observed source.

Since the atmosphere is virtually transparent to Čerenkov radiation, atmospheric Čerenkov detectors can observe cosmic γ-ray EAS from altitudes much lower than the showers themselves can penetrate. High altitude air shower arrays, on the other hand, rely on the direct detection of the shower itself to identify γ-rays; hence their lofty locations. They identify γ-rays by means of the absence of muons in γ-ray air showers and use fast timing techniques to pinpoint γ-ray sources.

The following sections describe in detail the physics behind the atmospheric Čerenkov technique in general, and the imaging atmospheric Čerenkov technique in particular.

3.5 Čerenkov Radiation

3.5.1 Introduction

Čerenkov radiation is the light emitted when a charged particle moves through a transparent medium, at a velocity greater than the speed of light in that medium. In many ways it is the electromagnetic analogue of the sonic boom generated by high-speed aircraft, such as Concorde, when they travel at supersonic speeds in air. The phenomenon was first observed around 1910, by Marie Curie and others, as a luminescence radiating from transparent substances placed in the vicinity of radioactive sources. The earliest attempt to experimentally elucidate its nature was undertaken by Mallet in the 1920's (Mallet, 1926, 1928, 1929), although no explanation was proposed. Čerenkov, for whom the effect is named, carried out a detailed study between 1934 and 1938, while Frank and Tamm proposed a theoretical explanation in 1937 (Frank and Tamm, 1937). However, despite these advances, it was only after the development of the photomultiplier tube that Čerenkov radiation was observed from a gas (Ascoli Balzanelli and Ascoli, 1953) and from the night-sky (Jelley and Galbraith, 1955). Although Jelley and Porter proposed its application to γ-ray astronomy in 1963 (Jelley and Porter, 1963), it wasn't until 1988 that the first successful identification of an astronomical γ-ray source was made using the Imaging Atmospheric Čerenkov Technique (Weekes et al., 1989).

The following subsections describe how Čerenkov radiation is produced, and how Čerenkov radiation from EAS is detected against the night-sky background.

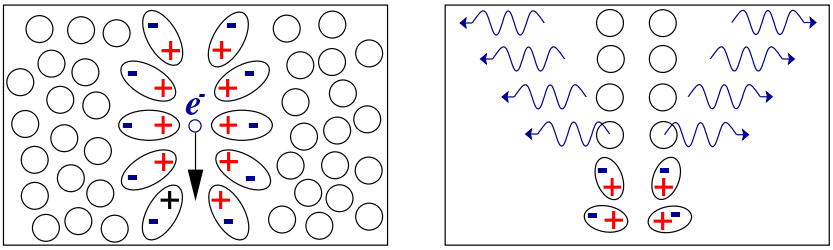

(a) As an electron moves through a dielectric it induces local transient polarisation.

(b) After the electron has passed the atoms relax to their initial state through the emission of electromagnetic radiation.

Figure 3.8: Čerenkov radiation production.

3.5.2 Production of Čerenkov Radiation

As an electron travels through a dielectric medium it induces local transient polarisation in the atoms beside which it passes; this is illustrated in Figure 3.8(a). Once the electron has passed, the atoms are free to relax back into their initial state and do so through the emission of brief pulses of electromagnetic radiation, 3.8(b). Čerenkov radiation occurs when these pulses are emitted coherently.

To understand how coherent Čerenkov radiation is generated, consider the wavefronts produced by an electron with velocity v_e moving through a dielectric medium, for which the speed of light is c_m (Figure 3.9(a)). When $v_e < c_m$, wavefronts are emitted in turn from each of the atoms, A_1, A_2 and A_3. Since these atomic emissions do not occur simultaneously, and since $v_e < c_m$, the wavefronts may never meet and interference cannot occur. However, if $v_e > c_m$ (Figure 3.9(b)), then the emitted wavefronts do overlap and interference can take place. In fact, as is clear from Figure 3.9(b), the wavefronts interfere constructively and produce a large coherent conical wavefront centered on the electron's trajectory, with semi-apex angle θ. This coherent emission is Čerenkov radiation and the cone of emission is referred to as the Čerenkov cone.

Using the Huygens construction of Figure 3.10, the criterion for Čerenkov emission may be derived. For a wavefront emitted by the atom A to be coherent with a wavefront emitted by the atom B, both wavefronts must be emitted at the same angle θ with respect to the electron's trajectory AB. Now, if Δt is the time taken for the electron to travel from A to B, v_e $(= \beta c)$ is the velocity of the electron, and v_m $(= \frac{c}{n})$ is the retarded velocity of light

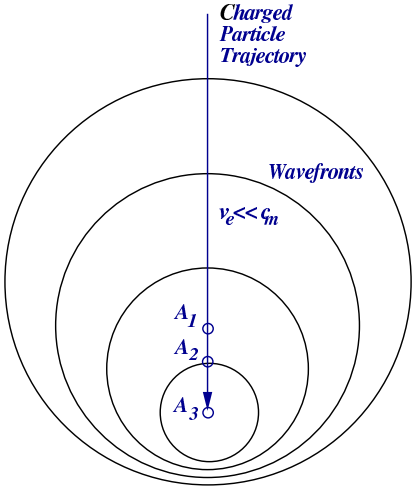

(a) When $v_e \ll c_m$, the wavefronts cannot interfere and no coherent Čerenkov radiation is produced.

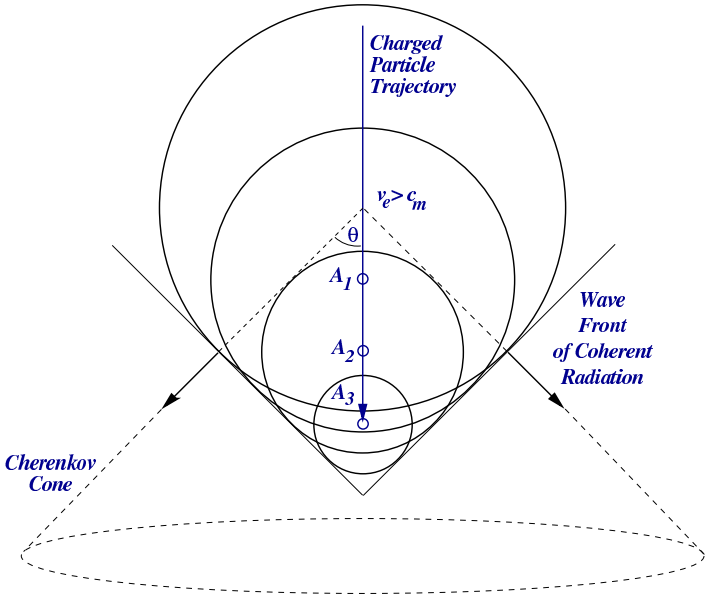

(b) When $v_e > c_m$, the wavefronts interfere constructively and a significant observable wavefront of coherent Čerenkov radiation is produced, in the form of a cone centered on the charged particle's trajectory.

Figure 3.9: Čerenkov radiation production.

in the medium (where n is the refractive index of the medium), then:

$$AB = \beta c \Delta t \tag{3.1}$$

Similarly, if the wavefront emitted at A travels to the point C in the same time period, Δt, then:

$$AC = \frac{c}{n} \Delta t \tag{3.2}$$

Using equations 3.1 and 3.2, we obtain the criterion for Čerenkov emission, known as the *Čerenkov relation*:

$$cos\theta = \frac{1}{\beta n} \quad \left(= \frac{AC}{AB} \right) \tag{3.3}$$

This relation governs the emission of Čerenkov radiation from a charged particle, such that the emission occurs in the form of a cone with semi-apex angle θ, centered about the particle's trajectory. Since negative variables are forbidden ($\beta \not< 0$, $n \not< 0$), the threshold velocity for Čerenkov emission occurs when $\theta \to 0$; hence the threshold velocity is given by:

$$\beta_{min} = \frac{1}{n} \tag{3.4}$$

Using equation 3.4 the minimum energy required by a particle in order to produce Čerenkov radiation is given by:

$$E_{min} = \frac{m_o c^2}{\sqrt{1 - \beta_{min}^2}} \tag{3.5}$$

For an electron moving in air, with refractive index 1.00028, this corresponds to an energy threshold of ~21 MeV. When a charged particle moves at extreme relativistic velocities, i.e. when $\beta \to 1$, there is a maximum angle of Čerenkov emission, given by:

$$\theta_{max} = cos^{-1} \left(\frac{1}{n} \right) \tag{3.6}$$

For air, with refractive index 1.00028, this result in a Čerenkov angle of 1.3°.

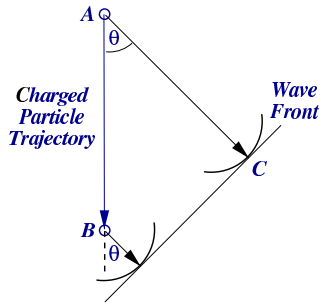

Figure 3.10: Huygens construction used to determine the Čerenkov relation. See text for explanation.

3.5.3 Detecting Atmospheric Čerenkov Radiation

The ability to detect Čerenkov radiation from EAS in the night-sky is the mainstay of the atmospheric Čerenkov technique. It is possible because of the short duration of Čerenkov pulses, when compared with the dominant night-sky background. The night-sky flux is approximately 10^{12} photons m^{-2} s^{-1} sr^{-1}, between 330 and 450 nm. A Čerenkov flash, from a 1 TeV γ-ray primary, lasts $\sim$5 ns and yields about 100 photons m^{-2}, within 100 m of the shower core. By matching the field-of-view of a detector to the angular extent of the γ-ray shower, which is of the order of 1°, then only 1 or 2 photons m^{-2} are detected from the night-sky in 5 ns. Thus, with a suitably focused detector and fast timing electronics, Čerenkov radiation from EAS may easily be detected above the night-sky background (Weekes et al., 1989).

The energy threshold for detecting EAS using the atmospheric Čerenkov technique depends not only on the night-sky background but also on the specific details of the detector used. For an unsophisticated detector, comprising a single photomultiplier tube at the focus of a reflecting dish, the ratio of Čerenkov signal to night-sky noise is simply given by:

$$\frac{S}{N} = \frac{\int_{\lambda_1}^{\lambda_2} C(\lambda)\,\varepsilon(\lambda)\,\Omega A d\lambda}{\sqrt{\int_{\lambda_1}^{\lambda_2} B(\lambda)\,\varepsilon(\lambda)\,\Omega t A d\lambda}} = \int_{\lambda_1}^{\lambda_2} C(\lambda) \sqrt{\frac{\varepsilon(\lambda)\,\Omega A}{B(\lambda)\,t}} d\lambda \qquad (3.7)$$

where

- C(λ) is the Čerenkov photon flux,
- B(λ) is the night-sky background flux,
- $\varepsilon(\lambda)$ is the quantum efficiency of the PMT,

- Ω is the solid angle of observation,
- t is the integration time (longer than the duration of the Čerenkov flash),
- A is the mirror area, and
- λ_1 and λ_2 are the minimum and maximum wavelengths between which the PMT responds.

The smallest detectable Čerenkov pulse, and hence the minimum shower energy, is inversely proportional to the signal to noise ratio. Thus

$$E_{min} \propto \frac{1}{C(\lambda)} \sqrt{\frac{B(\lambda)\, t}{\varepsilon(\lambda)\, \Omega A}} \tag{3.8}$$

This means that the minimum energy air shower detectable by an atmospheric Čerenkov detector, can be optimised by: (1) matching its integration time as closely as possible to the duration of the Čerenkov flash, (2) making its collection area for Čerenkov light as large as possible, and (3) maximising the quantum efficiency of its PMTs. Of course, the efficiency of a detector for detecting cosmic γ-rays, as opposed to all EAS, depends also on its response to the overwhelming background of hadron induced EAS. Thus the efficiency of the instrument and associated data analysis for rejecting hadron events must also be considered. In this context, the Monte Carlo simulation of γ-ray and hadron EAS is discussed below, with emphasis on the simulated differences between both types of shower.

3.6 Monte Carlo Simulations of EAS

The simulation of physical phenomena and detector responses is an important aspect of all high energy physics experiments. It facilitates the recognition of valuable data amongst a sea of background, and provides a basis for development of useful analytical techniques. For ground-based γ-ray astronomy, simulations are particularly important. They provide critical information on the differences between γ-ray and hadron EAS and enable measurements of detector performance and sensitivity.

Several sophisticated air shower simulation packages are currently used by the cosmic-ray community. For high-energy hadron induced showers the CORSIKA and MOCCA packages are mostly widely utilised. They simulate electromagnetic and hadronic cascades in some model atmosphere, using

Monte Carlo techniques, and track the trajectories of all secondary particles to relatively low energies ($\lesssim$1 MeV). Particle accelerator data is used, where possible, to describe the fundamental nuclear interactions.

For γ-ray astrophysics CORSIKA and MOCCA are utilised, together with the ALTAI and KASCADE packages. ALTAI is used primarily by the HEGRA and H.E.S.S. collaborations for simulations below $\sim$50 TeV. For full details on the ALTAI algorithms see Konopelko and Plyasheshnikov (2000). The KASCADE package (Kertzman and Sembroski, 1994) works very well at TeV energies and is used primarily to simulate γ-ray induced EAS. Currently the Whipple collaboration uses a derivative of the original KASCADE package, as modified at Iowa State University (Mohanty et al., 1998).

MOCCA, CORSIKA, ALTAI and KASCADE all have options for the production of Čerenkov radiation, and so are extensively used with atmospheric Čerenkov telescopes. For this thesis work the latest version of the KASCADE package (KASCADE 6) was exclusively used to produce simulated data. Accordingly, some details of the KASCADE simulation process are presented in the next section. Subsequent sections discuss the properties of, and differences between, γ-ray and hadron induced EAS as determined from EAS simulations, in the context of the Čerenkov light they emit. Detector response simulations for the Whipple telescope and analysis of simulated data are detailed at a later stage, in sections 4.10 and 5.5.

3.6.1 The KASCADE Simulations Package

The KASCADE Monte Carlo simulation code was developed by M. Kertzman and G. Sembroski, to simulate air showers in the energy range 0.1–10 TeV. It comprises two separate programs. The first is called "kascade" and is used to simulate shower particles. The second is called "kaslite" and is used to simulate Čerenkov emission from the particles produced by kascade. Both programs follow each particle/photon in detail in 3 dimensions, until it either interacts, decays, falls below its Čerenkov emission threshold, or hits the ground. In kascade all particle and photon tracks are finely segmented into slices of user-specified length. Electrons and positrons can interact via bremsstrahlung while γ-rays may Compton scatter or pair produce. For each slice the ionisation energy loss and change in direction of the particle due to scattering and magnetic effects is calculated, and used to build up a detailed tracking database. The database enables subsequent 3-dimensional reconstruction of the shower from its initial point of interaction, and is used by the kaslite program to determine the number of Čerenkov photons produced by each slice. Wavelength dependent detector parameters, such as mirror reflectivity and PMT efficiency are included in kaslite to ensure only

Čerenkov photons which may trigger the detector are produced. This saves on generating excess photons that cannot be detected, even if they survive atmospheric attenuation en route to the detector. Each photon is propagated at the appropriate Čerenkov angle for its altitude, with random azimuthal directionality. Individual photons are then followed to ground level and used to compile a second database, containing temporal, angular and positional information for all photons which may potentially trigger the detector. Kertzman and Sembroski (1994) provide specific details of all the algorithms and their developmental history.

3.6.2 Longitudinal Development of EAS

Due to the short mean free path for primary γ-ray interactions, γ-ray induced air showers are initiated high in the atmosphere. As the shower develops and falls to Earth its particle population increases geometrically until shower maximum is reached. This occurs at about 8 km above sea level for a 1 TeV γ-ray. After shower maximum the number of particles decreases exponentially as the shower dies away. This longitudinal evolution of a γ-ray induced shower impacts on its Čerenkov profile, as observed at ground-level. Figure 3.11 shows the simulated longitudinal development of showers initiated by γ-ray primaries of various energies. As expected, those showers initiated by more energetic primaries take longer to reach shower maximum and extend to greater atmospheric depths. The longitudinal spread of γ-ray induced EAS are generally different to those of hadron induced EAS (Figure 3.12) with hadronic showers penetrating to significantly greater depths, due to their lower points of initial interaction and their penetrating muonic components.

3.6.3 Lateral Development of EAS and the Čerenkov Light Pool

The lateral development of EAS and the spread of the Čerenkov light pool at ground-level is highly dependent on the longitudinal profile already discussed. At high altitudes, just after initialisation, the spread of both γ-ray and hadron induced showers is relatively narrow. As they travel deeper into the atmosphere they continue to expand laterally until shower maximum is reached. In general maximum spread is wider for more energetic showers as shower maximum occurs later in time and deeper in the atmosphere. After shower maximum, the showers begin to die away, with γ-ray showers fading exponentially and shrinking laterally, while hadronic showers fade more slowly—resulting in significant lateral fluctuations, due to individual muons.

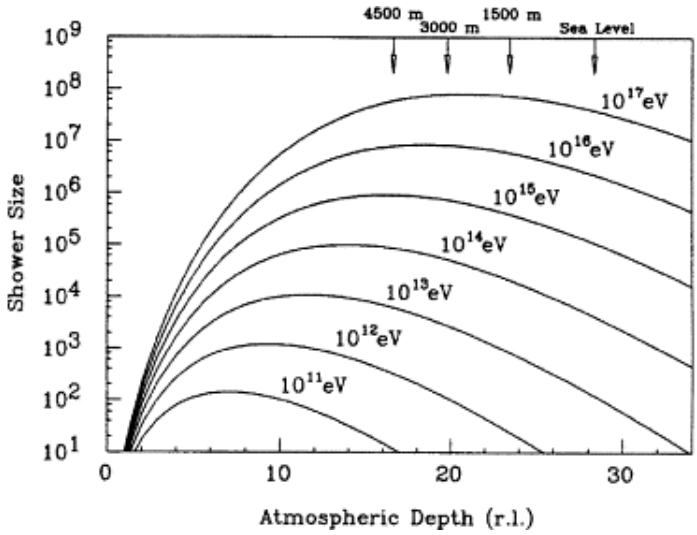

Figure 3.11: Longitudinal development of simulated EAS initiated by primary γ-rays of various energy. Shower size refers to the number of particles in the air shower. Atmospheric depth is given in radiation lengths (r.l.). The radiation length of air is $\sim$37 g cm^{-2}. From Ong (1998).

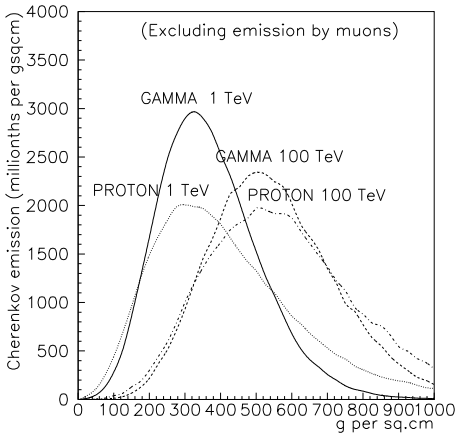

Figure 3.12: Simulated longitudinal developments of simulated γ-ray and proton showers. (Hillas, 1996)

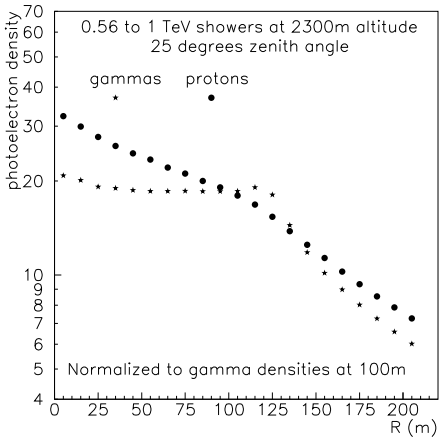

Figure 3.13: Čerenkov light pool for simulated γ-ray and proton showers. (Hillas, 1996)

At shower maximum for a 1 TeV γ-ray the majority of the Čerenkov emitting particles lie within $\sim$21 m of the shower axis, while for a 1 TeV proton the majority of the Čerenkov photons originate within a cylinder of radius $\sim$70 m from the axis. These very different lateral extents naturally result in different Čerenkov light pools at ground level. A plot of the simulated radial distribution of the Čerenkov light pool for both types of shower is presented in Figure 3.13. In the γ-ray light pool three distinct regions are immediately discernable:

1. An inner peak, approximately underneath the shower core. This region is strongly shower dependent, being more prominent for more penetrating showers, and arises as a result of light coming from the shower core.

2. A central flat plateau, known as the rim or shoulder. Photons in here originate mainly in the region around shower maximum and light intensity is a good indicator of primary photon energy. Light from this region is most desireable for γ-ray energy reconstruction and spectral analysis work (Mohanty et al., 1998).

3. The outer region, beyond the rim. The photon intensity decreases rapidly here, with increasing distance from the shower core. This region is the least sensitive to shower-to-shower fluctuations but diminishing photon density renders it less useful for spectral work.

Figure 3.14 illustrates how the Čerenkov angle is responsible for mapping light from different regions of the shower's development onto the Earth's

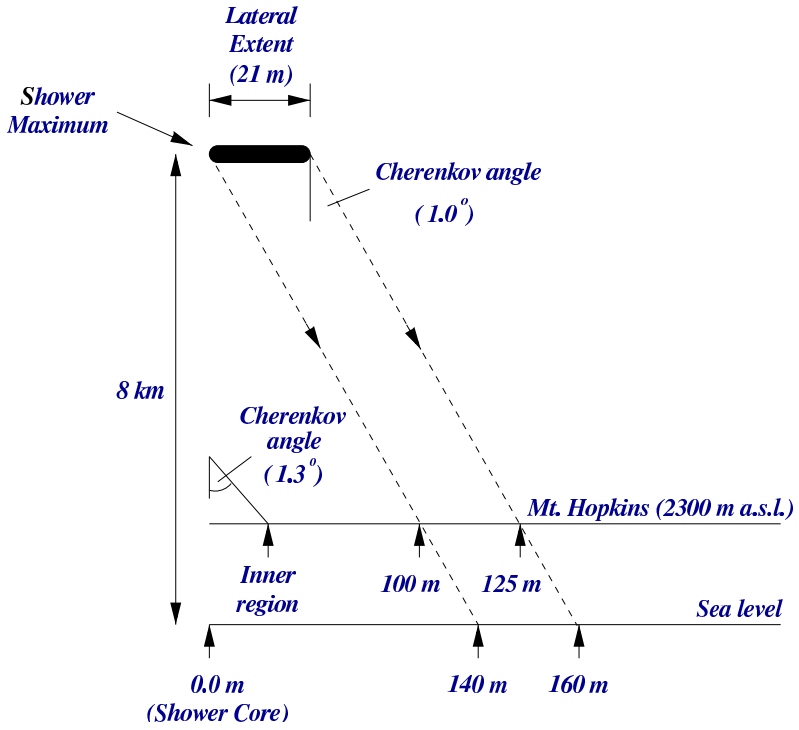

Figure 3.14: Mapping of shower maximum, for a 1 TeV γ-ray air shower, onto the Čerenkov light pool at ground level. For a 1 TeV γ-ray shower, maximum occurs at about an altitude of 8 km a.s.l., and has an lateral extent of about 21 m.

surface. In particular it shows how the lateral spread ($\sim$21 m for a 1 TeV γ-ray) at shower maximum results in spreading of light over a large area of the light pool.

3.7 Differences between γ-ray and Hadron EAS

The overwhelming majority of EAS produced by primaries, with energies in the range 100 GeV - 10 TeV, are instigated by hadrons. In order to identify the small number of γ-ray EAS, amongst this hadronic background, it is of prime importance that there exists a reliable method for distinguishing between them. The solution lies in exploiting the differences between their lateral and longitudinal developments, which are identifiable at ground level.

Figure 3.15 presents the developmental profiles, Čerenkov light pools, and focused Čerenkov images for a 150 GeV proton shower and a 500 GeV γ-ray shower, generated using the KASCADE simulations package. Several notable differences between the two simulations are discussed below:

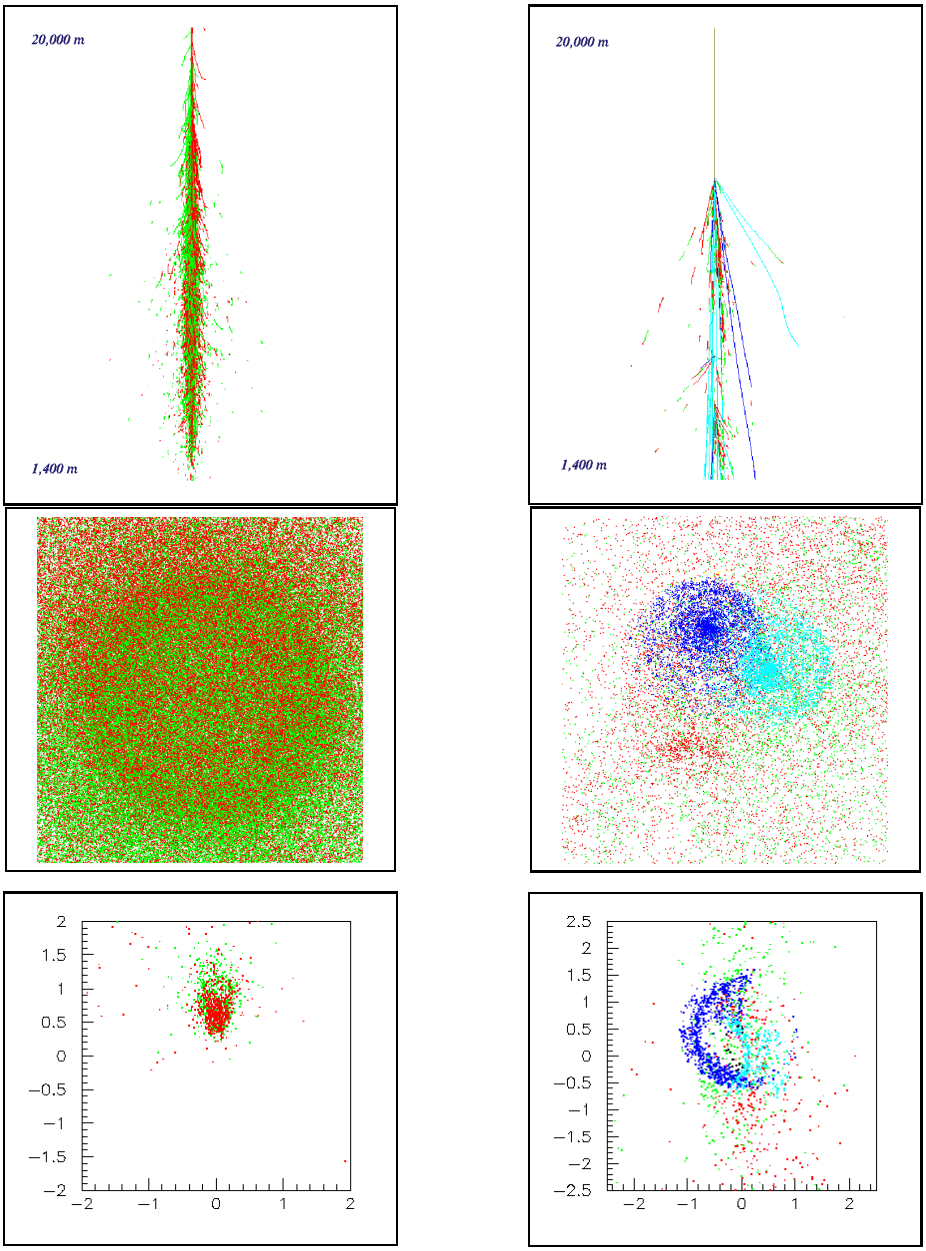

Figure 3.15: γ-ray and hadron simulations: shower development (top), Čerenkov light pool on the ground (center), and Čerenkov photons focused onto the Whipple 10 m detector (bottom). Plots on the left correspond to a 500 GeV γ-ray shower. Plots on the right correspond to a 150 GeV proton shower. Photons arising from electrons and positrons are coloured red and green respectively, while photons due to positive and negative muons are coloured dark blue and light blue respectively. See text for further details. Courtesy G. Sembroski and M. Kertzman.

- **Shower development.** The γ-ray shower's development is compact and uniform, without any major transverse spread from its axis, whereas the proton shower suffers greater spread and general lack of uniformity. It is also clear how the γ-ray shower is initialised at higher altitude than the proton shower, and that the proton shower penetrates to greater depth.

- **Čerenkov light pool.** The light pools at ground level bear the characteristics of the developmental profiles, in that the γ-ray light pool is uniform and centered about its impact parameter (extrapolated point of intersection of the shower's axis with the ground), while the proton light pool is non-centered and fluctuates wildly. The effect of the Earth's magnetic field is clearly visible in γ-ray light pool; photons arising from electrons are coloured green and more concentrated on the bottom, while those arising from positrons are coloured red and concentrated on the top. The Čerenkov ring, although blurred (due to Coulomb scattering), is also visible in the γ-ray pool, and represents the mapping of shower maximum onto ground-level at the Čerenkov angle. Individual Čerenkov rings visible in the proton pool arise from local penetrating muons which reach the ground.

- **Focused images.** When focused onto the focal plane of a telescope, the shower images again bear the general characteristics of the shower profile. The γ-ray image is compact and uniform while the proton image is irregularly shaped and non-uniform. Muon arcs are also discernible in the proton image.

Table 3.1 presents a summary of the main differences between hadronic and γ-ray showers. Identifying these differences, by means of the Čerenkov images they produce in the focal plane of a Čerenkov telescope, forms the basis of the Imaging Atmospheric Čerenkov Technique.

3.8 The Imaging Atmospheric Čerenkov Technique

The Imaging Atmospheric Čerenkov Technique has its origins in the early work of Hill and Porter (1961), Weekes and Turver (1977), Weekes (1981) and Cawley et al. (1983). Simple moment fitting routines were found to be most effective for use with the approximately elliptical EAS images recorded by PMT cameras with relatively poor resolution (MacKeown et al., 1983).

Property	**γ-ray EAS**	**Hadron EAS**
Initial interaction	High in atmosphere	Lower in atmosphere
Atmospheric Penetration	Negligible penetrating component	Muonic component can reach the Earth's surface
UV/visible ratio	Low (as absorbed by the atmosphere)	High (due to sub-ozone penetrating component)
Shower spread	Compact	Broad
Orientation of shower images	Towards point source	Random
Uniformity of particle spread	Uniform and regular	Irregular with significant fluctuations

Table 3.1: Summary of the main differences between γ-ray and hadron EAS.

Indeed, the concept of the imaging PMT camera employed at the Whipple observatory was based on γ/hadron discrimination via image orientation (Weekes, 1981). Hillas (1985) simulated the response of the Whipple 37-pixel camera to EAS produced by both γ-rays and hadrons, with impact parameters varied randomly over an area of radius 250 m. The results clearly showed that an imaging atmospheric Čerenkov telescope, of the type developed at the Whipple observatory, will record different images for γ-ray and hadron induced EAS. For each simulated image, Hillas used a moment-based analysis to calculate six parameters (now often referred to as the "Hillas parameters") which characterise its shape and orientation in the field-of-view. By identifying a "γ-domain" for each parameter, and by specifying that each image should have at least four of its parameters within this domain, Hillas predicted that it would be possible to efficiently discriminate between γ-ray and hadron images using the Whipple telescope.

The 37-pixel camera was subsequently replaced by a 109-pixel instrument (Cawley et al., 1990), and repeated simulations (Lang, 1991) were in excellent agreement with real data recorded by the new detector. A technique, now known as "Supercuts" (Punch et al., 1991), was developed to select γ-ray events based on their calculated parameters, and formed the basis for the first detection of a TeV γ-ray source using the Imaging Atmospheric Čerenkov Technique (Weekes et al., 1989). The Hillas parameters used in contemporary Supercuts analyses (see section 5.11) are described in table 3.2 and illustrated in Figure 3.16. A full description of the moment fitting technique may be found in (Reynolds et al., 1993); the derivation of the parameters is detailed in appendix A. The physical interpretation and use-

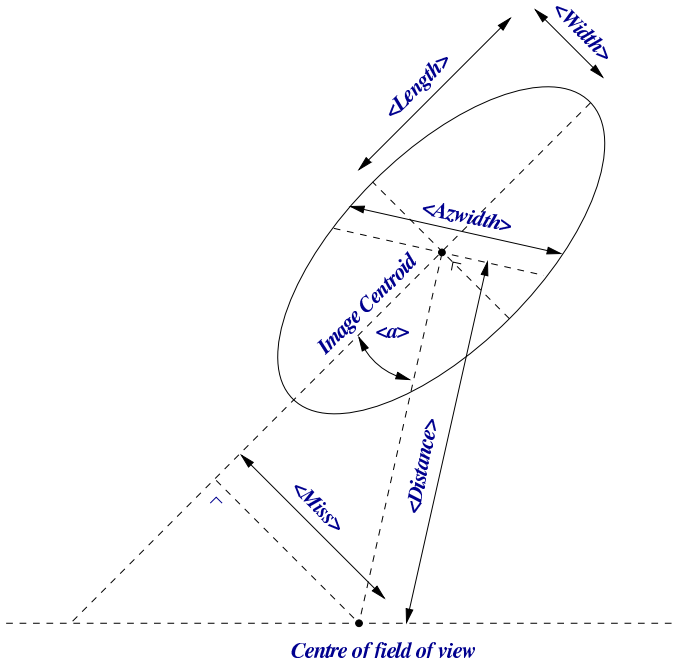

Figure 3.16: The Hillas parameters.

fulness of the Hillas parameters are discussed below (further discussion, in the context of data analysis, is provided in chapter 5):

- The *alpha* parameter is a particularly effective discrimination parameter, as γ-ray EAS, initiated by photons emanating from a source at the centre of the field-of-view, subtend small values of *alpha* (Figure 3.17). Hadron initiated showers, which arrive isotropically in the field-of-view, produce images which are randomly oriented over the complete range of *alpha*. Accordingly, γ-ray events, from the source, should clearly stand out above the background at small values of *alpha*. The "alpha plot" (after full Supercuts analysis) for γ-ray and background events from the direction of Markarian 421, during the strong flares of 2001 (Krennrich et al., 2001a) is presented in figure 3.18. The *miss* and *distance* parameters are used in the calculation of *alpha* ($= sin^{-1}(miss/distance)$).

- The *distance* parameter provides a measure of the impact parameter of a shower; this is illustrated in figure 3.19. Distance is important for spectral analysis of γ-ray events, as it is desireable that only events for which the detector is situated in the "plateau" region of the Čerenkov light pool (section 3.6.3) be used for γ-ray energy estimation (Mohanty et al., 1998).

Size	Sum of the number of counts in all of the tubes; corresponding to the total light content of the image.
Frac3	Percentage of the total light content of the image contained in the three highest tubes.
Length	RMS spread of light along the major axis of the image.
Width	RMS spread of light along the minor axis of the image.
Azwidth	RMS spread of light perpendicular to the line connecting the image centroid with the centre of the field of view; a measure of the width as well as the pointing.
Miss	Perpendicular distance between the major axis of the image and the centre of the field of view.
Distance	Distance from the centroid of the image to the centre of the field of view.
Alpha	Angle between the major axis of the ellipse and a line joining the centroid of the ellipse to the centre of the field of view.
Asymmetry	Measure of how asymmetric the image is. γ-ray images should have a cometary shape with their light distributions skewed towards their source position.

Table 3.2: The Hillas Parameters.

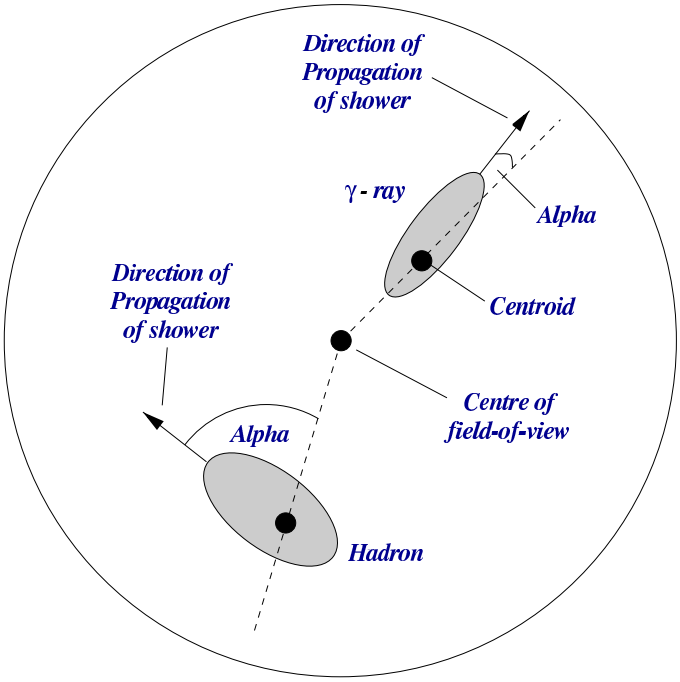

Figure 3.17: The *alpha* parameter. γ-ray images which originate at the centre of the field-of-view have small values of *alpha*. Hadron images which are isotropically distributed about the field-of-view generally have larger values of *alpha*.

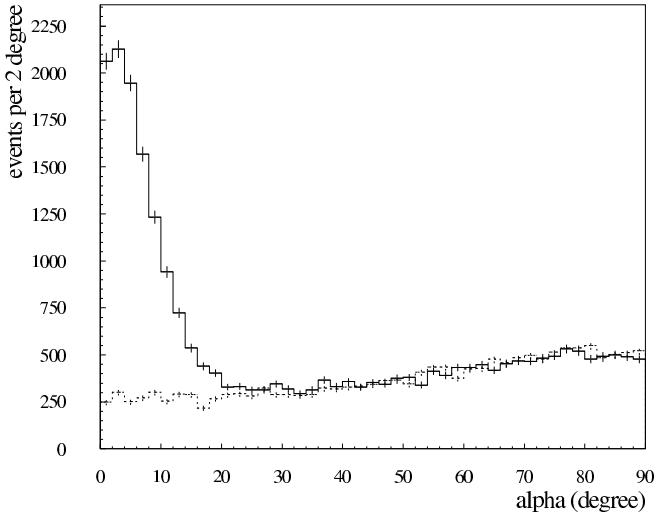

Figure 3.18: The *alpha* plot of γ-ray events ($alpha < 15$) and background events ($alpha > 15$) from the direction of Markarian 421, during strong flaring activity in 2001. From Krennrich et al. (2001a)

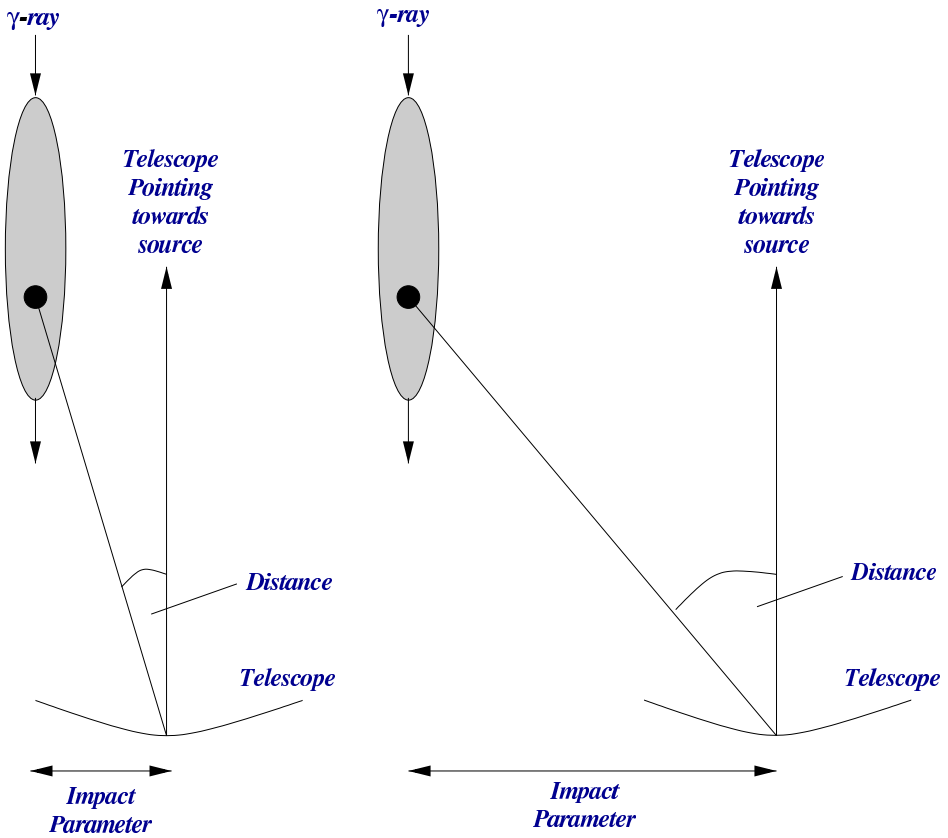

Figure 3.19: The *distance* parameter. γ-rays showers which fall close to the telescope have smaller values of distance than those which fall far from the telescope. In this way *distance* provides a measure of the impact parameter of an air shower.

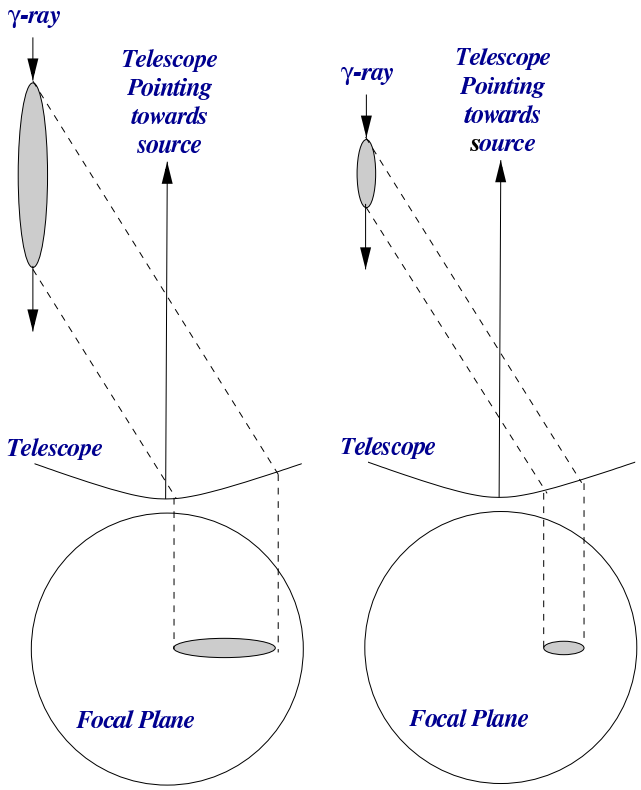

Figure 3.20: The *length* parameter. γ-rays showers which have large longitudinal development subtend large values of *length* in the detector. In a similar way showers with large lateral development subtend large values of *width* in the detector.

- *Length* and *width* provide a measure of the longitudinal and lateral extents of EAS, respectively. This is illustrated in figure 3.20. Although more energetic showers are longer and wider, while less energetic showers are shorter and narrower, *length* and *width* cannot be used to obtain an energy estimate, due to their dependance on impact parameter. For example: two showers of equal energy falling near and far from the detector will have geometrically different *length* and *width* values.

- The *centroid* of an image is the centre-of-gravity of its light content. It effectively maps the location of shower maximum onto the detector, and it is used to calculate the *distance*, and *miss* parameters.

- *Size* is a measure of the total light content of an image, in digital counts. It is a calorimetric parameter, in that it may be used to estimate the energy of a γ-ray event (Mohanty et al., 1998). In the present work

size is a particularly important parameter as γ-ray selection analyses are performed within discrete *size* bands, in order to search for pulsed γ-ray emission from the Crab pulsar at different energies. The *size*-energy relationship and the use of *size* bands are discussed in greater detail in chapter 5.

The Whipple 10 m telescope is used to record Čerenkov images of EAS, within its field-of-view. These images are then fitted with the Hillas parameters and analysed to select γ-ray events from a target source. The next chapter contains a detailed description of the Whipple 10 m telescope and its associated data acquisition system.

Chapter 4

The Whipple 10m Telescope

4.1 Overview

The Whipple collaboration, now known as the VERITAS (Very Energetic Radiation Imaging Telescope Array System) collaboration, is an international research effort involving astrophysicists from academic institutions in Ireland, the United Kingdom and the United States of America. The objective is a search for, and a study of, TeV γ-rays from galactic and extra-galactic sources using ground-based techniques. The collaboration operates and maintains a reflecting ten-metre Imaging Atmospheric Čerenkov Telescope (IAČT) (Figure 4.1) at the Fred Laurence Whipple Observatory on Mount Hopkins, Arizona. The observatory (latitude: 31° 41.3' N, longitude: 110° 53.1' W) is located at an elevation of 2320 metres above sea-level and includes several other optical and infra-red telescopes belonging to the Smithsonian Institution and the University of Arizona. The dry desert conditions and clear dark skies afforded by the Mount Hopkins site are ideal for ground-based γ-ray astronomy.

The Whipple 10 m IAČT may be considered the sum of two parts: the reflector and the detector. The reflector comprises the physical and optical structure of the instrument while the detector encompasses the electronic components which detect and record astronomical data. The characteristics of both the reflector and the detector, together with the various techniques employed in their utilisation, are discussed in detail in this chapter.

4.2 Description

The Whipple 10 m reflector was built in 1969 (Weekes et al., 1972) and is based on the Quartermaster solar-collector design proposed by Davies and

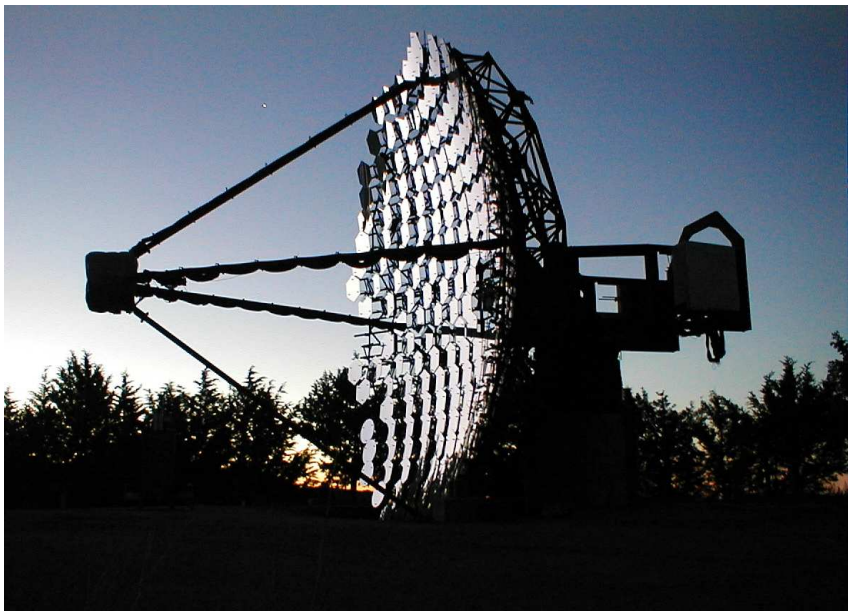

Figure 4.1: The Whipple 10m Telescope in Southern Arizona. The instrument is situated on Mt. Hopkins (latitude: 31° 41.3' N, longitude: 110° 53.1' W) at an altitude of 2320 m above sea level.

Cotton (Davies and Cotton, 1957) and first used for astronomical purposes by Hanbury-Brown (Hanbury-Brown, 1966). It has been used exhaustively for Čerenkov-light imaging since 1982 and remains one of the most productive and active instruments in the field of ground-based γ-ray astronomy. Acting as a large light-bucket the telescope collects, focuses and records images of Extensive Air Showers by means of the Čerenkov-light they produce in the upper atmosphere. The physical and optical characteristics of this instrument and the various techniques used to maintain and test it are discussed in detail in this chapter.

4.2.1 Davies-Cotton Reflector Design

In the Davies-Cotton design (Davies and Cotton, 1957) the dish of a light-collecting instrument is spherical in shape and has a radius of curvature exactly half that of the individual facet-mirrors which comprise its tesellated structure (Figure 4.2). Images collected by the reflecting dish are focused onto a plane at its centre of curvature.

For its use in ground-based γ-ray astronomy a Davies-Cotton detector has many advantages: (1) all facet-mirrors are identical in construction and optical characteristics, (2) mirror alignment is simple, (3) overall detector

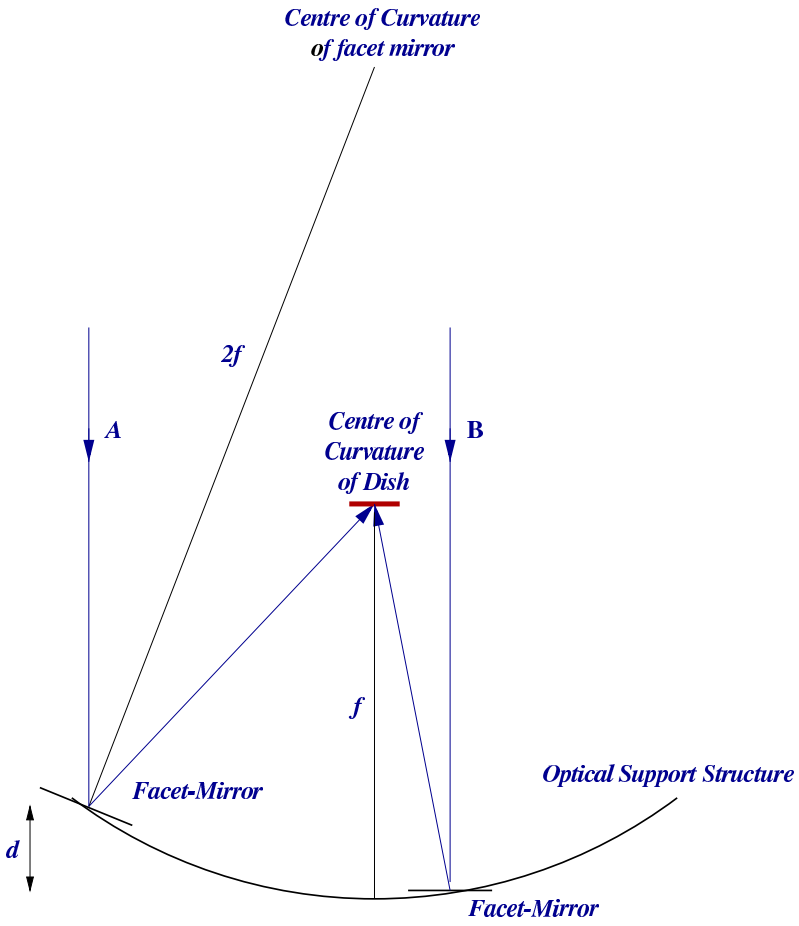

Figure 4.2: The Davies-Cotton reflector design. The spherical dish has a radius of curvature half that of an individual facet-mirror. The instrument is an-isochronous in that the parallel rays of light A and B will strike the focal plane at different times, due to the mirror separation d.

structure is compact and rigid and (4) both on- and off-axis aberrations are superior to parabolic reflectors (Lewis, 1990). A major disadvantage of the design, however, is that it is not isochronous. Its an-isochronous nature arises as a result of its spherical dish. Parallel rays of light from a given source, strike the outer mirrors first and begin their reflected journeys towards the focal plane before those striking the inner mirrors do so (Figure 4.2). Accordingly, there is some temporal broadening of light pulses recorded by the instrument and a subsequent reduction in the signal-to-noise ratio. For the Whipple reflector (see section 4.2.2) this pulse broadening is of the order of 6 ns approximately. In Čerenkov-light imaging short integration times are necessary in order to minimise contamination from the stochastic night-sky background. As such, the an-isochronous behaviour of the Davies-Cotton reflector is an undesirable property of an otherwise very suitable instrument. However, it does not impose a serious limitation to the search for cosmic point sources of γ-rays.

4.2.2 The Whipple 10 m Optical Reflector

The Whipple 10 m optical reflector consists of 248 identical spherical facet-mirrors mounted on a tubular steel framework and arranged in a hexagonal pattern of nine concentric rings (Figure 4.3). Each facet-mirror is hexagonal in shape, composed of 1 cm thick spherically-ground glass and individually mounted on a manually adjustable tripod structure for easy alignment. With a linear extent of 61 cm across, the mirrors conjointly provide an effective reflecting surface of 75 m^2. To obviate unwanted absorption of ultraviolet light by the glass substrate, the mirrors are front-aluminized and re-coated regularly. The metal structure forms a spherical dish with a 7.3 m radius of curvature, at the centre of which a conical focus-box is held in position by secure quadrapod arms. A large concrete pedestal holds the detector's alt-azimuth mount and several lead counterweights provide balance. To conform with the Davies-Cotton design the mirrors have a radius of curvature twice that of the structure (i.e. 14.6 m) and are aligned to an "alignment point" 14.6 m out along the optic-axis. With an opening diameter of 10 m the detector forms an f/0.73 focal-ratio system and has a plate-scale of 12.74 cm/deg. The current 490-pixel camera subtends a field-of-view of 3.5°. General dimensions and attributes of the Whipple instrument are listed in Table 4.1.

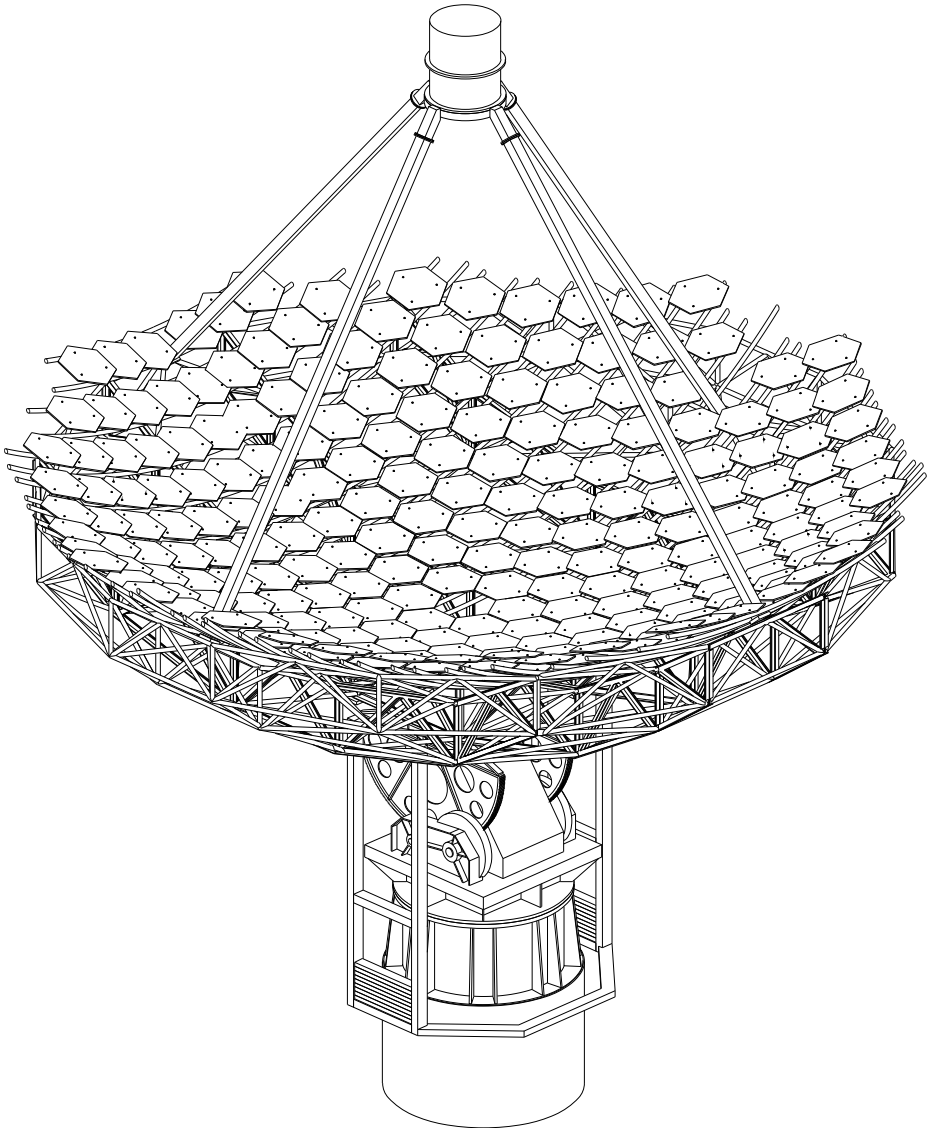

Figure 4.3: The Whipple 10 m detector. The instrument comprises 248 spherical mirrors mounted on a spherically shaped tubular steel framework with a focus-box held in position by secure quadrapod arms.

Attribute	Value
Opening Diameter	10 m
Focal Length	7.3 m
Radius of Dish	7.3 m
Radius of Facet-Mirror	14.6 m
Plate-Scale	12.74 cm/deg
Mount	Alt/Azimuth
No. of Facet-Mirrors	248
Reflecting Surface Area	75 m^2

Table 4.1: General dimensions and attributes of the Whipple detector.

4.3 Mirror Alignment

When considering mirror alignment it is often useful to think in terms of point or extended sources of light in the night-sky. If its mirrors are correctly aligned, light which arrives parallel to a telescope's optic-axis (i.e. from a point source at the centre of its field-of-view) should be reflected onto the centre-point of its focal plane. Rays of light which fall at an angle to the optic-axis (i.e. from the extremities of an extended source) should be displaced on the focal plane in proportion to the plate-scale (Figure 4.4). For a Davies-Cotton type instrument correct alignment is achieved when a normal to the centre of an individual facet-mirror intersects a point at a distance twice the radius of the structure out along its optic-axis. In this orientation the triangle formed by (1) the centre of the facet-mirror, (2) the centre of the focal plane, and (3) the intersection point, is isosceles (Figure 4.5). Thus light arriving parallel to the optic-axis is reflected onto the centre of the focal plane, as desired. Light originating at the intersection point on the optic-axis is retro-reflected along its own path and returns to its source. This important property is used as the basis for the Whipple reflector's alignment procedure and the point of intersection on the optic-axis is referred to as the *alignment point*.

Mirror alignment on the Whipple detector degrades slowly over an observing season and contributes to a deterioration in the instrument's optical image Point Spread Function (PSF). Without regular checking of the PSF and re-alignment of the mirrors the ability to discriminate between γ-rays and hadrons using the IAČT would degrade. Accordingly, mirror alignment plays a critical part in the reflector's maintenance. Mis-alignment is the product of many factors. These include the ambient atmospheric conditions, effects of gravity and the stability of mirror mounts. Notwithstanding the

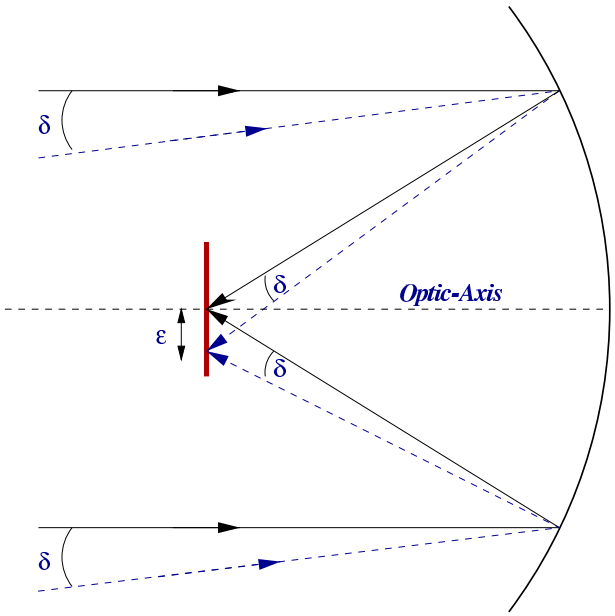

Figure 4.4: Plate-scale when correctly aligned. Rays of light arriving parallel to the optic-axis are focused to the centre of the focal place, rays arriving at an angle δ are displaced on the focal place by amount ϵ, in proportion to the plate-scale.

generally favourable climate of Southern Arizona, the Mount Hopkins site is occasionally exposed to adverse weather. Extreme temperatures, high winds and heavy monsoon showers all contribute to slight movements in the mirror support structures and mis-alignment.

4.3.1 Conventional Alignment Procedure

The conventional alignment procedure for the 10 m reflector is carried out by two people when the telescope is in the *home* position. In this position the instrument is at zero elevation[1] with its optic-axis lying horizontal and pointing towards the alignment point on the control building nearby. A large apparatus comprising a laser, beamsplitter and small translucent screen located at the alignment point is used to check the alignment of each facet-mirror, one at a time (see Figure 4.6). This apparatus is mounted on a pole and may be moved manually by a single operator to direct the laser beam at any desired facet-mirror. The beam is spread out so that it covers as much of the facet-mirror as possible. In this way imperfections in the mirror's

[1] elevation = 90° − zenith angle

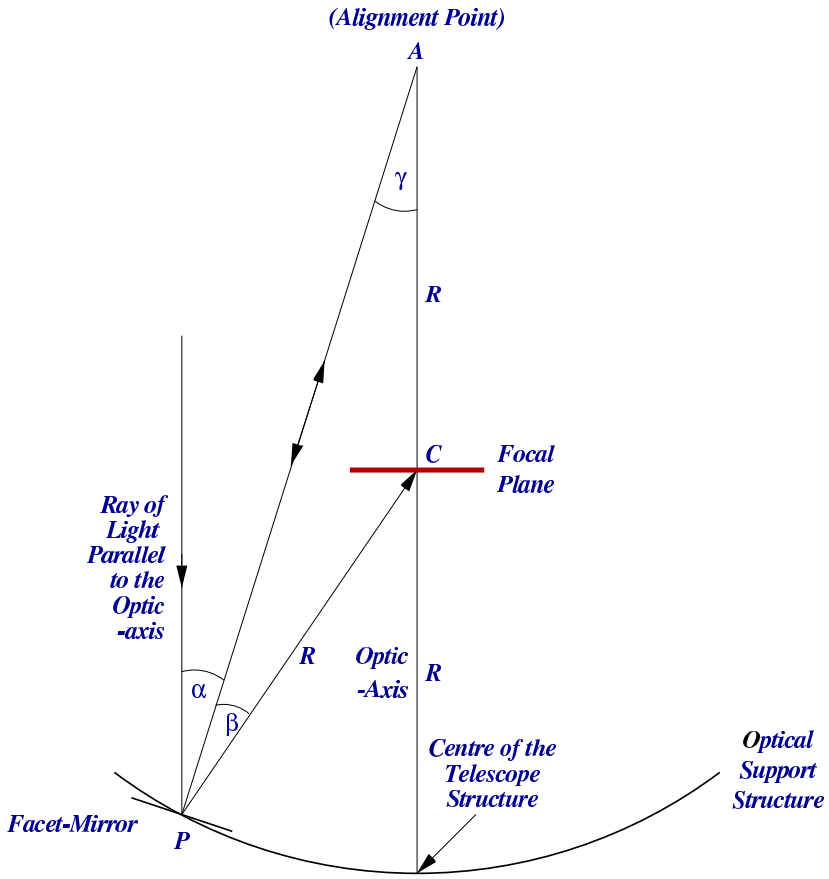

Figure 4.5: Correct alignment. When correctly aligned the triangle PAC is isosceles ($\alpha = \beta = \gamma$) and light arriving parallel to the optic-axis is focused onto the centre of the focal plane. Light originating at the Alignment Point is retro-reflected along its own path.

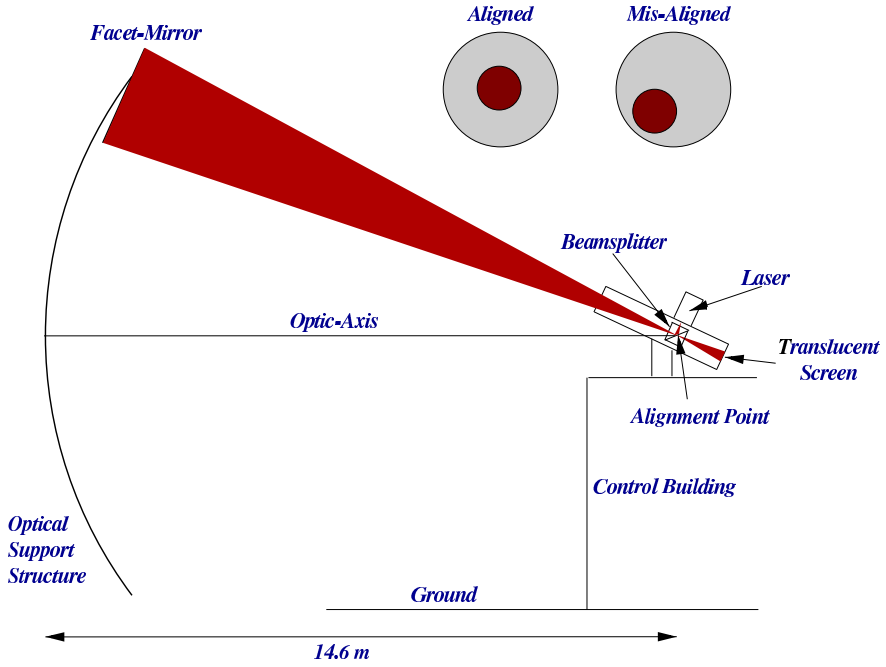

Figure 4.6: Conventional mirror alignment. An alignment apparatus comprising a laser, beamsplitter and a small translucent screen, is used to examine the alignment of each facet-mirror. Aligned mirrors produce centred spots while mis-aligned mirrors produce non-centred spots.

surface are averaged out. An aligned facet-mirror will reflect a circular laser spot onto the centre of the translucent screen. A mis-aligned facet-mirror will produce a non-centred circular spot and require manual adjustment by a second operator working at the reflector. In practice the spots observed are rather distorted owing to the less than perfect spherical shape of the facet-mirrors. According to Lewis et al. (1998), this procedure can be used to align individual facet-mirrors to an accuracy of about 0.1 degrees. Generally this conventional method is time-consuming and labour intensive, requiring two workers and about four hours of effort.

4.3.2 Semi-Automated Alignment System

Although adequate for current observations and data analysis, the conventional alignment procedure is cumbersome and time-consuming, and falls short of that required for the VERITAS array under construction. With this in mind a new Semi-Automated Alignment System (SAAS) was recently designed and a prototype tested on the 10 m reflector (Cawley, 1999; Kildea, 2000; Lang, 2001). The new system requires only one operator and is fast,

compact and efficient.

The basic principle behind the new technique is the same as the old, insofar as the telescope is moved to the home position and a light source at the alignment point is used to illuminate each facet-mirror in turn. It differs in several important respects, however - the most significant being its automated and computerized nature. The SAAS incorporates a diode laser, motorized Pan-Tilt Unit (PTU), beamsplitter, translucent screen, Charge-Coupled Device (CCD) camera, and laptop computer all mounted on an optical bench at the alignment point. Figure 4.7 is a schematic of the basic apparatus and setup. The PTU is essentially a small motorized alt-azimuth mount to which the beamsplitter is attached, its centre coinciding with the intersection of the PTU's axes. With the laser beam pointing into the centre of the beamsplitter it may be directed at any of the facet-mirrors on the 10 m bowl through movement of the PTU. Again the laser beam is spread out in an effort to average out mirror imperfections. The retro-reflected beam produces a spot on the screen behind the beamsplitter and is recorded by the CCD camera. The recorded image is immediately processed by the alignment-control software running on the laptop and the position of its centre-of-gravity estimated. This position is then compared with that expected for correct alignment and the degree of mis-alignment calculated. Based on this value the operator is instructed on how to adjust the mirror's position and by what amount. Upon adjustment the alignment is tested and the procedure repeated if necessary until satisfactory alignment is achieved. A major advantage of the SAAS is that it may be used to intentionally misalign the mirrors by a predetermined offset and thus perform a bias alignment as described in Section 4.5.

Expected positions of the laser spots on the screen were calculated using two different methods. The first involved a survey of the facet-mirrors on the reflector in an effort to determine their centre-points. The survey was undertaken with a digital theodolite at the alignment point and the telescope in its home position. The centre-points were then used along with the dimensions of the system, in ray-tracing simulations to predict spot positions for correct alignment. Figure 4.8 is a graphical representation of the x and y coordinates of each facet centre, as determined by the survey. The second method was more straightforward. Upon aligning the facet-mirrors using the conventional system, the PTU was used to point the laser beam as close as possible to the centre of each facet-mirror, as determined by eye. The coordinates of the centre-of-gravity of the reflected spots on the screen were then taken to be those expected for correct alignment. Coordinates determined by the second method are now used in the SAAS software for comparison purposes, to ascertain when correct alignment for a facet-mirror has been achieved.

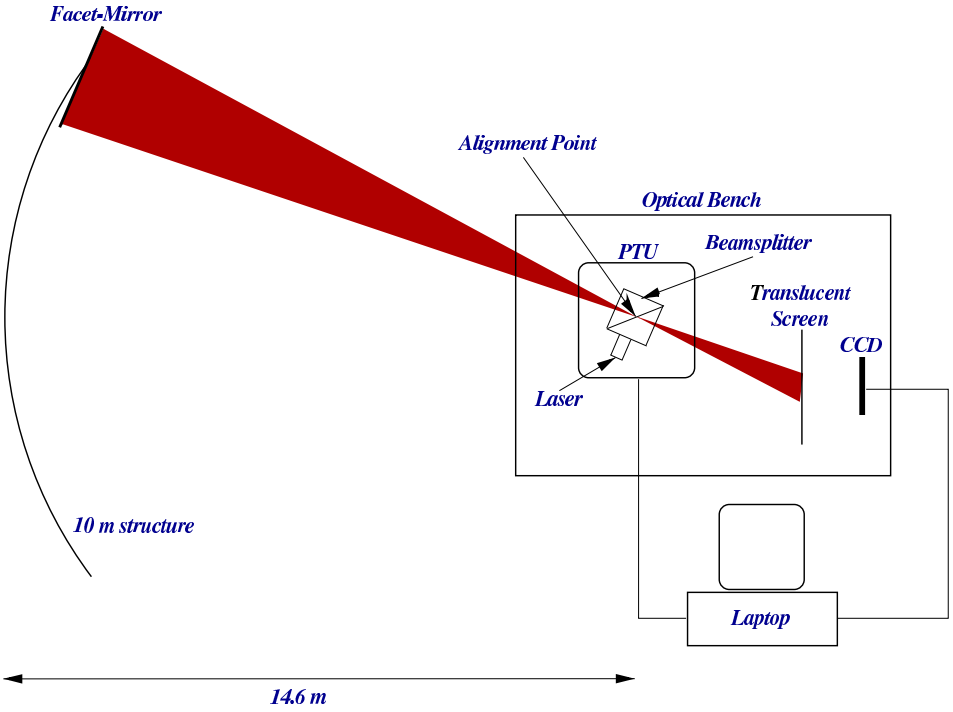

Figure 4.7: Semi-automated Alignment System. Using the laser and beamsplitter, light is directed at a facet-mirror. The reflected spot on the screen, as recorded by the CCD camera, is compared with that expected for correct mirror alignment.

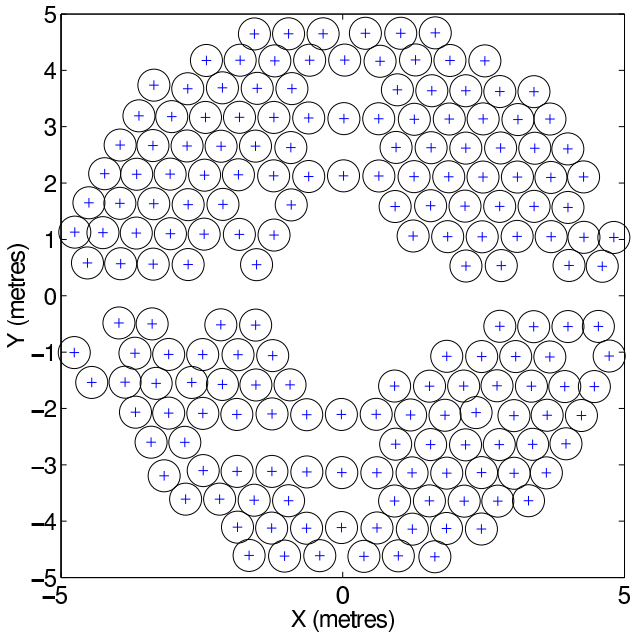

Figure 4.8: Centre-points for the facet-mirrors on the Whipple 10 m reflector, as determined by a mirror survey in 1999. (Note: several mirrors were not surveyed due to obstruction by the focus-box and quadrapod arms or their removal for re-coating. Mirrors on the reflector are hexagonal; circles are used here for representation.)

4.3.3 Foucault Alignment Method

The Foucault test is a popular procedure used to examine the shape of astronomical spherical mirrors. It was first used by its inventer Leon Foucault at the Paris observatory in 1851. It may be modified to examine the alignment of mirrors on a Davies-Cotton type instrument (LeBohec, 1999). When a light source is placed on the optic-axis of a correctly aligned facet-mirror just inside its centre of curvature, reflected light will form an image just beyond the centre of curvature (Figure 4.9). If a CCD-camera is positioned immediately behind the source and observes the mirror it will record a bright area centred on the mirror's surface. This area is actually the virtual image of the camera's aperture and its size depends directly on the aperture width. A mis-aligned mirror will produce a non-centred bright area. By using a camera with adjustable aperture the size of the bright area may be altered as desirable to best judge when it is centred. In this way the Foucault test may be easily adapted for use in mirror alignment of the Whipple reflector. Some preliminary tests of the technique were undertaken during the 1999/2000 observing season. Figure 4.10 is a sample photo taken using a *Mag-lite* flashlight with a fixed-aperture digital camera. Several mis-aligned mirrors are clearly visible and show the potential of the alignment technique.

4.4 Point Spread Function of the 10 m Reflector

Under perfect optical conditions a point source of light will give rise to an exceedingly small dot upon reflection onto the focal plane. In reality all optical systems are imperfect and the reflected dot is blurred or spread out. A measure of the blurring is called the Point Spread Function (PSF). The PSF for the Whipple reflector is quantified several times per observing season and provides a measure of mirror alignment. Sagging of the reflector under gravity, as it is moved around its elevation axis, greatly distorts the PSF image. As a consequence, its facet-mirrors may be finely aligned when lying horizontal but seriously mis-aligned at observing elevations.

The Whipple PSF is measured by recording the optical image of a tracked star, as seen in the focal plane, using a CCD camera with zoom lens mounted at the centre of the reflecting dish. Images are taken at different elevations both on- and off-axis and analysed subsequently to determine the FWHM spread of light. To provide a plate-scale based on the camera's pixelation, an image of the photomultiplier tubes under illumination is also recorded and compared with each stellar image. Since the centre of a stellar image

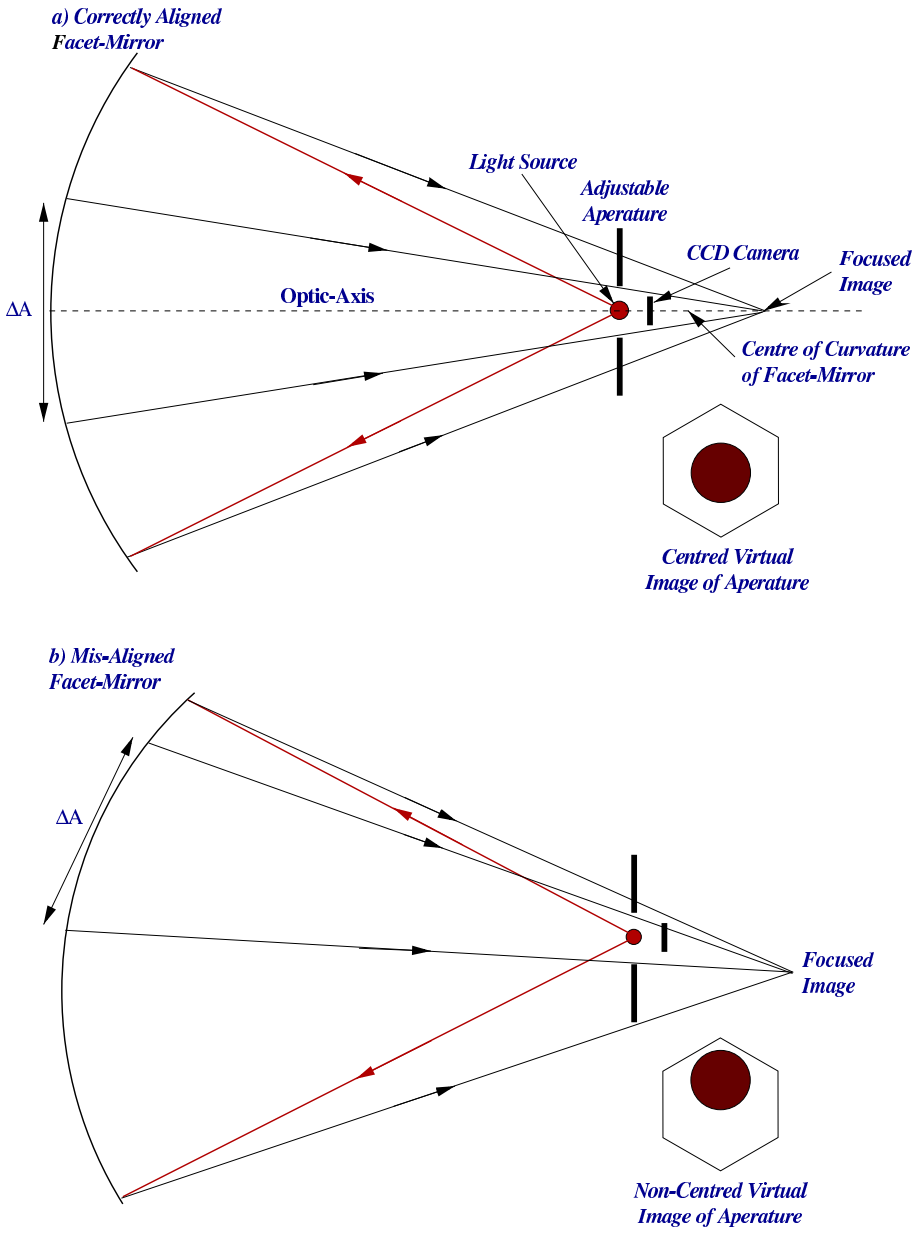

Figure 4.9: Mirror Alignment using the Foucault method. ΔA is the virtual image of the aperture as seen in the facet-mirror. (a) An aligned facet-mirror will produce a centred virtual aperture image. (b) A mis-aligned mirror will produce a non-centred image.

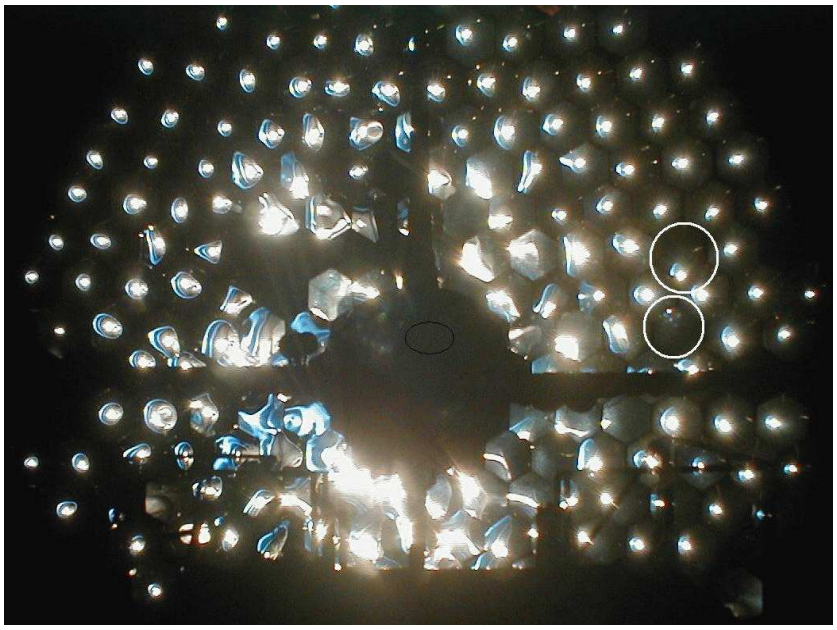

Figure 4.10: A sample Foucault-photo taken using a *Mag-lite* flashlight with a fixed-aperture digital camera**.** The clear mis-alignment of the two highlighted (circled) mirrors shows the potential of the Foucault alignment technique.

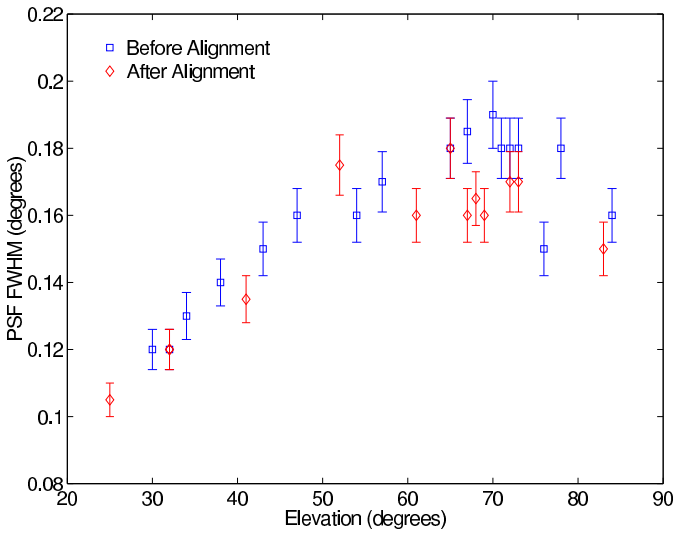

Figure 4.11: PSF measurements for the Whipple reflector in 2001, before and after conventional alignment. An improvement in PSF was achieved by aligning the mirrors. However, the perceptible increase in PSF with elevation is of concern and gave rise to further investigation as to the value of bias alignment.

should coincide with the centre of the focal plane, PSF measurements are sometimes used to examine the pointing accuracy of the Whipple instrument (see Section 4.8).

During the 2001 and 2002 observing seasons PSF measurements were taken over a wide range of elevations, both before and after mirror alignment, see Figure 4.11. A significant improvement in the PSF was observed after alignment at the higher elevations. However, the clear increase in the PSF with elevation was a cause for concern. Upon closer examination the stellar images revealed a form of structure at higher elevations that was not evident lower down. One such high elevation image is presented in Figure 4.12. As mentioned above, a possible explanation for this structure is sagging of the mirror support structure when moved upwards, causing the mirrors to twist out of alignment. An investigation of the instrument's flexure was, accordingly, undertaken during the summer of 2001.

4.5 Bias Alignment

Using results from the mirror-mounted laser investigations the SAAS may be used to perform a biased alignment. Bias alignment is a useful means to

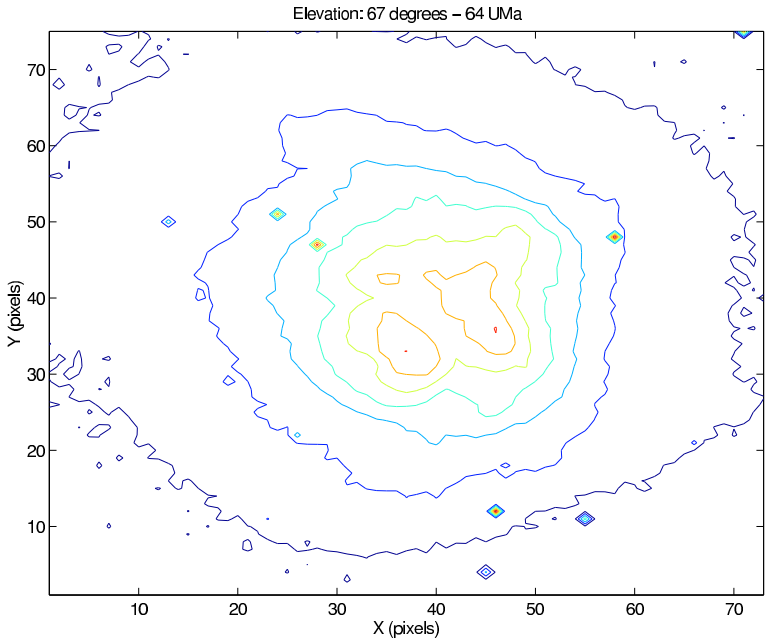

Figure 4.12: Point Spread function image of the star 64 Ursa Majoris, taken at 67° elevation. Structure is evident and may be due to flexure of the reflector at high elevation.

compensate for the movement of individual mirrors caused by the gravitational flexing of the OSS and quadrapod arms as the telescope is moved in elevation. If intentionally mis-aligned in the home position by the amount it is displaced at 70° elevation but in the opposite direction, it should be possible to cause a mirror to fall into correct alignment when observing at 70°. The typical elevation range for observations is 65° to 75°. Bias alignment was successfully carried out on the Whipple 10 m telescope during the 2001/2002 observing season. A measurement of the PSF as a function of elevation, before and after bias alignment (Figure 4.13), confirms the usefulness of the technique.

4.6 Camera

The imaging camera for the Whipple 10 m telescope is located at the focal plane and comprises a closely packed array of 490 fast-response, high quantum-efficiency photomultiplier (PMT) pixels. PMTs are used because their fast response and good sensitivity are well suited to the detection of faint Čerenkov flashes of short duration. In it's current configuration the

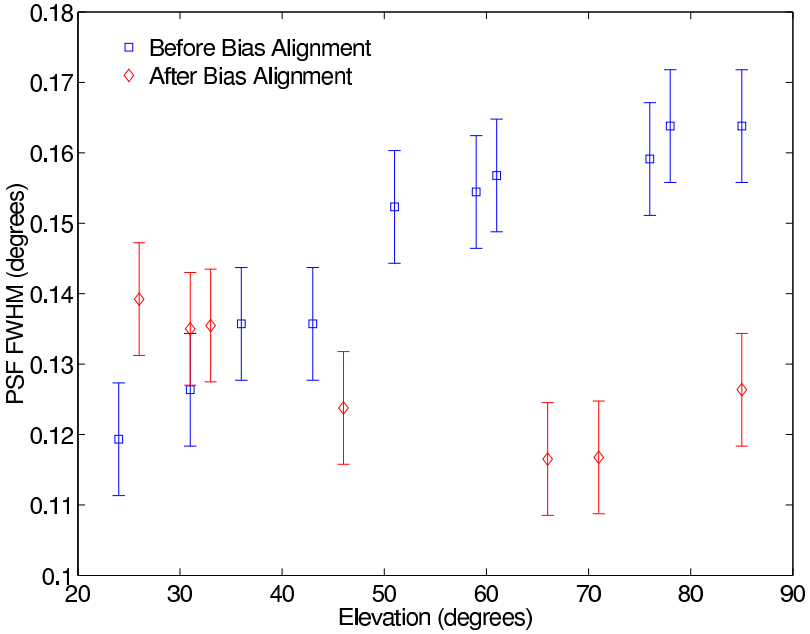

Figure 4.13: The PSF as a function of elevation, measured for the Whipple 10 m telescope, before and after bias alignment using the SAAS.

camera consists of an inner hexagonal array of 379 half-inch Hamamatsu H3165 PMTs surrounded by an annular outer array of 111 one-inch Hamamatsu R1398 PMTs (see section 5.3 for a discussion on the use of inner and outer pixels in data analysis). A photograph of the camera with light-cones (see section 4.6.1) is presented in Figure 4.14(a) and a map of the PMT array is shown in Figure 4.14(b).

4.6.1 Photomultiplier Tubes

Each PMT contains a photocathode enclosed within μ-metal shielding and plastic casing. The μ-shielding protects the photoelectrons produced in the PMT from deflection by the Earth's magnetic field. As shown in Figure 4.15, the shielding and casing take up considerable area, leaving only about 35 percent of the effective PMT area for active photocathode. For the inner region of the camera, light-guiding cones (Figure 4.14(a)) are used to salvage photons which would otherwise be lost to this dead space and in the hexagonal region of empty space surrounding each PMT. The light-cones are designed to accept only light which has come from the telescope's mirrors, thus reducing noise due to extraneous light. A discussion of the design and manufacture of the camera's light-cones may be found in Hillas (1997). With

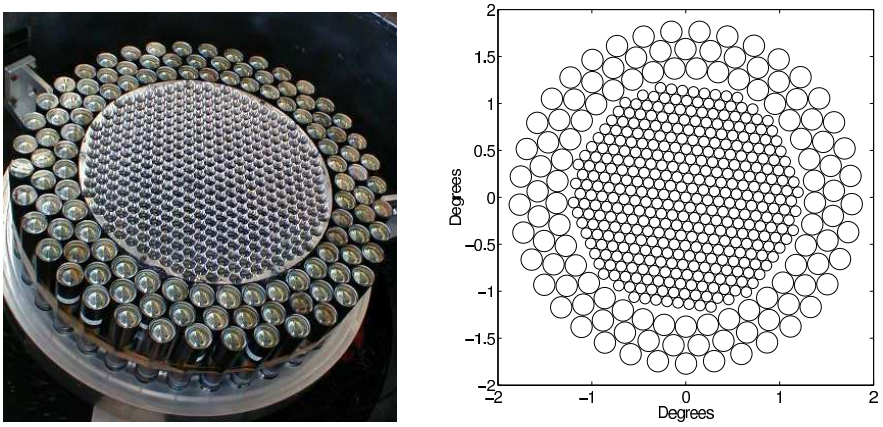

(a) Photograph **(b)** PMT map

Figure 4.14: The Whipple High Resolution Camera.

light-cones in place each inner PMT sees a region of sky spanning 0.117° and each outer PMT a region spanning 0.232°, resulting in a total field-of-view for the camera of 3.8°.

PMT spectral responses are chosen so as to match the peak of the Čerenkov spectrum in the blue to near-UV region, thus eliminating a considerable amount of the night-sky light which peaks toward the red end of the spectrum. The PMT rise times are necessarily extremely fast to cope with Čerenkov pulses of approximately 6 ns in duration. The camera as a whole however, detects a time-spread of about 10 - 15 ns for a complete shower.

4.6.2 High Voltage System

Voltages to the PMTs are controlled by three LeCroy High Voltage (HV) modules mounted in crates on the telescope counterweights. Communication with the HV modules is through custom control software which sends command signals via ethernet. The modules may also be controlled manually in case of broken ethernet connection and may be switched off in emergency by disconnecting power to the telescope. Anode current values from the PMTs are constantly sent to a current monitor to guard against over-heating, and the relative gain for all tubes is measured at the beginning of each observing night, through the use of a nitrogen arc lamp. Section 4.9 contains further discussion on monitoring and calibration.

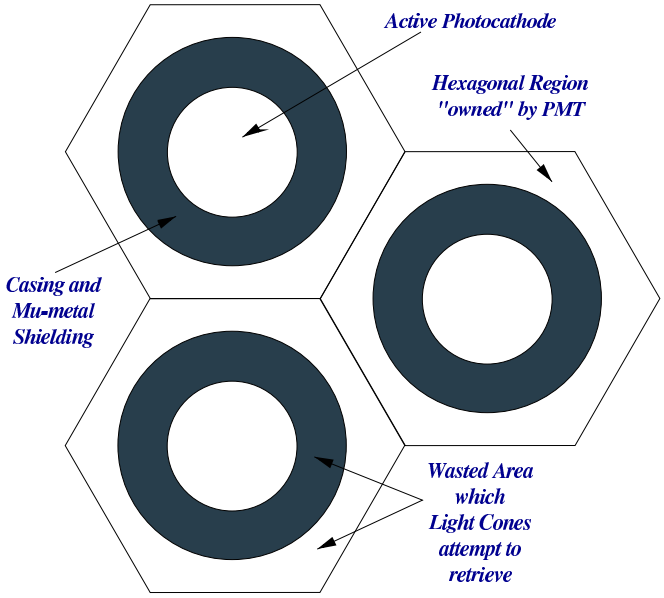

Figure 4.15: PMT structure.

4.6.3 Signal Transmission

Analog signals from the inner 379 PMTs are brought to the signal electronics via RG58 coaxial cable. Signals from the outer PMTs are converted at the focus-box into light pulses and then transmitted via fibre-optic cable to the signal electronics. Both the fibre-optic and coaxial cables are fed along the quadrupole arms of the reflector, though the telescope pedestal and underground to the control room.

4.6.4 Camera Evolution

The present 490-pixel camera was installed in the Autumn of 1999 and replaced a 331-pixel camera of one-inch PMTs with field-of-view 4.8°. Data used for the pulsar search analysis presented here was obtained with the 490-pixel camera, and includes observations spanning 1999 and 2002. Other camera configurations previously employed by the collaboration include a 151-pixel instrument for a brief period in 1997 and a 109-pixel instrument from 1988 to 1997.

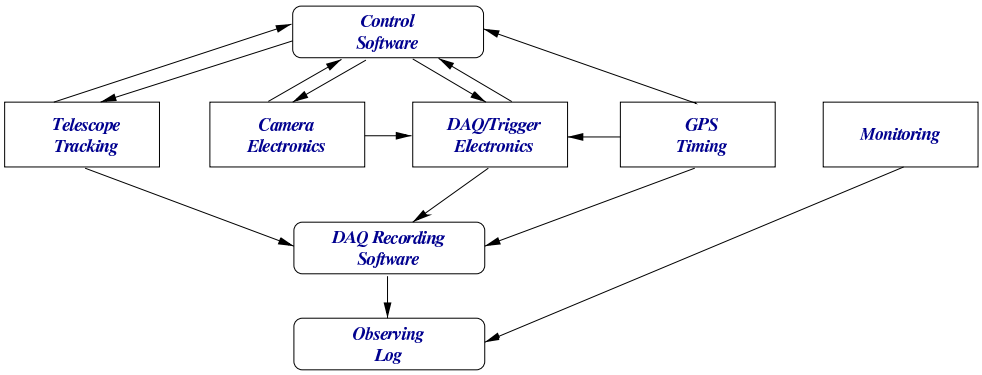

Figure 4.16: Overview of the Whipple DAQ system.

4.7 Data Acquisition System

The Whipple Data Acquisition (DAQ) system encompasses all aspects of telescope control and data-recording. Figure 4.16 presents an overview of the system, showing the main components involved and their interdependence. The Control Software includes programs to manage telescope tracking, voltages to the camera's PMTs and the signal electronics. The control programs are run, for the most part, on a PC operating under Linux. The DAQ recording software takes the telescope's coordinates, precise timing information from the GPS clock, together with the processed image from the electronics and records them in a strict pre-determined data format for off-line analysis. The recording software is run on a Digital Alpha Workstation operating under VMS.

4.7.1 DAQ Logic

The Whipple DAQ system is based on the CAMAC data bus system for DAQ electronic modules (Rose et al., 1995). The system allows the fast transfer of data and DAQ commands along the common backplane of an electronic crate. Through the use of List Processors, the DAQ modules may communicate with the DAQ computer. Čerenkov signals, as registered by the camera's PMTs, are transferred to the CAMAC modules for processing. Figure 4.17 shows the path followed by a signal from the camera to the DAQ computer.

As is the case for any electronic DAQ system, pre-amplification is the first stage of signal processing. Pre-amplification using a high quality amplifier is important as the Noise Factor of the system depends primarily on the Noise Factor of the first amplifier through which the signal passes. For the

Whipple system, amplification of signals from the inner PMTs is achieved using LeCroy 612A Amplifiers each with a gain factor of 10. Signals from the outer PMTs are transmitted to a Fibre-Optic receiver module, comprising photodiodes and amplifiers.

Each LeCroy 612A amplifier has three outputs:

- The first output is to the Current Monitor mentioned previously in section 4.6.2.
- The second output connects the 379 inner channels to the Analog to Digital Convertors (ADCs).
- The final output is used to feed amplified signals from the inner 331 PMTs to the Trigger electronics (see section 4.7.4 for details regarding the 331-pixel trigger).

Signals from the amplifier to the Current Monitor are DC-coupled to enable correct monitoring, while those to the ADCs are AC-coupled to remove the average night-sky background noise. Signal transmission from amplifier to ADC is via RG58 coaxial cable. The cable used is of sufficient length to provide the Trigger Generation Delay. While delayed en route to the ADCs the signal's fate is determined by the Trigger electronics.

The Trigger electronics (see section 4.7.4) decide whether a signal from the camera is a true Čerenkov-like signal or not. If its requirements are met then the trigger informs the Gate Generator and the system is triggered, otherwise the signal which arrives at the ADCs is discarded. When triggered, the Gate Generator sends a negative square pulse, of duration 25 ns approximately, to the ADCs via the Gate Width Discriminator. Since trigger generation and the Trigger Generation Delay are of the same duration (25 ns approximately), both the gate and signal pulses arrive at the ADCs simultaneously allowing digitization and recording. Figure 4.18 is an oscilloscope trace of simultaneous gate and Čerenkov pulses observed at an ADC using an oscilloscope.

The Whipple ADCs are 10-bit LeCroy 2249 modules which integrate the PMT signal over the duration of the gate signal. An ADC's pedestal value is the value of its output for zero input light. In order to determine the true output, the pedestal must be subtracted during analysis. To record pedestal values the system is artificially triggered, once per second. The artificial trigger pulse to the Gate Generator is provided by the system's GPS clock (see section 4.7.3). For the Whipple telescope, PMT pedestals comprise two components of distinct origin. The first component is due to night-sky noise fluctuations, while the second is artificially set at about 20 d.c. (digital counts).

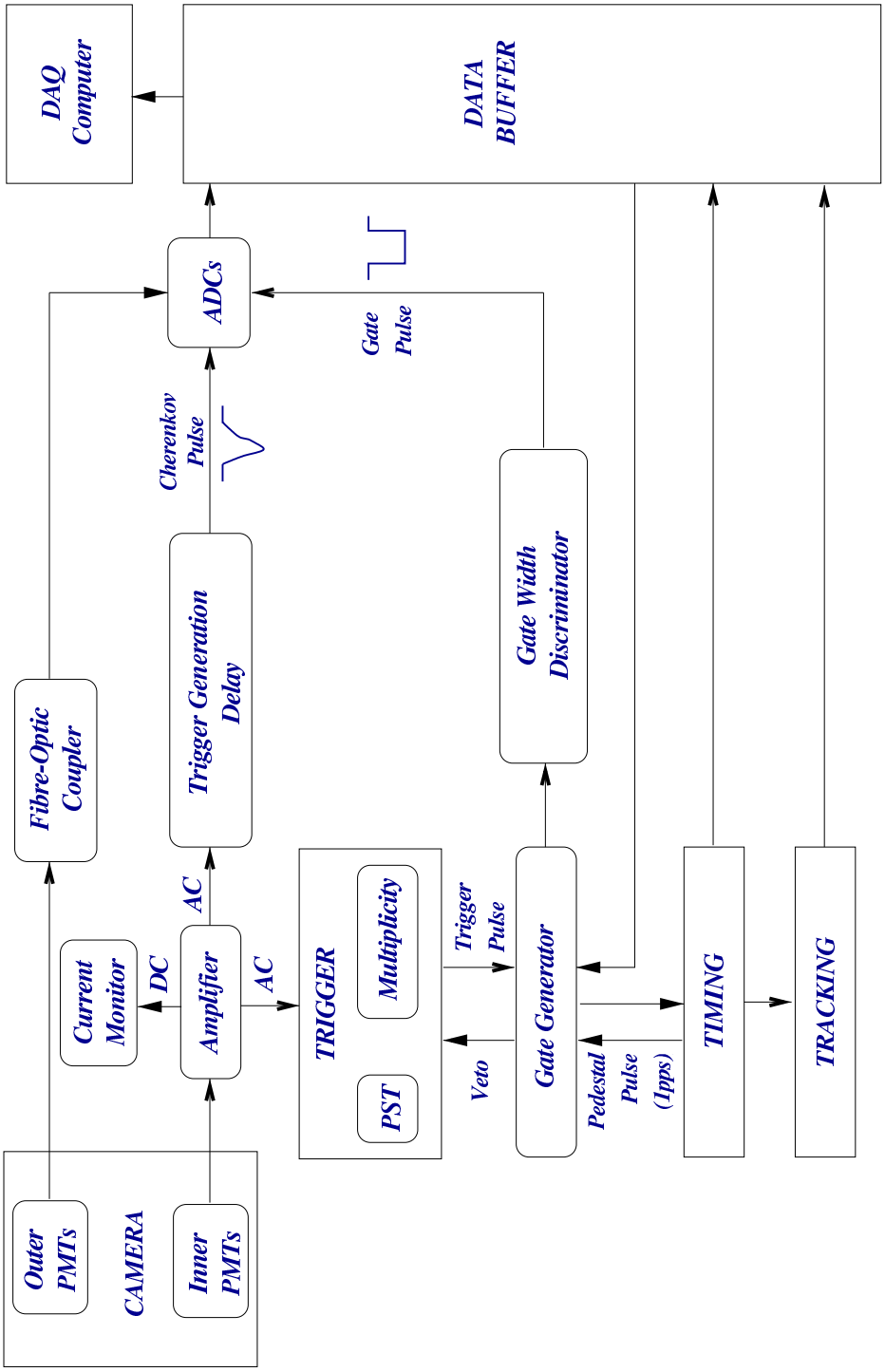

Figure 4.17: Path followed by a signal from the camera to the DAQ computer.

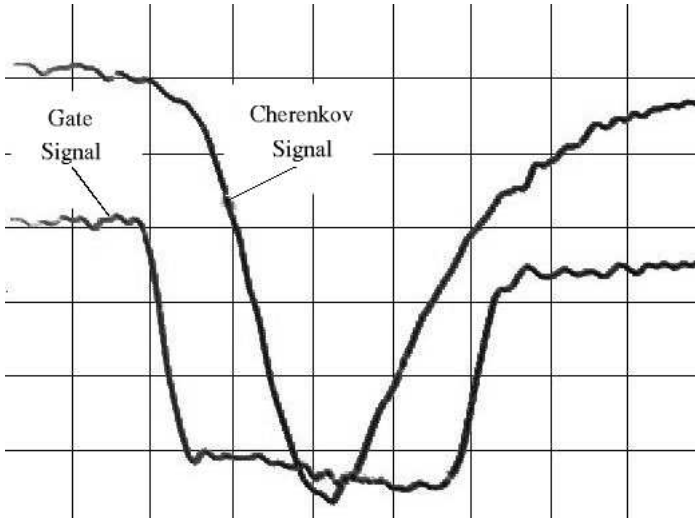

Figure 4.18: Oscilloscope trace of simultaneous gate and Čerenkov pulses at an ADC (each horizontal division represents 5 ns, each vertical division represents 100 mV).

Since the PMT signals are AC-coupled, the average DC night-sky noise is removed. As a result, true Čerenkov signals sit on an AC background which fluctuates above and below the average. By setting the artificial pedestal at about 20 d.c., negative fluctuations of up to 20 d.c below the average still result in positive pedestals values. Hence, the pedestal variance about the mean may be calculated for each PMT and used to quantify the AC night-sky background noise fluctuations. Details of pedestal subtraction analysis are provided in section 5.2.1.

4.7.2 Data Buffering and Recording

Events which trigger the system are recorded as d.c. values per PMT. Due to the high rate of trigger events a List Processor is used to buffer data between the CAMAC backplane and the DAQ computer. The List Processor, a Hytec 1341, is simply a computer with a very large memory buffer, which stores data until the DAQ computer can read it. Figure 4.19 shows the components involved in data buffering and recording and their interdependence. A Hytec 1365 Ethernet Crate Controller (ECC) is used as the interface between CAMAC and Ethernet (i.e. between CAMAC and the DAQ computer). Timing and tracking information are also fed to the DAQ computer. Timing information is CAMAC controlled while tracking information is fed directly via ethernet from the Tracking computer.

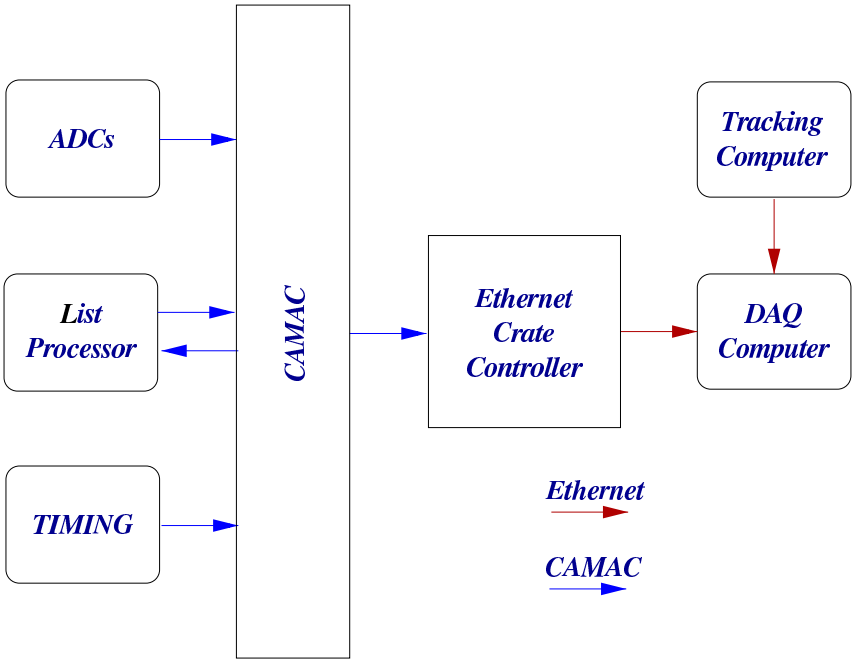

Figure 4.19: The DAQ components involved in data buffering and recording.

4.7.3 Timing

Timing is of utmost importance at any observatory. It is required for precise source tracking, temporal analysis of periodic or variable sources and synchronisation of collaborative observational campaigns. At the Whipple observatory two independent Global Positioning Satellite (GPS) clocks are normally used, together with a 10 MHz oscillator, to provide event timing to an accuracy of 0.1 μs.

Figure 4.20 shows how the various components of the Whipple timing system work together. A TrueTime GPS clock provides the main timing information for event recording. In fact, for the majority of the Crab pulsar data analysed in this work, the TrueTime clock is the only source of absolute timing information available. In order to function correctly, the TrueTime module must latch on to signals from at least three satellite atomic clocks. When connected with its satellites the clock has an absolute accuracy of 250 μs. However, through the use of a University of Wisconsin GRS2 memory module and a 10 MHz oscillator, the TrueTime GPS is in practise extrapolated to 0.1 μs. The GRS2 is used to count pulses, one per second, from the GPS and also pulses, one per 0.1 μs from the 10 MHz oscillator. To check the accuracy of the oscillator, the GRS2 resets itself each time it receives a TrueTime pulse, regardless of whether or not to has received its ten millionth

pulse from the oscillator. In this way the GRS2 holds timing information to an accuracy of 0.1 μs. To provide Čerenkov event timing, the GRS2 sends three 16 bit timing values to the List Processor, on receipt of an Interrupt Request from the Event Trigger.

Two 48 bit scalers are also used to count pulses from the 10 MHz oscillator. The elapsed-time scaler counts pulses, without interruption, from the start of an observing run until the end, while the live-time scaler counts pulses only when the trigger gate is open. Since the number of pulses received by each scaler is not checked by a GPS clock, the oscillator error accumulates and must be accounted for off-line during analysis.

4.7.4 Trigger

Two independent trigger mechanisms, the Multiplicity Trigger and the Pattern Selection Trigger (PST), comprise the Whipple event Trigger system and together they decide if an image from the camera should be recorded. Figure 4.21 shows the logic followed by a Čerenkov image through the trigger electronics. Only the inner 331 PMTs form part of the trigger; this is a legacy of the electronics built for the previous 331-pixel camera. LeCroy 3420 Constant Fraction Discriminators (CFDs) are used to determine which channels have fired. The CFDs take input signals from all 331 trigger PMTs and output a pulse of preset amplitude and duration if and when the input signal exceeds a prescribed threshold. The use of CFDs prevents "time walk" and allows for more accurate signal and trigger synchronisation than available with arbitrary value discriminators. CFD output pulses are sent to both the Multiplicity Trigger and the PST.

The Multiplicity Trigger triggers when the number of CFD pulses it receives exceeds a preset threshold. This threshold number is known as the multiplicity of the system and is determined from bias curves measured each observing season. The main use of the Multiplicity Trigger is to provide a jitter free signal to initiate the gate signal to the ADCs.

The PST decides whether or not an image should be recorded based on the spatial location of the tubes which comprise the image. The PST was installed in the Whipple system in 1998 and triggers only if a preset number of fired tubes are adjacent (Bradbury, 1997). The PST has the effect of biasing the camera in favour of true Čerenkov showers and guards against triggering on random PMTs fired by background light fluctuations. This results in an economy of scale in terms of the quantity of data which has to be recorded. With the accidental trigger rate reduced the camera can be operated at a lower CFD threshold; this is the main advantage of the PST. As is the case for the Multiplicity Trigger, the PST criteria are determined from seasonal bias

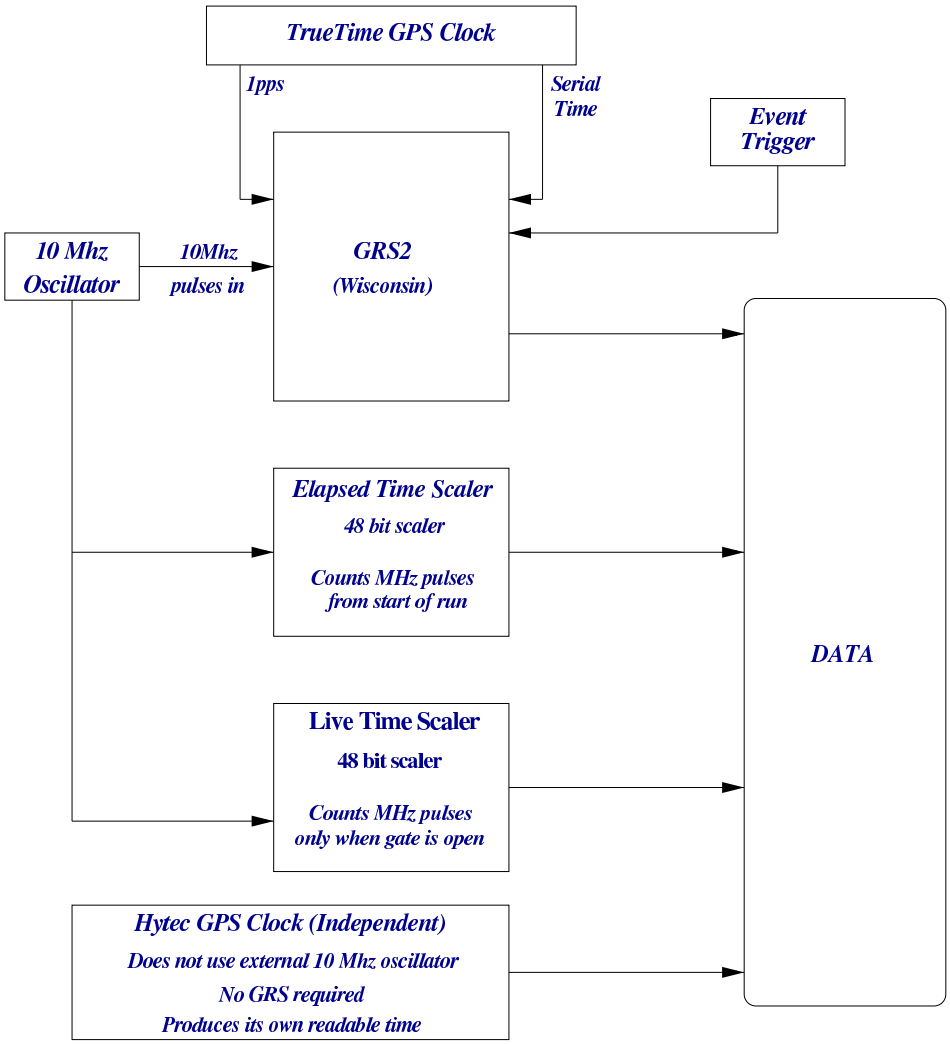

Figure 4.20: Whipple 10 m telescope timing system.

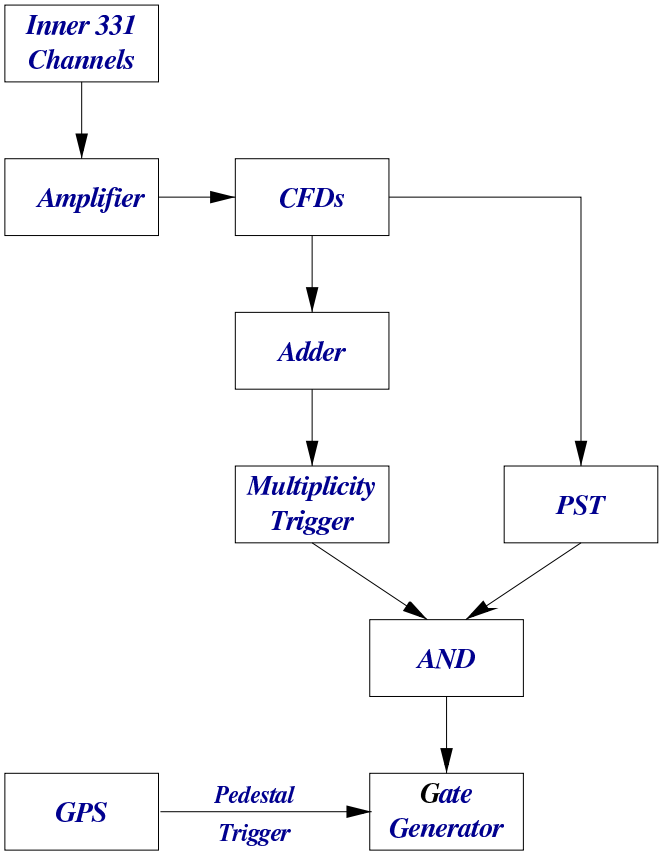

Figure 4.21: Whipple event trigger logic.

curves. Figure 4.22 presents two such trigger-rate discriminator-threshold bias curves taken at the zenith and clearly shows the threshold reduction gained by the PST.

The majority of the data used in this thesis work was recorded under the conditions of a 3-fold neighbour coincidence (i.e. 3-fold Multiplicity Trigger in conjunction with the PST) together with a CFD threshold of 32 mV. This corresponds to a pixel threshold of $\sim$ 8–10 photoelectrons (Finley and the VERITAS collaboration, 2001).

4.8 Tracking and Pointing

The Whipple telescope has an Alt-Azimuth mount with each axis independently controlled by variable speed motors with a resolution of 0.01°. The instrument can be slewed along each axis at a rate of 1° per second. It may be steered around to a maximum of 270° in both azimuthal directions and

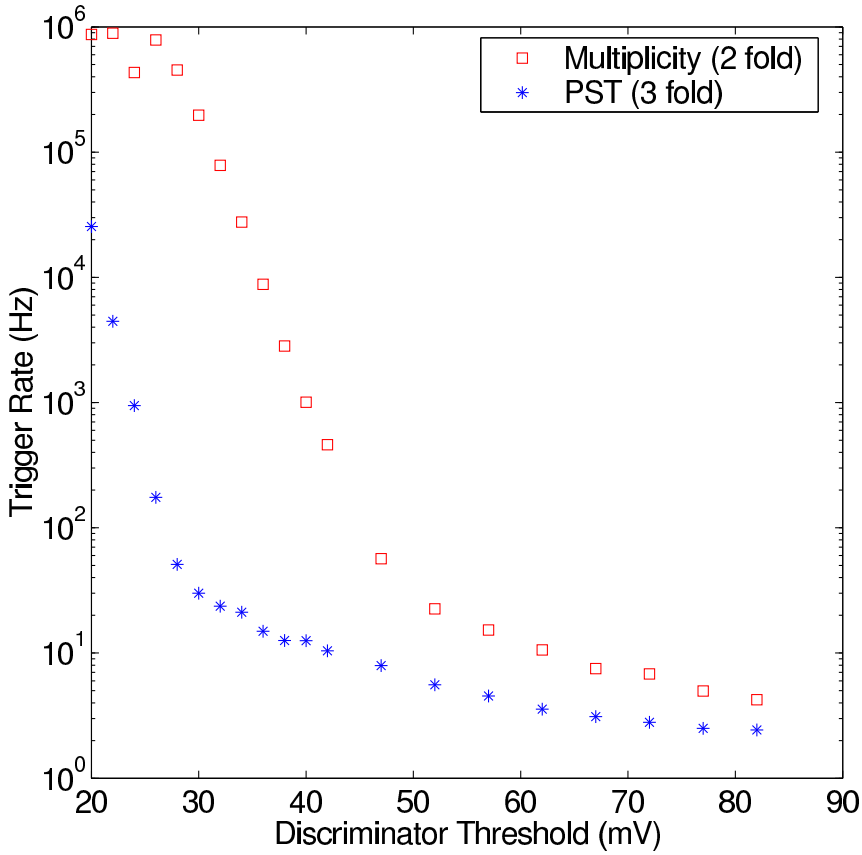

Figure 4.22: Bias curves taken at the zenith (26 October 2001). The reduction in trigger rate gained by the 3-fold PST can be clearly seen.

from 0° to +90° in elevation.

The tracking/pointing algorithms form the main part of the telescope's control software. The equatorial coordinates for the source under observation are taken from a local database and used to continuously set the telescope's altitude and azimuth. The local sidereal time needed to calculate the source coordinates is obtained from a remote Network Time Server. Using a fibre-optic link the tracking software sends tracking commands to and retrieves pointing information from the telescope's altitude and azimuth drives. In the event of a software failure the telescope may be controlled using a manual drive controller.

A system of limit switches is used to prevent the telescope from moving beyond its design limitations. Soft switches in the software are the first line of defense and instruct the drive controllers to stop if their limit values are exceeded. Physical hard switches on the telescope structure form the second line of defense and provide definite limits to the telescope's range.

Several modes of tracking are used for the IAČT. The most commonly used mode is ON/OFF. In this mode the telescope tracks the source (ON run) through the sky for a certain length of time, normally 28 sidereal minutes. The telescope is then moved back to its starting point and a control (OFF) run of the exact same duration is undertaken through the same range of azimuth and elevation. In this way, the background reading for the sky in the absence of the source is obtained. In TRACKING mode the source is continuously tracked without a control run being taken. TRACKING is used for continuous on-source observations, for example; when monitoring flaring AGN or pulsars. A Zenith run is one in which the telescope is set to zenith and left there for the duration of an observation. Zenith runs are important for calibrating the throughput of the telescope and are usually taken at the beginning of each observing night. Drift scans, in which the telescope is set to a particular position and left there while the sky drifts past, are also sometimes taken and used for engineering purposes.

4.9 Monitoring

4.9.1 Pointing Checks

The accuracy with which the telescope tracks the star to which it is pointing is of vital importance in the IAČT. The alpha parameter (section 3.8) depends completely on the position of the source in the field-of-view. To check the accuracy of the telescope's pointing, several crude pointing checks are performed each observing night. PSF measurements (see section 4.4) are

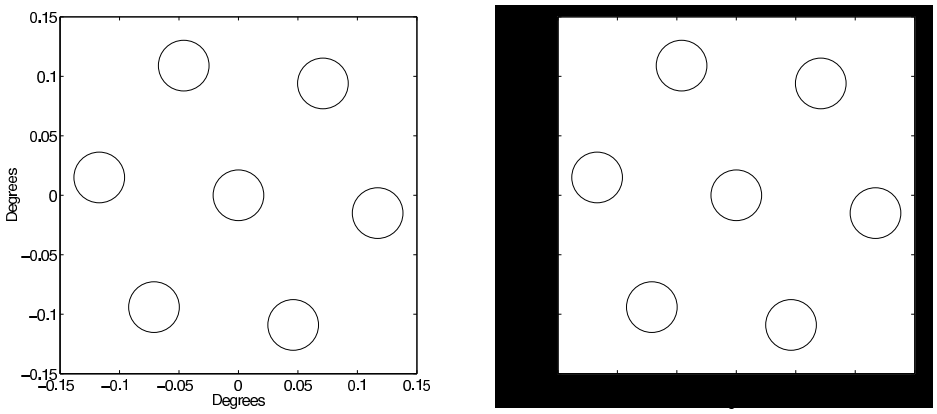

(a) Good Pointing (19 Jan 2001) **(b)** Bad Pointing (28 Oct 1999)

Figure 4.23: Pointing check readings. Relative anode current values are indicated by the size of the red disk in each PMT.

used when available to provide a more accurate measure of the instrument's pointing.

The nightly pointing check procedure is uncomplicated and merely necessitates moving the reflector to point at a reasonably bright star near the source under observation. Anode current readings from the inner seven PMTs are then recorded. When pointing correctly the current readings are normally reasonably symmetrical with a maximum reading in the centre-most tube. Poor pointing manifests itself through a non-centred maximum reading. Figures 4.23(a) and 4.23(b) show the current readings for both good and bad pointing situations.

4.9.2 Optical CCD Camera

An Electrim EDC1000L CCD camera with a 25 mm f/0.85 Fujinon lens and 8° field-of-view is mounted on the telescope near the focus box. It is aligned parallel to the telescope's optical axis and is used to monitor the PMT-camera's field-of-view. Star-field images from the CCD are displayed on a screen in the control room and afford the observers advance warning of bright-stars which may necessitate switching off voltages to certain PMTs. The CCD camera is occasionally also used to crudely monitor sky and weather conditions.

4.9.3 Nitrogen Arc Lamp

An Optitron nitrogen arc lamp and light-diffuser located at the centre of the optical support structure are used to uniformly illuminate the PMT-camera with a 1 kHz pulse-train of very-short-duration blue flashes for one minute at the beginning of each observing night. The purpose of this illumination is to enable the calculation of the gain of each PMT relative to the average gain. Although the PMT voltages are set for uniform sensitivity amongst tubes small differences remain and must be ironed out through a process known as "flat-fielding". The nitrogen gains are recorded and analysed off-line as part of the flat-fielding process (see section 5.2.2).

4.9.4 Weather Monitoring

Weather monitoring is important at any astronomical observatory. For atmospheric Čerenkov telescopes such as the Whipple 10 m, monitoring of sky clarity and weather conditions is vital. Although generally very dry and clear, the weather system of southern Arizona occasionally includes conditions unsuited for astronomical observations. Such conditions include the summer monsoon season and episodic occurrences of precipitation, high wind and high humidity. No observations are attempted if adverse conditions are forecast or if cloud cover is evident. When observations are possible qualitative sky-clarity is manually recorded as A, B or C weather by the observers on duty. Generally, A weather is recorded for perfect sky conditions, while B weather is used to denote almost perfect conditions in which isolated clouds or horizon haze are evident. The raw trigger rates should remain stable for both A and B weather. C weather is used to indicate cloudy conditions in which the raw trigger rates fluctuate during observations. Although an on-site weather station was used to quantitatively record observables such as wind speed, temperature and pressure; sky-clarity was not quantitatively measured for the observations used in this thesis. An FIR pyrometer currently under development will be used for observations made with the VERITAS telescope array (Dowdall, 2002).

4.10 Telescope Simulations

Telescope simulations used in this work were developed at Iowa State University and are routinely used by the Whipple collaboration to simulate the response of the Whipple 10 m telescope to Čerenkov photons from γ-ray EAS. Typical input parameters include details regarding the photoelectron to dig-

ital counts conversion factors, PMT quantum efficiencies, detailing regarding the use of light-cones, trigger mode and mirror reflectivities.

Chapter 5

Data Analysis for the Whipple 10m Telescope

The objective of atmospheric Čerenkov γ-ray astronomy is the detection of γ-rays from celestial objects by means of identifying γ-ray initiated EAS. In practical terms this involves detecting atmospheric Čerenkov signals and extracting, from amongst an overwhelming noise background, those signals which can be attributed to γ-rays. For a single atmospheric Čerenkov telescope, such as the Whipple 10 m, noise comes in the form of hadron initiated EAS, EAS from cosmic ray electrons, local muons, and night-sky background light. Figure 5.1 presents sample γ-ray and noise events as they appear in the Whipple 490-pixel camera.

The IACT (section 3.8) has proven a very powerful method for the selection of γ-ray initiated events (Fegan, 1996). By parameterising the shape and orientation of each recorded Čerenkov image within the telescope's field-of-view, and selecting only those images which have γ-ray-like parameters (as determined from simulations), the IACT can reject background noise with an efficiency of close to 100% while simultaneously rejecting no more than $\sim$50% of genuine γ-rays (Fegan, 1997).

The aim of the present work is the search for potential pulsed TeV-scale γ-ray emission from the Crab pulsar. In this quest the IACT is used to identify candidate γ-ray events which are then subjected to a periodicity analysis. In order to search for both the expected pulsed γ-ray cut-off within the $\sim$10 GeV to $\sim$200 GeV region (section 2.9), and also the inverse-Compton component predicted by the Outer Gap model (section 2.7.3), two main analysis methodologies (re-optimised Supercuts and the Kernel analysis) are applied over the complete dynamic range of γ-ray energies detected by the Whipple telescope. Upper limits for pulsed emission are also estimated in an effort to constrain emission models. This chapter provides details of the

Crab dataset, the observing strategies, and the analysis procedures used.

5.1 Observing Strategies

The similarities and differences between γ-ray and hadron initiated EAS, and their focused images were detailed in chapter 3. In general, γ-ray EAS form narrow elliptical images oriented towards the centre of the camera's field-of-view, whilst hadron showers give rise to large images with random orientations. By chance, however, hadron EAS may on occasion produce images that are sufficiently γ-ray-like to pass even the most rigorous γ-ray selection criteria. Indeed, occasional night-sky background noise fluctuations, Čerenkov radiation from local muons, and Čerenkov radiation from EAS generated by cosmic ray electrons, may all similarly pass as γ-ray images. To guard against any bias in the final γ-ray rate, caused by these spurious events, a quantification of the frequency of their occurrence must be determined. In the IACT, one of two background estimation methodologies is normally employed; the *ON/OFF* or *TRACKING* techniques.

5.1.1 ON/OFF

In ON/OFF mode the telescope tracks the astrophysical source of interest (ON-source) for a set duration of time (usually 28 minutes), and then slews back to re-track the same sky region in the absence of the source (OFF-source). In this way the number of chance γ-ray events observed in the OFF-data, after software padding (see section 5.2.4 below), may be used as an estimate of the background for the ON-data. The significance, σ, (i.e. the ratio of the signal to its standard deviation) of excess ON-source γ-ray events above the background OFF-source events can then be estimated, assuming a Poissonian noise distribution, as

$$\sigma = \frac{ON - OFF}{\sqrt{ON + OFF}} \tag{5.1}$$

where ON is the number of ON-source events passing the γ-ray selection criteria and OFF is the number of OFF-source events passing the same criteria. The significance measures the probability that the signal is a random fluctuation in the background level. Normally a 3σ signal ($\sim$2.6% probability) is interpreted as an indication of validity, while a 5σ signal, coupled with an equivalent result from an independent experiment, is considered a true source detection (Weekes, 1999). The corresponding γ-ray rate (and

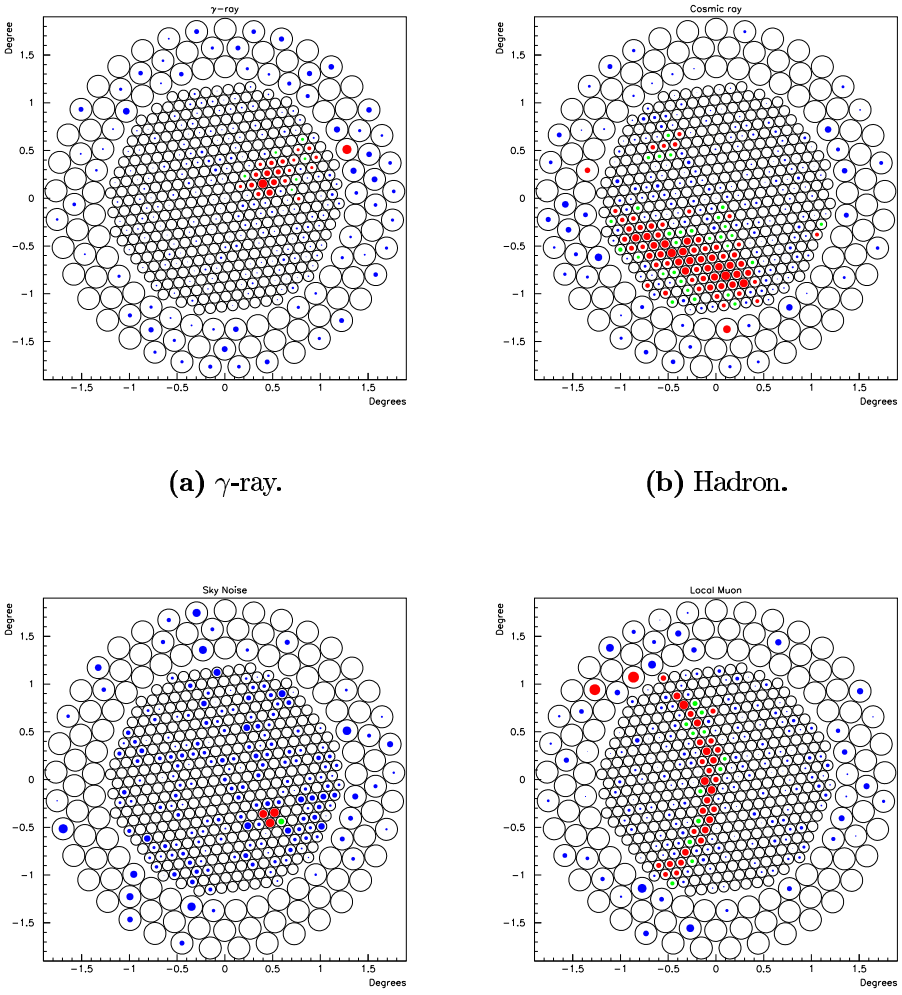

(a) γ-ray. **(b)** Hadron.

(c) Sky Noise. **(d)** Local Muon.

Figure 5.1: The four types of events which trigger the Whipple 10 m telescope, as observed in the 490-pixel camera. The area of each disk is proportional to the amount of Čerenkov light in that tube and the different colours are associated with the image cleaning process, section 5.2.3. From Dunlea (2001).

associated Poissonian error) is simply calculated as

$$Rate = \frac{ON - OFF}{duration} \pm \frac{\sqrt{ON + OFF}}{duration} \tag{5.2}$$

and is usually quoted in units of γ-ray events per minute.

The ON/OFF observing mode has proved a very effective and useful means for observing γ-ray sources. For determining the presence of a new source or estimating an accurate flux upper limit it is considered ideal. A clear disadvantage of this mode, however, lies in the 50% reduction of the ON-source duty cycle which it imposes. For observations of temporally variable sources such as pulsars and flaring AGN, it is desireable that maximum time be spent ON-source. As a result, the *TRACKING* technique was developed.

5.1.2 TRACKING

In TRACKING mode the telescope exclusively tracks the astrophysical source of interest for as long as possible, without any recourse to OFF-source observations. In the follow-up data analysis (TRACKING analysis) the shape of the *alpha*-plot (see chapter 3 and section 5.3 below, for information on the *alpha* parameter) in the absence of a γ-ray signal is estimated from the ON-source observations alone. Typically, *alpha* values for γ-ray events extend from 0° to 15° section 5.11. From Figure 3.18 it is clear that from 35° $\rightarrow$ 65° the *alpha*-plots for the ON data (solid line) and OFF data (dashed line) match very well. Hence, given the ratio of the number of events in the 35° $\rightarrow$ 65° region to those in the 0° $\rightarrow$ 15° region, for a set of independent OFF runs, the background number of events in the 0° $\rightarrow$ 15° region for a TRACKING run may be estimated using the number of events in *its own* 35° $\rightarrow$ 65° region. Although in the *alpha*-plot of Figure 3.18, the 65° $\rightarrow$ 90° regions for the ON and OFF runs also match reasonably well, the 65° $\rightarrow$ 90° region is not normally used for tracking analysis, due to truncation effects at the edge of the field-of-view, which tend to bias *alpha* angles to higher values.

Full details regarding the standard Whipple TRACKING analysis, and variations thereof, are available in Kerrick et al. (1995); Quinn et al. (1996); Hughes (2001) and Horan et al. (2002). No formal TRACKING analysis is presented here since there is ample ON/OFF data for flux estimation (section 5.15). However, some TRACKING mode data was used for temporal analysis purposes.

5.2 Data Calibration

As described in chapter 3, the identification of subtle differences between γ-ray and hadron EAS, by means of focusing and imaging the Čerenkov light they produce, is the backbone of the IACT. Under ideal conditions mere moment-fitting of the Čerenkov images recorded by the Whipple telescope, without any intermediate pre-processing, would suffice as a means to identifying their origins. In practise conditions are of course imperfect, and the pre-processing of all Čerenkov images is a vital first step in data analysis.

When triggered, the Whipple DAQ system records the light signal registered by each of the camera's 490 PMT-pixels. In recording the signal in all PMTs, both genuine Čerenkov light and extraneous background light are acquired. Since Čerenkov light from an air shower subtends a definite shape, orientation and distribution across just a subset of the PMT array, it is vital that only those PMTs with true Čerenkov signal are used for image parameterisation. Pedestal subtraction, PMT gain calibration, software padding and image cleaning are all pre-parameterisation procedures which help maximise the true Čerenkov light content of EAS images, while simultaneously minimising the effects of background noise. An overview of these techniques is provided here; for detailed discussions see Fegan (1996) and Fegan (1997).

5.2.1 Pedestal Subtraction

The deliberate use of artificial ADC pedestals of $\sim$20 d.c., to enable measurement of both positive and negative fluctuations in the night-sky background, was detailed in section 4.7.1. Before analysing the signal content in a PMT channel, its average pedestal value (artificial pedestal + night-sky fluctuation) must be subtracted and the pedvar (pedestal variance) calculated. This is accomplished by accumulating the 1 Hz pedestal signals, individually for each channel, over the duration of a data run ($\sim$1600 events in 28 minutes), calculating the mean per channel, and subtracting it from the measured signal of each recorded Čerenkov event. An alternative method for estimating pedestal values, which utilises the Čerenkov events themselves, is described in Fegan (1996)

The pedvar for each channel is simply its RMS pedestal deviation from the mean. Pedvars are used to quantify the level of noise in each channel and determine the difference in brightness between ON and OFF sky regions, for use in software padding (see section 5.2.4). Upon calculating the pedvar for each PMT, the pedvar mean and standard deviation for the PMT array are used to provide an initial determination of those PMTs which are too noisy to be considered part of the Čerenkov image—PMTs which happen to have

observed a star or a particularly bright region of sky generate large pedvars. Generally such tubes are physically switched off during observing. However, as a precaution, any tube with a pedvar larger than 2.0 times the standard deviation about the mean pedvar is also disabled in software.

5.2.2 PMT Gain Calibration

The process of flat-fielding using nitrogen arc lamp data (N2 data), mentioned previously in section 4.9.3, is used to normalise the relative gain of each channel and provide, in software, a uniform response across the camera. Gain determination for an individual tube involves calculating the ratio of the N2 signal in that tube to the mean N2 signal recorded by the camera. Gains for each tube are calculated on an event by event basis for each of the $\sim$4000 events in an N2 run and then used to obtain an average gain per tube. It is these average gains which are used to scale the individual ADC values of all true Čerenkov data events, thereby providing homogeneous sensitivity across the camera. An alternative method for estimating gains using the Čerenkov events themselves is detailed in Fegan (1996).

5.2.3 Picture and Boundary Cleaning

Before gains are applied, each event recorded by the camera is filtered to remove contributions arising from those tubes whose signal contains background noise only. The technique used to decide which tubes constitute the image is known as picture/boundary cleaning (Punch et al., 1991). In this technique a PMT's signal is considered part of the "picture" if it exceeds a certain high threshold. A PMT with a signal greater than a certain lower threshold but which is adjacent to a picture PMT, is considered part of the "boundary". Picture and boundary tubes comprise the "cleaned" image and signals in all other tubes are zeroed. Picture and boundary thresholds are generally multiples of the RMS pedestal deviation (σ_{ped}) for each tube. Their optimised values for the Whipple 490-pixel camera were found to be 4.25 σ_{ped} and 2.25 σ_{ped} respectively. Figure 5.2 shows a simulated γ-ray image before and after picture/boundary cleaning. Picture tubes are coloured red, boundary tubes green, and zeroed tubes blue.

5.2.4 Software Padding

In ON/OFF observing mode, differences in sky-noise between the ON and OFF sky regions will introduce bias. Bias arises as a result of the effects of noise on boundary tubes. Boundary tubes are more susceptible to noise

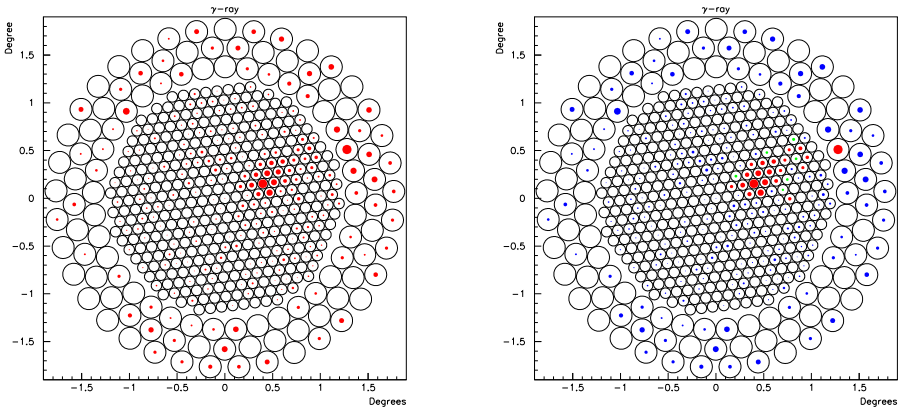

(a) Before cleaning. **(b)** After cleaning.

Figure 5.2: Simulated γ-ray image before and after picture/boundary cleaning. Picture tubes are coloured red, boundary tubes green, and zeroed tubes blue. From Dunlea (2001).

problems because they contain significant amounts of both Čerenkov signal and noise, compared to picture tubes which are mainly Čerenkov signal dominated. For a "quiet" tube viewing a dark region of sky, the Čerenkov signal will dominate and the tube will likely exceed its boundary threshold to become part of the image. However, for the same amount of true Čerenkov signal a "noisy" tube in a brighter region of sky will more likely fall short of its (increased) boundary threshold and be set to zero by the cleaning process. In effect, the Čerenkov image is clipped. Since gamma-ray selection criteria, such as Supercuts (see section 5.11), favour small shape (*length* and *width*) parameters, the clipping of a true Čerenkov tube from a hadron image can result in the image being mistakenly classified as a γ-ray. This is a form of positive bias which may result in an artificial γ-ray excess.

To overcome the problem of noise-introduced bias, a technique known as *software padding* was developed (Cawley, 1993). Software padding compensates for noise-introduced bias by deliberately adding additional Gaussian noise, on a pixel by pixel basis, to the less noisy region of sky. In other words, for an ON/OFF pair, the same pixel is examined in both the ON and OFF data to determine which is quieter, and software noise is then added to "pad" the quieter of either the ON or the OFF up to the same noise level as the noisier situation. Because noise-introduced bias and padding both effect the shape parameters (section 5.11.2), their effects can easily be demonstrated

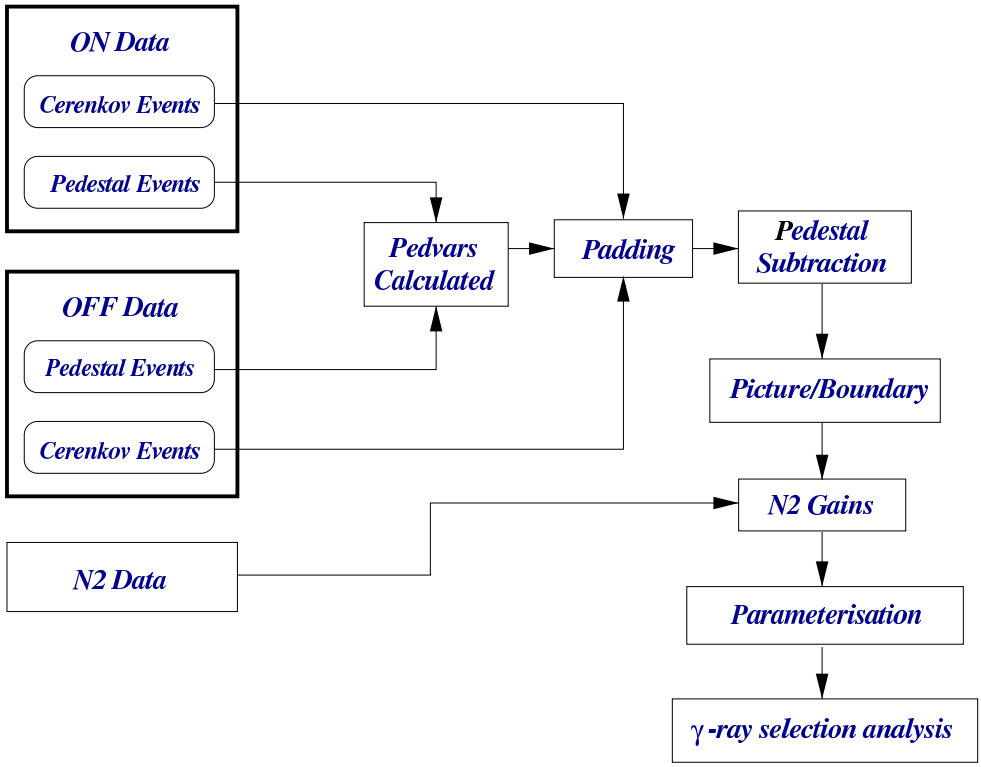

Figure 5.3: The data calibration process for ON/OFF data.

in simulations and real data. In seeking low energy γ-rays from the Crab pulsar, noise-introduced bias and padding are particularly important and so are further discussed in the context of Crab data in section 5.13.1 below. For a full discussion of the details of the Whipple software padding algorithms see Cawley (1993) or Fegan (1997).

An overview of the data calibration process for ON/OFF data is provided in Figure 5.3.

5.3 Image Parameterisation

Once all image calibration, cleaning and padding has been performed the images are subjected to moment fitting to determine their Hillas parameters. The Hillas parameters were discussed in detail in chapter 3 and their derivation is outlined in appendix A. The parameterisation procedure assumes that each pixel has the same influence on the final image. In the current 490-pixel camera the outer 111 pixels are larger, and are arranged differently to the

inner 379 pixels, see figure 4.14. Due to the inherent difficulty in combining Čerenkov signals from these two distinct PMT arrays, all image parameterisation (and also image calibration) performed in this work pertains *only* to the inner 379 pixels. Recent efforts to reconcile signals from the inner and outer PMTs are detailed in Fegan (2002b). The γ-ray image shown previously in its uncleaned and cleaned states (Figure 5.2), is presented in its parameterised form in Figure 5.4 with the fitted ellipse shown.

5.4 The Crab Pulsar Dataset

Observations of the Crab pulsar were made during moonless periods between 02 January 2000 and 17 February 2002. By adding the Whipple observatory log-sheet entries for all Crab runs between these dates to a *MYSQL* database, it was possible to select and categorise appropriate data files for analysis. The following selection criteria were used:

Weather Only observations made during A and B weather were selected (section 4.9.4).

Mode Both ON/OFF and TRACKING data files were selected.

Elevation The data was categorised by elevation band (section 5.9). Four elevation bands were used: $35° \rightarrow 50°$, $51° \rightarrow 60°$, $61° \rightarrow 70°$ and $71° \rightarrow 80°$.

Since optimisations of the γ-ray selection criteria, for the Supercuts and Kernel analyses, were performed on the *complete* elevation-specific datasets themselves, (see section 5.14 below), it was necessary to check beforehand the integrity of each individual data file to prevent optimisation biases. Integrity checks were carried out at two levels:

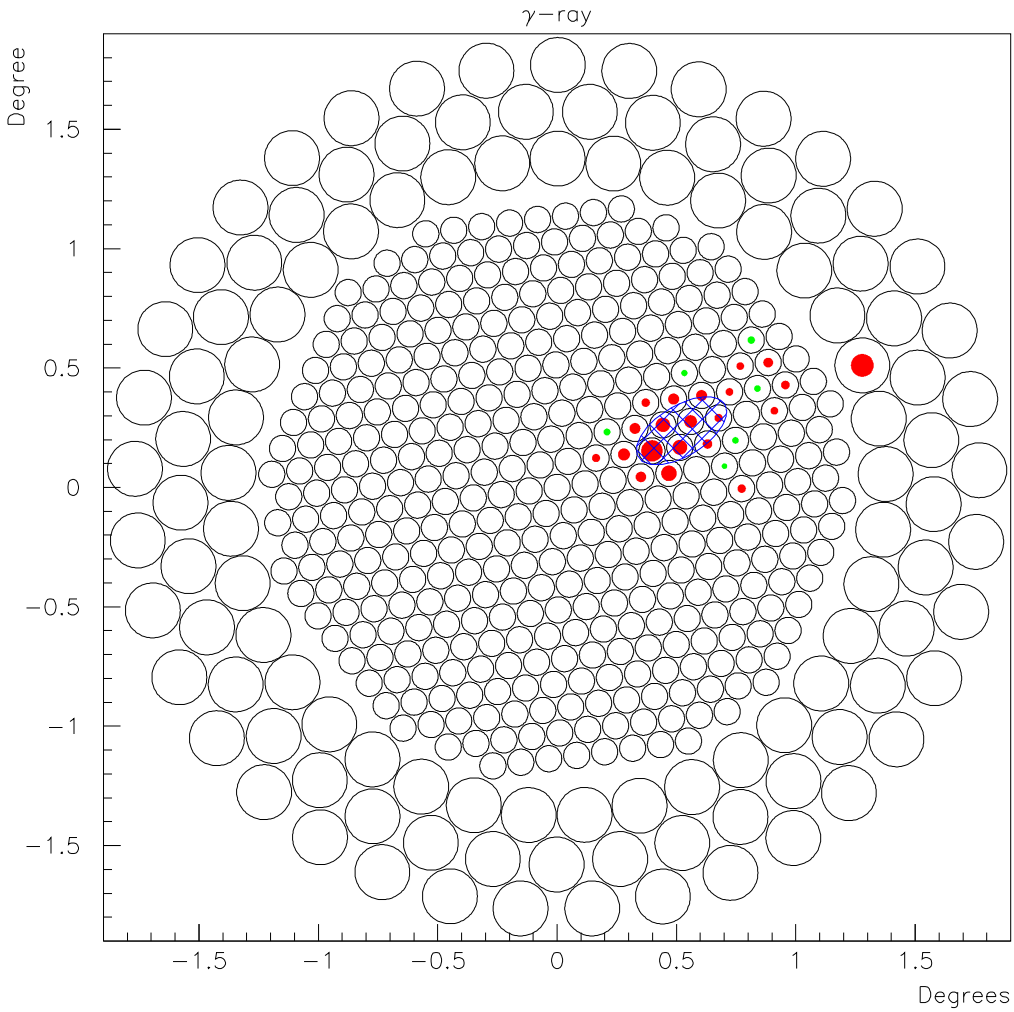

Figure 5.4: Parameterised simulated γ-ray, showing fitted ellipse. From Dunlea (2001).

Level 1 The level 1 integrity check was a diagnostic "fastlook" analysis in which the pedestals/pedvars, raw trigger rates, and the GPS timing fidelity were scrutinised. Data runs were rejected if they displayed wildly varying pedestals/pedvars, non-uniform trigger rates over the duration of the observing run (indicative of a cloud passing overhead, for example), or inconsistent times (i.e. inconsistency between the various timing measurements of figure 4.20).

Level 2 The level 2 integrity check involved a straightforward Supercuts 2000 γ-ray selection (see section 5.11 for a discussion of the Supercuts analysis technique), followed by a detailed examination of the number of events passing each of the pre-selection, shape, and orientation cuts. Any data files displaying unusual behaviour (such as negative γ-ray significances) were examined for duration mismatches between the ON and OFF runs. Duration mismatches when found were remedied by cutting the longer file to equate the duration of the shorter.

A breakdown of the final dataset which passed all the fidelity checks is provided in tables 5.1 and 5.2. This dataset (comprising 196 ON/OFF pairs and 29 TRACKING runs) was used in all the subsequent Crab pulsar analyses detailed below.

Dates	02 Jan 2000 – 17 Feb 2002	
Weather	A and B	
Mode	ON/OFF	84.28 hours (ON)
		84.28 hours (OFF)
	TRACKING	13.05 hours
Total ON-source		97.33 hours

Table 5.1: Breakdown, by observing mode, of the Crab pulsar dataset used in this work.

Elevation	No. hours
$0 - 50$	20.70
$51 - 60$	16.01
$61 - 70$	20.86
$71 - 80$	39.76
Total	97.33

Table 5.2: Breakdown, by elevation band, of the Crab pulsar dataset used in this work.

Elevation	45°	55°	65°	75°
No. EAS launched	300,000	300,000	300,000	300,000
Incident spectral index	-2.44	-2.44	-2.44	-2.44
Min. Energy (TeV)	0.05	0.05	0.05	0.05
Max. Energy (TeV)	15.0	15.0	15.0	15.0
Drop-zone[1] radius (m)	200	200	200	200
Pedestal Variance (d.c.)	4.8	4.8	4.8	4.8
No. triggering showers	23,260	21,287	43,304	47,407

Table 5.3: Production parameters of the MC data used in this thesis work.

5.5 Monte Carlo Simulations

The Monte Carlo (MC) γ-ray simulations used in this study were produced using the KASCADE simulations package, as implemented at Iowa State University (section 3.6.1). For each of the four elevation bands spanned by the Crab dataset two independent sets of MC data were produced. The first set was used for three main tasks: (1) production of γ-ray parameter distributions (section 5.6), (2) input to the Kernel analysis (section 5.12) and (3) collection area determinations for the Supercuts analysis (section 5.15.1). The second set was used exclusively for collection area determinations for the Kernel analysis. A second set of independent simulations was considered appropriate when estimating collection areas for the Kernel analysis due to its heavy dependence on the first set for γ-ray identification. The production parameters input to the simulation algorithms are listed in table 5.3. For the present work in which low energy events (small EAS) are of considerable importance, a drop-zone radius of 200 m was considered adequate, although larger drop-zones are generally preferable for IACT simulations.

Muon simulations produced at the Whipple observatory (Horan, 2001)

[1] As per usual practice, the drop-zone is defined in a plane perpendicular to the optical-axis of the telescope.

and used previously by Dunlea (2001) were also used qualitatively in this work. The simulations are at several discrete energies from 4 GeV to 100 GeV, and are subjected to similar trigger and noise conditions as the γ-ray simulations.

5.6 Parameter Distributions

In any parameter-based analysis it is advantageous to examine the distribution of the parameters used, in both real data and in simulations. Such an examination provides details regarding the regions in parameter space where signal and noise lie (i.e. the γ-ray and background domains for the IACT). For the present work five main parameters are used by the Supercuts and Kernel selection mechanisms, in the identification of γ-ray events. They are: *size*, *length*, *width*, *alpha* and *distance* (section 3.8). Their distributions for simulated γ-rays (solid lines) and for real uncut raw Crab data (dashed lines) are presented in Figure 5.5 and discussed here:

size fig. 5.5(a)	The typically smaller *size*s of γ-ray simulations compared to the real data reflects the compact nature of γ-ray images when compared to hadrons.
length fig. 5.5(a)	Simulated γ-rays appear shorter than their background counterparts. This is due to the irregular spread of hadron EAS, as discussed in section 3.7.
width fig. 5.5(a)	Simulated γ-rays are in general narrower than their background counterparts; due to the greater transverse spread of hadronic EAS.
alpha fig. 5.5(a)	Since the simulated γ-rays arise from showers originating at the centre of the telescope's field-of-view, they typically subtend small values of *alpha*. Background events, which arrive isotropically in the field-of-view, produce a flat distribution of *alpha* values. The slight peaking of the background *alpha* distribution near 90° can be attributed to truncation effects at the edge of the camera.

distance
fig. 5.5(a)

The distribution of the *distance* parameter for both γ-rays and background events increases towards the edge of the telescope's field-of-view. In general this is due to the greater physical detection area (larger detection solid angle) available near the edge of the camera, compared to at its centre. For both the simulated and real data, however, the distributions peak before reaching camera's edge (379-pixel camera). One would expect the distribution for γ-rays to peak at $\sim$1.3°due to the Čerenkov angle (section 3.6.3), and the distribution of background events to monotonically increase towards the camera's edge. For the current camera, in which the outer tubes are not used (see section 5.3), the lower than expected *distance* peaks may be attributed to truncation effects at the edge of the relatively narrow field-of-view ($\sim$1.2°half angle). The expected *distance* distributions are more clearly demonstrated using data from the Whipple wide-field (2.4°half angle) 331-pixel camera (see Masterson 1999 for example).

5.7 ON–OFF Parameter Distributions

Parameter distributions may also be used to crudely show the presence of an ON-source γ-ray excess in ON/OFF data prior to any selection analysis. By subtracting OFF-source parameter distributions from their corresponding ON-source distributions, excesses in the ON data, attributable to γ-ray events, stand out clearly in the γ-ray domains indicated by the simulated distributions of Figure 5.5. To demonstrate this point, the ON–OFF uncut distributions for the *size*, *length*, *width*, *alpha* and *distance* parameters, together with the simulated γ-ray distributions, are given in Figure 5.6. It can be clearly seen that ON excesses in the raw data exist, by in large, in the regions of parameter space where simulations indicate the presence of γ-rays. Discrepancies between the ON–OFF and simulated distributions indicate those regions of parameter space in which γ-ray excesses are difficult to extract, due to similarities between γ-rays and background events (e.g. at small values of *distance*). The anomalous OFF excess evident in the ON–OFF *size* distribution at small values of *size* (Figure 5.6(a)) is discussed later, in section 5.13.1, in the context of sky-noise problems.

Altogether, ON–OFF distributions provide a useful means to examine

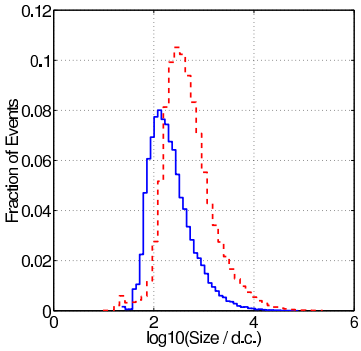

(a) Size.

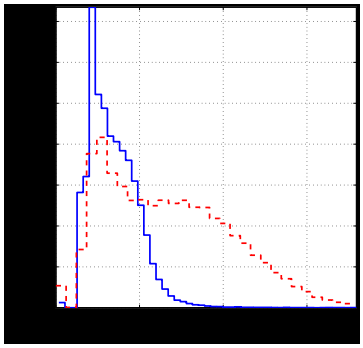

(b) Length.

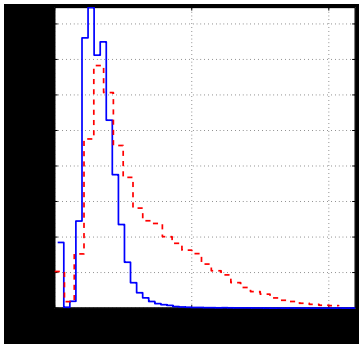

(c) Width.

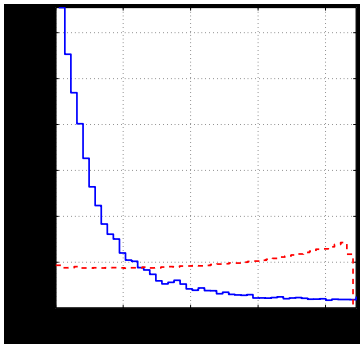

(d) Alpha.

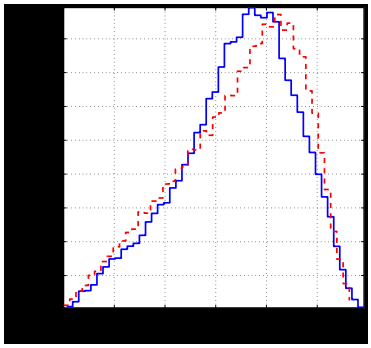

(e) Distance.

Figure 5.5: Pre-selection parameter distribution histograms for simulated γ-rays (solid line) and real data (dashed line).

prima facie the potential for a γ-ray signal from a dataset before selection cuts are applied. They also help illustrate possible problems in the data and indicate the effectiveness of the γ-ray selection cuts used.

5.8 Local Muons

Radiating muons represent a double-edged sword in atmospheric Čerenkov astronomy (Fegan, 1997)—on one hand they may be used to calibrate the IACT (for example Vacanti et al. 1994 and Horan 2001), while on the other they form a grave source of unwanted background events. Moriarty et al. (1997) point out the insidious nature of individual muons which pass within $\sim$50 m of the Whipple reflector. Čerenkov light from such muons is imaged as a complete or partial ring, depending upon the orientation of the muons's trajectory relative to the reflector's optical-axis.

Selection mechanisms designed to eliminate hadrons have no difficulty in also rejecting large muon rings. Small muon arcs, however, are difficult to distinguish from γ-ray events and so present a serious barrier to the lowering of a telescope's energy threshold. Indeed, the telescope triggering rate due to muons of energy greater than 8 GeV becomes a major component of the background for γ-ray energies below 300 GeV. As this work is concerned with a wide range of γ-ray energies, not least at the low end of the TeV regime, some parameter distributions for muons are presented in Figure 5.7. These distributions serve to identify the muon-domain and γ-ray simulations are again used for comparison purposes. Some further discussion regarding muons, in the context of the *length/size* parameter, is presented in section 5.11.

5.9 Elevation Banding

The IACT, unfortunately, is not an elevation independent technique. Rather, since it is highly dependent on the distribution of Čerenkov light reaching the detector, it suffers the elevation-dependent effects of atmospheric absorption, and projection effects. Low elevations present relatively long path lengths for Čerenkov photons to travel, thereby allowing for more absorption and an increase in the telescope's energy threshold, compared to high elevations for which the opposite is true.

Since γ-ray EAS occur further away from the telescope for low elevation observations than for high elevations (see Figure 5.8), their focused images are necessarily smaller, even though their Čerenkov light pools on the ground

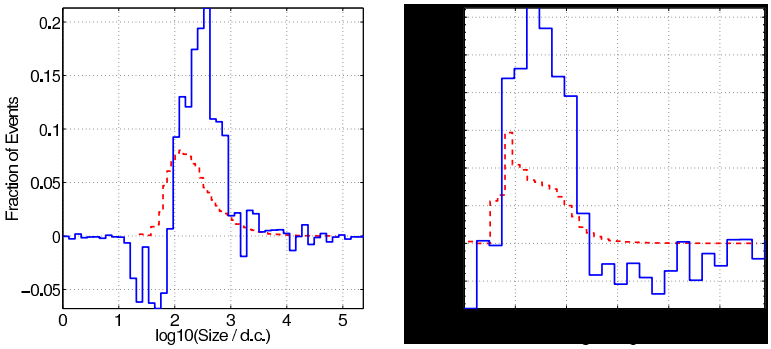

(a) Size. **(b)** Length.

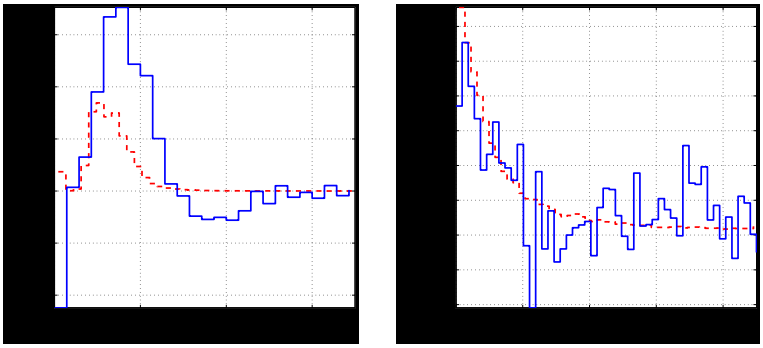

(c) Width. **(d)** Alpha.

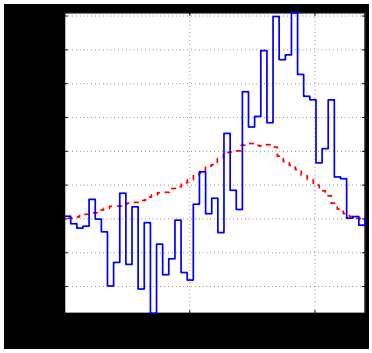

(e) Distance.

Figure 5.6: ON–OFF parameter distributions for raw Crab plerion data (83 ON/OFF pairs combined at elevations 71° → 80°). γ-ray simulations (dashed lines) are used to indicate the γ-ray domain for each parameter.

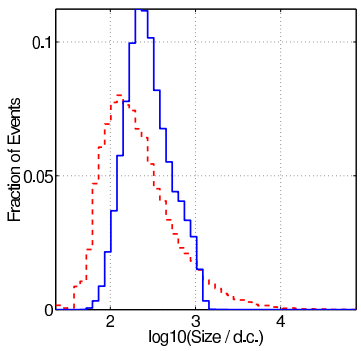

(a) Size.

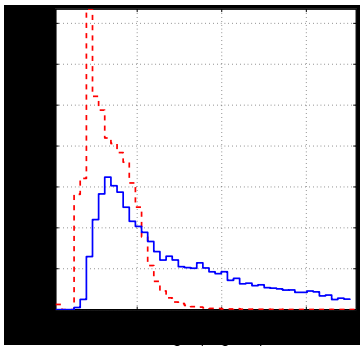

(b) Length.

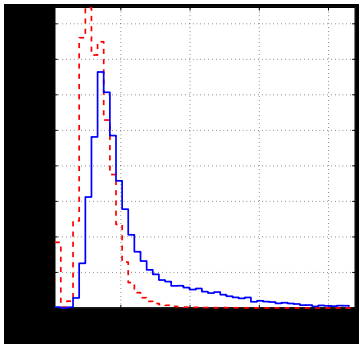

(c) Width.

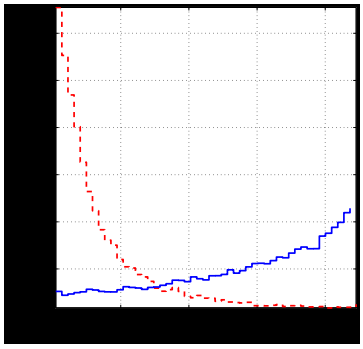

(d) Alpha.

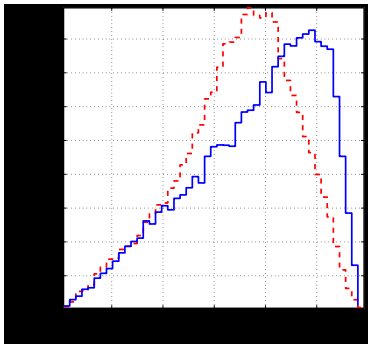

(e) Distance.

Figure 5.7: Parameter distribution histograms for simulated muons (solid lines) and simulated γ-rays (dashed lines).

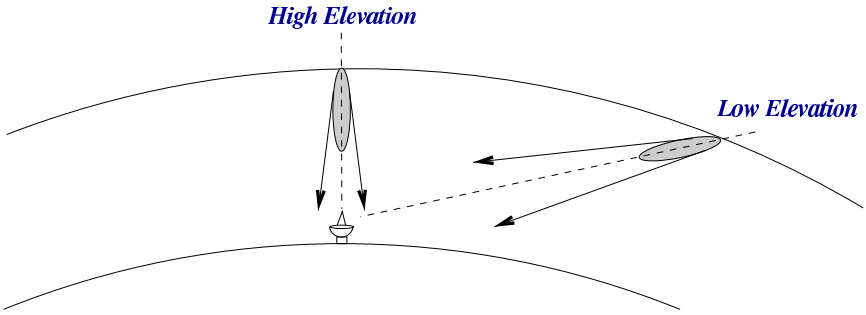

Figure 5.8: EAS observed at low elevations develop further away from the telescope than EAS which are observed at high elevations, and their light-pools on the ground are larger.

are larger. For this reason, γ-ray selection criteria optimised at typical (high) elevations are not strictly suitable for application to low elevation data, and low elevation observations have larger collection areas (see section 5.15.1). Figure 5.9 presents the shape (*length* and *width*) parameter distributions for high elevation (solid line) and low (dashed line) elevation γ-ray simulations, after all other cuts have been applied. It is clear that the distributions for low elevation data are slightly shifted to smaller values. Since the present 490-pixel camera has the highest resolution of any camera thus far employed by the Whipple collaboration, it is ideal for recording the smaller images presented by low elevation observations. Furthermore recent optical alignment work on the reflector should assist in this regard, although it should be noted that optical sacrifices made at low elevations, as a result of bias-alignments (section 4.5), can seriously hamper low elevation observations.

It was pointed out earlier (section 4.5) that the typical elevation range for astronomical observations with the Whipple telescope is $65° \rightarrow 75°$ above the horizon. Nonetheless, the complete dynamic range of the telescope's elevation axis is utilised during the course of each observing dark period. Indeed, as detailed in section 5.4, the Crab dataset used for the current analysis extends over a large elevation range. In order to extract the maximum γ-ray signal available from the Crab dataset, for use in temporal analyses, the γ-ray selection criteria of both the Supercuts (section 5.11) and the Kernel analyses are independently optimised and applied in each of the four elevation bands listed in table 5.2.

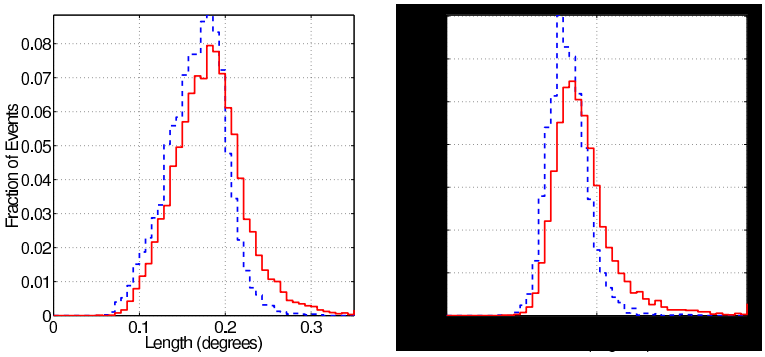

(a) Length. **(b)** Width.

Figure 5.9: Parameter distribution histograms for the shape parameters for high elevation (solid line) and low elevation (dashed line) simulated γ-ray data.

5.10 The *Size*-Energy Relationship

The *size* of a γ-ray image is a measure of its total Čerenkov light content. *Size* is a calorimetric parameter, in that it indicates the energy of the instigating γ-ray; more energetic γ-rays produce larger EAS and hence more Čerenkov light. A plot of energy versus *size* for a set of simulated γ-rays is provided in Figure 5.10. It shows clearly the linear relationship between *size* and energy.

In spectral analyses *size* is a critical parameter for γ-ray energy estimation, see for example Mohanty et al. (1998). Although the present work is concerned with energy, no explicit energy-reconstruction is pursued. Instead, as outlined below, the data is split into discrete *size* bands and analysis methodologies are optimised to identify γ-ray events falling within each band. An energy characterisation for each band is then provided using simulations (section 5.15.2).

5.11 Supercuts Analysis

The Supercuts analysis technique (Punch et al., 1991) is the standard method employed by the Whipple collaboration to discriminate between γ-rays and hadron events. The technique selects probable γ-ray events on the basis of each image's shape (*length* and *width*) and orientation (*distance* and *alpha*) in the telescope's field-of-view. By setting strict lower and upper bounds on a "γ-ray domain" in Hillas parameter space, and requiring that only those

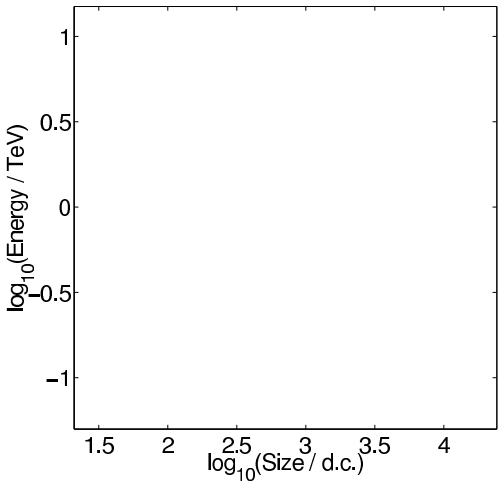

Figure 5.10: Energy versus *size* for a set of simulated γ-ray events, incident at 45° elevation. Note: only γ-rays simulated at 45° elevation are used here, as low elevation γ-ray images are typically smaller and so suffer less from truncation effects at the edge of the field-of-view than their higher elevation counterparts.

$max1 > 30$ d.c.
$max2 > 30$ d.c.
$0.05° < width < 0.12°$
$0.13° < length < 0.25°$
$0.4° < distance < 1.00°$
$alpha < 15°$
$length/size < 0.0004°$

Table 5.4: The Supercuts 2000 selection criteria.

images whose parameters fall within these bounds can pass the analysis, Supercuts provides a straightforward means of selecting probable γ-rays and rejecting probable hadrons. Although simulations provide details of the initial γ-ray domain in parameter space (Figure 5.5), the Supercuts technique is by-in-large simulations independent as it is optimised on contemporaneous ON/OFF data for a particular telescope configuration. The current Supercuts criteria (Supercuts 2000) used by the Whipple collaboration are presented in table 5.4. The various selection cuts which comprise the complete Supercuts analysis are presently described.

5.11.1 Pre-selection

Before any shape and orientation selections are made the raw data is reduced by means of a pre-selection analysis. Pre-selection criteria come in three forms:

Software Trigger Cuts The software trigger cuts serve to reject background events that are too small to have meaningful parameter values, and are effectively a software analogue to the hardware trigger (Quinn et al., 1995). Basically, the top two (*max1*, *max2*) or top three (*max1*, *max2*, *max3*) tubes in an image are required to register digital count signals above certain thresholds. Events which fail these criteria are not passed to the final Supercuts analysis.

max3 was not used in the software trigger for the present work. This was considered reasonable (despite the 3-fold hardware trigger) as trial optimisations (of the type described in section 5.11.6 below) which did include *max3* yielded little or no improvement above trial optimisations which did not.

frac3 cut The *frac3* cut requires that the percentage of the total light content in the top three tubes be below a certain level. This eliminates events in which the total light is dominated by the light in just three or fewer tubes. Such events are undesirable as they are predominantly caused by cosmic ray particles passing directly through the camera.

***size* cuts** The *size* cuts serve to impose, in software, a form of energy filter on the events which are analysed. The standard Supercuts analysis does not employ an explicit *size* cut, although an effective lower *size* limit is imposed as a result of the other selection criteria (section 5.11.5).

Pre-selection cuts based on *size* form an integral part of the present work (both for Supercuts and for Kernel analysis) as energy filtering is important if Crab pulsar events within a particular energy regime are to be analysed for periodicity.

5.11.2 Shape Selection

Typical distributions of *length* and *width* for γ-ray simulations and real background events were plotted in Figures 5.5(b) and 5.5(c) respectively. It can be seen that γ-ray images tend to have smaller *length* and *width* values than their background counterparts. By imposing upper and lower limits to the *length* and *width* parameters, Supercuts provides a means of selecting only those events with γ-ray-like shapes.

5.11.3 Orientation Selection

The *distance* and *alpha* parameters are important "orientation" parameters for the selection of γ-rays from a point source (one-dimensional analysis). For the present analysis the Crab plerion is effectively a point source at the centre of the telescope's field-of-view (the angular resolution of the IACT for a single telescope does not permit two dimensional mapping of the Crab nebula). Hence *distance* and *alpha* are useful in this work. Details of analysis methods for the selection of γ-rays from extended and/or off-axis sources (two dimensional analysis) may be found in Masterson (1999) and Lessard et al. (2001).

Since γ-rays from a point source at the centre of the field-of-view subtend small values of the *alpha* parameter (Figure 5.5(d)), Supercuts identifies probable γ-ray events as having low *alpha* values (typically below 15°).

The Supercuts selection criteria include upper and lower limits on the value of *distance*. The lower limit is intended to reject events with very small impact parameters (such events have poorly defined *alpha* values and are unsuitable for γ-ray energy estimation, section 3.8) while the upper limit is effectively defined by the telescope's field-of-view. For the current camera the *distance* upper limit is moved slightly inwards from its maximum value in order to avoid the effects of image truncation at the camera's edge.

Although *asymmetry* is also an orientation parameter it is not used in the present analysis due to the rather narrow field-of-view of the current camera.

5.11.4 *length/size* Selection

The *length/size* cut was introduced in the Supercuts 1995 selection criteria for the Whipple 109-pixel camera (Catanese et al., 1995). Muon arcs, which perniciously resemble γ-ray events (section 5.6), have low light levels per pixel and are long for the amount of light they contain, compared to γ-ray images (Figure 5.1). Figure 5.11 shows the $\log_{10}(size)$ versus *length* and *length/size* distributions for simulated γ-rays and simulated local muons. The standard

length/size selection cut for γ-rays (< 0.0004) currently employed by Whipple collaboration is shown also. Clearly the *length/size* cut is very effective at reducing the muon background. For this reason it is considered a valuable component of the Supercuts selection criteria.

5.11.5 Supercuts 2000 – Effective Lower Size Threshold

The Supercuts 2000 γ-ray selection criteria for the current Whipple camera (table 5.4), have proven very effective for the selection of γ-rays with high significance from a number of sources (for example Krennrich et al. 2001a; Horan et al. 2002). Nevertheless, their strict lower and upper bounds on the Hillas parameters are sometimes too harsh a selection mechanism. Since the Supercuts 2000 criteria were optimised for maximum significance (Lessard, 1999) they tend to sacrifice low energy (small *size*) events which are hard to distinguish from hadrons, in order to obtain maximum significance using larger events which have more clearly defined γ-ray characteristics. Figure 5.12 presents the ON−OFF *size* distribution for raw data (solid line) and for Supercuts 2000 selected data (dashed line), recorded for the Crab plerion in the $71^\circ \rightarrow 80^\circ$ elevation band. The clear raw ON excess in the *size* range $\sim$100 d.c. to $\sim$1400 d.c shows that there is a large population of γ-rays available within this range. The lower *size* boundary ($\sim$320 d.c) of the ON excess which remains after Supercuts 2000, however, demonstrates that an effective lower *size* threshold is imposed by the Supercuts 2000 criteria.

In the search for a new hard-spectrum γ-ray source, where maximum significance is desireable, the lower *size* threshold imposed by Supercuts 2000 is generally not a problem. However, for data analysis efforts concerned with sources for which low energy events are required (e.g. pulsars and distant AGN with intrinsic spectral cutoffs) Supercuts 2000 is too restrictive. By rejecting events below $\sim$320 d.c. the technique is neglecting a large number of γ-ray events which may contain valuable information regarding the source. In this work, where small *size* events are considered vital—in order to probe potential pulsed γ-ray emission at the low end of the TeV regime—the Supercuts 2000 criteria are clearly inadequate. Since TeV-scale γ-ray emission from the Crab plerion is well established at high levels of significance, what is required here is a selection mechanism to extract γ-rays from the Crab at low energies. The potential increase in the number of γ-rays, to be gained by probing the small *size* domain, provided the motivation behind a Supercuts re-optimisation for the present work

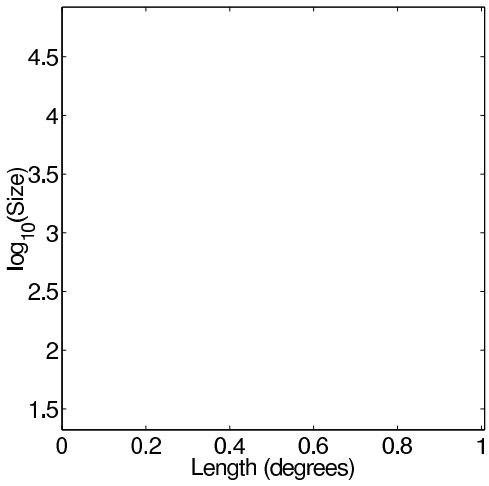

(a) $\log_{10}(size)$ vs *length*.

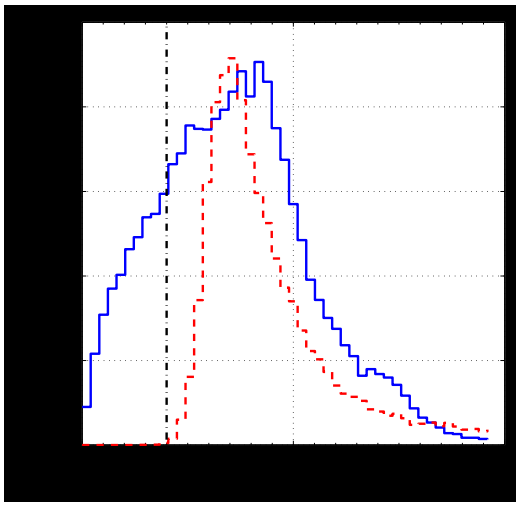

(b) *length*/*size* histogram.

Figure 5.11: (a) $\log_{10}(size)$ versus *length* distribution for γ-rays (blue), muons (green) and Supercuts 2000 selected γ-rays (red). The Supercuts 2000 *length*/*size* cut is represented by the solid line. (b) the *length*/*size* parameter distribution for γ-rays (solid line) and simulated muons (dashed line). The Supercuts 2000 *length*/*size* cut is represented by the dot-dashed line.

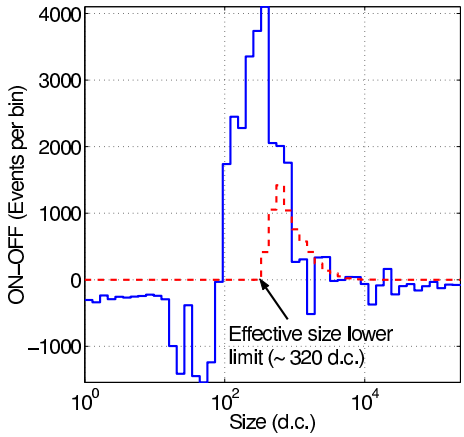

Figure 5.12: The ON–OFF *size* distributions of raw (solid line) and Supercuts 2000 analysed (dashed line) Crab data—39.76 hours of data taken in the 71° → 80° elevation range. A clear raw ON excess is visible between *size* ∼100 d.c. and ∼1400 d.c. Supercuts 2000 misses out on a large proportion of the raw ON excess by setting an effective *size* lower limit at ∼320 d.c. (The OFF excess visible below ∼100 d.c. is discussed in section 5.13.1 in the context of night-sky background noise).

5.11.6 Supercuts Re-optimisation

The Supercuts criteria have traditionally been optimised for each version of the Whipple PMT-camera to give maximum γ-ray significance on a subset of contemporaneous Crab data. The optimised cuts are tested on the remaining Crab dataset and on data from other confirmed TeV sources such as Markarian 421 and Markarian 501. Generally, to avoid bias, the Crab optimisation dataset is not used in any further scientific analyses.

The objective of the present Supercuts re-optimisation is to extract the largest possible number of γ-rays with highest significance from the Crab dataset, over the complete dynamic range of γ-ray energies available (as indicated by the *size* parameter). In this regard several alterations to the standard optimisation procedure are implemented:

Complete Dataset Optimisation The selection criteria are optimised on the complete Crab dataset *itself*. Although generally a source of bias, optimising on the dataset itself for the present work is not considered unreasonable. Since TeV γ-rays from the direction of the Crab plerion are now firmly established and since the present study is mainly a search for periodicity, bias does not arise.

Size/Elevation Bands The cuts are also independently optimised in discrete *size* ranges for each of the four elevation bands spanned by the Crab dataset. In other words, multiple optimisations are performed. A re-optimisation of Supercuts in restricted *size* ranges was considered important for the present work in order to constrain the selection criteria to select small *size* events, which an optimisation over all *size* values would sacrifice, in favour of the higher significances available at larger *size*. Ultimately, a transformation from *size* band to γ-ray energy is performed; this is outlined in section 5.15.2.

Due to the inherent difficulty in extracting a meaningful γ-ray signal from events with *size* values less than 150 d.c. no Supercuts re-optimisations were attempted below this value.

Optimisation of γ-ray Significance All cuts for this work are optimised on ON/OFF data for maximum γ-ray significance above the background. Although the cuts were also optimised for maximum γ-ray rate in several trial *size* ranges, only significance optimisations are used in the final Crab pulsar analysis. The rate-optimised cuts were found to be too unstable (fluctuating rate values from data-file to data-file) to reliably select candidate γ-ray events.

length/size Several previous workers have attempted, with some success, to select low energy events from γ-ray sources by optimising Supercuts in a restricted low *size* domain. The "Smallcuts" criteria derived by Moriarty et al. (1997) proved quite effective at extracting such events from the Whipple 109-pixel camera, at *size* < 400 d.c. In their work Moriarty et al. used the *length/size* cut to reject muon-like events. They demonstrated its usefulness in reducing the number of background events and improving the γ-ray significance. However, it was recently pointed out by Krennrich et al. (2001b) that the *length/size* cut, when applied to current 490-pixel data, has the effect of substantially increasing the Whipple telescope's energy threshold. For this reason, *length/size* is not used in the Supercuts re-optimisations undertaken in this work.

Optimisation Methodology

Several methods have been tried and tested by the Whipple collaboration for Supercuts optimisation. These include the *grid search* method (Quinn, 1997), the *single parameter variation* method (Lessard, 1999; Quinn et al., 1997) and the *simplex method* (Moriarty et al., 1997). The *grid search method* is generally considered inefficient for the optimisation of more than three parameters and so is seldom used to optimise the complete set of Supercuts

Cut	Initial Value
max1	0 d.c.
max2	0 d.c.
Lower *width*	0.00°
Upper *width*	0.04°
Lower *length*	0.00°
Upper *length*	0.1°
Lower *distance*	0.00°
Upper *distance*	0.5°
Upper *alpha*	0°

Table 5.5: The γ-ray selection cuts re-optimised in this work, and their initial values for the *single parameter variation method*.

criteria. For the present work the *single parameter variation* method is exclusively utilised and it is described briefly here.

In the *single parameter variation* method each selection cut is initialised to a plausible starting value before optimisation begins. The optimum set of selection criteria are then searched for with respect to one cut at a time, by applying all cuts except the one under optimisation. The peak in a plot of γ-ray significance versus cut-value for the cut under optimisation represents its first "best-estimate" value. Once the first best-estimate of each cut is found the process is repeated with the first best-estimates replacing the initial values. The second best-estimate cuts then replace the first in the following iteration, and so on. After several iterations the best-estimate cuts converge on their optimised values. For the present analysis the cuts were found to sufficiently converge on their optimised values after three iterations.

Table 5.5 provides a list of the cuts which were optimised as part of this work along with their initial values. The γ-ray significance versus cut-value plots for a trial optimisation over all *size* values is presented in Figure 5.13, as examples of the type of plots obtained in the optimisation process.

5.12 Kernel Analysis

The Kernel multivariate analysis technique is applied, in addition to the standard Supercuts selection technique employed by the Whipple collaboration, to the Crab dataset used in this thesis work. The usefulness of the Kernel technique in imaging atmospheric Čerenkov astronomy has been demonstrated previously by Dunlea (2001); Dunlea et al. (2001) and Moriarty and Samuelson (2000). An overview of the technique and its implementation is

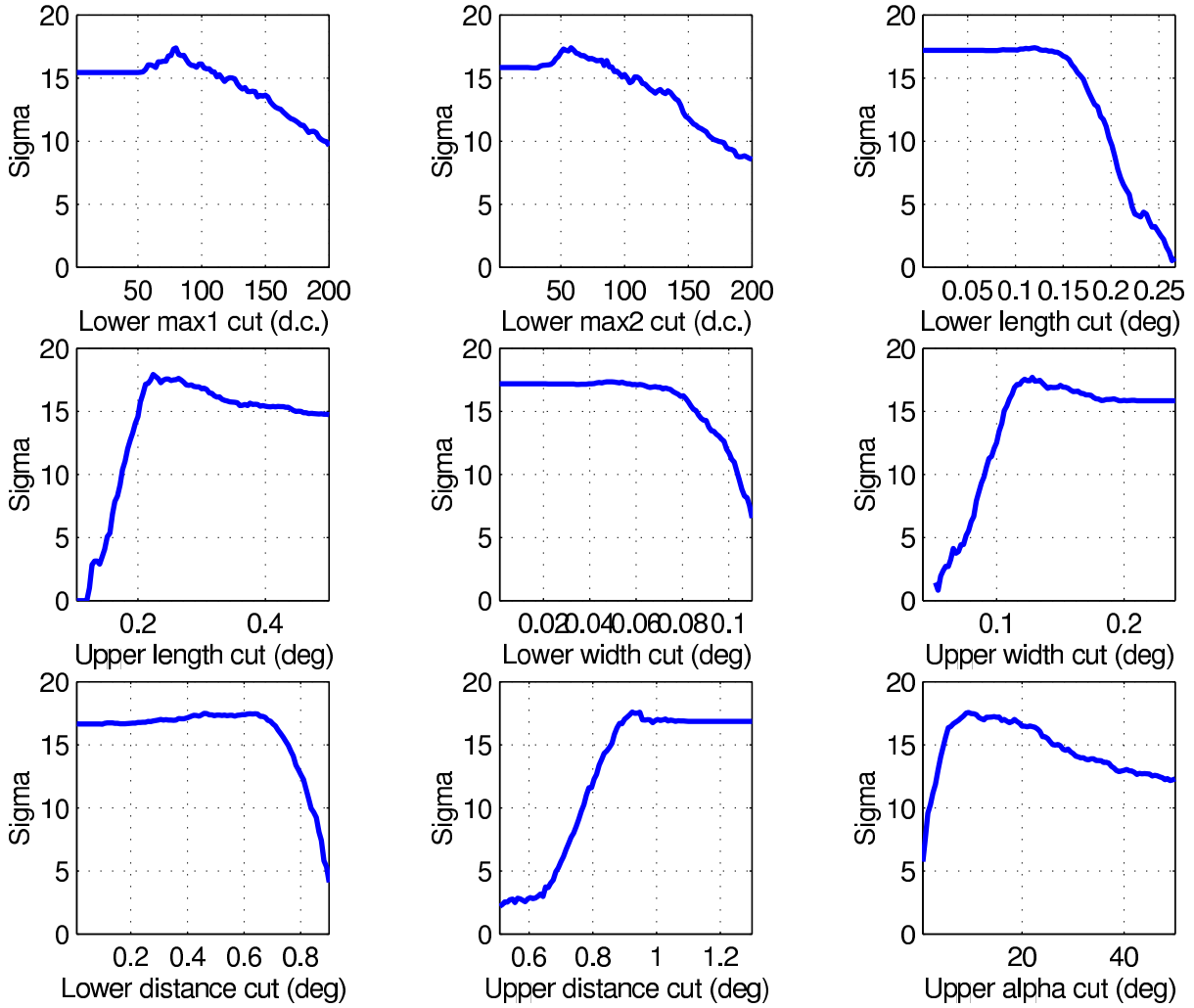

Figure 5.13: Significance of γ-ray excess versus Supercuts selection cut, from the re-optimisation of Supercuts over all *size* values.

presented here.

5.12.1 The Kernel Approximation

No simple function (or estimator) can describe the probability density distribution of γ-ray images nor the distribution of background events. The Kernel technique attempts to estimate these distributions by convolving each *sample* data point with a point-spread-function to obtain a smooth continuous approximation to the probability density distribution.

A simple diagramatic representation of the Kernel technique for a hypothetical univariate situation is shown in Figure 5.14. In short, the probability density distribution of the univariate data X, comprising data points $X_1, X_2 \ldots X_n$, can be crudely represented by a histogram. The histogram, though, is a less than ideal representation due to its heavy dependence on the binning parameters used, and its discontinuous nature. A much smoother, continuous approximation can be obtained by convolving each point in X with a point-spread-function to form a "kernel" for each X_i. By summing the kernels, a smooth approximation to the true probability density distribution of X is obtained (this is not unlike Fourier analysis in which a single-valued periodic function may be built as a summation of individual sinusoidal components). The formula describing the Kernel estimator, $f(x)$, for this simple univariate situation is

$$f(x) = \frac{1}{nh} \sum_{i=1}^{n} K\left(\frac{x - X_i}{h}\right) \tag{5.3}$$

where x is the sample point at which the probability density is calculated, h is the *window width* or *scaling factor* which describes the spread of the point-spread-function, and the Kernel function K (see below) satisfies the condition

$$\int_{-\infty}^{\infty} K(x)\, dx = 1 \tag{5.4}$$

In the case of Čerenkov images, obtained using the IACT, the data points are multivariate, depending on a number of parameters such as *size*, *length*, *width*, etc. The basic Kernel estimator for this situation may be written as

$$f_\gamma(p) = \frac{1}{N_\gamma h_\gamma} \sum_{i=1}^{N_\gamma} K\left(\frac{p - \gamma_i}{h_\gamma}\right) \tag{5.5}$$

where p is a point in parameter space and $\gamma_1, \ldots, \gamma_{N_\gamma}$ are vectors of parameters of a set of N_γ simulated γ-rays. In effect, the simulated γ-rays provide

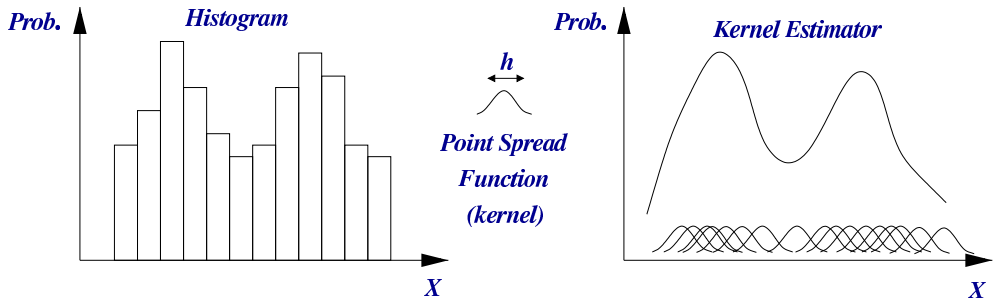

Figure 5.14: Simple diagramatic representation of the Kernel technique for a hypothetical univariate situation. In short, the probability density distribution of X can be crudely represented by a histogram. However, a much smoother, continuous approximation can be obtained by convolving each point in X with a point-spread-function, to form a "kernel" at each point, and then adding up the kernels.

the γ-ray probability density distribution from which the probability, $f_\gamma(p)$, is calculated for the real data point p.

The point spread, or kernel, function, K, can be any scalar function in n-dimensional space (Hand, 1982; Scott, 1992). In this work, a multivariate Gaussian is used as the Kernel function,

$$K = \frac{1}{\sqrt{(2\pi)^n |\xi_\gamma|}} e^{-\frac{1}{2}((p-\gamma)/h_\gamma)^\mathsf{T} \xi_\gamma^{-1} ((p-\gamma)/h_\gamma)} \tag{5.6}$$

where n is the number of parameters and ξ_γ is the covariance matrix of the γ-ray dataset. The background distribution can be similarly defined.

Scott (1992) has shown that if the Kernel is a product of univariate Gaussians (one for each dimension), then the scaling factor that minimises the mean integrated squared error between an actual distribution and its Kernel estimator is given by

$$h_\gamma = \left(\frac{4}{N_\gamma (n+2)} \right)^{1/(n+4)} \tag{5.7}$$

The γ-ray probability density distribution may thus be written in full as

$$f_\gamma(p) = \frac{1}{N_\gamma h_\gamma \sqrt{(2\pi)^n |\xi_\gamma|}} \sum_{i=1}^{N_\gamma} e^{-\frac{1}{2h_\gamma^2}(p-\gamma_i)^\mathsf{T} \xi_\gamma^{-1} (p-\gamma_i)} \tag{5.8}$$

In a similar manner, the probability density distribution, f_b, for a set of

background events in an OFF-source dataset may be defined as

$$f_b(p) = \frac{1}{N_b h_b \sqrt{(2\pi)^n |\xi_b|}} \sum_{i=1}^{N_b} e^{-\frac{1}{2h_b^2}(p-b_i)^\top \xi_b^{-1}(p-b_i)} \tag{5.9}$$

where ξ_b is the covariance matrix for the background dataset, comprising N_b real background (OFF-source) events with vectors $b_1, \cdots, b_{N_b}$. Again, as in the case of the γ-ray distribution, the background probability, $f_b(p)$, at the point p is effectively estimated from the background probability distribution of the N_b real background events.

5.12.2 The Log-likelihood Function, log(R)

The crux of the Kernel technique is the use of the Kernel estimator to determine the logarithm of the likelihood function R

$$\log(R(p)) = \log\left(\frac{f_\gamma(p)}{f_b(p)}\right) \tag{5.10}$$

where f_γ, f_b, and p, retain their previous meanings. In essence, for analysis of the type presented here, $\log(R)$ provides a score for each real data event processed. Thus, in a distribution of $\log(R)$ scores, those events which arise from γ-ray showers are expected to possess positive $\log(R)$ values, and background events negative values. The distributions of $\log(R)$ for γ-ray simulations (solid line) and real background events (dashed line) are presented in Figure 5.15(a) while Figure 5.15(b) shows their ON–OFF distribution.

In an ideal situation in which γ-ray and background events are distinctly different, a simple $\log(R)$ selection-cut at zero would adequately isolate the positively-scored γ-rays from the negatively-scored background. However, as is clear from Figure 5.15(a), there is an intrinsic overlap in the distribution of γ-rays and background; an explicit blind $\log(R)$ cut at zero would, therefore, undesirably classify a significant number of background events as γ-rays. To provide for an optimum signal-to-noise ratio (i.e. the most significant number of γ-rays) the $\log(R)$ cut may be optimised using real ON/OFF data. In a plot of γ-ray significance (σ) versus $\log(R)$ (see Figure 5.16 for an example) the peak represents the $\log(R)$ cut value above which the optimum signal-to-noise ratio is obtained. In Dunlea et al. (2001), for instance, the $\log(R)$ cut was optimised on contemporaneous Crab nebula data and then applied to data taken on the BL Lac object Markarian 421.

The optimisation methodology outlined previously for the Supercuts analysis (optimisation in *size* and elevation bands), is performed is a similar manner for the Kernel analysis, to again extract the maximum number of γ-rays

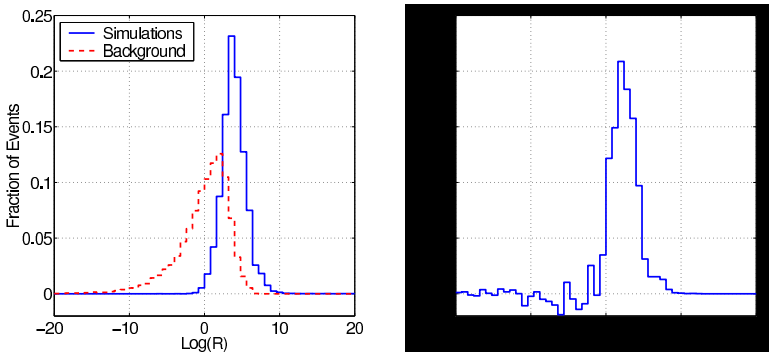

(a) Raw data: Simulations + Background.

(b) Raw ON–OFF data.

Figure 5.15: Log(R) distribution histograms.

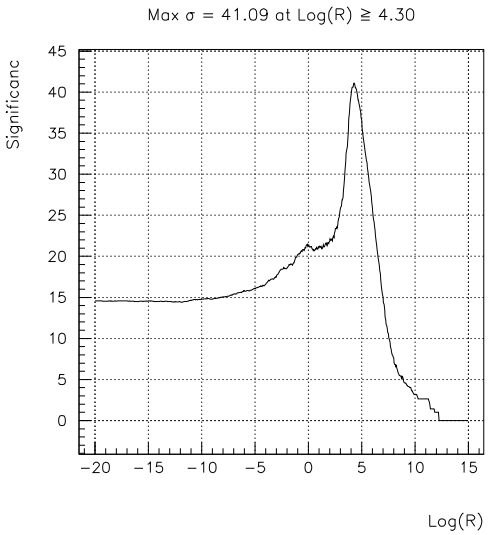

Figure 5.16: Log(R) plot for ON/OFF Crab data in the 71° → 80° elevation band, for events with *size* >150 d.c. The peak, at log(R) = 4.3, represents the log(R) value above which the optimum signal-to-noise ratio is obtained.

originating from the direction of the Crab pulsar. Since the Kernel technique is highly dependent on the γ-ray simulations and background data to which the real data is compared, elevation-specific simulations and elevation-specific background data are used in this work. The list of background data files used is provided in table 5.6; the γ-ray simulations were discussed in section 5.5. No Kernel optimisations were attempted in the size regime below 150 d.c. (see section 7.3.1) As for the Supercuts optimisations, this region was deemed too noise-dominated for meaningful optimisation using ON/OFF data. Nevertheless, the Kernel analysis was deemed appropriate for the analysis of tiny *size* (<150 d.c.) Crab pulsar data, due to its ability to extract events of very low energy, even when optimised for *size* > 150 d.c.; this is elaborated on in section 5.13.1.

Elevation	Data ID	UT Date	MJD
35 – 50	gt017525	010324	51992
51 – 60	gt016745	001228	51906
61 – 70	gt016412	001129	51877
71 – 80	gt016383	001128	51876

Table 5.6: The elevation specific background data used by the Kernel analysis.

5.12.3 Kernel Analysis in Practice

In general, the original Kernel analysis work performed using Whipple collaboration data was intended to establish the Kernel technique, and utilised data analysed with other techniques, such as Supercuts and neural networks, for comparison purposes. Unlike these earlier efforts, the present work represents an application of the established Kernel technique without formal comparison, and seeks to employ its methodology in extracting the maximum number of γ-rays from the Crab pulsar dataset with an optimum signal-to-noise ratio. In this regard, several practical changes to the analysis procedure have been implemented. The analysis procedure as used for this work is illustrated in Figure 5.17 with some important details outlined here.

By its very nature, Kernel analysis is computationally intensive; every real event must be compared with every simulation and with every background event. Previous workers, for example Dunlea (2001), have succeeded in reducing this computational overhead by employing pre-selection and a lattice analysis.

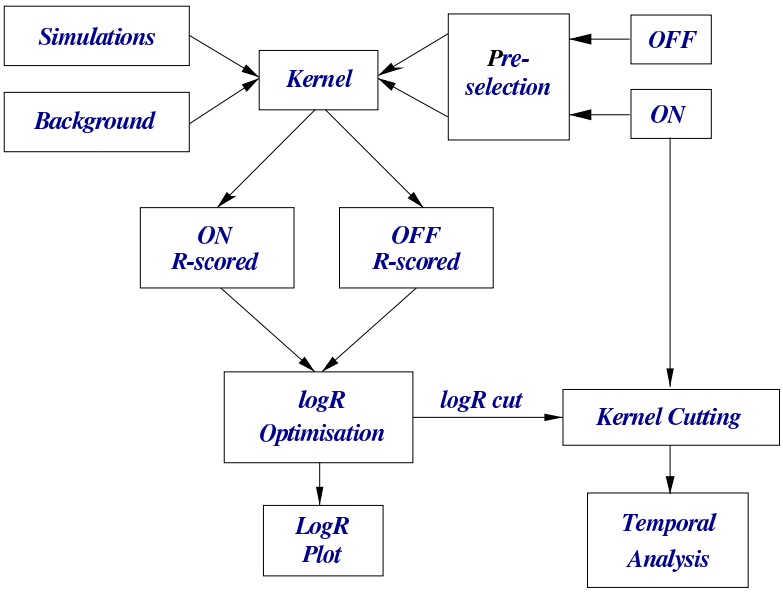

Figure 5.17: The Kernel analysis procedure in practice.

$0.0 < length < 0.36$
$0.0 < width < 0.2$

Table 5.7: The pre-selection cuts use by the Kernel analysis in this work.

Pre-selection

As shown earlier (section 5.6) there are "background" regions of parameter space in which few γ-rays but many background events reside. By rejecting, in advance, those events whose parameters values fall within the background regions, it is possible to reduce the Kernel analysis computational workload, without significantly reducing the final γ-ray rate. The arbitrarily chosen pre-selection cuts used for this work are given in table 5.7. With reference to Figure 5.5 it is clear that these rather loose cuts do not severely limit the number of γ-ray events selected for analysis. Indeed, for the elevation specific simulations and background data files listed in section 5.9, the pre-selection criteria accept on average 89% of the simulated γ-ray events and only 64% of the background events.

Lattice Analysis

The lattice technique involves the evaluation of the log-likelihood function, $\log(R)$, for a lattice of points in n-dimensional parameter space, and then interpolating between these points to estimate the $\log(R)$ value of a partic-

ular point p. Forming the lattice itself is, of course, an extremely demanding computational process. Nevertheless, its benefit lies in the fact that it need only be carried out once for a given dataset. This work, however, due to its elevation-specific nature, was considered unsuitable for a lattice analysis—forming a separate lattice for each elevation band is computationally inefficient. As such, apart from pre-selection, no other technique was employed to reduce the computational overhead for the present analysis.

Optimisations

As demonstrated earlier, for Supercuts analysis, large *size* γ-rays are more easily separated from their hadronic counterparts than small *size* γ-rays from small *size* hadrons; this imposes an effective *size* lower limit on γ-ray selection by Supercuts (Figure 5.12). The same is true for the Kernel analysis—optimised $\log(R)$ cuts preferentially select larger *size* γ-ray events. Accordingly, in order to force the Kernel analysis into seeking out small *size* (low energy) events, *size*-band optimisations are required. This is a significant deviation from previous Kernel analyses which obtained their $\log(R)$ cuts by optimising over the complete range of *size*.

5.13 Tiny Events Analysis - Below the Muon Region

Tiny events, in the context of this work, are taken to mean events with *size* values below ~200 d.c; i.e. at the lower end of muon region in Figure 5.11(a). Although such events are not normally utilised by the Whipple collaboration, because of the inherent difficulty in successfully identifying γ-rays amongst them, they are of interest to the present work due to their very low energies. For this Crab pulsar study it is desireable that the energy threshold of the Whipple telescope be pushed as low as possible, albeit with reduced γ-ray selection efficiency, in order to probe potential pulsed emission from the Crab pulsar at energies heretofore outside the ambit of the IACT.

5.13.1 Kernel Analysis Sensitivity to Tiny Events

As mentioned previously, the Supercuts and Kernel analysis techniques employed in the present work are optimised in *size* and elevation bands on the Crab pulsar dataset itself, in an attempt to extract the best possible γ-ray signal over the widest energy range. However, these optimisations only extend

down to a minimum *size* of 150 d.c. Curiously though, the Kernel analysis, when optimised for *size* values above 150 d.c., appears quite sensitive to events below 150 d.c.. This is demonstrated in Figure 5.18(a), which shows the $\log_{10}(size)$ versus *length* distribution of simulated γ-ray events before and after the optimised Kernel cut is applied. The upper population of events is within the region normally selected by Supercuts; i.e. just above the muon region. The lower population, however, suggests a γ-ray sensitivity for the Kernel technique within the muon region. This is borne out in Figure 5.18(b) which shows the *length*/*size* distributions of the two Kernel-selected populations (dotted line), together with the *length*/*size* distributions for muons (dashed line) and for raw γ-ray simulations (solid line). The *length*/*size* cut used by Supercuts 2000 is indicated by the dot-dashed line.

5.13.2 Kernel Analysis and Tiny Events - Application to Crab Data

Crab ON/OFF data was used to study the two populations effect in real data. The results, unfortunately, were not encouraging. Figure 5.19(a) shows the *size* distributions for the ON (solid line) and OFF data (dashed line) after Kernel analysis. As expected two *size* populations are evident. Alas, when the ON–OFF *size* distributions are plotted, Figure 5.19(b), the lower *size* population is swallowed up by the raw OFF excess evident below ∼150 d.c. This unfavourable OFF excess may be attributed to sky-noise differences between the ON and OFF data, which software padding seems not to fully compensate for in this very small and difficult *size* regime. Currently, new methods of padding for very small events are being examined (Fegan 2002, private communication).

Sky-noise Problems

To demonstrate how an excess of OFF-data events of tiny *size* may be generated from sky-noise differences, two sets of simulations, each with equal numbers of simulated Čerenkov events but with different sky-noise levels (sky noise is set in simulations by specifying the pedestal variance, section 5.2.1) are compared. Figure 5.20(a) shows the raw *size* distributions for the low sky-noise (pedvar=3.5 d.c. –solid line) and high sky-noise (pedvar=4.8 d.c –dashed line) situations. It is immediately clear that the *size* distribution for the high sky-noise situation is shifted to smaller *size* values relative to the high sky-noise situation.

By subtracting the high sky-noise *size* distribution from the corresponding low sky-noise distribution the true effect of sky-noise can be examined.

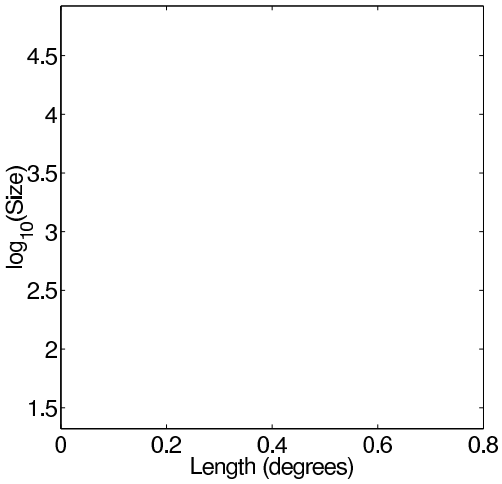

(a) $\log_{10}(size)$ vs *length*.

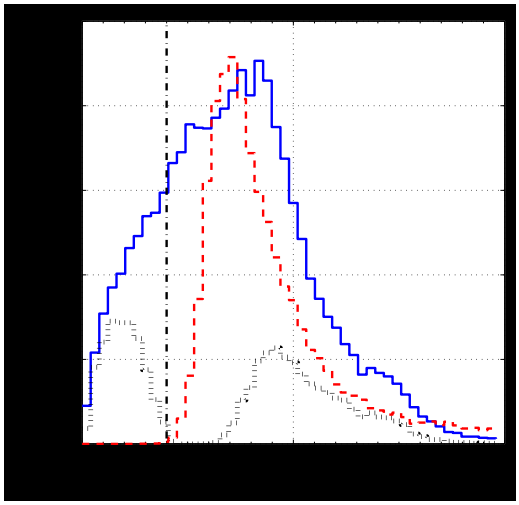

(b) *length*/*size* histogram.

Figure 5.18: (a) simulated γ-rays before (blue) and after (red) the Kernel cut of log(R) $>$ 4.3 is applied. Two event populations are evident after the Kernel analysis. The upper population corresponds mainly to Supercuts selected events above the *length*/*size* cut, while the lower population is a new set of events deep within the muon region. The Supercuts 2000 *length*/*size* cut is represented as the solid line. (b) the *length*/*size* parameter distribution for γ-rays (solid line), simulated muons (dashed line) and Kernel (log(R) $>$ 4.3) selected γ-rays (dotted line).

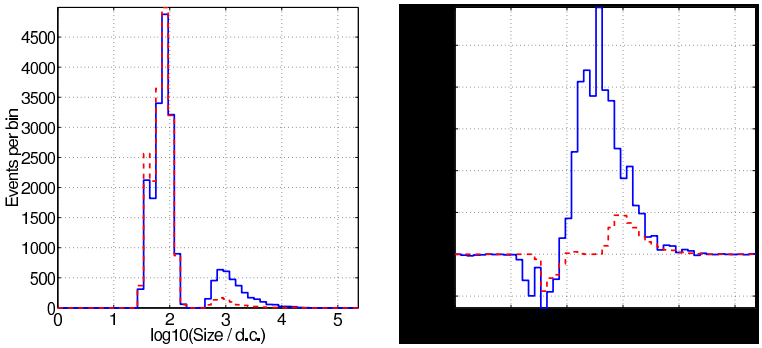

(a) ON (solid line) and OFF (dashed line) *size* distributions after Kernel selection.

(b) ON–OFF *size* distributions before (solid line) and after (dashed line) Kernel selection.

Figure 5.19: ON and OFF, and ON–OFF size distributions for Crab data after Kernel selection.

The result, Figure 5.20(b), reveals that for ON/OFF data, in which the OFF sky region is noisier than the ON (which is the case for the Crab), an OFF excess at small *size* values is an intrinsic consequence of ON/OFF analysis. This is not unexpected considering the effects of high sky-noise on boundary tubes, as advanced in section 5.2.4. It is unfortunate, however, that software padding does not adequately compensate for these noise differences in real data. To see what effect padding actually has on real data, ON–OFF *size* distributions for Crab data were examined before and after padding. The results are presented in Figure 5.21 and show that, although padding does significantly reduce the OFF excess at small *size*, it does not eliminate it completely. A re-evaluation of the software padding algorithm seems necessary, although it is beyond the scope of the present work.

To further test the assertion that sky-noise differences between the Crab ON and OFF fields are the reason why the tiny *size* population, evident in simulations, does not make it through into the real ON–OFF data, an independent Kernel analysis of the BL Lac object H1426+428 was conducted. This object was recently confirmed a TeV emitter (Horan et al., 2002) and contains very dark ON-source and OFF-source sky regions. As such, sky-noise problems should not exist in this data and the tiny *size* (<150 d.c.) population should exist after ON/OFF analysis. An analysis of thirteen H1426 ON/OFF pairs, taken during the 2001/2002 observing season, revealed only a 0.53σ excess after Supercuts analysis but yielded a more significant

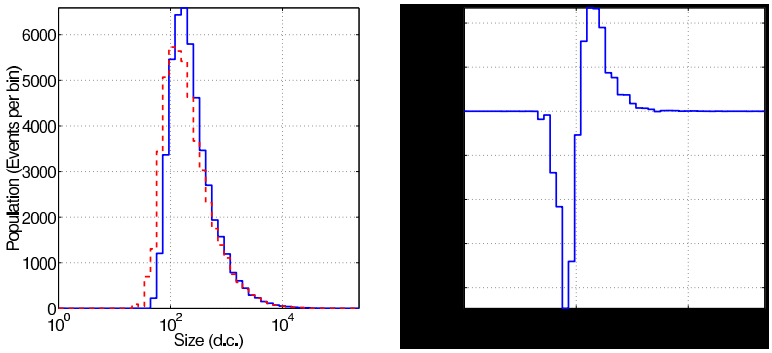

(a) Low sky-noise (solid line) and high sky-noise (dashed line).

(b) (Low sky-noise)–(High sky-noise).

Figure 5.20: *size* distributions for low and high sky-noise simulations. The distributions reveal the expected effect of picture/boundary cleaning on high-noise data—i.e. the images are clipped and their *size* distribution moves to lower values. This gives rise to an OFF excess in the tiny *size* regime, as is observed in real Crab data.

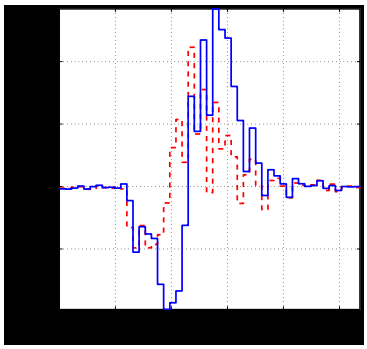

Figure 5.21: ON–OFF *size* distributions for Crab plerion data before (solid line) and after (dashed line) software padding was applied. The distributions show clearly that although padding reduces the OFF excess at tiny *size* it does not eliminate it.

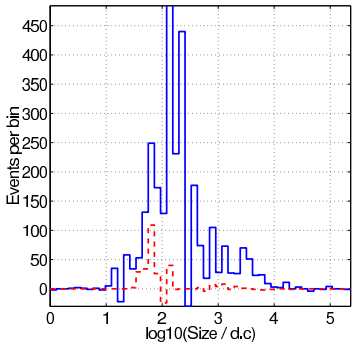

Figure 5.22: ON–OFF *size* distribution for the BL Lac object H1426+428 before (solid line) and after (dashed line) the Kernel analysis was applied. The population of γ-ray events with tiny *size*, predicted by simulations but not present in Crab data, is evident here.

3.22σ after the Kernel technique was applied. Since the 13 pairs fell into the $71° \rightarrow 80°$ elevation band, the optimised Kernel cut for that band ($\log(R) > 4.3$) was used. An examination of the ON–OFF *size* distribution (Figure 5.22) for the 13 pairs, after the Kernel analysis was applied, confirms that the gain in significance achieved by the Kernel technique is made in the tiny *size* regime. This reinforces the conclusion that sky-noise differences between the Crab plerion's ON and OFF fields adversely effect the Kernel analysis. Furthermore, it points to the usefulness of the Kernel technique in the tiny *size* regime, for sources such as H1426, which do not suffer differences in ON/OFF sky-noise.

5.14 Crab Pulsar Analysis - Optimisation Strategies

For this work both the Supercuts and Kernel analysis techniques were optimised in discrete elevation and *size* bands, in an attempt to extract the maximum number of γ-rays from the Crab pulsar dataset, with optimum significance. For each of the elevation bands listed in table 5.2 the Crab pulsar dataset was analysed in nine discrete *size* bands. Table 5.8 presents the matrix of elevation and *size* bands used, in which each independent band is represented by an I and each combined band by a C. Optimisations were performed in the independent bands and the results subsequently combined in the combined bands (see chapter 7). The optimised cut values determined for each independent band are provided in appendix C, for both the Supercuts and Kernel techniques.

Size Range (d.c.)	Elevation Bands (degrees) 35-50	51-50	61-70	71-80	Combined Elevations
150-250	I	I	I	I	C
250-350	I	I	I	I	C
350-450	I	I	I	I	C
450-550	I	I	I	I	C
550-650	I	I	I	I	C
650-750	I	I	I	I	C
750-1000	I	I	I	I	C
1000-2000	I	I	I	I	C
>2000	I	I	I	I	C
Aggregate *size* bands	C	C	C	C	C

Table 5.8: The *size* and elevation bands in which the Supercuts and Kernel techniques were optimised for this work. Independent bands are represented by I and combined bands by C.

5.15 γ-ray Flux Determination

In order to provide useful physical information regarding an astrophysical source, the IACT must allow for an estimation of the γ-ray flux emanating from the source. For a given threshold energy, E_{th}, the integral flux above the threshold is defined as

$$Flux(E > E_{th}) = \frac{N}{TA_{eff}} \tag{5.11}$$

where N is the number of γ-rays detected in the time T, given an effective collection area A_{eff}. Accordingly, in order to convert a measured γ-ray signal from a given source into a flux, it is necessary to perform an exact calibration of the flux collector (i.e. the telescope and the γ-ray selection technique), both in terms of its energy response and its collection area (Cawley and Weekes, 1995; Kertzman and Sembroski, 1994). Neither are easily defined; the collection area, $A(E)$, increases as a function of energy while the γ-ray flux from an object decreases with increasing energy, thereby complicating the detector's energy response. The collection area may be estimated directly from γ-ray simulations but the energy response determination requires *a priori* knowledge (or assumptions) regarding the source's γ-ray spectrum, usually a power law spectrum with some spectral index α.

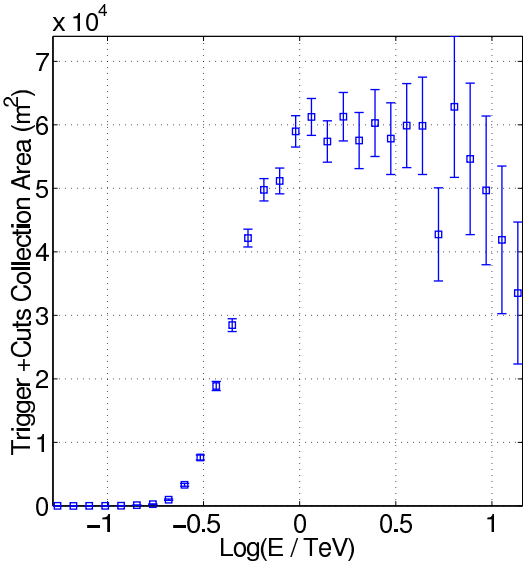

Figure 5.23: The collection area curve for Supercuts 2000, for γ-ray simulations at 75° elevation.

5.15.1 Collection Area Estimation

In general, the γ-ray collection area for a Čerenkov flux collector provides a measure of its efficiency for detecting and identifying γ-ray initiated EAS. The collection area, A, at a particular energy, E, may be calculated by simulating a large number of showers with that energy falling randomly onto a "drop-zone" of area A_0, and recording the number of events which trigger the telescope and pass the subsequent γ-ray selection criteria of the particular analysis. Thus

$$A\,(E) = A_0 \left(\frac{\text{number of } \gamma - \text{rays passing at E}}{\text{number of } \gamma - \text{rays simulated at E}} \right) \tag{5.12}$$

In this work the drop-zone comprises a disc of radius 200 m (table 5.3), in the plane perpendicular to the telescope's optical-axis. The collection area curve for the Supercuts 2000 cuts, applied to γ-ray simulations at elevation 75°, is presented in Figure 5.23. This curve compares favourably with the curve derived previously by Krennrich et al. (2001b) for the same cuts.

Since the Crab data used in this work is analysed using specific selection criteria optimised according to elevation bands, these must be properly accounted for in calculating overall collection areas for flux (or flux upper limit) determinations. Because of the different quantities of data available for analysis in each elevation band, it was considered appropriate to weight

the collection area curves derived for each band by a scaling factor, dependent upon the relative contribution of that band to the overall observing duration. The scaling factors used are presented in table 5.9. Individual and combined collection area curves for each of the four elevation bands, for both Supercuts 2000 and for Kernel analysis of events with *size* above 150 d.c., are presented in Figure 5.24. In their own right, the elevation-specific collection area curves provide an interesting synopsis of the elevation dependent sensitivity of the Whipple telescope and further reinforce the argument for the type of elevation-specific analysis employed in this work. It is clear from Figure 5.24(b) that the collection area curves for the Kernel analysis are somewhat different to those for Supercuts 2000, in that the Kernel curves do not reach a plateau at high energies. This may be attributed to the looseness of the Kernel technique in selecting γ-ray events compared to the strict parameter boundaries imposed by Supercuts.

Elevation	**Scaling Factor**
$35 - 50$	0.22
$51 - 60$	0.16
$61 - 70$	0.19
$71 - 80$	0.43
Total	1.0

Table 5.9: The scaling factors used to weight the collection area curves for each elevation band.

5.15.2 Differential Response Curve and Peak Response Energy

Although the collection area curve of a flux collector provides a measure of its sensitivity for detecting γ-rays of different energies, derived from a uniform distribution, it offers little information regarding the response of the collector to a particular γ-ray source. This being the case, it is necessary to introduce into the collection area the source spectrum. By convolving the collection area curve with the source spectrum a "differential response curve" is obtained; it provides a measure of the true sensitivity of the collector to γ-rays from the source under observation.

The energy at which the peak in the differential response curve occurs represents the collector's Peak Response Energy (PRE) and is often referred to as the energy threshold (E_{th}), as indeed is the case in this work. The differential response curve for the Supercuts 2000 cuts, obtained by convolving the

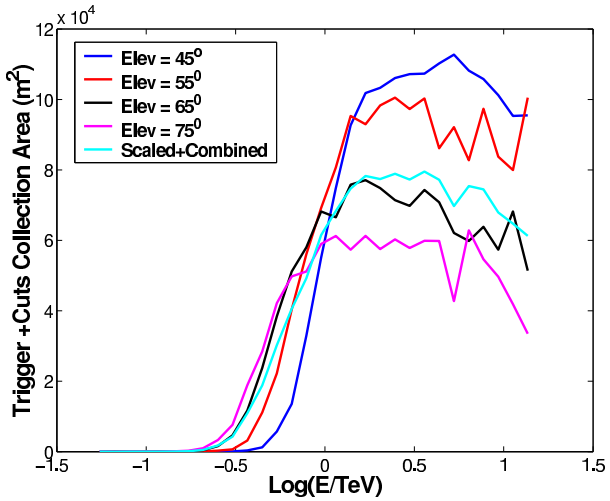

(a) Supercuts 2000.

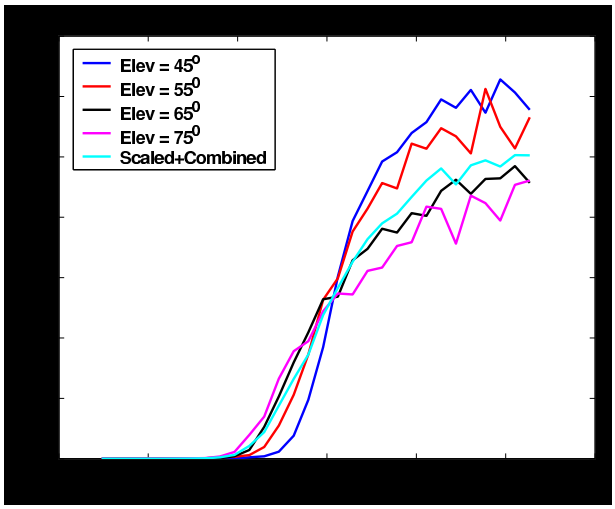

(b) Kernel analysis (*size* $>$ 150 d.c.).

Figure 5.24: Individual and scaled+combined collection area curves for Supercuts 2000 and the Kernel analysis, for each of the four elevation bands used in this analysis.

scaled and combined collection areas of Figure 5.24(a) with the differential spectrum for the Crab nebula ($3.20 \times 10^{-7} \times (E/1\ TeV)^{-2.49}$ $m^{-2}s^{-1}TeV^{-1}$, Hillas et al. 1998), is presented in Figure 5.25(a). The PRE for this curve occurs at 517 GeV $\pm$ 100 GeV and compares very well with a previous calculation of 520 GeV $\pm$ 90 GeV for the same selection criteria, by Krennrich et al. (2001b). The differential response curve for all elevations combined, derived for the Kernel analysis of events with *size* greater than 150 d.c. is shown in Figure 5.25(b); the PRE in this case was found to be 578 GeV $\pm$ 100 GeV;

For each of the narrow *size* bands, in which the γ-ray selection criteria are optimised as part of the present work (section 5.14), the resulting PRE is estimated. The PRE for each *size* band is then taken to represent the threshold energy of the γ-rays falling within that band, for which an integral flux upper limit is calculated using equation 5.11. The PRE's estimated for each *size* band are presented in chapter 7.

By integrating the area under the differential response curve the *expected* rate of γ-ray detections from the source may be determined. This rate should match the *true* experimentally detected γ-ray rate. For Supercuts 2000 the expected rate, for all elevations combined, was calculated at 2.51 ± 0.34 min^{-1}, while the true detected rate was 2.31 ± 0.05 min^{-1}. The agreement between the expected and measured rates verifies the accuracy of the method used to estimate the collection area and collector response of the Supercuts analysis. Unfortunately the same level of agreement is not present for the results of the Kernel analysis. For the Kernel, the expected rates are consistently higher than their true detected values. This indicates that the Kernel technique is more sensitive to γ-ray simulations than to real γ-ray events. The most probable reason for this bias is the use of γ-ray simulations by the Kernel in identifying γ-ray events in real data (section 5.12). Although the simulations used in the collection area determination were independent of those used by the analysis to identify γ-rays, it appears as though the Kernel technique more easily identifies simulated γ-rays images than real γ-ray events, for whatever reason. A full investigation of this problem was beyond the scope of the present work. Nevertheless these findings serve as a caveat against the use of the Kernel analysis for serious spectral work, unless appreciable further study is conducted.

5.15.3 Effective Area Calculation

The effective area of a flux collector, A_{eff}, is normally defined in terms of its collection area for γ-rays, $A(E)$, and its energy threshold, E_{th}, for the particular source under observation. The expression for the effective area is

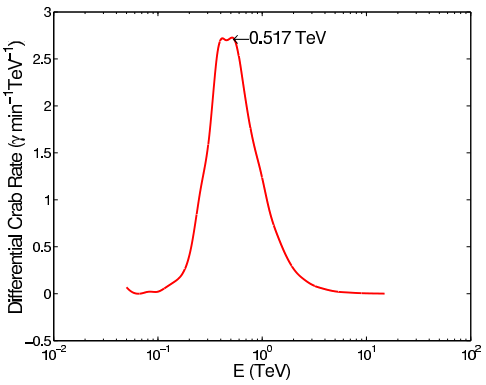

(a) Supercuts 2000.

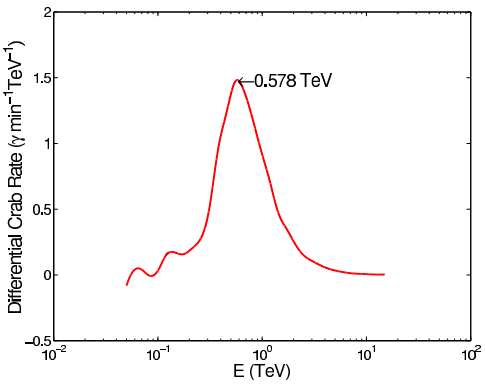

(b) Kernel analysis (*size* > 150 d.c.).

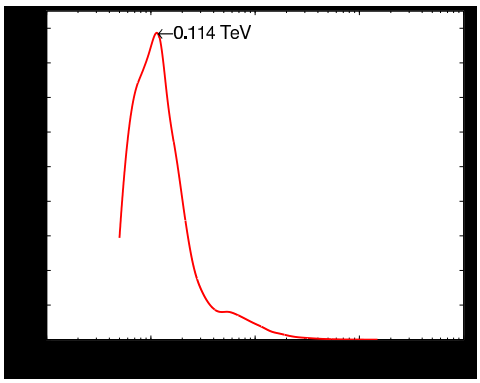

(c) Kernel analysis (all *size* values included).

Figure 5.25: Differential response curves for the Supercuts 2000 and the Kernel analysis techniques.

written as:

$$A_{eff} = \frac{\int_0^\infty I_\gamma E^{-\alpha} A(E)\, dE}{\int_{E_{th}}^\infty I_\gamma E^{-\alpha} dE} \tag{5.13}$$

where the numerator is the area under the differential response curve and the denominator is the area under the source spectrum, from the energy threshold upwards. In this work, concerning γ-rays from the Crab pulsar, the energy threshold is taken to mean the peak of the differential response curve of the Whipple telescope and associated data analysis, for a source with the same spectrum as the Crab nebula. Using the Supercuts 2000 selection cuts the effective area was estimated at $5.17 \pm 0.73 \times 10^4$ m^2. Once again, a comparison with previous work shows good agreement.

For each of the γ-ray selection criteria used in this work (i.e. re-optimised Supercuts and the Kernel analysis, in discrete elevation and *size* bands) the effective area is calculated. A flux upper limit is then calculated using equation 5.11 with a γ-ray *number upper limit* determined from the Crab pulsar periodicity analysis (outlined in chapter 6).

5.16 Summary of γ-ray Selection Strategies for Crab Pulsar Analysis

In this work a large volume of Crab pulsar data (97.33 hours in total), spanning four different elevation bands (35° →50°, 51° →60°, 61° →70° and 71° →80°), recorded in the period from January 2000 until February 2002, is used to provide candidate γ-ray events with GeV →TeV energies for use in a Crab pulsar periodicity analysis. Two independent selection mechanisms are used to identify the candidate γ-rays; the Supercuts and the Kernel analyses. Both techniques are re-optimised in this work. Indeed, multiple optimisations are performed in discrete elevation and *size* bands, in order to select the largest number of γ-ray events available, over the widest energy range. The sensitivity of the Kernel analysis to γ-ray events with tiny (<150 d.c.) *size* is also exploited, to provide γ-rays in a regime hitherto unexplored by the IACT. By estimating collection area and differential response curves for both techniques, effective γ-ray collection areas are provided for use with the results of a periodicity analysis.

Figure 5.26 provides a complete functional overview of the analyses described in this chapter while the next chapter provides full details of the Crab periodicity analysis.

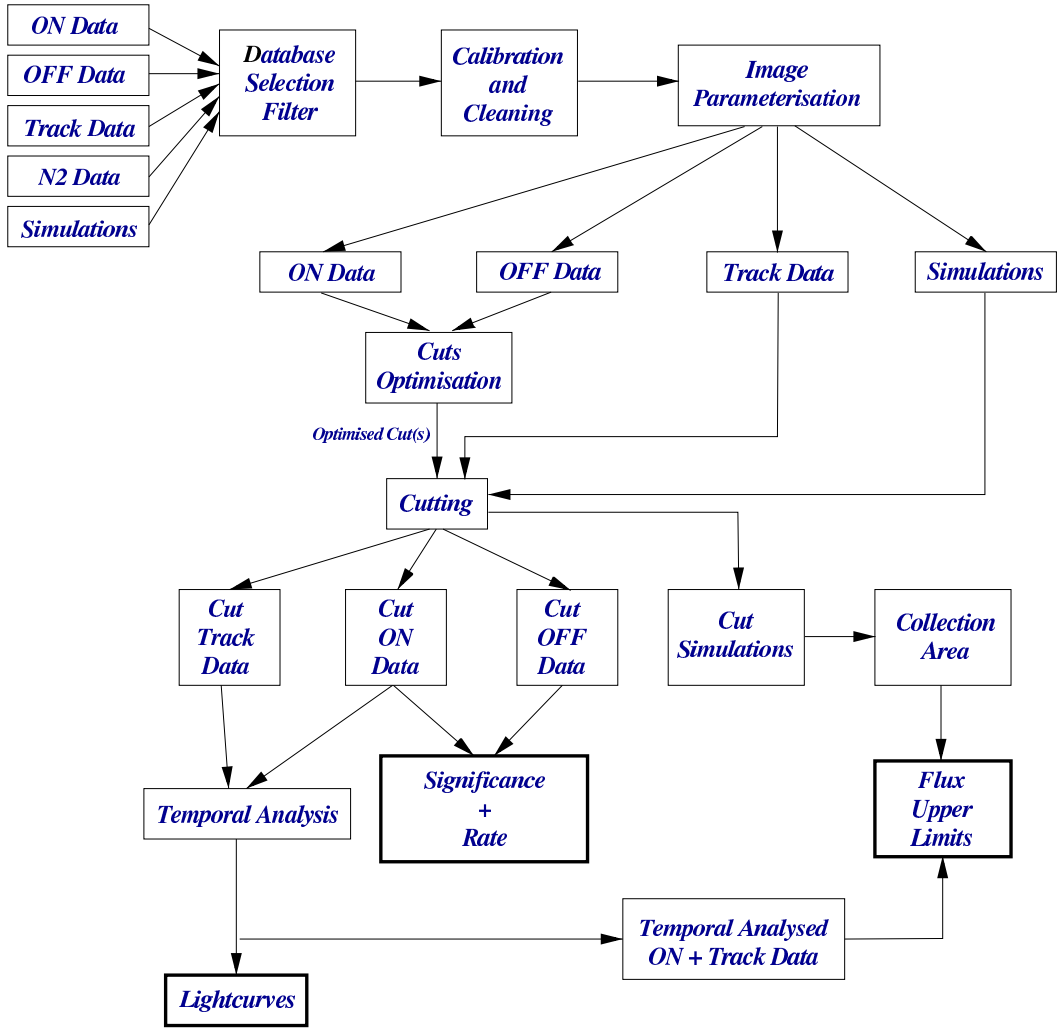

Figure 5.26: Overview of the analysis mechanisms described in this chapter.

Chapter 6

Temporal Analysis of Astrophysical Time Series Data

Unlike photon detection techniques that operate at low energies, the high-energy IAC technique must deal with a photon flux which rapidly decreases with increasing energy. As a consequence, in order to attain adequate statistics, it is imperative that there exists a means to seamlessly combine temporally separated IAC observations of the same source. In general, observations of non-variable sources are merged after merely accounting for the flat-fielding and pedestal subtraction considerations, described in chapter 5. Observations of variable sources, however, for which timing is critical, are not so easily combined—timing delays introduced by the Earth's motion can, if left uncorrected, render independent datasets incompatible.

Pulsars naturally fall into the category of variable sources. Indeed, identification of pulsed γ-ray emission from pulsars relies heavily upon finding precise temporal modulation in the γ-ray signal at the period of known radio or optical emission. Hence, it is essential that all γ-ray photons are accurately time-stamped upon detection, and that the timestamps are subsequently calibrated to account for timing delays introduced en route from the source, and for intrinsic pulsar slowdown.

This chapter describes in detail the temporal corrections and periodicity analysis applied to the dataset of candidate Crab pulsar γ-ray events identified by the Whipple IAC technique.

6.1 Epoch Folding – Rotational Phase

To combine candidate γ-ray events from independent observations of a pulsar, it is first required that event times are transformed to a meaningful parameter

in an inertial reference frame. This typically means tagging each γ-ray event with a relative phase of pulsar rotation. In other words, the arrival time of each detected photon is used to determine the relative fraction of a complete revolution (i.e. phase) of the rotating neutron star at the moment it was emitted.

The rotational phase ϕ at any time T, after a reference epoch T_0, is determined by calculating the number of complete rotations since T_0 and taking the fractional part (figure 6.1), so that

$$\phi(T) - \phi(T_0) = \int_{T_0}^{T} \frac{dT}{P(T)} = \int_{T_0}^{T} f(T)dT \tag{6.1}$$

where $P(T)$ and $f(T)$ are the pulsar's time-dependent period of rotation and frequency, respectively. Since the first frequency derivative $\dot{f}(T)$ is measured for most pulsars, the frequency $f(T)$ may be Taylor expanded about the epoch T_0, such that

$$f(T) = f(T_0) + \dot{f}(T_0)(T - T_0) + \frac{1}{2}\ddot{f}(T_0)(T - T_0)^2 + \ldots \tag{6.2}$$

Thus, equation 6.1 may be integrated to obtain the phase

$$\phi(T) = \phi(T_0) + f(T_0)(T - T_0) + \frac{1}{2}\dot{f}(T_0)(T - T_0)^2 \tag{6.3}$$

If T_0 is the precise emission epoch (generally taken to mean the arrival time at the Solar System barycentre) of a particular radio pulse from the pulsar, then any γ-ray emission modulated at the pulsar's radio period should stand out as a peak in a histogram of phases.

The phase determination process described above is known as *epoch folding* and the histogram of phases is referred to as a *phaseogram* or *lightcurve*. For good counting statistics and correct timing parameters, epoch folding should result in a distinct pulse shape if the source is indeed periodic (see section 6.4.2 for a well-defined example at optical wavelengths). In the absence of a periodic signal a flat phase distribution is expected, within Poisson counting errors. To test for periodicity, statistical tests such as the χ^2 test, may be applied to compare the real distribution with expectations derived from Poisson statistics.

Since the Earth is undergoing significant acceleration relative to the pulsar, the arrival time, T, of a particular photon at the observatory, cannot in

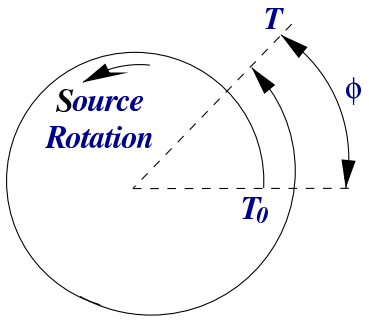

Figure 6.1: The rotational phase ϕ of an event at time T is determined by counting the number of complete rotations of the source since the epoch T_0 and taking the fractional part.

practise be merely substituted into equation 6.3. Rather, it must first be treated to remove the Doppler delay caused by the Earth's motion. This treatment involves transforming T to a time T_b at the solar system barycentre. Before discussing in detail the barycentering process, it is first worthwhile examining the effect of the Earth's orbital motion on photon arrival times, and demonstrating the necessity of correct timing.

6.2 Effect of the Earth's Motion

The relative time-of-flight delays experienced by photons from a pulsar as a result of the Earth's orbital motion are depicted in Figure 6.2. Two extreme situations are immediately discernable, a maximum delay and a maximum advance, when the Earth is respectively at its furthest and closest points to the pulsar. Approximating the Earth's orbit to a circle and assuming that the pulsar lies on the orbital plane, then the maximum greater or shorter distance a photon pulse must travel is simply the orbital radius ($\sim$149.6$\times$10^9 m). The corresponding time of flight is of the order of 500 s. The delay amplitude plot of Figure 6.3 demonstrates how the timing delay varies sinusoidally throughout the year as a function of the pulsar's ecliptic latitude. The plot's phase is determined by the pulsar's ecliptic longitude, which in all the calculations presented here is taken for simplicity to be zero.

The effect of the Earth's motion on the observed period of a pulsar, may be treated as an effective *rate* of period change, $\dot{P}_{eff}$.[1] Including $\dot{P}_{eff}$ in

[1] $\dot{P}_{eff}$ is separate to the intrinsic rate of period change of the pulsar due to its slowdown over time, which is adequately accounted for in the Taylor expansion given in equation 6.2.

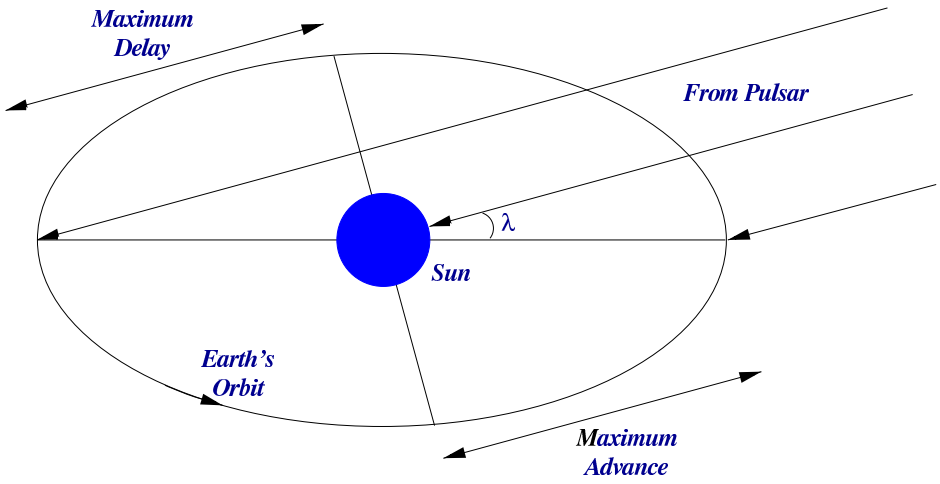

Figure 6.2: The relative time-of-flight delays experienced by photons from a pulsar, due to the Earth's orbital motion. Two extremes stand out: a maximum delay and a maximum advance, when the Earth is respectively at its furthest and closest points to the pulsar.

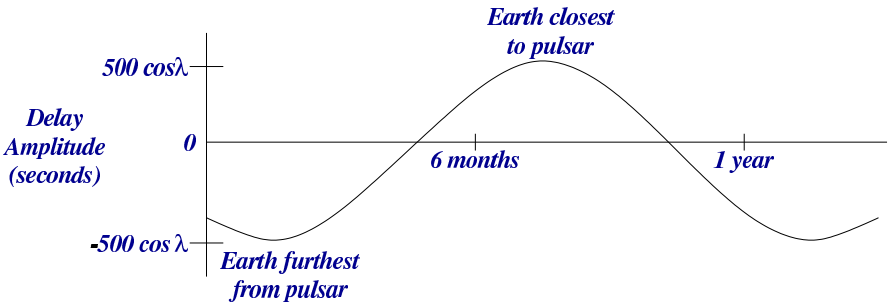

Figure 6.3: The variation in timing delays experienced by photons from a pulsar over the course of one year, as a function of the pulsar's ecliptic latitude, λ.

equation 6.1, yields

$$\phi(T) - \phi(T_0) = \int_{T_0}^{T} \frac{dT}{P_0 + \dot{P}_{eff}T} = \frac{1}{\dot{P}_{eff}} ln(P_0 + \dot{P}_{eff}T) \mid_{T_0}^{T} \tag{6.4}$$

where it is assumed that the period of the source, P_0, and the effective rate of change in period, $\dot{P}_{eff}$, are constant over the duration, $T - T_0$, of a particular observation. Arbitrarily setting $T_0 = 0$, and $\phi(T_0) = 0$, we obtain

$$\phi(T) = \frac{1}{\dot{P}_{eff}} \left[ln(P_0 + \dot{P}_{eff}T) - ln(P_0) \right]$$

$$= \frac{1}{\dot{P}_{eff}} ln \left(1 + \frac{\dot{P}_{eff}T}{P_0} \right) \tag{6.5}$$

In the trivial case of no relative motion between the pulsar and the Earth, the effective rate of period change is zero, and the phase at some time T, given simply by equation 6.1, is

$$\phi(T) = \frac{T}{P_0} \tag{6.6}$$

where again $T_0 = 0$, $\phi(T_0) = 0$, and P_0 is assumed constant over the observing duration T. The effect of $\dot{P}_{eff}$ on the rotational phase may be ascertained by taking the difference of equations 6.6 and 6.5, and expanding the logarithm

$$\Delta\phi = \frac{T}{P_0} - \frac{1}{\dot{P}_{eff}} ln \left(1 + \frac{\dot{P}_{eff}T}{P_0} \right)$$

$$\approx \frac{1}{2} \dot{P}_{eff} \left(\frac{T^2}{P_0^2} \right) \tag{6.7}$$

It is useful at this stage to examine the *true* effective rate of change in the Crab pulsar's period due to the Earth's orbital motion. To do this we obtain an expression for the delay between the emission of two consecutive pulses (i.e. the delay corresponding to a time interval of one complete period of the source) and differentiate it. Consider the situation depicted in Figure 6.4, where the Earth is moving in that part of its orbit which reflects maximum

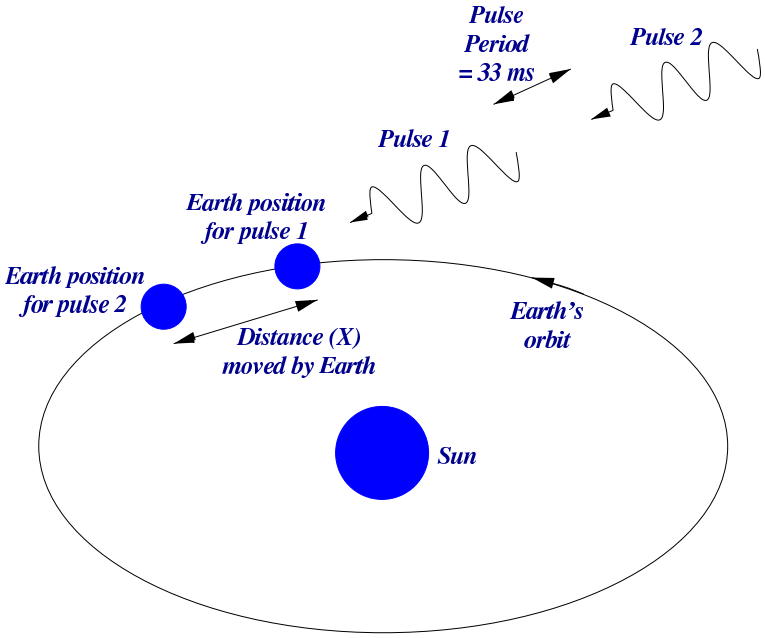

Figure 6.4: In the 33 ms between the emission of two consecutive pulses from the Crab pulsar, the Earth (which is in that part of its orbit which is at a maximum acceleration away from the pulsar) moves a distance X.

acceleration away from the pulsar. Because the Earth moves a distance X away from the pulsar between the emission of pulses 1 and 2, pulse 2 takes X/c seconds longer to reach the Earth. Hence the delay may be written as

$$\Delta P = P_1 - P_2 = \frac{X}{c}$$

Since the instantaneous orbital velocity of the Earth, v, may be approximated by X/P_0, where P_0 is the true period of the pulsar, then

$$c\Delta P = X = vP_0$$

$$\Rightarrow \frac{\Delta P}{P_0} = \frac{v}{c}$$

Substituting $v \simeq 3 \times 10^4$ m s^{-1} for the Earth's orbital velocity, and $P_0 = 33 \times 10^{-3}$ s for the Crab pulsar period, yields

$$\Delta P = \frac{v}{c} P_0 \approx 3.3 \times 10^{-6} \text{ s} \tag{6.8}$$

Hence, 3.3×10^{-6} s represents the maximum possible delay between the arrival of two consecutive pulses from the Crab pulsar, due to the Earth's orbital motion. In terms of a modulating influence over the period of a complete terrestrial year it may be described more exactly as

$$\Delta P = (3.3 \times 10^{-6} \text{ s}) sin\lambda$$

which is the expression for the true delay between the arrival of two consecutive pulses, as a function of the pulsar's ecliptic latitude λ. Thus the effective rate of period change introduced by the Earth's orbital motion is

$$\dot{P}_{eff} = \frac{d(\Delta P)}{dt} = (3.3 \times 10^{-6} \text{ s}) cos\lambda \frac{d\lambda}{dt}$$

With $\frac{d\lambda}{dt} = \frac{2\pi}{T} = \frac{2\pi}{\text{no. seconds in 1 year}}$, we arrive at the true effective rate of period change for the Crab pulsar

$$\dot{P}_{eff} \approx 6.5 \times 10^{-13} \, cos\lambda \tag{6.9}$$

At a glance $\dot{P}_{eff}$ seems negligible. However, its impact over the course of just one day, on the Crab pulsar's phaseogram, is substantial. Substituting for $\dot{P}_{eff}$, T (= 1 day), and P_0 (= 33×10^{-3} s) into equation 6.7 returns a value of $\Delta\phi = 2.2$ pulsar cycles. Such a drastic shift in phase clearly has disastrous consequences for the shape of the phaseogram, rendering independent observations recorded over just a single day incompatible, unless formally corrected. Although the arguments outlined here assume the worst case scenario (i.e. $cos\lambda = 1$, and an ecliptic longitude of zero), they demonstrate clearly the effects of the Earth's orbital motion on pulsar observations and the absolute necessity of timing corrections.

6.3 Barycentering

The acceleration of isolated pulsars, such as the Crab, relative to the Solar System Barycentre (SSB), is sufficiently small that the SSB may be used as an inertial reference frame for the purpose of examining pulse arrival times. Barycentering is the name given to the procedure whereby Earth-bound photon arrival times are corrected to arrival times at the SSB. There are two main stages in the barycentering process, namely the conversion of Coordinated Universal Time (UTC), as measured at a terrestrial observatory

to Barycentric Dynamical Time (TDB) at the SSB, and a correction for the time-of-flight difference due to the spatial separation of the observatory and the SSB.

6.3.1 Converting UTC to TDB

In the transformation of time from UTC to TDB the following time definitions are used:

TAI *International Atomic Time.* TAI is the primary terrestrial time standard. It a continuous time scale resulting from ongoing analyses by the *Bureau International des Poids et Mesures* in Paris, of atomic time standards around the world, each corrected for known environmental and relativistic effects.

UTC *Universal Coordinated Time.* UTC is the time displayed by GPS clocks. By definition, UTC and TAI have the same rate, but UTC differs from TAI by an integral number of "leap" seconds in order to hold solar noon at the same UTC each day, in spite of the Earth's rotational slowdown. The relationship between TAI and UTC is

$$UTC - TAI = \text{number of leap seconds}$$

Over the course of the Crab pulsar observations used in this work no new leap seconds were added; the offset between TAI and UTC for all observations is +32 seconds (correct since 01 January 1999).

TDT *Terrestrial Dynamical Time.* TDT is used as the time scale of ephemerides for observations from the Earth's surface. It is tied to TAI by a constant offset of 32.184 seconds, required to provide continuity with conventions used before its introduction 1984.

$$TDT - TAI = 32.184 \text{ seconds}$$

TDB *Barycentric Dynamical Time.* TDB is the same as TDT, except for relativistic corrections to move the origin to the SSB. These corrections amount to as much as $\sim \pm 1.6$ ms and are periodic with an average of zero. The differences between TDT and TDB caused by variations in the gravitational potential around the Earth's orbit (c.f. page B5 of the *Astronomical Almanac*) are given by:

$$TDB - TDT = 0^s.0016\,58\, sin(g) + 0^s.000\,014\, sin(2g)$$

where:

$$g = 357^o.53 + 06^o.985\,600\,28(JD - 245\,1545.0)$$

is the mean anomaly of the Earth in its orbit about the Sun, and JD is the Julian date. Note: higher order terms have been neglected. Since planetary motions are now computed using TDB, it is the time scale required when working with the JPL DE200 Planetary Ephemeris (see below).

Given the above definitions, the transformation of time from UTC on the Earth to TDB at the SSB may be summarised as:

$$t_{\mathrm{TDB}} = t_{\mathrm{UTC}} + \Delta_{\mathrm{TAI-UTC}} + \Delta_{\mathrm{TDT-TAI}} + \Delta_{\mathrm{TDB-TDT}} \tag{6.10}$$

6.3.2 Time-of-Flight Corrections

The propagation delay, Δ_{Prop}, represents the time-of-flight delay a photon from a pulsar experiences in travelling to the telescope on Earth, as opposed to the SSB. There are two main components to Δ_{Prop}. The larger component is the time-of-flight difference for photons arriving at the Earth-centre and at the SSB. It can be of the order of hundreds of seconds and forms the largest part of the overall barycentering correction. The other component is the time-of-flight difference for photons arriving at the observatory and at the centre of the Earth.

Time-of-Flight from Earth-centre to SSB

The time-of-flight delay for photons arriving at the Earth-centre, may be calculated with reference to Figure 6.5, by noting that

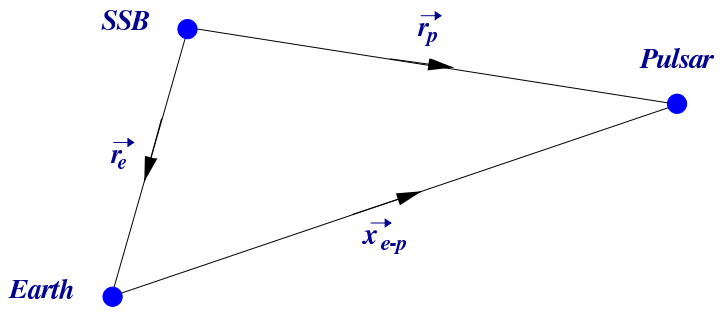

Figure 6.5: The vector notation used when calculating the time-of-flight delay for photons arriving at the Earth-centre and at the SSB.

$$\vec{r}_p = \vec{r}_e + \vec{x}_{e-p}$$

where $\vec{r}_p$ is the vector from the SSB to the pulsar, $\vec{r}_e$ is the vector from the SSB to the Earth-centre, and $\vec{x}_{e-p}$ is the vector from the Earth-centre to the pulsar. The path length difference for $r_e \ll r_p$ is

$$\begin{aligned}
\Delta r &\equiv r_p - x_{e-p} \\
&= r_p - \sqrt{r_p^2 - 2\vec{r}_p \cdot \vec{r}_e + r_e^2} \\
&\simeq r_p - \left\{ r_p - \frac{\vec{r}_p \cdot \hat{r}_e}{r_p} r_e + \frac{1}{2}\left[\frac{(\vec{r}_p \cdot \hat{r}_e)^2}{r_p^3} - \frac{1}{r_p} \right] r_e^2 + \ldots \right\} \\
&\simeq \hat{r}_p \cdot \vec{r}_e - \frac{(\hat{r}_p \cdot \vec{r}_e)^2 - r_e^2}{2r_p}
\end{aligned} \tag{6.11}$$

Since the magnitude r_p is simply the pulsar distance D, this results in a time-of-flight delay of

$$\Delta_{\text{Earth}\to\text{SSB}} = \frac{\Delta r}{c} \simeq \frac{\hat{r}_p \cdot \vec{r}_e}{c} - \frac{(\hat{r}_p \cdot \vec{r}_e)^2 - r_0^2}{2cD} \tag{6.12}$$

For the Crab pulsar, $D \gg r_e$, hence

$$\Delta_{\text{Earth}\to\text{SSB}} \simeq \frac{\hat{r}_p \cdot \vec{r}_e}{c} \tag{6.13}$$

The position of the Earth-centre relative to the SSB (i.e. $\vec{r}_e$), at the barycentric dynamical time calculated using equation 6.10, is obtained from the JPL DE200 Planetary and Lunar Ephemeris (Standish, 1982, 1997); and the J2000.0 Crab pulsar coordinates (table 6.1) are used to calculate $\hat{r}_p$. It follows that with $\vec{r}_e$ and $\vec{r}_p$ in place, $\Delta_{\text{Earth}\to\text{SSB}}$ can be calculated.

Right Ascension	Declination
$05^h\ 34^m\ 31^s.973$	$22^\circ\ 00^m\ 52^s.061$

Table 6.1: J2000.0 coordinates of the Crab pulsar.

	Geodetic	Geocentric
Longtitude	$-110^o\ 52^m\ 45^s.1$	-110.87919 degrees
Latitude	$31^o\ 40^m\ 49^s.7$	31.508796 degrees
Altitude	2.336 km a.s.l	
Radius		6374.611 km

Table 6.2: Geodetic and Geocentric coordinates for the Whipple 10 m telescope.

Time-of-Flight from Observatory to Earth-centre

The time-of-flight correction from the observatory to the centre of the Earth requires the telescope's geocentric coordinates and the zenith angle of the pulsar at the time of observation. The observatory's geodetic coordinates, as measured using a GPS receiver in 1996, were used to calculate the geocentric coordinates (Gillanders, 2000); both sets are provided in table 6.2. The source's zenith angle at the time of observation is calculated using the reduction of precession formulae on page B18 of the *Astronomical Almanac*. Ultimately, the observatory to Earth-centre time-of-flight correction is determined as

$$\Delta_{Observatory \rightarrow Earth} = \frac{1}{c} r_o \, cos(Z) \tag{6.14}$$

where r_o is the distance from the observatory to the Earth-centre and Z is the zenith angle of the source.

6.3.3 Barycentering Summary

Combining the various corrections outlined above, the overall barycentering correction process may be summarised as

$$\begin{aligned} t_b = \quad & t_{\mathrm{UTC}} + \Delta_{\mathrm{TAI-UTC}} + \Delta_{\mathrm{TDT-TAI}} \\ & + \Delta_{\mathrm{TDB-TDT}} + \Delta_{\mathrm{Earth \rightarrow SSB}} + \Delta_{Observatory \rightarrow Earth} \end{aligned}$$

A worked example for a real event arrival time is provided in Figure 6.6.

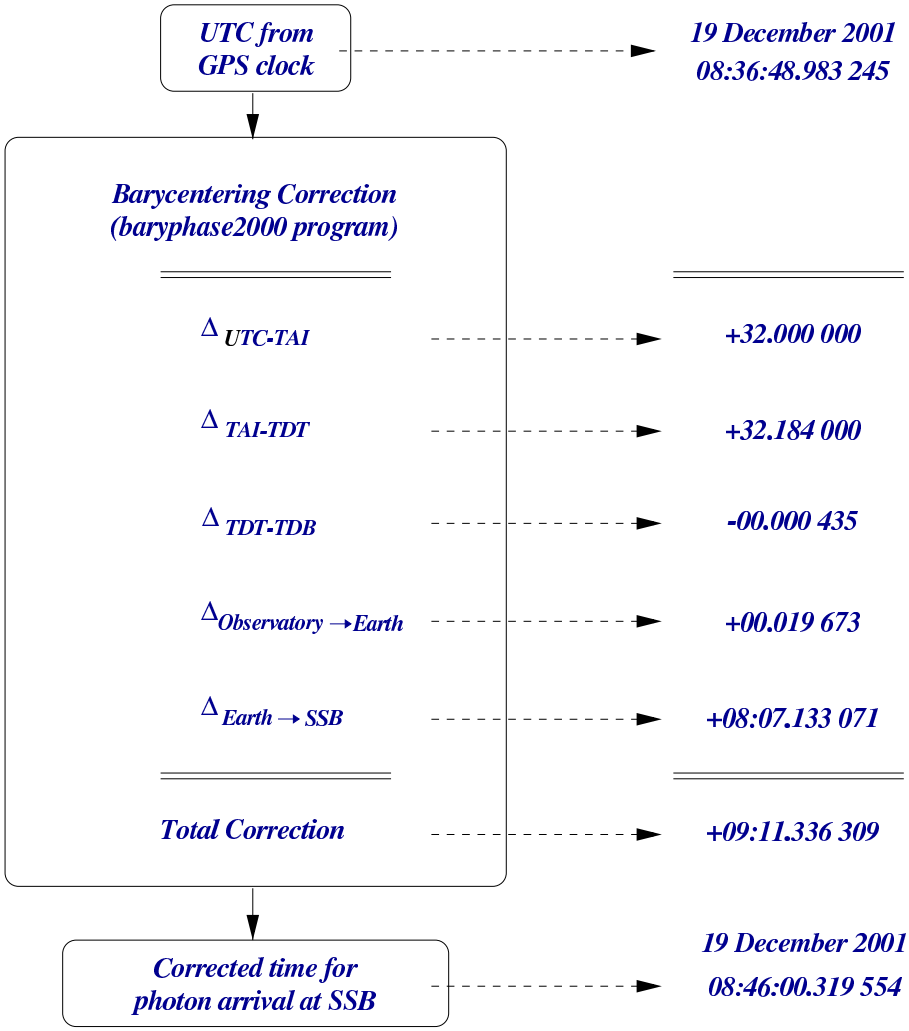

Figure 6.6: A worked barycentering example for a real γ-ray event, showing the various corrections needed to transform the event's arrival time at the observatory to an arrival time at the Solar System Barycenter (SSB).

6.4 Crab Pulsar Periodic Analysis

In order to search for pulsed emission in Crab pulsar γ-ray data, the phase of each candidate event must be determined, subsequent to the application of all timing corrections, and folded to produce a lightcurve. The lightcurve may then be examined for evidence of a periodic signal, and a flux upper limit for pulsed emission determined. The phase determination, lightcurve development, and periodic searching analyses, used in this thesis work, are described here.

6.4.1 Phase Determination

The monthly Crab pulsar radio ephemeris supplied by the Jodrell Bank radio observatory (Lyne et al., monthly updates), is used to determine the phase of each of the Crab pulsar γ-ray events selected by the supercuts and kernel selection techniques described in chapter 5. The Jodrell Bank ephemeris is produced on the 15th day of each month and contains the following timing parameters, relevant to the present analysis:

MJD	The modified Julian date for the day of observation (15th day of each month).
t_{JPL}	The arrival time of the centre of the first main radio pulse after midnight at infinite frequency at the barycentre of the solar system. Measured in seconds.
f	The observed barycentric frequency at the quoted arrival time, derived using the DE200 ephemeris. Measured in Hertz.
$\dot{f}$	The first derivative of the observed barycentric frequency. Measured in 10^{-15} sec^{-2}.

Given these parameter values, the phase of each γ-ray event is calculated using equation 6.3. The value used for $(T - T_0)$ is simply the difference, in seconds, between the event's barycentered timestamp (T_b), and the arrival time of the first main radio pulse at the solar system barycentre ($T_0 = MJD + t_{JPL}$). The calculated phases are binned into 25 bins and the resulting lightcurve examined for periodicity using the χ^2 statistic (see section 6.4.3). In general, the lightcurve from phase 0 to 1 is repeated from phase 1 to 2; this helps distinguish the main pulse which straddles phase 0, see Figure 6.7(b) below. The phase of the Crab pulsar event barycentered in the worked example of Figure 6.6 was determined, using equation 6.3, to be 0.9517 of a phase cycle. The various timing parameter values relevant to its

Parameter	Value	Units
f	29.8230631881	Hertz
$\dot{f}$	-374050.09	10^{-15} sec^{-2}
T_0	0.083361	Seconds
Complete Phase	11248046.9517	Cycles
Folded phase	0.9517	Of a cycle

Table 6.3: The timing parameter values used in the phase calculation of the example γ-ray event which was barycentered in Figure 6.6.

calculation are presented in table 6.3.

6.4.2 Optical Data Test

The main software used to barycentre the dataset presented in this thesis is a modified version of the BRYPHASE2000 code used for pulsar analysis at the National University of Ireland, Galway (Gillanders, 2000). To check the integrity of the modified code, two independent tests were performed.

The first involved a simple comparison between barycentered times output by BRYPHASE2000 and those output by an independent control program (Fegan, 2002a), for the same subset of Crab γ-ray data. Excellent agreement between both sets of results was established.

The second test used optical Crab pulsar data, recorded during a ten minute run at the Multiple Mirror Telescope in December 1996 using the electronics of the Whipple 10 m telescope (Srinivasan, 1996). The ten minutes of optical data was epoch-folded both before and after the barycentering process. Phases were calculated in the pre-barycentering analysis using just the raw photon arrival times, while the post-barycentering analysis used the corrected times. Lightcurves for the pre- and post-barycentering analyses are presented in Figures 6.7(a) and 6.7(b) respectively (*Nota bene*: in this work all lightcurves are presented with two rotations shown, i.e. the lightcurve from phase 0 to 1 is repeated from 1 to 2). It is clear from the plots that, although some periodicity is discernable in the raw data, it is smeared and significantly reduced compared to the unambiguous main and intrapulse peaks evident in the post-barycentered data. These results reinforce the case for barycentering while simultaneously demonstrating the fidelity of the barycentering code.

Another examination of the temporal reliability of the timing system used at the Whipple 10 m telescope (see section 4.7.3) was undertaken by Srinivasan et al. (1997). By applying an aperture to the central tube of the Whipple PMT-camera and zeroing the high-voltage supply to all other tubes,

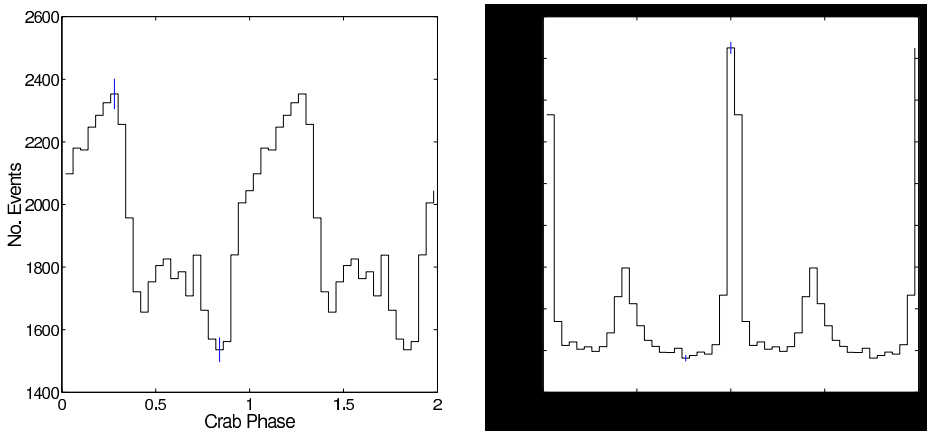

(a) Before barycentering **(b)** After barycentering.

Figure 6.7: Lightcurves produced using the barycentering program BRYPHASE200, for optical Crab pulsar data recorded at the Multiple Mirror Telescope in 1996.

they effectively operated the 10 m instrument as an optical telescope with a photometer at its focus. Their work established clear optical pulsations from the Crab pulsar and demonstrated the temporal reliability of the electronic system, which has remained unchanged since.

6.4.3 The χ^2 Test for Non-statistical Behaviour

The χ^2 statistic is the traditional test used in γ-ray astronomy to search for modulation in pulsar data. Other popular tests include the Z^2_m statistic (Beran, 1969; Buccheri, 1983; Buccheri and Sacco, 1985) and the H-test (de Jager et al., 1989). In general χ^2 for a distribution of data is its total squared deviation from the expected distribution, so that

$$\chi^2 = \sum_{i=1}^{K} \frac{(O_i - E_i)^2}{\sigma_i^2} \tag{6.15}$$

where

- K is the number of bins,
- O_i are the number of observed counts in each bin,
- E_i is the expected number of counts in each bin, and

- σ_i^2 are the variances in the expected values.

In the absence of pulsation, the observed phases should be uniformly distributed, so that $E_i = \langle O \rangle$, where $\langle O \rangle$ is the mean value of the O_i. For a sufficient γ-ray detection rate, the counts should obey Poisson statistics such that

$$\sigma_i^2 \simeq \langle O \rangle$$

Hence,

$$\chi^2 = \sum_{i=1}^{K} \frac{(O_i - \langle O \rangle)^2}{\langle O \rangle} \tag{6.16}$$

is the formula used to calculate the χ^2 values for the lightcurves presented in this thesis.

The epoch-folding/χ^2 test is the only test used to search for non-statistical lightcurves in this work. It is considered sufficient, as the Crab pulsar pulse profile is well defined and well established from radio waves to low-energy γ-rays, and pulsed TeV emission, should it exist, is not expected to deviate from the profile seen at lower energies.

6.4.4 Statistical Considerations

The χ^2 sum may be converted into a probability, P_{χ^2}, that the observed lightcurve really matches a flat distribution, by using the incomplete gamma function $gammaq(a, x)$ (Press et al., 1988)

$$P_{\chi^2} = gammaq\left(\frac{d}{2}, \frac{\chi^2}{2}\right) \tag{6.17}$$

where d is the number of degrees of freedom. In this work, in which the mean is the only constraint on data, the number of degrees of freedom is $N - 1$, where N is the number of lightcurve bins; generally 25 bins. The number of trials is factored into the χ^2 probability according to

$$P_{trials} = 1 - (1 - P_{\chi^2})^{N_{trials}} \tag{6.18}$$

For this work, the number of trials is taken to mean the number of times the same dataset is split to obtain separate lightcurves—since each data file is analysed with just the one test period, derived from the radio ephemeris,

there is no contribution to the number of trials arising from different test periods. So, for example, from the complete dataset available, four subsets representing each of the four elevation bands discussed in section 5.4, may be produced; thus the number of trials is four. Further splitting of the data, into size bands etc, results in an increased number of trials, all of which must be accounted for when calculating the relevant χ^2 probabilities.

6.4.5 EGRET Pulse Profile and Flux Upper Limits for Periodic TeV Emission

In the absence of a clear pulsed signal from the Crab pulsar, an upper limit of pulsed emission may be determined. Given the number of detected counts within an expected phase range, N_{ON}, and the number of background counts, N_{OFF}, outside that range, the method of Helene (1983) allows for the determination of a number upper limit, $N_{u.l.}$, at a specific confidence level. $N_{u.l.}$ may then be used to obtain an absolute integral flux upper limit of pulsed emission according to

$$Flux_{u.l.}(E > E_{PRE}) < \frac{N_{u.l.}}{TA_{eff}} \tag{6.19}$$

where T is the observing duration, and E_{PRE} and A_{eff} are respectively the peak response energy and the effective collection area, for the γ-ray detection technique.

In this work the expected phase intervals used in the recent Crab pulsar publications of Lessard et al. (2000); Oser et al. (2001); and de Naurois et al. (2002) are employed. These intervals correspond to the Crab pulse profile seen by EGRET (see Figure 6.8)—i.e. pulsed emission is assumed to occur within the phase ranges of both the main pulse, phase 0.94–0.04, and the intrapulse, phase 0.32–0.43. Accordingly, N_{ON} is simply the number of γ-ray events with phases within the expected intervals, while N_{OFF} is an estimate of the number of background events, determined by multiplying the number of events with phases outside the expected intervals by the ratio of the phase ranges spanned by the main pulse and intrapulse profiles. The expected phase intervals are hereafter collectively referred to as the *EGRET range*.

The significance of the excess counts within the EGRET range may also be calculated, using the standard formula for γ-ray significance's:

$$\sigma = \frac{N_{ON} - N_{OFF}}{\sqrt{N_{ON} + N_{OFF}}}$$

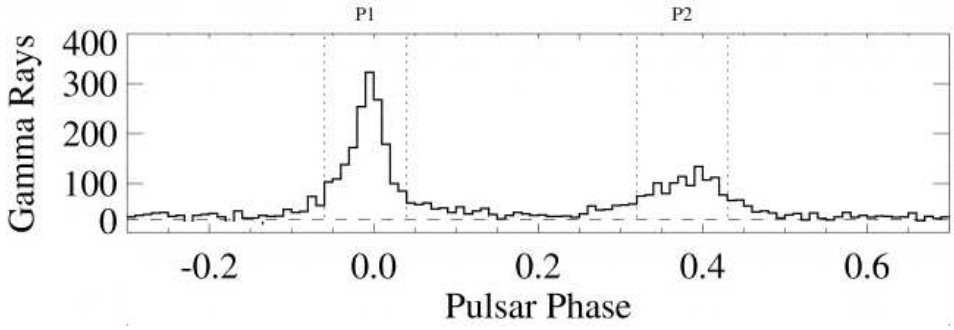

Figure 6.8: The Crab pulsar profile as seen by the EGRET telescope above 100 MeV. The regions P1 (phase 0.94–0.04) and P2 (phase 0.32–0.43) correspond to the main pulse and intrapulse respectively. Modified version of the original from Fierro et al. (1998)

Some authors, for example Aharonian et al. (1999); Oser et al. (2001), choose not to present an absolute flux upper limit for pulsed emission, and instead express their pulsed upper limit as a fraction of the observed steady DC signal from the Crab. In this work both methods of presentation are employed. It should be noted, however, that in calculating the pulsed upper limit as a fraction of the DC emission, the DC emission rate is determined from data taken exclusively in ON/OFF mode, thereby eliminating the need for a *tracking ratio*; just ON-source data is used in determining the absolute flux upper limits.

6.4.6 Search for Episodic Emission

To search for episodic emission of the type reported previously by Gibson et al. (1982); Bhat et al. (1986); and Acharya et al. (1992), the complete set of Crab data files used in this work were analysed for evidence of pulsed emission. This involved examining the data on a run-by-run basis for an excess in the EGRET range, and for a χ^2 value incompatible with a flat distribution.

Monte Carlo simulated lightcurves were used to determine the expected distribution of EGRET range significance values and χ^2 values. Figure 6.9 presents these expected distributions, produced using 100,000 simulated lightcurves. Any deviation of the real data from the expected distributions would indicate the presence of non-statistical lightcurves, and thereby indicate potential evidence for episodic pulsed TeV-scale emission from the Crab pulsar.

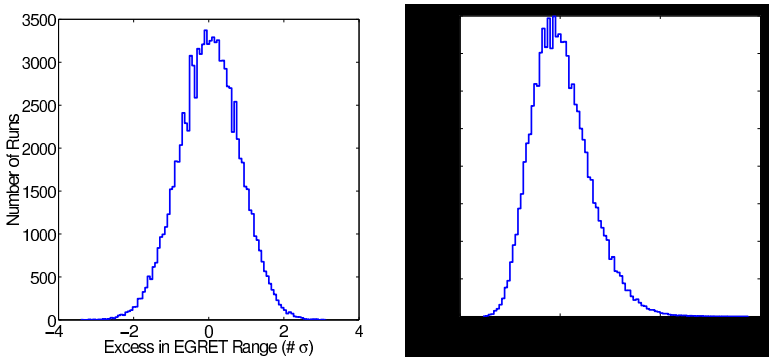

(a) Simulated pulsed σ histogram..

(b) Simulated χ^2 distribution.

Figure 6.9: The distribution of excess events in the EGRET range and the distribution of χ^2 values for a flat distribution, produced using 100,000 simulated lightcuves, of 25 bins each.

6.4.7 Analysis in Practise

An overview of the temporal analysis strategy, as implemented for this work, is provided in Figure 6.10. The list of all data files analysed, together with all the relevant parameters used to obtain rotation phases is presented in appendix B.

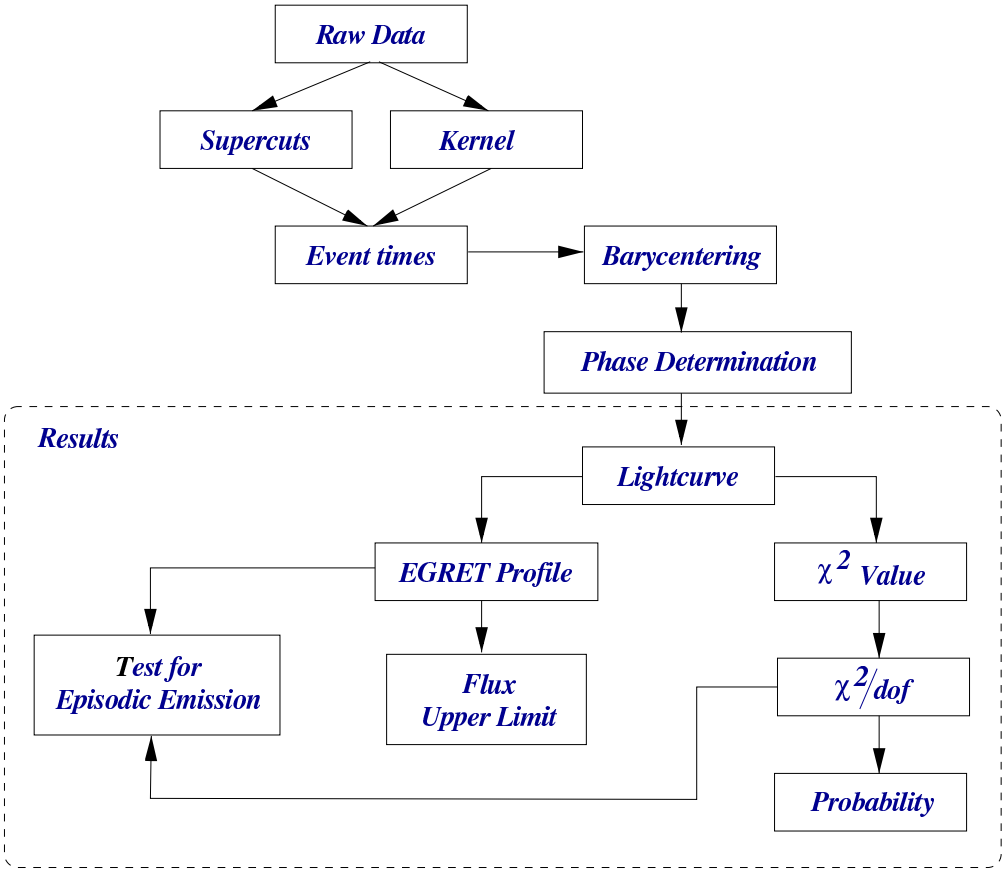

Figure 6.10: An overview of the temporal analysis methodology used to search for pulsed γ-ray emission from the Crab pulsar.

Chapter 7

Analysis, Results and Conclusions

7.1 Introduction

This chapter details the results of the DC and periodic analyses described in chapters 5 and 6 respectively, and applied to the 2000–2002 Whipple Crab plerion γ-ray dataset. The objective was to utilise the IACT in an attempt to constrain, as much as possible within the confines of the current Whipple 10 m telescope, the γ-ray emission models pertaining to pulsed GeV–TeV emission from the Crab pulsar. In practical terms this involved extracting the optimum[1] number of candidate γ-ray events from the Crab dataset over the complete dynamic range of detected energy, followed by a rigorous periodicity analysis of their barycentered arrival times.

In order to extract the optimum number of γ-ray events, two independent selection mechanisms, Supercuts (section 5.11) and Kernel analysis (section 5.12), were optimised for maximum significance using the complete ON/OFF dataset. Multiple optimisations were performed—in discrete elevation and *size* bands—in a deliberate attempt to force the selection techniques to identify γ-ray images over the complete dynamic range of energies (section 5.11.6). Subsequently, for each optimisation band the results of the DC analysis were recorded and ultimately combined. Using γ-ray simulations the PREs (Peak Response Energies) and effective collection areas for each of the independent and combined optimisation bands were determined, and subsequently utilised to provide flux upper limits for pulsed γ-ray emission from the Crab pulsar at different energies (section 5.15).

[1] Optimum, in this context, refers to the number of ON-source γ-ray events with highest *significance* above the background OFF-source events.

The arrival times of all Čerenkov events recorded by the Whipple telescope were registered by a GPS clock with an absolute resolution of 250 μs. A 10 MHz oscillator, calibrated by GPS second marks, was used to interpolate the timestamps to a resolution of 0.1 μs (section 4.7.3). Before periodicity analysis was applied, all times were transformed to the solar system barycentre, by utilising the JPL DE200 Planetary and Lunar Ephemeris (section 6.3).

Periodicity analysis involved folding the corrected times to produce phases modulo the Crab pulsar radio period (section 6.4.1), and analysing the resulting lightcurves for non-statistical behaviour (section 6.4.3) or evidence of excess emission within the pulsed phase profile observed by EGRET (section 6.4.5). A search for episodic emission of the type reported by several previous workers (section 2.9) was also conducted, on the time scale of $\sim$28 minutes, by performing a run-by-run search for periodic emission.

There are five main sections in this chapter. The first and second detail the results of the Supercuts and Kernel analyses respectively, including all DC and periodicity work. The third section provides a brief summary of these results, while the fourth provides a discussion of their implications in the context of pulsar emission models and previous work. In the fifth and final section the possibilities for future pulsar observations, using the next generation of γ-ray detectors, is discussed.

7.2 Results of the Supercuts-based Analysis

7.2.1 DC Analysis

Standard Supercuts 2000

Prior to performing any optimisations, the standard selection criteria currently used by the Whipple collaboration, Supercuts 2000 (table 5.4), were applied to the complete Crab plerion dataset. The results of this "standard" analysis are summarised in table 7.1 and the final *alpha*-plot is presented in Figure 7.1.

To demonstrate the elevation-dependent nature of the results, the elevation-specific data subsets, listed previously in table 5.2, were each individually subjected to the Supercuts 2000 analysis. The resulting rates and $\sigma/\sqrt{hour}$ (i.e. the significance of excess events per square root of observing duration)[2] are presented in Figure 7.2. It is clear from these plots that Supercuts 2000

[2] $\sigma/\sqrt{hour}$ is a useful parameter for comparing γ-ray significances derived from datasets of differing duration, as it removes the duration dependence of each significance value.

No. ON events.	49781
No. OFF events	37484
Rate (γ/min) ...	2.32
Significance.....	41.7

Table 7.1: Summary of the results for the Supercuts 2000 selection criteria applied to the complete Crab plerion dataset used in this work.

performs better at higher elevations, both in terms of γ-ray rate and significance. Indeed, the elevation dependent nature of the results presented here further justifies the use of elevation-specific analyses in this work.

Re-optimised Supercuts Results

The Supercuts optimisation methodology, outlined in section 5.11.6, was used to re-optimise the Supercuts selection criteria for maximum significance in each optimisation band of table 5.8. Re-optimised cut values are provided in appendix C.

γ-ray Rates Final γ-ray DC rates, tabulated after applying each set of optimised cuts to the appropriate subset of Crab data, are listed in table 7.2. The aggregate *size* rates, calculated after combining cut data from each *size* range, are shown separately for individual elevation bands and for all elevations bands combined. Supercuts 2000 rates are also presented for comparison.

A salient feature of these results is that the aggregate *size* rate for each elevation band is significantly higher than the corresponding Supercuts 2000 rate. This is bourne out in Figure 7.3, which is a plot of the rates obtained for each *size* range after all elevations bands were combined (i.e. the rightmost column of table 7.2). Furthermore, it is clear from the plot that the major contribution to the aggregate *size* rate must be provided by small *size* events; a desireable result in the present context of seeking low energy γ-rays for periodicity analysis.

γ-ray Significances An examination of the γ-ray significances, after re-optimisation, was conducted by individually tabulating the $\sigma/\sqrt{hour}$ for each optimisation band. Table 7.3 presents the results of this examination. Again, aggregate *size* results are presented, together with the combined elevation results and the Supercuts 2000 results. The $\sigma/\sqrt{hour}$ achieved in each *size* range for all elevation bands combined is plotted in Figure 7.4.

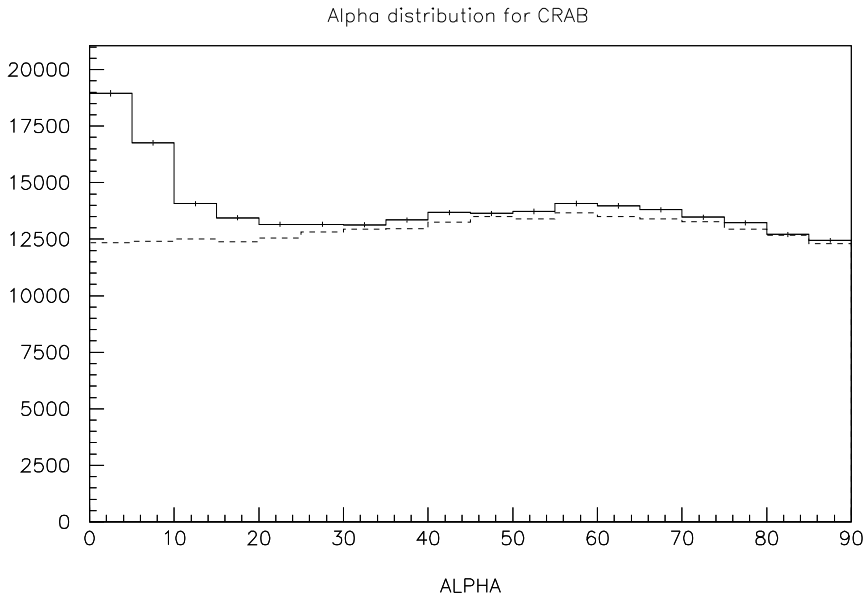

Figure 7.1: The *alpha* plot for Čerenkov events from the direction of the Crab plerion (solid line) and the Crab OFF-source region (dashed line), after Supercuts 2000 analysis, for all ON/OFF data used in this work. The excess of ON-source events below α=15° is at the level of 41.7 σ.

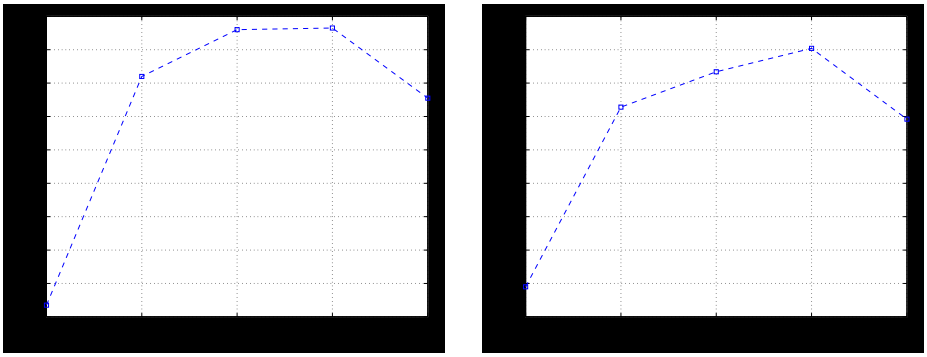

(a) γ-ray Rate. **(b)** $\sigma/\sqrt{hour}$.

Figure 7.2: γ-ray rate and $\sigma/\sqrt{duration/hours}$ for the Crab plerion data used in this work, as a function of observing elevation.

Size Range (d.c.)	Elevation Bands (degrees) 35-50	51-50	61-70	71-80	Combined Elevations
150-250	0.82 ± 0.15	0.02 ± 0.005	1.43 ± 0.26	2.31 ± 0.27	1.44 ± 0.13
250-350	1.25 ± 0.19	0.02 ± 0.01	1.14 ± 0.16	1.04 ± 0.14	0.94 ± 0.08
350-450	0.60 ± 0.09	1.08 ± 0.15	0.69 ± 0.09	0.74 ± 0.08	0.75 ± 0.05
450-550	0.29 ± 0.04	0.24 ± 0.03	0.22 ± 0.03	0.44 ± 0.04	0.33 ± 0.02
550-650	0.12 ± 0.02	0.29 ± 0.04	0.29 ± 0.03	0.27 ± 0.02	0.24 ± 0.01
650-750	0.17 ± 0.03	0.23 ± 0.02	0.21 ± 0.02	0.28 ± 0.02	0.24 ± 0.01
750-1000	0.07 ± 0.01	0.24 ± 0.02	0.37 ± 0.03	0.35 ± 0.02	0.27 ± 0.01
1000-2000	0.36 ± 0.05	0.39 ± 0.03	0.42 ± 0.03	0.59 ± 0.02	0.48 ± 0.02
>2000	0.09 ± 0.01	0.23 ± 0.02	0.33 ± 0.02	0.32 ± 0.01	0.26 ± 0.01
Aggregate *size*	3.76 ± 0.27	2.75 ± 0.17	5.09 ± 0.32	6.33 ± 0.32	4.94 ± 0.16
Supercuts 2000	1.10 ± 0.13	2.50 ± 0.14	2.72 ± 0.13	2.79 ± 0.08	2.36 ± 0.06

Table 7.2: Breakdown of γ-ray rates (γ-rays per minute) for the re-optimised Supercuts analyses by elevation and *size* band. Supercuts 2000 results are also shown.

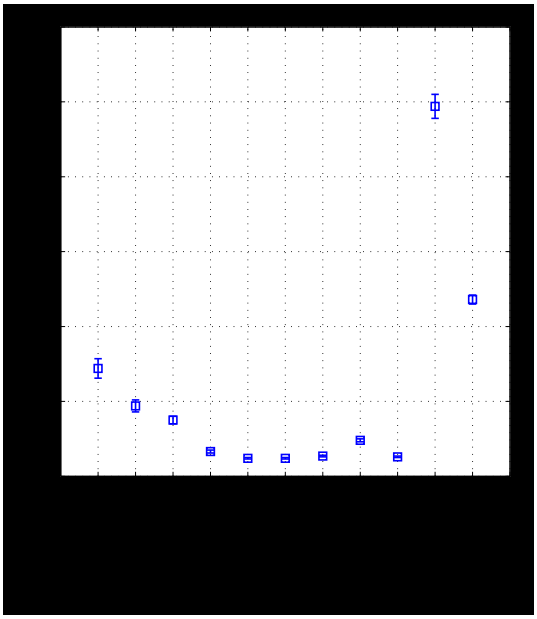

Figure 7.3: Rates for re-optimised Supercuts selection, obtained for each *size* range after results from all elevation bands were combined (the rightmost column of table 7.2).

Size Range (d.c.)	Elevation Bands (degrees)				Combined Elevations
	35-50	51-50	61-70	71-80	
150-250	1.27	1.09	1.37	1.39	1.18
250-350	1.46	0.87	1.74	1.18	1.24
350-450	1.55	1.89	1.91	1.60	1.68
450-550	1.64	2.04	1.58	1.96	1.79
550-650	1.61	2.19	2.36	2.44	2.21
650-750	1.45	2.63	2.38	2.38	2.17
750-1000	1.28	2.83	3.40	3.19	2.85
1000-2000	1.61	3.59	4.02	4.44	3.16
>2000	1.63	3.08	3.86	3.62	3.23
Aggregate *size*	3.18	4.39	3.89	3.22	3.23
Supercuts 2000	1.95	4.64	5.17	5.52	4.46

Table 7.3: Breakdown of significance per $\sqrt{hour}$ for the re-optimised Supercuts analyses by elevation and *size* band. Supercuts 2000 results are also shown.

Of particular interest in these results are the relatively high significances obtained for the aggregate *size* ranges, in each independent elevation band, and also when all elevation bands are combined. It is encouraging to note that these high significance values are associated with high rates (table 7.2)—an indication that the increased γ-ray rate, obtained by forcing the selection criteria into a lower than normal *size* regime, is gained without seriously compromising overall γ-ray significance. Of note also is the relatively low significance value obtained by the Supercuts 2000 analysis in the $35° \rightarrow 50°$ elevation band. This may be explained by the fact that the Supercuts 2000 cuts were optimised at a much higher elevation and are unsuitable for application to low elevation data.

Detector Response

Collection Areas Using appropriate γ-ray simulations (section 5.5) and the analysis methodology described in section 5.15.1, the collection area curve for each optimisation band was derived. Unlike the collection area curve for Supercuts 2000 (Figure 5.23), which steadily increases with energy, the collection area curves for the individual optimisation bands used in this work have artificial "energy ceilings"; imposed by the strict *size* ranges used. This is demonstrated in Figure 7.5, in which the collection area curve for the 350–450 d.c. *size* range in the $71° \rightarrow 80°$ elevation band is presented. The energy ceilings on the collection area curves used in this work represent the type of sacrificed collection areas for pulsar analysis, referred to by de Jager (2002). This issue is discussed in greater detail in section 7.6.2 below.

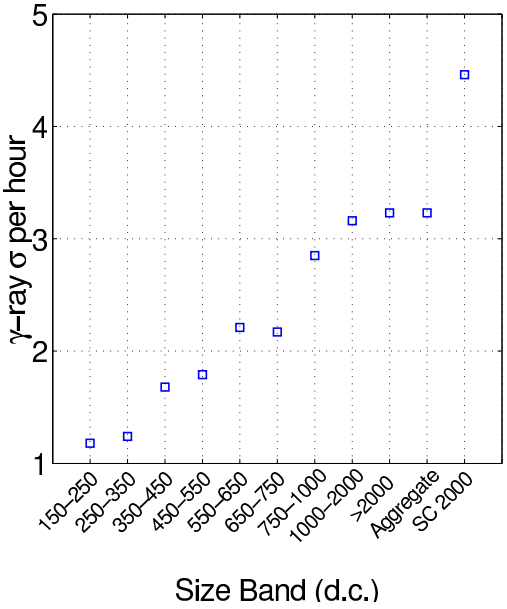

Figure 7.4: $\sigma/\sqrt{hour}$ for the re-optimised Supercuts selection, obtained when all elevation bands were combined (the rightmost column of table 7.3).

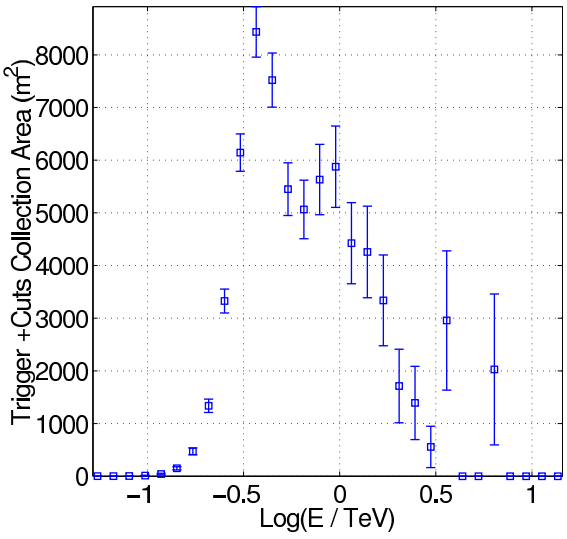

Figure 7.5: The collection area curve for the re-optimised Supercuts criteria in the 350–450 d.c. *size* range, applied to γ-ray simulations at 75° elevation.

Size Range (d.c.)	Elevation Bands (degrees) 35-50	51-50	61-70	71-80	Combined Elevations
150-250	0.400 ± 0.07	0.308 ± 0.06	0.228 ± 0.04	0.160 ± 0.03	0.177 ± 0.03
250-350	0.550 ± 0.10	0.211 ± 0.04	0.293 ± 0.06	0.241 ± 0.05	0.259 ± 0.05
350-450	0.771 ± 0.15	0.493 ± 0.10	0.349 ± 0.07	0.304 ± 0.06	0.326 ± 0.06
450-550	0.844 ± 0.15	0.487 ± 0.09	0.506 ± 0.10	0.375 ± 0.07	0.385 ± 0.07
550-650	0.876 ± 0.18	0.623 ± 0.12	0.502 ± 0.10	0.381 ± 0.07	0.397 ± 0.07
650-750	1.288 ± 0.27	0.706 ± 0.12	0.545 ± 0.10	0.482 ± 0.09	0.511 ± 0.10
750-1000	1.287 ± 0.27	0.896 ± 0.18	0.673 ± 0.12	0.586 ± 0.10	0.615 ± 0.12
1000-2000	2.077 ± 0.39	1.344 ± 0.27	0.948 ± 0.18	0.819 ± 0.15	0.872 ± 0.18
>2000	3.114 ± 0.57	2.149 ± 0.39	1.759 ± 0.32	1.470 ± 0.27	1.606 ± 0.32
Aggregate *size*	0.537 ± 0.10	0.559 ± 0.10	0.257 ± 0.05	0.199 ± 0.04	0.209 ± 0.04
Supercuts 2000	0.875 ± 0.18	0.658 ± 0.12	0.493 ± 0.10	0.389 ± 0.07	0.517 ± 0.10

Table 7.4: Breakdown of Peak Response Energies (in TeV) for the re-optimised Supercuts analyses, by elevation and *size* band. The Supercuts 2000 PREs are also shown.

Peak Response Energies By convolving the collection area curves determined in each optimisation band with the differential Crab nebula spectrum derived by Hillas et al. (1998), in the manner described in section 5.15.2, the differential response curve and PRE for each optimisation band was determined. It is appropriate to use the DC Crab spectrum in the derivation of PREs as the TeV γ-ray data used in this work pertains mainly (if not exclusively) to steady emission from the Crab plerion. The list of PREs derived for each optimisation band are provided in table 7.4, and the differential response curve corresponding to the collection area curve of Figure 7.5 is presented in Figure 7.6.

In general, as expected, the PRE values decrease from low elevation to high elevation (across table 7.4) and increase from small *size* to large *size* (down table 7.4). Indeed, the increase in PRE from small *size* to large *size* is further demonstrated in Figure 7.7, which presents the *size*-range-specific PRE values for the four elevation bands combined, ascertained by combining and scaling the appropriate collection area curves of each independent elevation band, in the manner detailed in section 5.15.1. The roughly linear increase in energy with *size* range is a natural consequence of the *size*-energy relationship discussed in section 5.10.

The lowest PRE reached by the re-optimised Supercuts analysis was 0.16 ± 0.03 TeV, for γ-ray events with *size* 150–250 d.c. in the $71^\circ \rightarrow 80^\circ$ elevation band. This represents a very low energy regime previously unexplored by the Whipple telescope (a full discussion of the implications of this result for future pulsar observations is provided in section 7.6.2). Furthermore, when *all* candidate γ-ray events, selected after applying all re-optimised cuts in *all* optimisation bands, were combined, the overall PRE was 0.209 ± 0.04 TeV. This is much lower than the 0.517 ± 0.1 TeV achieved by Supercuts 2000

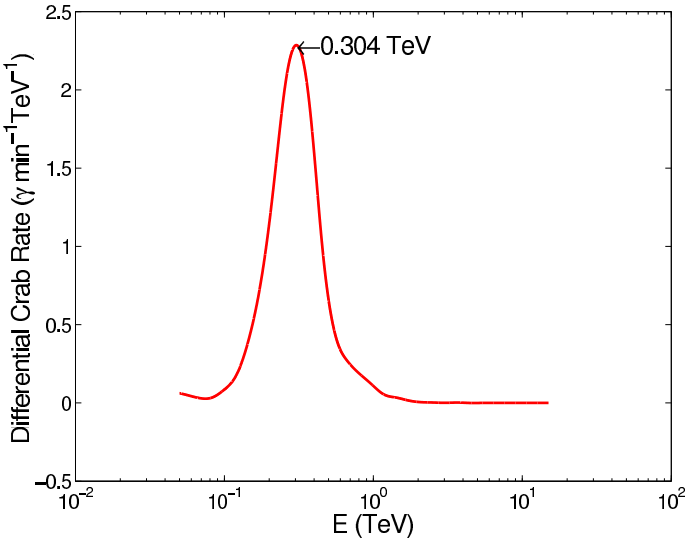

Figure 7.6: The differential response curve for the re-optimised Supercuts criteria in the 350–450 d.c. *size* range, applied to γ-ray simulations at 75° elevation. This plot was obtained by convolving the collection area curve of Figure 7.5 with the Crab spectrum derived by Hillas et al. (1998).

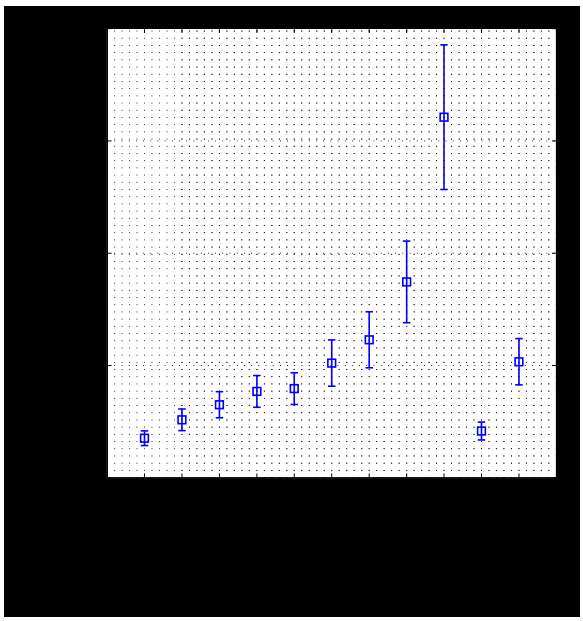

Figure 7.7: Re-optimised Supercuts PRE values evaluated for each *size* range after all elevation bands were combined (the rightmost column of table 7.4).

Size Range (d.c.)	Elevation Bands (degrees) 35-50	51-50	61-70	71-80	Combined Elevations
150-250	7.73 ± 0.86	0.005 ± 0.003	15.03 ± 1.77	16.27 ± 1.97	10.93 ± 1.67
250-350	19.35 ± 2.00	0.023 ± 0.015	11.02 ± 1.25	13.42 ± 1.59	10.03 ± 1.73
350-450	18.87 ± 2.38	9.14 ± 1.30	4.87 ± 0.63	4.55 ± 1.31	4.35 ± 0.97
450-550	11.83 ± 1.79	3.87 ± 0.62	3.27 ± 0.54	4.95 ± 0.66	3.50 ± 0.90
550-650	5.82 ± 1.15	8.09 ± 1.41	5.48 ± 0.72	3.02 ± 0.46	2.82 ± 0.88
650-750	9.52 ± 2.07	7.14 ± 1.38	5.14 ± 0.75	5.34 ± 0.81	4.43 ± 1.39
750-1000	9.17 ± 1.93	16.25 ± 2.93	11.70 ± 1.53	10.38 ± 1.33	8.58 ± 2.30
1000-2000	54.69 ± 10.70	55.10 ± 9.76	29.24 ± 3.92	30.29 ± 3.93	26.45 ± 6.45
>2000	86.88 ± 20.77	69.27 ± 16.20	57.23 ± 11.07	49.08 ± 9.16	47.24 ± 15.32
Combined_sizes	62.42 ± 5.88	52.28 ± 5.63	50.65 ± 4.80	54.61 ± 5.35	39.41 ± 4.76
Supercuts2000	95.93 ± 11.53	78.40 ± 8.70	51.61 ± 4.66	32.24 ± 2.85	51.69 ± 7.31

Table 7.5: Breakdown of effective collection areas ($\times 10^7$ cm^{-2}s^{-1}) for the re-optimised Supercuts analyses, by elevation and *size* band. The Supercuts 2000 effective areas are also shown.

for the same data, and demonstrates the clear reduction in energy threshold gained by the Supercuts re-optimisation technique.

Effective Areas The effective area of a flux collector (section 5.15.3) takes account of both its collection area and the γ-ray spectrum of the source under observation. As such it is a critical parameter for integral flux (or flux upper limit) calculations. The effective areas calculated after Supercuts re-optimisation analysis, using appropriate collection area and differential response curves, for all independent and all combined optimisation bands, are given in table 7.5. Figure 7.8 presents the effective areas calculated for each *size* range when all elevation bands are combined and shows the trend followed by the effective areas as a function of *size* range. This trend, in which effective areas initially decrease as a function of *size* and then increase, may be attributed to several factors—these include the process of optimising for significance, the power-law fall-off in the Crab spectrum as a function of energy, and the physical increase in collection area of the IACT with increasing γ-ray energy.

7.2.2 Periodicity Analysis

Lightcurves Each of the candidate γ-ray events which passed the re-optimised Supercuts selection criteria were used in a Crab pulsar periodicity analysis of the type described in chapter 6. The resulting lightcurves, with all elevation bands combined, for each of the nine independent *size* ranges, for the aggregate *size* range, and for the Supercuts 2000 events are presented in Figures 7.9 and 7.10. It is immediately clear that no evidence was found, in these results, for emission at the Crab pulsar radio period. The reduced χ^2

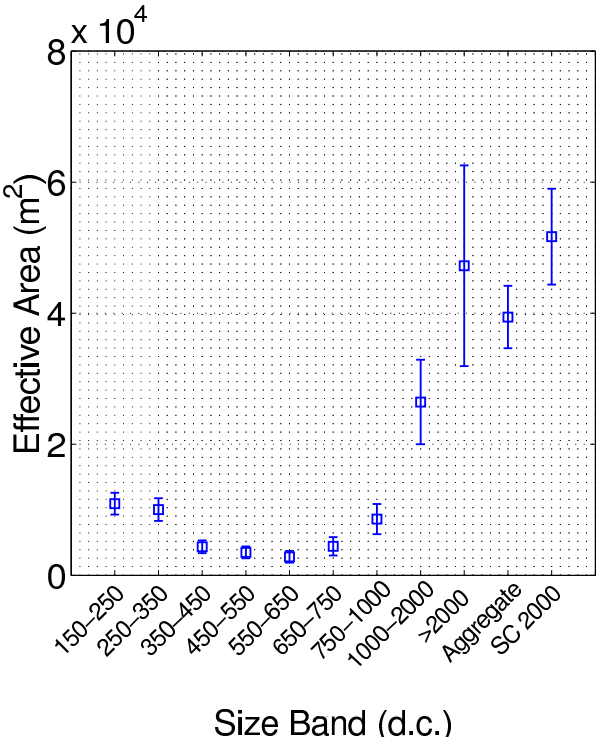

Figure 7.8: Effective collection areas after Supercuts re-optimisation, evaluated for each *size* band when all elevation bands were combined (the rightmost column of table 7.5).

Size Range (d.c.)	Elevation Bands (degrees) 35-50	51-50	61-70	71-80	Combined Elevations
150-250	-0.53	-0.38	0.36	1.95	1.74
250-350	0.30	-0.43	0.52	-0.13	0.25
350-450	-0.27	0.29	0.51	-0.83	-0.34
450-550	0.04	1.76	-1.85	0.66	0.45
550-650	1.07	-0.46	-0.93	2.25	1.21
650-750	-1.78	0.12	-0.54	0.49	-0.63
750-1000	-0.01	0.50	1.20	1.14	1.63
1000-2000	0.72	0.04	1.91	-0.93	0.58
>2000	0.23	0.56	-0.18	-0.23	0.03
Aggregate *size*	-0.10	0.67	0.65	1.64	1.69
Supercuts 2000	-2.17	0.18	0.85	0.14	-0.50
150-350	-0.08	-0.57	0.58	1.67	1.61
150-450	-0.17	0.24	0.70	1.42	1.43
150-550	-0.16	0.64	0.49	1.49	1.48
150-650	-0.08	0.51	0.39	1.63	1.57
150-750	-0.27	0.52	0.35	1.66	1.52
>550	0.21	0.21	0.80	1.11	1.27
>650	-0.11	0.56	1.43	0.16	0.82
>750	0.74	0.57	1.82	-0.10	1.26
>1000	0.76	0.36	1.38	-0.89	0.51

Table 7.6: Statistical significance values (in σ) of excess γ-ray events inside the EGRET range for the individual, cumulatively summed, and aggregate *size* ranges, after the re-optimised Supercuts analyses.

sums for flat distributions and associated probabilities (including allowances for trials) are presented with each lightcurve—there are no particularly interesting or significant values of these parameters evident in this analysis.

EGRET range Since pulsed TeV-scale γ-ray emission is not expected to deviate from the pulsed phase profile seen at lower γ-ray energies, the significances of excess γ-ray events in the EGRET range (c.f. Figure 6.8) were calculated from the lightcurves constructed within each optimisation band. Excesses inside the EGRET range were calculated using the methodology described in section 6.4.5. In order to comprehensively search the data for evidence of periodicity at low energies, the lightcurves in the <750 d.c *size* domain were cumulatively summed and examined for periodic emission. In a similar manner integral lightcurves for *size* lower bounds of 550, 650, 750, 1000 and 2000 d.c. were examined for periodicity at high energies. Significance values (in σ) of excess γ-ray events inside the EGRET range for the individual, cumulatively summed, and integral *size* ranges, after appropriate re-optimised Supercuts analysis, are presented in table 7.6. Figure 7.11 presents a histogram of this data, indicating no evidence for non-statistical excesses within the pulsed phase region observed by EGRET.

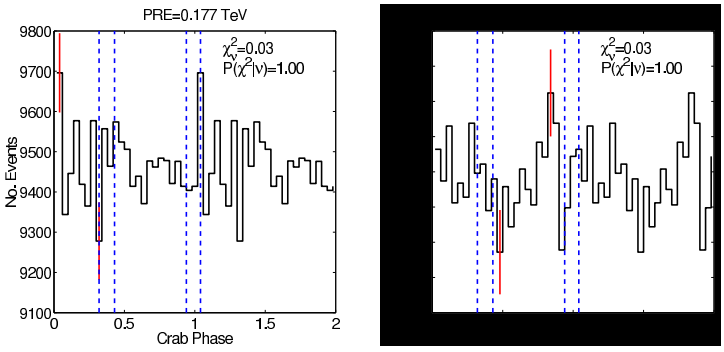

(a) 150–250 d.c.

(b) 250–350 d.c.

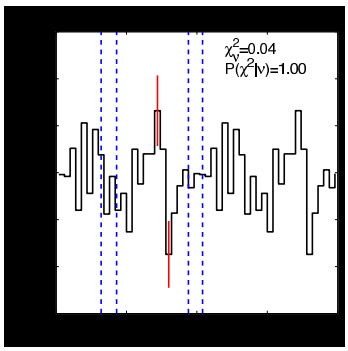

(c) 350–450 d.c.

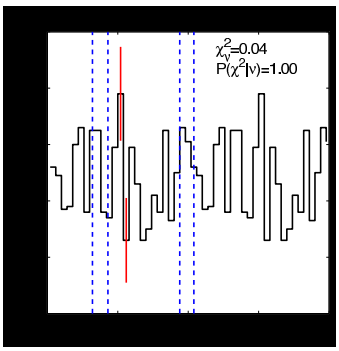

(d) 450–550 d.c.

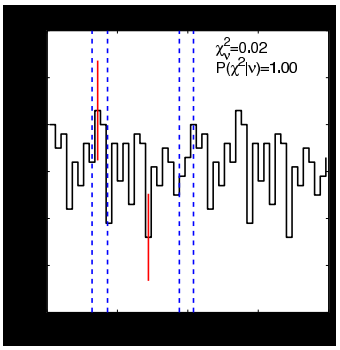

(e) 550–650 d.c.

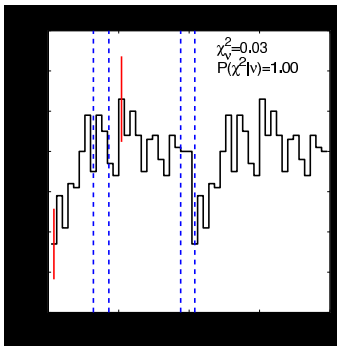

(f) 650–750 d.c.

Figure 7.9: Lightcurves of those candidate γ-ray events (derived from all elevation bands) which pass the the first six re-optimised Supercuts criteria. The χ^2 probability for each is consistent with a flat distribution. Dashed lines depict the EGRET main and intrapulse phase ranges. There is no evidence for pulsed γ-ray emission.

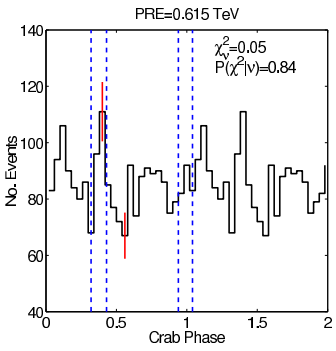

(a) 750–1000 d.c.

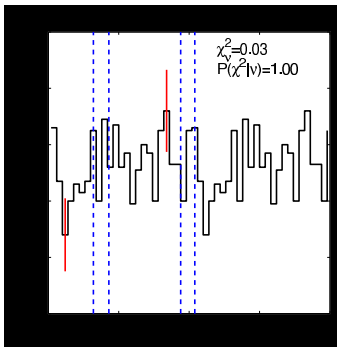

(b) 1000–2000 d.c.

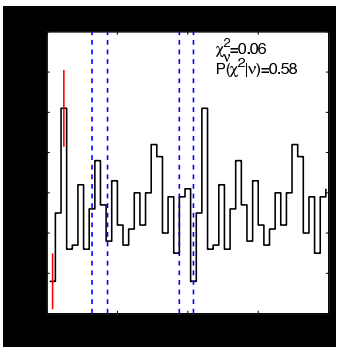

(c) >2000 d.c.

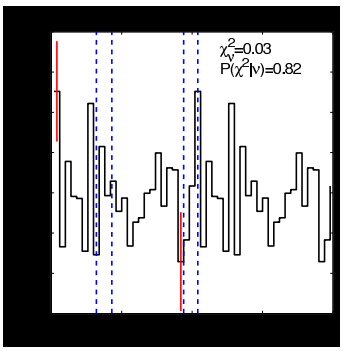

(d) Aggregate *size*.

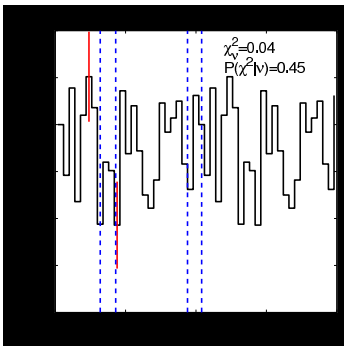

(e) Supercuts 2000

Figure 7.10: Lightcurves consisting of the phases of those candidate γ-ray events (derived from all elevation bands) which pass the the last three re-optimised Supercuts criteria, the combined aggregate *size* band, and the Supercuts 2000 criteria. There is no evidence for pulsed γ-ray emission.

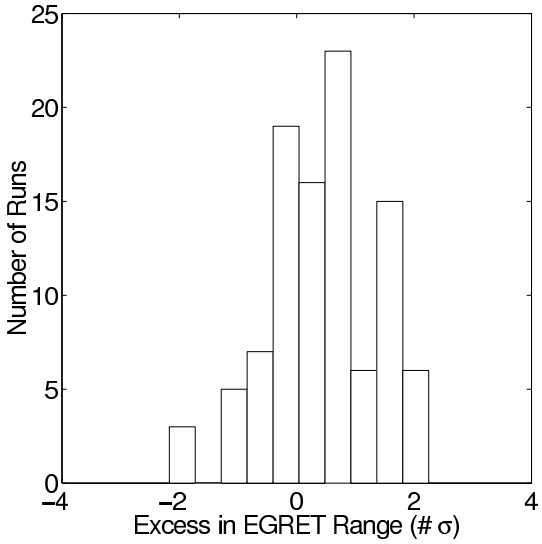

Figure 7.11: Histogram of significance values for excess γ-ray events in the EGRET phase range, listed in table 7.6.

Integral Upper Limits for Pulsed Emission

As described above, no evidence for pulsed γ-ray emission from the Crab pulsar was found in the phases of those Čerenkov events which passed the re-optimised Supercuts analyses. Accordingly, integral flux upper limits for pulsed emission were estimated. The 99.9% confidence level integral flux upper limits, calculated using the upper limit estimation methodology of Helene (1983) (section 6.4.5) are listed in table 7.7, together with all relevant parameters used in their estimation. Of note is the flux upper limit derived for the lowest PRE (0.160 TeV); it is used in section 7.5 in an attempt to constrain pulsar emission models. Figure 7.12 presents a scatter plot of these values as a percentage of the Crab DC flux versus PRE, for all independent and combined optimisation bands.

Table 7.7: Breakdown of the results used in the calculation of integral flux upper limits for the re-optimised Supercuts analysis, by elevation and *size* band.

Size Band (d.c.)	**PRE (TeV)**	$\mathbf{N_{ON}}$	$\mathbf{N_{OFF}}$	$\mathbf{N_{u.l.}}$ **99.9% (Helene)**	$\mathbf{A_{eff}}$ **(cm^2)** $\times 10^7$	$\mathbf{Flux_{u.l.}}$ **(cm^{-2}s^{-1})** $\times$ **10** $^{-13}$	$\mathbf{Flux_{u.l.}}$ **(% DC)**
			35° → 50°				
150-250	0.400 ± 0.07	3091	11780	175.98	7.73 0.86	326.6	18.54
250-350	0.550 ± 0.10	5510	20599	300.08	19.35 ± 2.00	222.7	20.70
350-450	0.771 ± 0.15	1165	4430	116.67	18.87 ± 2.38	88.8	16.71
450-550	0.844 ± 0.15	261	978	60.49	11.83 ± 1.79	73.4	18.11

Table 7.7: Breakdown of the results used in the calculation of integral flux upper limits for the re-optimised Supercuts analysis, by elevation and *size* band.

Size Band (d.c.)	**PRE (TeV)**	$\mathbf{N_{ON}}$	$\mathbf{N_{OFF}}$	$\mathbf{N_{u.l.}}$ **99.9% (Helene)**	$\mathbf{A_{eff}}$ **(cm^2)** $\times 10^7$	$\mathbf{Flux_{u.l.}}$ **(cm^{-2}s^{-1})** $\times$ **10** $^{-13}$	$\mathbf{Flux_{u.l.}}$ **(% DC)**
550-650	0.876 ± 0.18	65	201	39.32	5.82 ± 1.15	97.0	28.09
650-750	1.288 ± 0.27	98	468	22.26	9.52 ± 2.07	33.6	11.42
750-1000	1.287 ± 0.27	27	102	19.15	9.17 ± 1.93	30.0	25.20
1000-2000	2.077 ± 0.39	427	1527	93.74	54.69 ± 10.70	24.6	22.37
>2000	3.114 ± 0.57	34	121	22.92	86.88 ± 20.77	3.8	22.25
Aggregate *size*	0.537 ± 0.10	10678	40206	371.10	62.42 ± 5.88	85.3	8.50
S. Cuts 2000	0.875 ± 0.18	2330	9326	97.23	95.93 ± 11.53	14.5	7.63
			51° → 60°				
150-250	0.308 ± 0.06	6	28	8.24	0.005 ± 0.003	32881.4	48.47
250-350	0.211 ± 0.04	4	20	6.70	0.023 ± 0.015	5753.5	37.22
350-450	0.493 ± 0.10	1868	6958	173.91	9.14 ± 1.30	371.8	18.82
450-550	0.487 ± 0.09	119	351	62.77	3.87 ± 0.62	317.0	30.18
550-650	0.623 ± 0.12	118	471	35.21	8.09 ± 1.41	85.1	14.03
650-750	0.706 ± 0.12	65	239	30.91	7.14 ± 1.38	84.5	15.46
750-1000	0.896 ± 0.18	64	220	33.87	16.25 ± 2.93	40.7	16.68
1000-2000	1.344 ± 0.27	99	370	37.28	55.10 ± 9.76	13.2	11.23
>2000	2.149 ± 0.39	55	185	31.96	69.27 ± 16.20	9.0	16.31
Aggregate *size*	0.559 ± 0.10	2398	8842	219.92	52.28 ± 5.63	82.2	9.36
S. Cuts 2000	0.658 ± 0.12	1814	6781	165.96	78.40 ± 8.70	41.4	7.77
			61° → 70°				
150-250	0.228 ± 0.04	6988	26115	343.81	15.03 ± 1.77	384.8	24.18
250-350	0.293 ± 0.06	2810	10421	227.75	11.02 ± 1.25	347.7	20.19
350-450	0.349 ± 0.07	893	3277	128.08	4.87 ± 0.63	442.7	18.84
450-550	0.506 ± 0.10	118	557	23.94	3.27 ± 0.54	123.1	11.08
550-650	0.502 ± 0.10	112	475	30.05	5.48 ± 0.72	92.2	10.51
650-750	0.545 ± 0.10	65	268	25.65	5.14 ± 0.75	83.9	12.39
750-1000	0.673 ± 0.12	125	402	56.64	11.70 ± 1.53	81.4	15.60
1000-2000	0.948 ± 0.18	139	410	70.05	29.24 ± 3.92	40.3	16.68
>2000	1.759 ± 0.32	77	298	30.88	57.23 ± 11.07	9.1	9.56
Aggregate *size*	0.257 ± 0.05	11327	42222	475.62	50.65 ± 4.80	157.9	9.43
S. Cuts 2000	0.493 ± 0.10	2055	7523	213.71	51.61 ± 4.66	69.6	7.93
			71° → 80°				
150-250	0.160 ± 0.03	40031	148448	1245.29	16.27 ± 1.97	570.17	24.12
250-350	0.241 ± 0.05	11094	41784	375.72	13.42 ± 1.59	208.57	16.18
350-450	0.304 ± 0.06	3107	11928	161.98	4.55 ± 1.31	265.28	9.85
450-550	0.375 ± 0.07	825	3002	128.29	4.95 ± 0.66	192.87	13.13
550-650	0.381 ± 0.07	271	831	106.12	3.02 ± 0.46	261.31	17.78
650-750	0.482 ± 0.09	276	995	70.61	5.34 ± 0.81	98.44	11.14
750-1000	0.586 ± 0.10	273	929	83.25	10.38 ± 1.33	59.73	10.65
1000-2000	0.819 ± 0.15	367	1476	54.21	30.29 ± 3.93	13.33	4.11
>2000	1.470 ± 0.27	183	705	46.83	49.08 ± 9.16	7.11	6.52
Aggregate *size*	0.199 ± 0.04	56427	210098	1376.54	54.61 ± 5.35	187.74	9.72
S. Cuts 2000	0.389 ± 0.07	4280	16043	252.60	32.24 ± 2.85	58.36	4.04

Table 7.7: Breakdown of the results used in the calculation of integral flux upper limits for the re-optimised Supercuts analysis, by elevation and *size* band.

Size Band (d.c.)	**PRE (TeV)**	N_{ON}	N_{OFF}	$N_{u.l.}$ **99.9% (Helene)**	A_{eff} (cm^2) $\times 10^7$	**Flux**$_{u.l.}$ ($cm^{-2}s^{-1}$) $\times$ **10** $^{-13}$	**Flux**$_{u.l.}$ **(% DC)**
Combined elevations							
150-250	0.177 ± 0.03	50116	186371	1327.82	10.93 ± 1.67	386.21	17.58
250-350	0.259 ± 0.05	19418	72824	555.77	10.03 ± 1.73	176.09	11.30
350-450	0.326 ± 0.06	7033	26594	281.18	4.35 ± 0.97	205.49	7.12
450-550	0.385 ± 0.07	1323	4888	153.28	3.50 ± 0.90	139.31	8.83
550-650	0.397 ± 0.07	566	1978	122.58	2.82 ± 0.88	138.13	9.62
650-750	0.511 ± 0.10	504	1971	69.17	4.43 ± 1.39	49.68	5.60
750-1000	0.615 ± 0.12	489	1652	125.86	8.58 ± 2.30	46.66	8.84
1000-2000	0.872 ± 0.18	1032	3783	140.14	26.45 ± 6.45	16.84	5.63
>2000	1.606 ± 0.32	349	1309	69.82	47.24 ± 15.32	4.70	5.21
Aggregate *size*	0.209 ± 0.04	80830	301369	1667.93	39.41 ± 4.76	134.53	6.44
S. Cuts 2000	0.517 ± 0.10	10479	39672	327.22	51.69 ± 7.31	20.13	2.65

7.2.3 Search for Episodic Emission

To search for possible short time scale pulsed emission from the Crab pulsar, lightcurves of all individual Crab data runs, rendered by each of the re-optimised Supercuts analyses, were examined for non-statistical behaviour and excess emission within the EGRET phase range. Although previous reports of TeV-scale pulsed emission from the Crab pulsar (section 2.9) claim evidence for episodic emission on time scales of several minutes, no evidence for such emission was found in this work. The distribution of statistical significance of excess γ-ray events in the EGRET range, and the distribution of reduced χ^2 values for a flat distribution, for the lowest energy *size* range (0.177 TeV, 150–250 d.c), encompassing the complete dataset of Crab runs over all elevation bands, are presented in Figure 7.13. Both distributions resemble the statistical expectation for zero excess, generated using lightcurve simulations (section 6.4.6).

7.3 Results of the Kernel-based Analysis

7.3.1 DC Analysis

The Kernel multivariate analysis technique, described in detail in section 5.12, was used as an alternative to Supercuts, for the selection of candidate Crab plerion γ-ray events prior to periodicity analysis. This was motivated by a desire to uncover a set of small γ-ray images. The "standard" Kernel

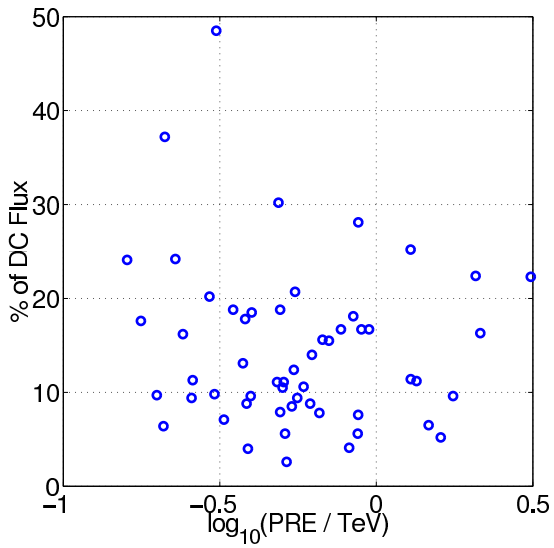

Figure 7.12: Integral flux upper limit values for pulsed γ-ray emission from the Crab pulsar as a percentage of the Crab DC flux, estimated using the Supercuts-based analysis, versus corresponding PRE.

analysis, in the context of this work, was taken to mean the $\log(R)$ cut derived by optimising for maximum γ-ray significance over all *size* values above 150 d.c. Previous workers (for example Dunlea et al. 2001) obtained their standard $\log(R)$ cuts by optimising on a subset of Crab plerion data for all *size* values. In this work, however, it was found that optimising the standard selection cut on data with a lower *size* bound of 150 d.c. (i.e. above the tiny *size* regime dominated by OFF-source data) improved the overall significance result.

Optimisation Strategy The banded optimisation strategy employed in the Supercuts re-optimisation was also utilised for the Kernel technique. For each optimisation band $\log(R)$ cuts values were determined by optimising for maximum γ-ray significance on the complete Crab plerion ON/OFF dataset within each band. Resultant optimised $\log(R)$ cuts are provided in appendix D.

γ-ray Rates and Significances γ-ray rates and $\sigma/\sqrt{hour}$ values for each independent and combined optimisation band, subsequent to application of appropriate re-optimised $\log(R)$ cuts, are listed in tables 7.8 and 7.9 respectively. The trend for these results closely resembles that of the re-optimised Supercuts work, in that the aggregate *size* rate for each elevation band rep-

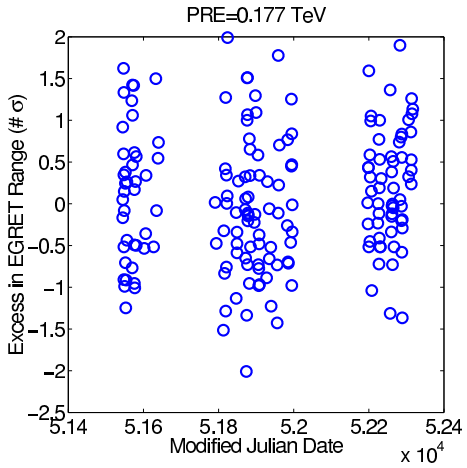

(a) σ as function of run date.

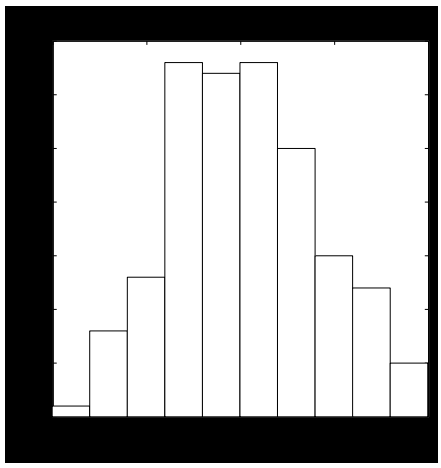

(b) Histogram of σ.

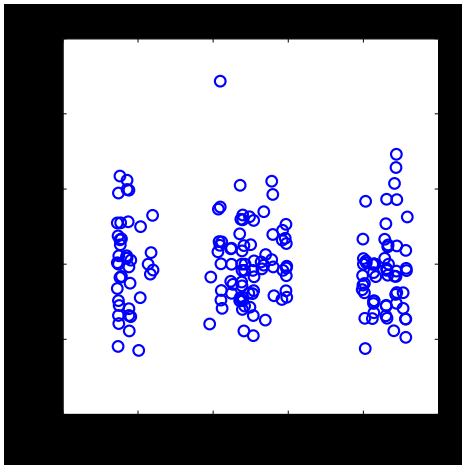

(c) Reduced χ^2 as function of run date.

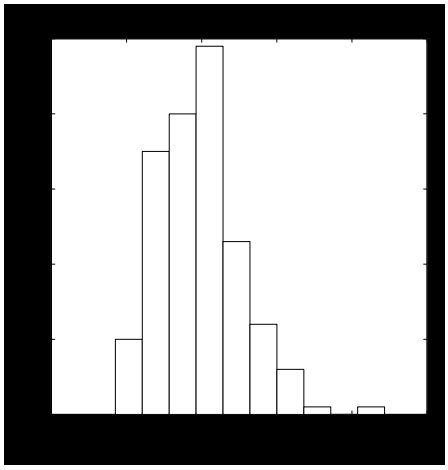

(d) Reduced χ^2 histogram.

Figure 7.13: The distribution of statistical significance of excess γ-ray events in the EGRET range, and the distribution of reduced χ^2 values for a flat distribution, for data files analysed with the re-optimised Supercuts analysis in the 150–250 d.c *size* range.

Size Range (d.c.)	Elevation Bands (degrees) 35-50	51-50	61-70	71-80	Combined Elevations
150-250	0.44 ± 0.11	1.38 ± 0.39	2.32 ± 0.42	2.27 ± 0.28	1.73 ± 0.16
250-350	0.26 ± 0.05	0.30 ± 0.11	2.52 ± 0.38	1.23 ± 0.19	1.10 ± 0.11
350-450	1.07 ± 0.20	0.32 ± 0.06	0.63 ± 0.08	0.47 ± 0.06	0.61 ± 0.05
450-550	0.12 ± 0.02	0.64 ± 0.08	0.66 ± 0.07	0.32 ± 0.03	0.39 ± 0.02
550-650	0.16 ± 0.03	0.24 ± 0.03	0.34 ± 0.03	0.29 ± 0.02	0.26 ± 0.01
650-750	0.09 ± 0.01	0.27 ± 0.03	0.29 ± 0.03	0.29 ± 0.02	0.24 ± 0.01
750-1000	0.10 ± 0.01	0.30 ± 0.03	0.50 ± 0.04	0.57 ± 0.03	0.41 ± 0.01
1000-2000	0.10 ± 0.01	0.51 ± 0.03	0.66 ± 0.04	0.75 ± 0.03	0.55 ± 0.01
>2000	0.10 ± 0.01	0.37 ± 0.03	0.43 ± 0.03	0.46 ± 0.02	0.36 ± 0.01
Aggregate *size*	2.44 ± 0.24	4.33 ± 0.42	8.35 ± 0.58	6.65 ± 0.35	5.66 ± 0.20
Standard	0.56 ± 0.04	0.97 ± 0.04	1.26 ± 0.05	1.31 ± 0.03	1.08 ± 0.02

Table 7.8: Breakdown of γ-ray rates (γ-rays per minute) for the optimised Kernel analyses, by elevation and *size* band. Standard Kernel results for *size* $>$ 150 d.c. are also shown.

Size Range (d.c.)	Elevation Bands (degrees) 35-50	51-50	61-70	71-80	Combined Elevations
150-250	0.97	0.97	1.41	1.36	1.20
250-350	1.13	0.72	1.69	1.11	1.11
350-450	1.25	1.37	2.12	1.31	1.24
450-550	1.45	2.21	2.27	2.01	1.92
550-650	1.42	2.10	2.64	2.56	2.25
650-750	1.45	2.44	2.41	2.53	2.29
750-1000	1.70	2.78	3.56	3.50	3.07
1000-2000	1.97	4.20	4.67	4.86	4.23
>2000	1.93	3.79	4.01	3.99	3.60
Aggregate *size*	2.42	2.80	3.66	3.21	3.06
Standard	3.39	5.99	6.99	6.92	6.06

Table 7.9: Breakdown of significance per $\sqrt{hour}$ for the optimised Kernel analyses by elevation and *size* band. Standard Kernel results for *size* $>$ 150 d.c. are also shown.

resents a substantial improvement on the rate obtained by standard analysis, without serious compromise of statistical significance. Figure 7.14 presents a plot of the Kernel rates and $\sigma/\sqrt{hour}$ values obtained for each *size* range when all elevation bands were combined.

Detector Response

Collection Areas and PREs The collection area curves for optimised Kernel analyses were derived in the manner used to obtain the corresponding re-optimised Supercuts curves. In this case, however, an independent set of γ-ray simulations was employed (section 5.5). As for the Supercuts work, the Kernel collection areas were restricted by effective energy ceilings, imposed by the strict *size* ranges used in the optimisation process.

PRE values determined for the Kernel analysis in each of the independent and combined optimisation bands are listed in table 7.10. Again, the roughly

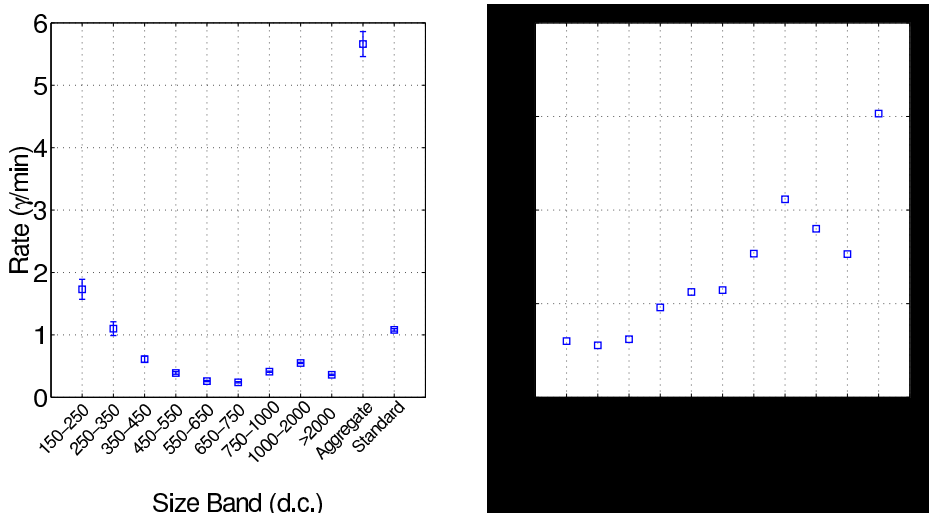

(a) γ-ray rates. **(b)** $\sigma/\sqrt{hour}$.

Figure 7.14: Kernel γ-ray rates and $\sigma/\sqrt{hour}$ values, calculated for each *size* range after results from all elevation bands were combined.

linear *size*–energy relationship is bourne out by these results (Figure 7.15). With reference to table 7.4, it is evident that the PREs independently derived by the Kernel and Supercuts techniques, for the same optimisation bands, are in good agreement.

Differential Response Curve – Scaling The simulated γ-ray rate for a flux collector is obtained by summing the area under its differential response curve. The simulated rate should match the observed rate, assuming correct modeling of the detector and equal treatment of the real and simulated data by the γ-ray selection technique (section 5.15.2). For the Supercuts results described earlier the simulated and experimental rates were in excellent agreement. In the case of the Kernel analysis results, however, despite utilising independent EAS simulations for γ-ray selection and collection area analyses, the simulated and experimentally observed rates did not match so well. In general, the simulated rates exceeded their experimentally measured values. Figure 7.16 presents a plot of the differences between the simulated and measured Kernel rates, for each *size* range after all elevation bands were combined.

The clear difference between the simulated and experimentally measured rates was considered a serious problem for the application of the Kernel anal-

Size Range (d.c.)	Elevation Bands (degrees) 35-50	51-50	61-70	71-80	Combined Elevations
150-250	0.377 ± 0.07	0.266 ± 0.05	0.205 ± 0.04	0.165 ± 0.03	0.198 ± 0.04
250-350	0.555 ± 0.10	0.386 ± 0.07	0.259 ± 0.05	0.224 ± 0.04	0.234 ± 0.05
350-450	0.661 ± 0.12	0.464 ± 0.09	0.365 ± 0.07	0.311 ± 0.06	0.320 ± 0.06
450-550	0.940 ± 0.18	0.606 ± 0.12	0.407 ± 0.09	0.368 ± 0.07	0.383 ± 0.07
550-650	0.878 ± 0.18	0.612 ± 0.12	0.466 ± 0.09	0.433 ± 0.09	0.458 ± 0.09
650-750	1.129 ± 0.22	0.665 ± 0.12	0.593 ± 0.12	0.491 ± 0.10	0.543 ± 0.10
750-1000	1.255 ± 0.22	0.926 ± 0.18	0.765 ± 0.15	0.627 ± 0.12	0.637 ± 0.12
1000-2000	1.969 ± 0.39	1.362 ± 0.27	0.958 ± 0.18	0.803 ± 0.15	0.849 ± 0.15
>2000	3.528 ± 0.69	2.461 ± 0.47	1.809 ± 0.32	1.470 ± 0.27	1.507 ± 0.27
Aggregate *size*	0.405 ± 0.09	0.275 ± 0.05	0.229 ± 0.05	0.210 ± 0.04	0.218 ± 0.04
Standard	1.095 ± 0.22	0.670 ± 0.12	0.577 ± 0.10	0.529 ± 0.10	0.578 ± 0.10

Table 7.10: Breakdown of Peak Response Energies (in TeV) for the optimised Kernel analyses by elevation and *size* band. Standard Kernel results for *size* > 150 d.c. are also shown.

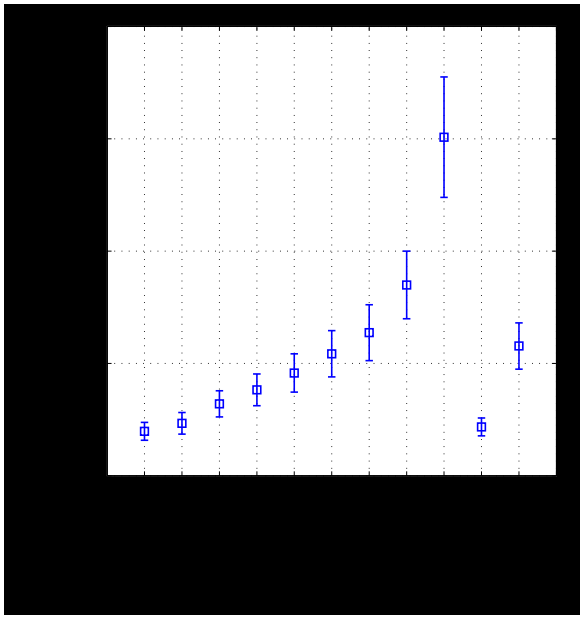

Figure 7.15: Kernel analysis PRE values, evaluated for each *size* range after all elevation bands were combined (the rightmost column of table 7.10).

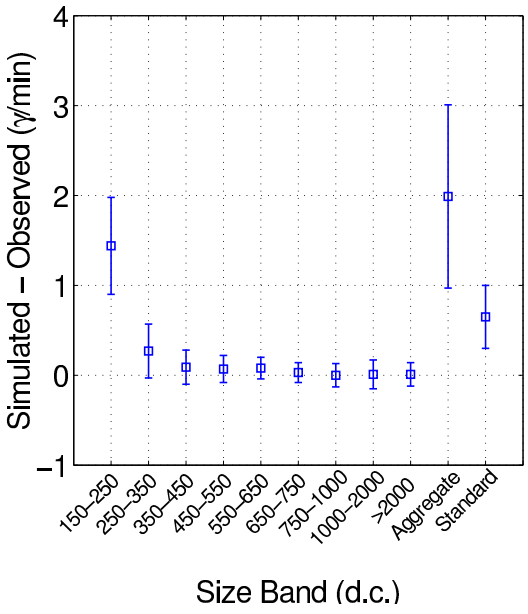

Figure 7.16: Differences between simulated and observed γ-ray rates for the Kernel analysis technique, for each *size* range after all elevation bands were combined.

ysis to the estimation of flux upper limits for pulsed emission (section 5.15.2); a higher than expected area under the differential response curve results in an increased effective area, with ultimate manifestation as an artificially low flux upper limit. Hence, it was considered prudent in this work to scale the Kernel analysis differential response curves to provide for a rate equal to the observed value (section 5.15.2), prior to calculating flux upper limits.

Effective Areas Effective area values evaluated for each optimisation band, using the appropriate Kernel collection areas and scaled differential response curves, are listed in table 7.11. A plot of the effective areas, for all elevation bands combined, as a function of *size* range is provided in Figure 7.17. The results here match reasonably well with those obtained independently for the Supercuts technique, and, thus, indicate the integrity of scaling each differential response curve according to the observed γ-ray rate.

7.3.2 Periodicity Analysis

Lightcurves Lightcurves generated using the phases of those Čerenkov events, from all elevation bands, that passed the optimised Kernel selection analyses are presented in Figures 7.18 and 7.19, for each of the nine indepen-

Size Range (d.c.)	Elevation Bands (degrees) 35-50	51-50	61-70	71-80	Combined Elevations
150-250	4.56 ± 1.16	14.85 ± 3.46	16.83 ± 3.33	11.85 ± 2.66	11.95 ± 3.61
250-350	6.21 ± 1.15	3.28 ± 1.18	26.05 ± 2.52	10.25 ± 1.89	9.76 ± 2.50
350-450	18.88 ± 2.41	5.26 ± 1.26	6.10 ± 1.05	3.15 ± 0.76	4.29 ± 1.27
450-550	7.83 ± 2.42	18.25 ± 2.27	8.14 ± 1.28	3.15 ± 0.74	4.19 ± 1.60
550-650	12.68 ± 2.25	6.98 ± 1.85	5.62 ± 1.21	4.08 ± 0.86	4.14 ± 1.93
650-750	12.83 ± 2.58	9.27 ± 1.81	7.94 ± 1.72	5.37 ± 1.03	5.48 ± 2.41
750-1000	22.44 ± 4.15	19.06 ± 4.23	19.96 ± 3.75	17.43 ± 2.38	12.92 ± 4.16
1000-2000	22.20 ± 12.28	62.49 ± 12.18	44.47 ± 7.28	36.79 ± 4.65	29.90 ± 8.73
>2000	57.40 ± 31.54	117.51 ± 26.47	83.39 ± 18.85	63.84 ± 11.67	52.03 ± 19.59
Aggregate *size*	29.79 ± 3.70	49.11 ± 7.16	71.91 ± 7.83	50.07 ± 7.34	45.08 ± 7.99
Standard	47.59 ± 16.26	33.72 ± 7.86	32.62 ± 6.00	28.33 ± 4.69	27.99 ± 9.23

Table 7.11: Breakdown of effective collection areas ($\times 10^7$ cm^{-2}s^{-1}) for the optimised Kernel analyses, by elevation and *size* band. Standard Kernel results for *size* $>$ 150 d.c. are also shown.

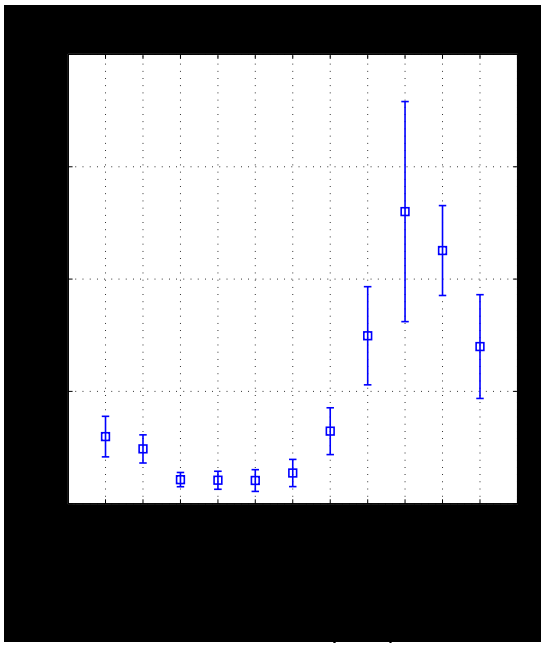

Figure 7.17: Effective collection area derived for the optimised Kernel analysis technique (after appropriate differential response curve scaling) for each *size* range, after all elevation bands were combined (the rightmost column of table 7.11).

Size Range (d.c.)	Elevation Bands (degrees) 35-50	51-50	61-70	71-80	Combined Elevations
150-250	0.16	-0.53	-0.23	1.32	0.70
250-350	-0.49	-0.14	-0.23	-1.03	-0.98
350-450	-1.58	0.90	-0.63	-1.37	-1.93
450-550	-0.20	0.80	-1.58	2.04	0.55
550-650	-0.02	0.16	-0.85	1.56	0.68
650-750	-0.13	-0.24	1.66	0.97	1.37
750-1000	-0.51	-0.02	1.30	1.02	1.30
1000-2000	-0.65	1.04	0.92	-0.24	0.54
>2000	1.04	-0.89	0.73	-0.63	-0.22
Aggregate *size*	-1.41	-0.20	-0.35	0.64	-0.14
Standard	0.62	-0.27	1.80	1.76	2.21
150-350	-0.08	-0.55	-0.32	0.53	0.02
150-450	-1.40	-0.40	-0.41	0.28	-0.50
150-550	-1.41	-0.23	-0.61	0.46	-0.43
150-650	-1.41	-0.21	-0.67	0.56	-0.38
150-750	-1.41	-0.23	-0.56	0.62	-0.29
>550	-0.10	0.12	1.71	1.12	1.67
>650	-0.12	0.06	2.29	0.57	1.52
>750	-0.06	0.20	1.72	0.19	1.03
>1000	0.32	0.25	1.17	-0.57	0.29

Table 7.12: Significance values of excess γ-ray events inside the EGRET range for the individual, cumulatively summed, and integral *size* ranges, after optimised Kernel analyses.

dent *size* ranges, for the aggregate *size* range, and for data analysed using the standard $\log(R)$ cuts. Reduced χ^2 sums for flat distributions and associated probabilities (including trials) are presented with each lightcurve. Although several lightcurves, when examined at a glance (particularly those of the 250–350 d.c. *size* range and the standard kernel analysis), are suggestive of peaked profiles, statistical examination provides no evidence, in this data, for any pulsed γ-ray emission at the Crab pulsar radio period.

EGRET range The significance of excess Kernel-selected γ-ray events inside the phase range for which EGRET observed pulsed γ-ray emission was calculated for each independent and each combined optimisation band. As in case of the re-optimised Supercuts results, Kernel lightcuves were cumulatively summed at low energies (*size* < 750 d.c.) and integrally summed at high energies (*size* > 500 d.c.), in order to facilitate a comprehensive search for periodic emission. Results of this work are presented in tabular form in table 7.12 and as a histogram in Figure 7.20. Again no evidence is indicated for any TeV-scale pulsed emission from the Crab pulsar.

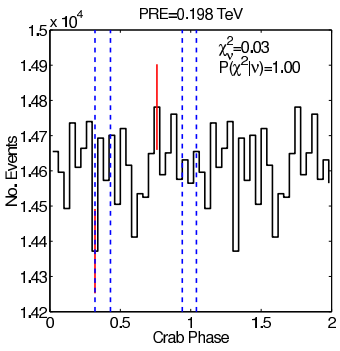

(a) 150–250 d.c.

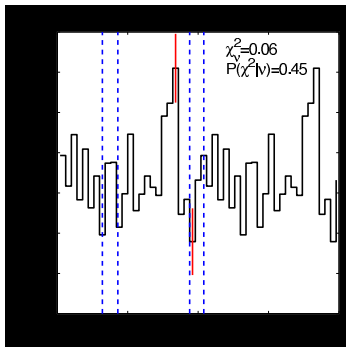

(b) 250–350 d.c.

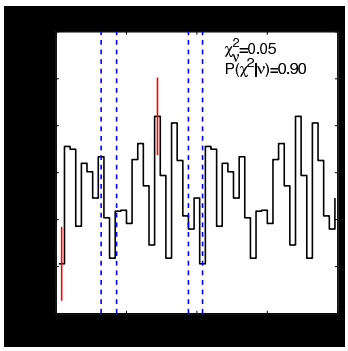

(c) 350–450 d.c.

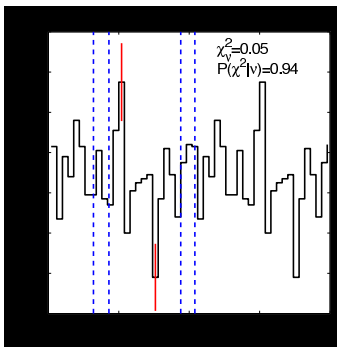

(d) 450–550 d.c.

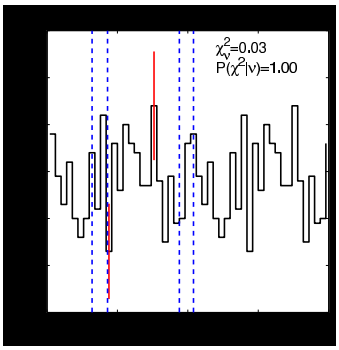

(e) 550–650 d.c.

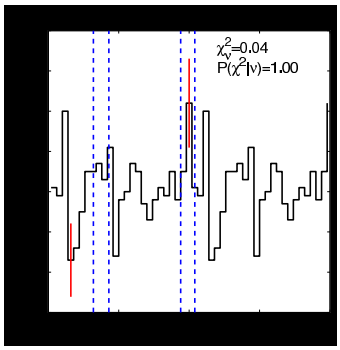

(f) 650–750 d.c.

Figure 7.18: Lightcurves of those candidate γ-ray events (derived from all elevation bands) which pass the appropriate *size* band optimised Kernel $\log(R)$ cuts. The χ^2 probability for each is consistent with a flat distribution. Dashed lines depict the EGRET main and intrapulse phase ranges. There is no evidence for pulsed γ-ray emission.

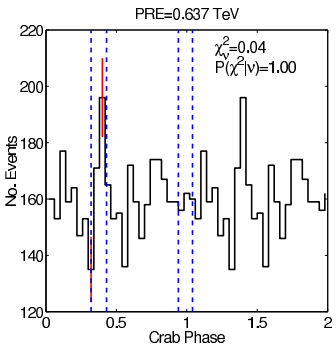

(a) 750–1000 d.c.

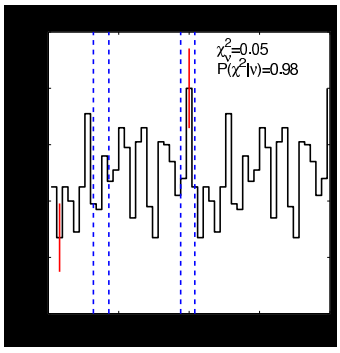

(b) 1000–2000 d.c.

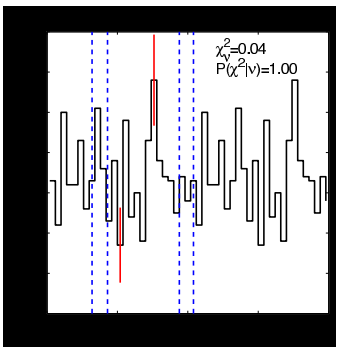

(c) >2000 d.c.

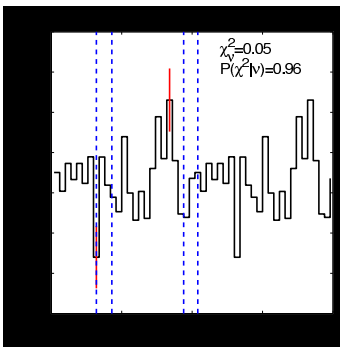

(d) Aggregate *size*.

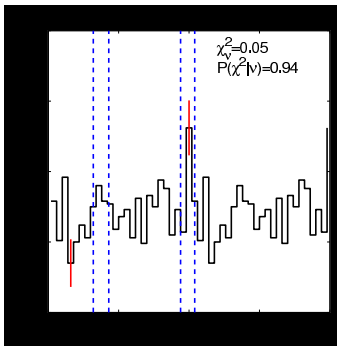

(e) Standard Kernel

Figure 7.19: Lightcurves consisting of the phases of those candidate γ-ray events (derived from all elevation bands) which pass the optimised $\log(R)$ cuts for Kernel analysis in the final three *size* bands, the aggregate *size* band, and the Standard Kernel $\log(R)$ cut. There is no evidence for pulsed γ-ray emission.

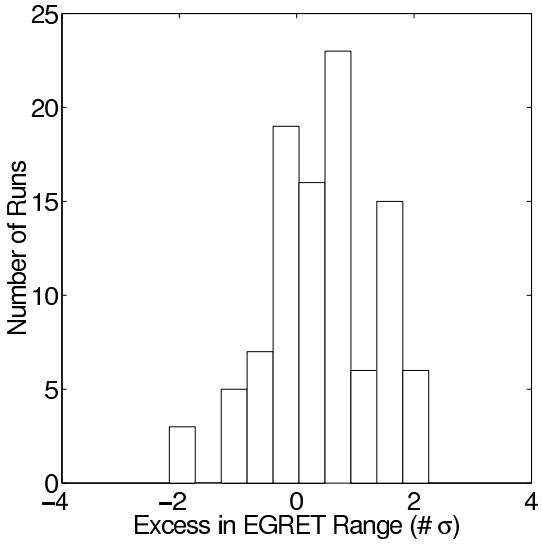

Figure 7.20: Histogram of the significance values, for excess Kernel-selected γ-ray events in the EGRET phase range, as listed in table 7.12.

Integral Flux Upper Limits for Pulsed Emission

Integral flux upper limits for pulsed γ-ray emission were calculated for each of the Kernel optimisation bands. Again the methodology of Helene (1983) was employed, at the 99.9% confidence level. Resulting flux upper limits are listed in table 7.13, together with all relevant parameters used in their estimation. Figure 7.21 presents a scatter plot of these values, as a percentage of the corresponding Crab DC flux, versus PRE.

Table 7.13: Breakdown of the results used in the calculation of integral flux upper limits for the optimised Kernel analysis, by elevation and *size* band.

Size Band (d.c.)	**PRE (TeV)**	N_{ON}	N_{OFF}	$N_{u.l.}$ **99.9% (Helene)**	A_{eff} (cm^2) $\times 10^7$	**Flux**$_{u.l.}$ ($cm^{-2}s^{-1}$) $\times$ **10** $^{-13}$	**Flux**$_{u.l.}$ **(% DC)**
			35° → 50°				
150-250	0.377 ± 0.07	1453	5431	147.84	4.56 ± 1.16	497.1	31.1
250-350	0.555 ± 0.10	370	1442	61.73	6.21 ± 1.15	152.4	22.2
350-450	0.661 ± 0.12	5018	19469	166.15	18.88 ± 2.41	135.0	14.3
450-550	0.940 ± 0.18	63	245	27.86	7.83 ± 2.42	54.6	20.8
550-650	0.878 ± 0.18	111	418	38.88	12.68 ± 2.25	47.0	21.7
650-750	1.129 ± 0.22	37	143	21.80	12.83 ± 2.58	26.1	22.0
750-1000	1.255 ± 0.22	32	136	18.22	22.44 ± 4.15	12.5	16.7
1000-2000	1.969 ± 0.39	25	112	15.51	22.20 ± 12.28	10.7	14.4
>2000	3.528 ± 0.69	35	101	28.41	57.40 ± 31.54	7.6	26.8
Aggregate *size*	0.405 ± 0.09	7144	27498	207.99	29.79 ± 3.70	107.1	7.9
Standard	1.095 ± 0.22	264	940	71.51	47.59 ± 16.26	23.0	11.7
			51° → 60°				

Table 7.13: Breakdown of the results used in the calculation of integral flux upper limits for the optimised Kernel analysis, by elevation and *size* band.

Size Band (d.c.)	**PRE (TeV)**	$\mathbf{N_{ON}}$	$\mathbf{N_{OFF}}$	$\mathbf{N_{u.l.}}$ **99.9% (Helene)**	$\mathbf{A_{eff}}$ **(cm^2)** $\times 10^7$	$\mathbf{Flux_{u.l.}}$ **(cm^{-2}s^{-1})** $\times$ **10** $^{-13}$	$\mathbf{Flux_{u.l.}}$ **(% DC)**
150-250	0.266 ± 0.05	10474	39671	324.00	14.85 ± 3.46	447.7	28.9
250-350	0.386 ± 0.07	929	3516	108.28	3.28 ± 1.18	678.4	44.2
350-450	0.464 ± 0.09	319	1116	84.68	5.26 ± 1.26	330.7	32.9
450-550	0.606 ± 0.12	505	1804	104.21	18.25 ± 2.27	117.2	20.1
550-650	0.612 ± 0.12	89	327	36.45	6.98 ± 1.85	107.2	18.9
650-750	0.665 ± 0.12	85	332	31.80	9.27 ± 1.81	70.4	14.3
750-1000	0.926 ± 0.18	87	328	34.36	19.06 ± 4.23	37.0	14.0
1000-2000	1.362 ± 0.27	131	431	56.03	62.49 ± 12.18	18.4	13.6
>2000	2.461 ± 0.47	73	317	24.50	117.51 ± 26.47	4.3	8.1
Aggregate *size*	0.275 ± 0.05	12692	47842	393.12	49.11 ± 7.16	164.3	11.2
Standard	0.670 ± 0.12	212	818	49.91	33.72 ± 7.86	30.4	6.3
			61° → 70°				
150-250	0.205 ± 0.04	16221	61144	441.07	16.83 ± 3.33	471.0	20.5
250-350	0.259 ± 0.05	13273	50048	398.40	26.05 ± 2.52	274.9	17.0
350-450	0.365 ± 0.07	572	2231	73.78	6.10 ± 1.05	217.3	12.5
450-550	0.407 ± 0.09	521	2156	53.69	8.14 ± 1.28	118.5	8.7
550-650	0.466 ± 0.09	120	502	31.81	5.62 ± 1.21	101.7	10.1
650-750	0.593 ± 0.12	132	400	64.82	7.94 ± 1.72	146.6	24.4
750-1000	0.765 ± 0.15	185	605	70.99	19.96 ± 3.75	63.9	15.2
1000-2000	0.958 ± 0.18	195	667	66.33	44.47 ± 7.28	26.8	10.8
>2000	1.809 ± 0.32	116	395	48.73	83.39 ± 18.85	10.5	12.3
Aggregate *size*	0.229 ± 0.05	31335	118148	591.08	71.91 ± 7.83	147.7	7.6
Standard	0.577 ± 0.10	350	1143	110.24	32.62 ± 6.00	60.7	9.4
			71° → 80°				
150-250	0.165 ± 0.03	38539	143533	1050.50	11.85 ± 2.66	698.4	21.8
250-350	0.224 ± 0.04	16618	63190	352.99	10.25 ± 1.89	271.3	13.6
350-450	0.311 ± 0.06	1769	6962	104.64	3.15 ± 0.76	261.7	10.5
450-550	0.368 ± 0.07	461	1508	133.61	3.15 ± 0.74	334.3	19.7
550-650	0.433 ± 0.09	264	862	90.60	4.08 ± 0.86	174.8	14.8
650-750	0.491 ± 0.10	261	900	77.97	5.37 ± 1.03	114.4	12.7
750-1000	0.627 ± 0.12	505	1779	110.28	17.43 ± 2.38	49.9	9.2
1000-2000	0.803 ± 0.15	480	1833	75.62	36.79 ± 4.65	16.2	4.8
>2000	1.470 ± 0.27	267	1059	50.48	63.84 ± 11.67	6.2	5.2
Aggregate *size*	0.210 ± 0.04	59164	221627	1085.01	50.07 ± 7.34	170.7	7.7
Standard	0.529 ± 0.10	824	2835	169.06	28.33 ± 4.69	47.0	6.1
			Combined elevations				
150-250	0.198 ± 0.04	66687	249780	1171.58	11.95 ± 3.61	330.6	13.7
250-350	0.234 ± 0.05	31190	118196	490.22	9.76 ± 2.50	169.3	9.0
350-450	0.320 ± 0.06	7678	29778	187.15	4.29 ± 1.27	147.0	6.2
450-550	0.383 ± 0.07	1550	5714	170.60	4.19 ± 1.60	137.5	8.8
550-650	0.458 ± 0.09	584	2110	108.28	4.14 ± 1.93	88.3	8.3
650-750	0.543 ± 0.10	515	1775	121.48	5.48 ± 2.41	74.8	10.1
750-1000	0.637 ± 0.12	809	2848	150.29	12.92 ± 4.16	39.2	7.4
1000-2000	0.849 ± 0.15	831	3043	124.39	29.90 ± 8.73	14.0	4.6
>2000	1.507 ± 0.27	491	1872	76.99	52.03 ± 19.59	5.0	4.3
Aggregate *size*	0.218 ± 0.04	110335	415115	1178.23	45.08 ± 7.99	88.1	4.2
Standard	0.578 ± 0.10	1650	5736	264.62	27.99 ± 9.23	31.9	5.0

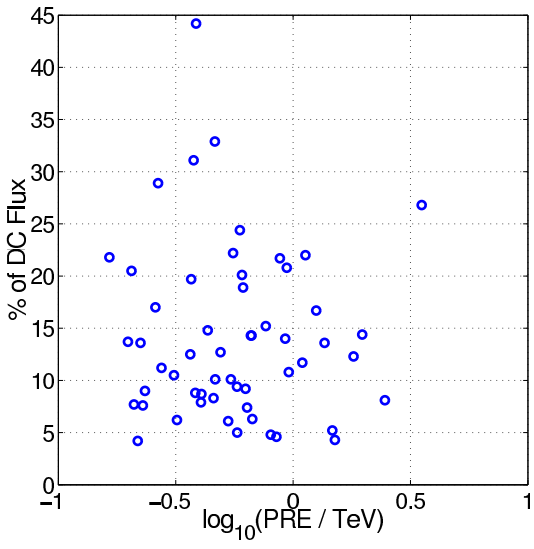

Figure 7.21: Integral flux upper limit values for pulsed γ-ray emission from the Crab pulsar, estimated using the Kernel-based analysis, versus corresponding PRE.

7.3.3 Search for Episodic Emission

Results of the Kernel analysis were also examined on a run-by-run basis to search for evidence of episodic pulsed emission from the Crab pulsar. As was the case for the Supercuts analysis, no evidence for any episodic emission within the EGRET phase range or any non-statistical behaviour is reported here. The distribution of excess γ-ray events in the EGRET range for the lowest energy optimisation band after all elevations were combined (0.198 TeV, *size* 150–250 d.c.) is presented in Figure 7.22, together with the corresponding distribution of reduced χ^2 values.

7.3.4 Kernel Analysis of Tiny Events

As detailed in section 5.13.1, the Kernel analysis was considered appropriate for the selection of tiny events (*size* $<$ 150 d.c.) for use in a periodicity analysis. Although the significance of these events, calculated in an ON/OFF analysis, is negative, their utilisation in the present work was considered valuable due to their very low energies. Accordingly, since ON/OFF analysis is unreliable these events are examined for periodicity at the Crab pulsar radio period but flux upper limits and DC γ-ray rates and significances are

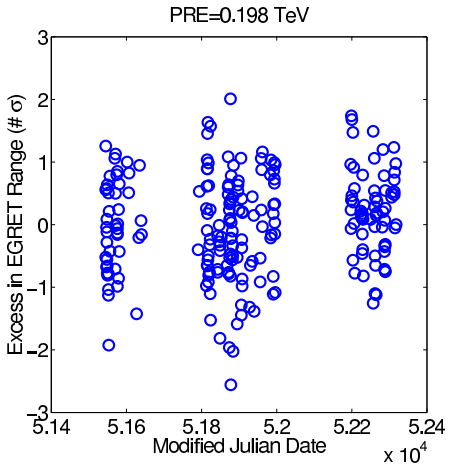

(a) σ as function of run date.

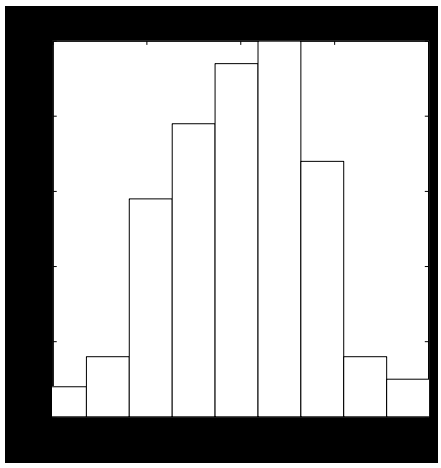

(b) Histogram of σ.

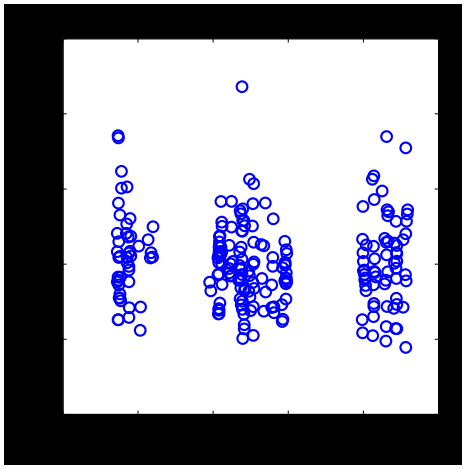

(c) Reduced χ^2 as function of run date.

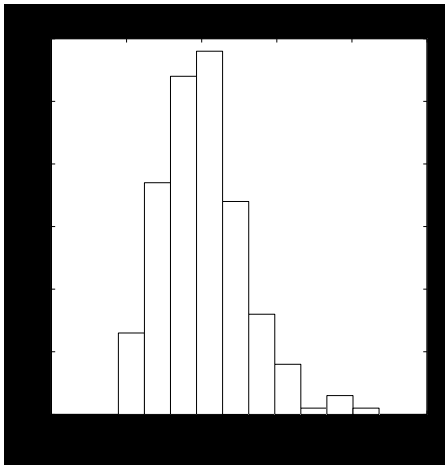

(d) Reduced χ^2 histogram.

Figure 7.22: The distribution of statistical significance of excess γ-ray events in the EGRET range, and the distribution of reduced χ^2 values for a flat distribution, for data files analysed with the optimised Kernel analysis in the 150–250 d.c *size* range.

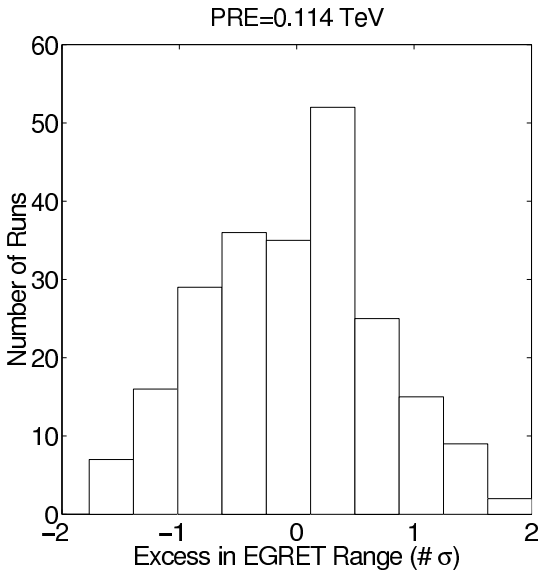

Figure 7.23: The distribution of statistical significance of excess γ-ray events in the EGRET range for tiny *size* (<150 d.c) which passed the Kernel analysis.

not determined[3]. The PRE for the 0–150 d.c. *size* regime was estimated, from simulations, to be 0.114 $\pm$ 0.02 TeV when all elevation bands were combined. PREs for each individual elevation band are listed in table 7.14. These energies represent the lowest energy regime yet explored using by the Whipple telescope and are very significant in the potential they indicate for future work using the IACT. Further discussion on this topic is provided in section 7.6.2 below.

Lightcurves generated using Kernel-selected tiny events, for each of the four independent elevation bands and for all elevation bands combined are presented in Figure 7.24. No evidence for any pulsed emission from the Crab pulsar is proffered by these results. Figure 7.23 presents the corresponding distribution of γ-ray excesses, determined from the the complete dataset on a run-by-run basis. Again there is no suggestion in these results of any evidence for episodic pulsed emission from the Crab pulsar.

[3]Although ON/OFF analysis is not normally required to estimate flux upper limits, it was considered necessary in the case of the Kernel analysis in order to scale the appropriate differential response curve to provide for the correct γ-ray rate, prior to calculating effective areas.

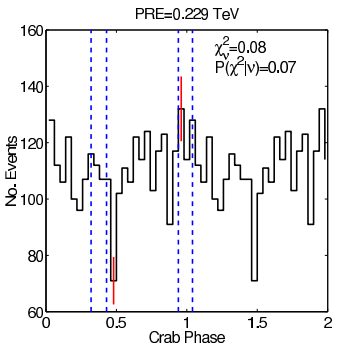

(a) $35° \rightarrow 50°$.

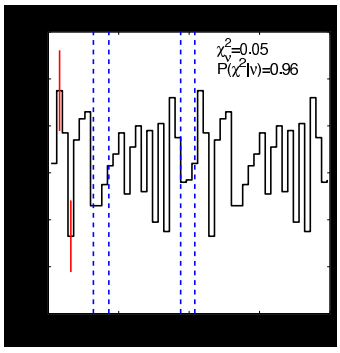

(b) $51° \rightarrow 60°$.

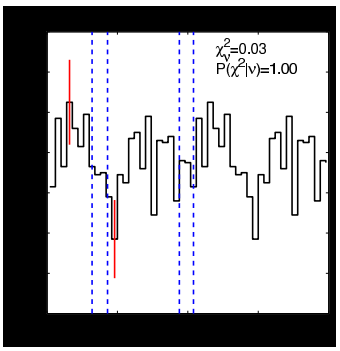

(c) $61° \rightarrow 70°$.

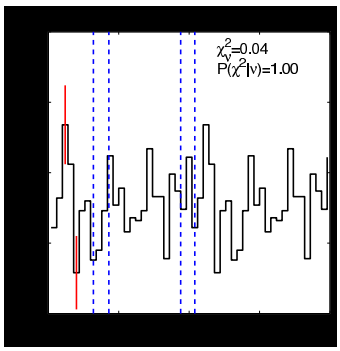

(d) $71° \rightarrow 80°$.

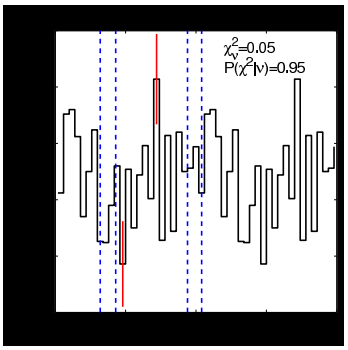

(e) All elevations combined.

Figure 7.24: Lightcurves consisting of the phases of tiny events (*size* < 150 d.c) which passed the Kernel analysis, for each of the four elevation bands used in this work and for all elevation bands combined. There is no evidence for pulsed γ-ray emission.

Elevation Degrees	PRE (TeV)
35–50	0.229 ± 0.05
51–60	0.138 ± 0.03
61–70	0.119 ± 0.02
71–80	0.106 ± 0.02
Combined	0.114 ± 0.02

Table 7.14: List of peak response energies for the tiny *size* < 150 d.c. regime, after Kernel analysis (optimised for *size* > 150 d.c.). Errors quoted are statistical only.

7.4 Summary of Periodic Analysis Results

Two independent selection mechanisms, Supercuts and the Kernel analysis, were used to search for pulsed TeV-scale γ-ray emission from the Crab pulsar. Both analyses were optimised in discrete elevation and *size* bands. γ-ray events selected within each band were analysed for periodic emission and individual optimisation bands were merged to provide results for all elevations combined and for aggregate *size*. The optimisation strategy was considered successful in that it allowed for an analysis of low energy γ-ray events heretofore below the ambit of the IACT.

Neither analysis methodology proffered results suggesting any statistically significant evidence for pulsed very high energy emission from the Crab pulsar. Accordingly, flux upper limits for pulsed emission were estimated, based on the γ-ray pulsed phase profile observed by EGRET.

A search for episodic emission on a time scale of ∼28 minutes was conducted by examining individual data runs, after Supercuts and Kernel analysis, for evidence of non-statistical behaviour or enhanced emission within the EGRET phase range. Contrary to several previous claims for evidence of episodic emission, made before the realisation of the IACT, and in-line with the majority of results reported since its realisation, no evidence for pulsed episodic emission from the Crab pulsar is reported here.

7.5 Interpretation of Results

The EGRET instrument has detected pulsed γ-ray emission from the Crab pulsar up to ∼10 GeV, and has determined a photon spectral index of -2.15 within the energy range 50 MeV to 10 GeV (Nolan et al., 1993). Ground-based γ-ray telescopes have not, thus far, convincingly observed pulsed emis-

sion from the Crab or any other pulsar. Since ground-based instruments generally operate in the energy range above ∼100 GeV, the Crab pulsar's pulsed emission cut-off must lie somewhere in the 10 GeV to 100 GeV region.

Two main models have been proposed to describe γ-ray emission from the EGRET-observed pulsars; the polar cap and outer gap models. Both models predict pulsed emission cut-offs within the 10–100 GeV regime. The polar cap model, by virtue of its assumption that particle acceleration and γ-ray production occur near the neutron star surface, predicts a super-exponential cut-off at just a few GeV, due to pair-production by high-energy γ-rays in the strong magnetic field close to the stellar surface. The outer gap model avoids this magnetic-field induced pair-production scenario by providing for γ-ray generation in vacuum gaps far out in the neutron star's magnetosphere. As such, the pulsed emission cut-offs predicted by outer gap models are generally more gradual than those for polar cap models. Moreover, modern outer gap models predict very low levels of pulsed emission at energies of ∼1 TeV (section 2.7.5). A clear detection of pulsed or unpulsed emission in the gap between 10 GeV and 100 GeV would, therefore, settle the model issue.

In the present work integral flux upper limits were determined for banded Crab plerion data at a variety of energies (tables 7.7 and 7.13). Although the Kernel analysis technique used in this work provided for sensitivity down as far as ∼100 GeV, no flux upper limits were determinable in this energy-regime due to the problem of sky-noise (see section 5.13.2). Future work will attempt to address and resolve the systematics which prevail in this difficult energy range. A search for pulsed emission was nevertheless conducted but yielded no evidence for excess γ-ray emission within the pulsed phase profile observed by EGRET.

In order to discriminate in favour of one pulsar emission model or the other, either a definitive pulsed detection or low level flux upper limits in the 10–100 GeV regime are required. Although the present results cannot provide either, they nonetheless offer the possibility of constraining the emission models. The methodology used by Lessard et al. (2000) to constrain the pulsed emission cut-off is followed here.

A function of the form

$$\frac{dN}{dE} = KE^{-\gamma}e^{-\frac{E}{E_0}} \tag{7.1}$$

is used to model the Crab's pulsed γ-ray spectrum, where E is the photon energy, γ is the photon spectral index, and E_0 is the cutoff energy. Since the source is well fitted in the EGRET energy range by a power law with a photon spectral index of -2.15 $\pm$ 0.04, equation 7.1 may be used to extrapo-

late the EGRET spectrum to the energies observed in this work. The most constraining of the low energy flux upper limits (i.e. the flux upper limit for aggregate *size* Supercuts selected data, 0.209 ± 0.04 TeV) estimated in the present work can be used to constrain the extrapolation. When applied, this mechanism yields a cut-off energy of $E_0 \leq 63$ GeV; marginally higher than that the 60 GeV cut-off estimated by Lessard et al. (2000).

Figure 7.25 presents the two most constraining upper limits of the present work (the results derived in the 150–250 d.c and aggregate *size* bands of the Supercuts analysis) in the context of the efforts of previous workers. It is clear that the upper limit at 60 GeV, recently reported by the CELESTE group de Naurois et al. (2002), remains the most constraining upper limit available. However, it should be noted that the CELESTE upper limit is not directly comparable to the present work or to the other efforts due to the methodology employed in its calculation. In their work, de Naurois et al. (2002) employed a narrow detector acceptance, produced by folding into their simulated acceptance the broken power law EGRET spectrum reported by Fierro et al. (1998), attenuated by an exponential cut-off. In the present work it was considered adequate to utilise the simple power law spectrum of Nolan et al. (1993) as the broken power-law of Fierro et al. (1998) refers to emission at all phase values, whereas the Nolan et al. spectrum refers exclusively to the pulsed component. Indeed, the phase resolved study of Fierro et al. reports a spectrum very similar to that of Nolan et al. The robustness of using the steady Crab spectrum in evaluating the detector response was demonstrated by Lessard et al. (2000). Therefore its use is not considered unreasonable in this work.

Several key requirements are identified as critical for future pulsar observations with imaging atmospheric Čerenkov telescopes (see section 7.6.2 below). One requirement is the development of dedicated "pulsar cuts" to select low-energy γ-ray events for temporal analyses. These cuts should provide sensitivity below 50 GeV for the next generation of ground-based γ-ray detectors, albeit with an inescapable loss in collection area above 50 GeV (de Jager, 2002). The banded re-optimisations of the Supercuts and Kernel techniques used in the present work may be regarded as pulsar cuts for the present Whipple 10 m telescope—they provide sensitivity in a low energy regime at the expense of collection area at high energies. As such, they demonstrate the potential of dedicated pulsar cuts for reducing the energy threshold of an imaging telescope. The lowest energy threshold achieved for flux upper limit calculations in this work was 0.16 ± 0.03 TeV; clearly well above the predicted Crab pulsar spectral cut-off. Nevertheless, this represents the lowest energy at which the Whipple telescope has, thus far, provided meaningful γ-ray data. The VERITAS array, if equipped with a "pulsar trig-

ger" (see section 7.6.2 below) and used in conjunction with band-optimised pulsar cuts, should yield significant γ-ray sensitivity in the energy regime below $\sim$50 GeV, due to the noise rejection power of stereoscopic observations.

Of perhaps even greater importance to future ground-based pulsar observations, this work demonstrates the sensitivity of the Kernel analysis technique to γ-ray events with energies in the 100 GeV to 200 GeV energy domain (table 7.14). With the improved background noise rejection to be provided by stereoscopic imaging and with detailed Čerenkov pulse information offered by flash ADCs, it is reasonable to expect the Kernel technique to allow VERITAS operate with good sensitivity in the energy regime below $\sim$50 GeV. This being so, the potential for observing or seriously constraining the pulsed γ-ray emission cut-offs of the Crab and other pulsars is greatly improved. Of course, further refinement of the Kernel technique is required, particularly in the area of ON/OFF analysis for sky-regions with different noise levels. Nevertheless, the Kernel analysis should be enlisted as a serious tool for future γ-ray selection in pulsar observations.

7.6 Future Work – Closing the Gap

The outlook for γ-ray pulsar observations is excellent. With the next generation of satellite and Čerenkov telescopes coming online, the gap in the γ-ray spectrum between 10 GeV and 100 GeV will soon close. Ultimately the launch of GLAST in 2007 will finally and conclusively close the gap. In the meantime, however, a number of experiments have the potential to shed light on pulsar spectral cut-offs by extending their sensitivities into the gap. In particular the GRID instrument onboard AGILE, the third generation of imaging Čerenkov detectors, and the existing solar arrays, all have something to offer. A brief overview of possible future pulsar observations is provided here.

7.6.1 Satellite Detectors

AGILE The Italian-sponsored AGILE satellite is due for launch in 2003 and will carry three detectors GRID, MC and Super-AGILE (section 1.2.1). The GRID detector, with a dynamic energy range extending from 30 MeV to 50 GeV, will provide data of interest regarding high-energy pulsars. GRID is anticipated to have an on-axis sensitivity for point sources comparable to EGRET, with an expected factor of two improvement in angular resolution. Although AGILE is not expected to have a major impact on the search for pulsed spectral cut-offs, due to its very limited energy resolution, whatever

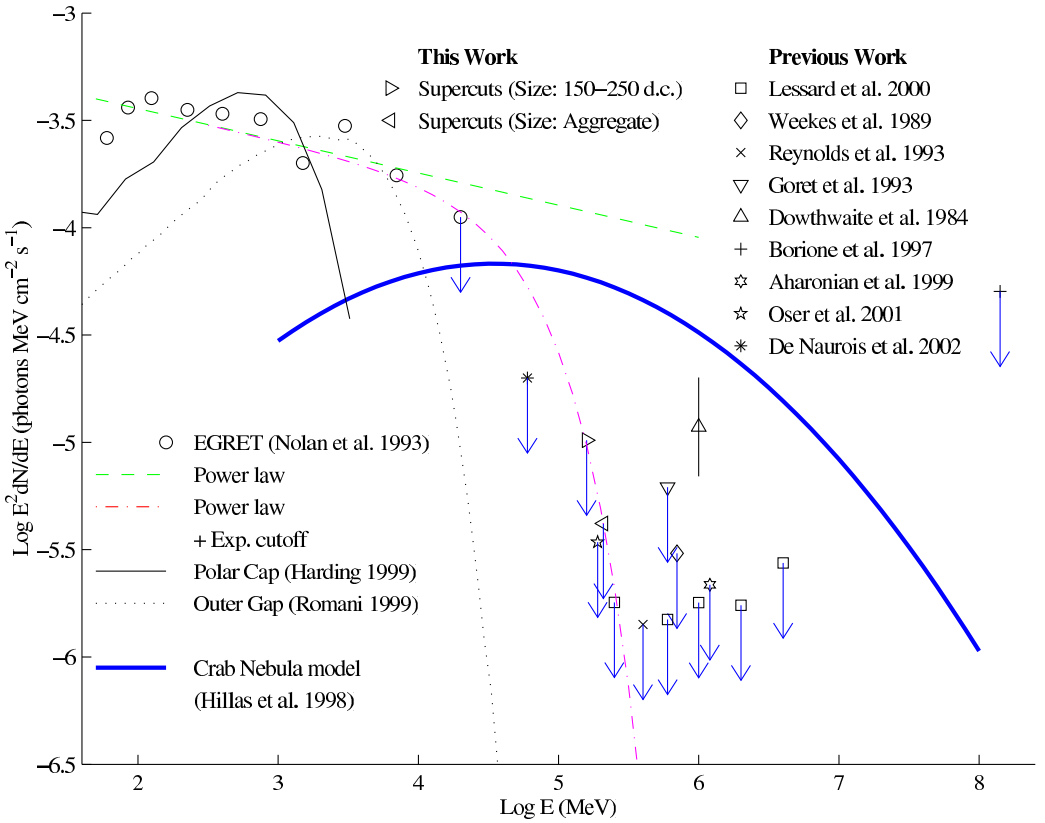

Figure 7.25: Pulsed photon spectrum of the Crab pulsar. Based on Lessard et al. (2000), and updated to include this and other recent work (the Aharonian et al. 1999 data point shown here is slightly shifted to the right of its 1 TeV position for clarity). The most constraining upper limits derived by the present work are shown as right and left pointing triangles. Although these upper limits were derived at energies below the previous lowest point reported by the Whipple collaboration Lessard et al. (2000), they do not impose any stricter constraint on the emission models. *Note: the STACEE upper limit is shown in the position calculated from the data provided in the publication of Oser et al. (2001). The representation of this point in the publication of de Naurois et al. (2002) appears at odds with the present calculations.*

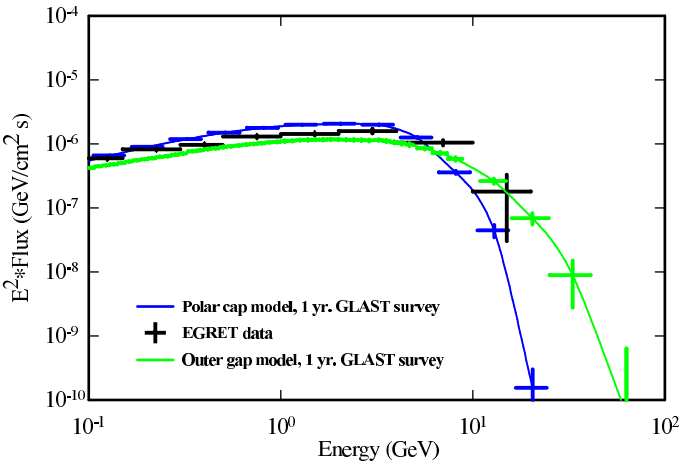

Figure 7.26: The projected sensitivity of GLAST to the modeled polar cap and outer gap spectra of Vela. Figure from: http://cossc.gsfc.nasa.gov/images/epo/gallery/pulsars/

high-energy pulsar observations it can provide will, nonetheless, be examined with great interest.

GLAST GLAST, when launched in 2007 will improve on the angular and energy resolution of AGILE and is expected to provide detailed information on high-energy γ-ray pulsars. Its dynamic energy range will overlap significantly with the range of ground-based Čerenkov telescopes, extending over four decades from 20 MeV to 300 GeV. Indeed, it is anticipated that GLAST observations will definitively settle the polar cap versus outer gap model issue. The projected sensitivity of GLAST to the modeled polar cap and outer gap spectra of Vela is provided in Figure 7.26. With its improved sensitivity compared to EGRET, GLAST is also capable of undertaking more accurate phase-resolved observations of all the known γ-ray pulsars. There is little doubt that GLAST will discover tens, if not hundreds, of new γ-ray pulsars, and determine the period of a great many without recourse to X-ray or optical observations.

7.6.2 Ground-based Detectors

Excellent reviews of the potential for future pulsar observations above 1 GeV are provided by de Jager et al. (2002), Konopelko (2002) and de Jager et al. (2001). In order to observe the pulsed γ-ray emission cut-offs expected for

Problem	Solution
Increased night-sky background noise	Extraneous photons from the night-sky background may be reduced through the use of stereoscopic array triggering and signal digitisation with flash ADCs (or equivalent).
Problematic γ/hadron discrimination	Stereoscopic imaging and signal digitisation can help overcome the problems caused by poorer image reconstruction in the low-energy regime.
Contamination from local muons	Stereoscopic imaging or improved analysis techniques (for example the Kernel analysis) are required.
Cosmic ray electron background	Cannot be eliminated—ON/OFF analysis is necessary.
Increased detector deadtime due to high trigger rates	A multi-level trigger scheme can keep trigger rates and deadtime at acceptable levels.

Table 7.15: List of potential problems and solutions presented by lowering a Čerenkov detector's energy threshold.

the EGRET pulsars, the energy thresholds of current Čerenkov detectors must be significantly lowered. Reducing the energy threshold is a non-trivial task and presents a number of problems. In general, though, solutions are available either in hardware or software. Table 7.15 presents a number of anticipated problems with possible solutions.

In general, three main types of ground-based instrument offer potential for high-energy pulsar observations; large single telescope's such as MAGIC, telescope arrays of the VERITAS/H.E.S.S. type, and solar array detectors such as STACEE and CELESTE. The merits of each are discussed below.

Single Large Telescopes Single large telescopes such as MAGIC will operate with much lower energy thresholds than current single telescopes, due mainly to their larger mirror collection areas, but also as a result of innovative techniques and new technologies incorporated into their designs. The low energy threshold ($\sim$30 GeV initially, and later $\sim$12 GeV for MAGIC) is of great importance for pulsar observations and should allow positive detections of pulsed γ-rays from the EGRET pulsars. At such low energies, however, background noise rejection is a serious issue, particularly in the absence of stereoscopic imaging.

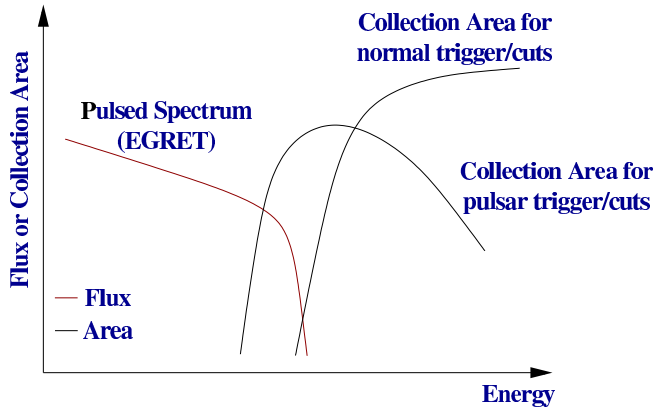

Figure 7.27: The type of collection area envisaged by de Jager (2002) when a pulsar trigger and pulsar cuts are utilised by an atmospheric Čerenkov telescope. Such a strategy provides maximum sensitivity to the tail-end of pulsed emission from EGRET pulsars at the expense of collection area at higher energies. From de Jager (2002).

Telescope Arrays Arrays of Čerenkov telescopes, such as VERITAS and H.E.S.S., offer improved background rejection through stereoscopic imaging. However, these instruments have difficulty extending their sensitivities below $\sim$50 GeV for pulsar observations without the use of a dedicated pulsar trigger and pulsar cuts. de Jager et al. (2001) discuss the concept of a topological trigger used in non-imaging mode with the H.E.S.S array, for detecting γ-ray pulsars, and claim such a trigger can accept low energy γ-rays while still rejecting >99% of the background. This trigger and associated pulsar cuts would sacrifice sensitivity at higher energies above 50 GeV in favour of maximising sensitivity to low energy events. In the context of dedicated TeV pulsar searching, this is a sacrifice worth making.

The banded optimisations used in the present work represent a form of pulsar cuts, for the Whipple 10 m telescope, and demonstrate the usefulness of such a strategy in lowering a Čerenkov detector's energy threshold. Figure 7.27 presents a graphical representation of the pulsar cuts concept. It is useful, in this context, to refer back to Figure 7.5, which shows the how the collection area for the 350–450 d.c. *size* band of the re-optimised Supercuts analysis was maximised at low energies, at the expense of sensitivity at higher energies.

Solar Array Detectors At present the best chance for detecting pulsed γ-ray emission using a ground-based technique is offered by the solar array detectors. At present four such detectors are operating; STACEE, CELESTE,

GRAAL and Solar Two. These instruments offer very large collection areas and hence low energy thresholds of 30–100 GeV. Indeed, as discussed in section 7.5, the most constraining upper limit for TeV-scale pulsed emission from the Crab pulsar is that determined by the CELESTE group (de Naurois et al., 2002) at 60 GeV. The upper limit reported by STACEE (Oser et al., 2001) is at a somewhat higher energy than the results of the present work (190 GeV), but may be reduced in future work using the full complement of 64 heliostats now available to that instrument.

In summary, the outlook for future γ-ray observations of pulsars is good. GLAST offers the most definitive solution to the polar cap versus outer gap model issue, with pre-GLAST observations using ground-based detectors, utilising dedicated pulsar triggers/cuts, offering possible pulsed detections in the meantime.

Epilogue

> Any suspicions that pulsars would be a nine-days wonder must by now have been dispelled by a glance at the diverse topics of the collected papers. It would, of course, have been encouraging to find a visible object in one of the accurately determined positions, but the chance of finding the type of the pulsating stars through their visible spectra now seems very slight. As compensation, it may become clearer that the star is one which cannot be reached optically, so that the radio pulses offer the only means of detection of an object the physical processes of which are of great interest. The theory of the internal constitution of a star which cannot only resonate at a frequency of about 1 Hz but which contains a driving mechanism to sustain such an oscillation scarcely exists. The place of the star in the evolutionary sequence, and the contribution of its mas to the general composition of the galaxy, both raise extremely interesting problems.
>
> —F. G. Smith. The Pulsating Stars, Nature Supplement 1969.

Not a nine day wonder! Hopefully in the next few years the TeV signature of pulsars will be detected and a suitable postscript will then have been written to the fascinating intellectual challenge which pulsars have proven to be over the past 35 years.

Appendix A

Definition of the Hillas Parameters

Suppose the i^{th} PMT is given coordinates x_i, y_i (in degrees) and registers a signal s_i. The origin of the coordinate system is in the centre of the array of PMTs. An ellipse is fitted to the image and the Hillas parameters are calculated relative to the arbitary point x_o, y_0. For this thesis all data is ON-source, with the Crab pulsar at the centre of the field-of-view, thus x_o and y_o are taken to be the origin..

The fitting of the ellipse employs the following simple moments:

$$\begin{aligned}
\langle x \rangle &= \frac{\Sigma s_i x_i}{\Sigma s_i}, \\
\langle y \rangle &= \frac{\Sigma s_i y_i}{\Sigma s_i}, \\
\langle x^2 \rangle &= \frac{\Sigma s_i {x_i}^2}{\Sigma s_i}, \\
\langle y^2 \rangle &= \frac{\Sigma s_i {y_i}^2}{\Sigma s_i}, \\
\langle xy \rangle &= \frac{\Sigma s_i x_i y_i}{\Sigma s_i}, \\
\langle x^3 \rangle &= \frac{\Sigma s_i {x_i}^3}{\Sigma s_i}, \\
\langle y^3 \rangle &= \frac{\Sigma s_i {y_i}^3}{\Sigma s_i}, \\
\langle x^2 y \rangle &= \frac{\Sigma s_i {x_i}^2 y_i}{\Sigma s_i}, \\
\langle x y^2 \rangle &= \frac{\Sigma s_i x_i {y_i}^2}{\Sigma s_i},
\end{aligned}$$

and

$$\begin{aligned}
\sigma_{x^2} &= \langle x^2\rangle - \langle x\rangle^2, \\
\sigma_{y^2} &= \langle y^2\rangle - \langle y\rangle^2, \\
\sigma_{xy} &= \langle xy\rangle - \langle x\rangle\langle y\rangle, \\
\sigma_{x^3} &= \langle x^3\rangle - 3\langle x\rangle\langle x^2\rangle + 2\langle x\rangle^3, \\
\sigma_{y^3} &= \langle y^3\rangle - 3\langle y\rangle^2\langle y\rangle + 2\langle y\rangle^3, \\
\sigma_{x^2y} &= \langle x^2y\rangle - 2\langle xy\rangle\langle x\rangle + 2\langle x\rangle^2\langle y\rangle - \langle x^2\rangle\langle y\rangle, \\
\sigma_{xy^2} &= \langle xy^2\rangle - 2\langle xy\rangle\langle y\rangle + 2\langle x\rangle\langle y\rangle^2 - \langle x\rangle\langle y^2\rangle.
\end{aligned}$$

Given the following definitions:

$$\begin{aligned}
k &= \sigma_{y^2} - \sigma_{x^2}, \\
l &= \sqrt{k^2 + 4\sigma_{xy}^2}, \\
m &= \langle y^2\rangle - \langle x^2\rangle, \\
n &= \sqrt{m^2 + 4\langle xy\rangle^2}, \\
u &= 1 + \frac{k}{l}, \\
v &= 2 - u,
\end{aligned}$$

the Hillas parameters are calculated from:

$$\begin{aligned}
\langle Size\rangle &= \sum s_i, \\
\langle Length\rangle^2 &= \frac{\sigma_{x^2} + \sigma_{y^2} + l}{2}, \\
\langle Width\rangle^2 &= \frac{\sigma_{x^2} + \sigma_{y^2} - l}{2}, \\
\langle Miss\rangle^2 &= \frac{u\langle x\rangle^2 + v\langle y\rangle^2}{2} - \frac{2\langle xy\rangle\sigma_{xy}}{l}, \\
\langle Distance\rangle^2 &= \langle x\rangle^2 + \langle y\rangle^2, \\
\langle Alpha\rangle &= \sin^{-1}\left(\frac{\langle Miss\rangle}{\langle Distance\rangle}\right), \\
\langle Azwidth\rangle^2 &= \frac{\langle x^2\rangle + \langle y^2\rangle - n}{2}.
\end{aligned}$$

The calculation of the parameter *Asymmetry* requires the angle, ψ, between the x-axis and the major axis of the ellipse. It is convenient to define p:

$$\begin{aligned}
\psi &= \tan^{-1}\left(\frac{(k+l)\langle y\rangle + 2\sigma_{xy}\langle x\rangle}{2\sigma_{xy}\langle y\rangle - (k-l)\langle x\rangle}\right), \\
p &= \sigma_{x^3}\cos^3\psi + 3\sigma_{x^2y}\sin\psi\cos^2\psi + 3\sigma_{xy^2}\cos\psi\sin^2\psi \\
&+ \sigma_{y^3}\sin^3\psi, \\
\langle Asymmetry\rangle^3 &= \frac{p}{\langle Length\rangle}.
\end{aligned}$$

Appendix B

The Crab Pulsar Dataset

The following data was used for the Crab pulsar analysis described in this thesis.

Table B.1: All data in the 35° → 51° elevation range.

UT Date	MJD	ON ID	OFF ID	N2 ID	t_{JPL}	f	$\dot{f}$
000109	51552	gt014321	gt014322	gt014307	0.026218	29.8457007754	-374567.92
000205	51579	gt014538		gt014529	0.01135	29.8446975585	-374545.55
000207	51581	gt014560	gt014561	gt014549	0.01135	29.8446975585	-374545.55
000228	51602	gt014646	gt014647	gt014638	0.01135	29.8446975585	-374545.55
000303	51606	gt014719	gt014720	gt014711	0.027688	29.8437591143	-374529.34
000304	51607	gt014742	gt014743	gt014732	0.027688	29.8437591143	-374529.34
000330	51633	gt014856	gt014857	gt014852	0.027688	29.8437591143	-374529.34
000401	51635	gt014889	gt014890	gt014888	0.025612	29.8427560295	-374507.21
000405	51639	gt014956	gt014957	gt014954	0.025612	29.8427560295	-374507.21
000406	51640	gt014975	gt014976	gt014973	0.025612	29.8427560295	-374507.21
000904	51791	gt015607	gt015608	gt015596	0.001922	29.8378063425	-374389.59
000907	51794	gt015624	gt015625	gt015617	0.001922	29.8378063425	-374389.59
001126	51874	gt016307	gt016308	gt016280	0.001004	29.8358332658	-374340.27
001204	51882	gt016468	gt016469	gt016457	0.022104	29.834863023	-374308.34
001217	51895	gt016528	gt016529	gt016522	0.022104	29.834863023	-374308.34
001219	51897	gt016550	gt016551	gt016545	0.022104	29.834863023	-374308.34
001228	51906	gt016746		gt016728	0.022104	29.834863023	-374308.34
001229	51907	gt016767	gt016768	gt016753	0.022104	29.834863023	-374308.34
001229	51907	gt016769	gt016770	gt016753	0.022104	29.834863023	-374308.34
001230	51908	gt016787	gt016788	gt016775	0.022104	29.834863023	-374308.34
001230	51908	gt016789	gt016796	gt016775	0.022104	29.834863023	-374308.34
001231	51909	gt016815	gt016816	gt016804	0.003678	29.8338605155	-374288.11
001231	51909	gt016817	gt016818	gt016804	0.003678	29.8338605155	-374288.11
010126	51935	gt017039	gt017040	gt017025	0.003678	29.8338605155	-374288.11
010130	51939	gt017056	gt017057	gt017048	0.003678	29.8338605155	-374288.11
010131	51940	gt017074	gt017075	gt017069	0.020124	29.8328580721	-374256.92
010216	51956	gt017160	gt017161	gt017151	0.020124	29.8328580721	-374256.92
010216	51956	gt017162	gt017163	gt017151	0.020124	29.8328580721	-374256.92
010219	51959	gt017201	gt017202	gt017192	0.020124	29.8328580721	-374256.92
010219	51959	gt017203	gt017204	gt017192	0.020124	29.8328580721	-374256.92
010220	51960	gt017225	gt017226	gt017214	0.020124	29.8328580721	-374256.92
010222	51962	gt017265	gt017266	gt017256	0.020124	29.8328580721	-374256.92
010315	51983	gt017368	gt017369	gt017361	0.017119	29.831952689	-374239.2
010316	51984	gt017381	gt017382	gt017371	0.017119	29.831952689	-374239.2
010317	51985	gt017396	gt017397	gt017388	0.017119	29.831952689	-374239.2
010318	51986	gt017414	gt017415	gt017407	0.017119	29.831952689	-374239.2

UT Date	MJD	ON ID	OFF ID	N2 ID	t_{JPL}	f	$\dot{f}$
010323	51991	gt017503		gt017500	0.017119	29.831952689	-374239.2
010324	51992	gt017524	gt017525	gt017521	0.017119	29.831952689	-374239.2
010326	51994	gt017568	gt017569	gt017565	0.017119	29.831952689	-374239.2
010326	51994	gt017570	gt017571	gt017565	0.017119	29.831952689	-374239.2
010327	51995	gt017586	gt017587	gt017585	0.017119	29.831952689	-374239.2
010327	51995	gt017588	gt017589	gt017585	0.017119	29.831952689	-374239.2
010327	51995	gt017590	gt017591	gt017585	0.017119	29.831952689	-374239.2
010328	51996	gt017605	gt017606	gt017604	0.017119	29.831952689	-374239.2
010328	51996	gt017607	gt017608	gt017604	0.017119	29.831952689	-374239.2
020114	52288	gt019159	gt019160	gt019143	0.090366	29.8220613683	-374017.76

Table B.2: All data in the $51° \rightarrow 60°$ elevation range.

UT Date	MJD	ON ID	OFF ID	N2 ID	t_{JPL}	f	$\dot{f}$
000104	51547	gt014232	gt014233	gt014219	0.026218	29.8457007754	-374567.92
000105	51548	gt014254	gt014255	gt014241	0.026218	29.8457007754	-374567.92
000106	51549	gt014276	gt014277	gt014264	0.026218	29.8457007754	-374567.92
000109	51552	gt014319	gt014320	gt014307	0.026218	29.8457007754	-374567.92
000202	51576	gt014478	gt014479	gt014471	0.01135	29.8446975585	-374545.55
000324	51627	gt014835	gt014836	gt014832	0.027688	29.8437591143	-374529.34
000926	51813	gt015739	gt015738	gt015734	0.001922	29.8378063425	-374389.59
000928	51815	gt015769	gt015770	gt015759	0.001922	29.8378063425	-374389.59
000929	51816	gt015811		gt015794	0.001922	29.8378063425	-374389.59
000930	51817	gt015833	gt015834	gt015819	0.001922	29.8378063425	-374389.59
001026	51843	gt016009		gt015994	0.020611	29.8368359484	-374379.64
001120	51868	gt016159	gt016160	gt016147	0.001004	29.8358332658	-374340.27
001124	51872	gt016239	gt016240	gt016215	0.001004	29.8358332658	-374340.27
001126	51874	gt016305	gt016306	gt016280	0.001004	29.8358332658	-374340.27
001127	51875	gt016335	gt016336	gt016325	0.001004	29.8358332658	-374340.27
001128	51876	gt016388	gt016389	gt016364	0.001004	29.8358332658	-374340.27
001129	51877	gt016413	gt016414	gt016394	0.001004	29.8358332658	-374340.27
001130	51878	gt016436	gt016437	gt016419	0.001004	29.8358332658	-374340.27
001205	51883	gt016478		gt016472	0.022104	29.834863023	-374308.34
001206	51884	gt016490	gt016491	gt016487	0.022104	29.834863023	-374308.34
001207	51885	gt016500	gt016501	gt016498	0.022104	29.834863023	-374308.34
001217	51895	gt016531	gt016530	gt016522	0.022104	29.834863023	-374308.34
001219	51897	gt016552	gt016553	gt016545	0.022104	29.834863023	-374308.34
001228	51906	gt016744	gt016745	gt016728	0.022104	29.834863023	-374308.34
001229	51907	gt016765	gt016766	gt016753	0.022104	29.834863023	-374308.34
010222	51962	gt017263	gt017264	gt017256	0.020124	29.8328580721	-374256.92
010323	51991	gt017502		gt017500	0.017119	29.831952689	-374239.2
010324	51992	gt017522	gt017523	gt017521	0.017119	29.831952689	-374239.2
010326	51994	gt017566	gt017567	gt017565	0.017119	29.831952689	-374239.2
011018	52200	gt018386	gt018387	gt018371	0.066574	29.8250347341	-374113.09
011116	52229	gt018697	gt018698	gt018677	0.060946	29.8240327562	-374078.89
011117	52230	gt018730	gt018731	gt018699	0.060946	29.8240327562	-374078.89
011118	52231	gt018757	gt018758	gt018733	0.060946	29.8240327562	-374078.89
011207	52250	gt018833	gt018834	gt018826	0.083361	29.8230631881	-374050.09
011220	52263	gt018967	gt018968	gt018958	0.083361	29.8230631881	-374050.09
011224	52267	gt019014	gt019015	gt019011	0.083361	29.8230631881	-374050.09

Table B.3: All data in the 61° → 70° elevation range.

UT Date	MJD	ON ID	OFF ID	N2 ID	t_{JPL}	f	$\dot{f}$
000102	51545	gt014204	gt014205	gt014193	0.026218	29.8457007754	-374567.92
000105	51548	gt014252	gt014253	gt014241	0.026218	29.8457007754	-374567.92
000106	51549	gt014274	gt014275	gt014264	0.026218	29.8457007754	-374567.92
000111	51554	gt014358	gt014359	gt014350	0.026218	29.8457007754	-374567.92
000113	51556	gt014382	gt014383	gt014381	0.026218	29.8457007754	-374567.92
000131	51574	gt014463	gt014464	gt014461	0.01135	29.8446975585	-374545.55
000202	51576	gt014469	gt014470	gt014471	0.01135	29.8446975585	-374545.55
000202	51576	gt014476	gt014477	gt014471	0.01135	29.8446975585	-374545.55
000205	51579	gt014527	gt014528	gt014529	0.01135	29.8446975585	-374545.55
000926	51813	gt015740	gt015741	gt015734	0.001922	29.8378063425	-374389.59
000927	51814	gt015755	gt015756	gt015744	0.001922	29.8378063425	-374389.59
000928	51815	gt015771		gt015759	0.001922	29.8378063425	-374389.59
000929	51816	gt015812		gt015794	0.001922	29.8378063425	-374389.59
000929	51816	gt015813		gt015794	0.001922	29.8378063425	-374389.59
000930	51817	gt015835		gt015819	0.001922	29.8378063425	-374389.59
001001	51818	gt015852		gt015837	0.020611	29.8368359484	-374379.64
001001	51818	gt015853	gt015854	gt015837	0.020611	29.8368359484	-374379.64
001002	51819	gt015871	gt015870	gt015858	0.020611	29.8368359484	-374379.64
001004	51821	gt015905	gt015904	gt015899	0.020611	29.8368359484	-374379.64
001006	51823	gt015932		gt015921	0.020611	29.8368359484	-374379.64
001006	51823	gt015933		gt015921	0.020611	29.8368359484	-374379.64
001007	51824	gt015943	gt015944	gt015937	0.020611	29.8368359484	-374379.64
001026	51843	gt016010		gt015994	0.020611	29.8368359484	-374379.64
001101	51849	gt016063	gt016064	gt016045	0.001004	29.8358332658	-374340.27
001123	51871	gt016209	gt016210	gt016192	0.001004	29.8358332658	-374340.27
001124	51872	gt016237	gt016238	gt016215	0.001004	29.8358332658	-374340.27
001127	51875	gt016334		gt016325	0.001004	29.8358332658	-374340.27
001129	51877	gt016411	gt016412	gt016394	0.001004	29.8358332658	-374340.27
001130	51878	gt016434	gt016435	gt016419	0.001004	29.8358332658	-374340.27
001201	51879	gt016453	gt016454	gt016440	0.022104	29.834863023	-374308.34
001204	51882	gt016466	gt016467	gt016457	0.022104	29.834863023	-374308.34
001205	51883	gt016477		gt016472	0.022104	29.834863023	-374308.34
001206	51884	gt016488	gt016489	gt016487	0.022104	29.834863023	-374308.34
001222	51900	gt016596	gt016597	gt016580	0.022104	29.834863023	-374308.34
010119	51928	gt016882	gt016883	gt016877	0.003678	29.8338605155	-374288.11
010121	51930	gt016925	gt016926	gt016915	0.003678	29.8338605155	-374288.11
010323	51991	gt017501		gt017500	0.017119	29.831952689	-374239.2
011016	52198	gt018346	gt018347	gt018331	0.066574	29.8250347341	-374113.09
011017	52199	gt018366	gt018367	gt018352	0.066574	29.8250347341	-374113.09
011115	52228	gt018668		gt018651	0.060946	29.8240327562	-374078.89
011217	52260	gt018898	gt018899	gt018883	0.083361	29.8230631881	-374050.09
011218	52261	gt018923	gt018924	gt018908	0.083361	29.8230631881	-374050.09
011220	52263	gt018965	gt018966	gt018958	0.083361	29.8230631881	-374050.09
011222	52265	gt018991	gt018992	gt018986	0.083361	29.8230631881	-374050.09
011223	52266	gt019002	gt019003	gt019001	0.083361	29.8230631881	-374050.09
020109	52283	gt019073	gt019074	gt019067	0.090366	29.8220613683	-374017.76
020112	52286	gt019106	gt019107	gt019105	0.090366	29.8220613683	-374017.76
020114	52288	gt019153	gt019154	gt019143	0.090366	29.8220613683	-374017.76
020115	52289	gt019171	gt019172	gt019167	0.090366	29.8220613683	-374017.76
020201	52306	gt019262	gt019263	gt019260	0.068878	29.8210596457	-373986.6

Table B.4: All data in the 71° → 80° elevation range.

UT Date	MJD	ON ID	OFF ID	N2 ID	t_{JPL}	f	$\dot{f}$
000102	51545	gt014200	gt014201	gt014193	0.026218	29.8457007754	-374567.92
000102	51545	gt014202	gt014203	gt014193	0.026218	29.8457007754	-374567.92
000104	51547	gt014228	gt014229	gt014219	0.026218	29.8457007754	-374567.92
000104	51547	gt014230	gt014231	gt014219	0.026218	29.8457007754	-374567.92
000105	51548	gt014248	gt014249	gt014241	0.026218	29.8457007754	-374567.92
000105	51548	gt014250	gt014251	gt014241	0.026218	29.8457007754	-374567.92
000106	51549	gt014272	gt014273	gt014264	0.026218	29.8457007754	-374567.92
000107	51550	gt014295	gt014296	gt014285	0.026218	29.8457007754	-374567.92
000109	51552	gt014315	gt014316	gt014307	0.026218	29.8457007754	-374567.92
000109	51552	gt014317	gt014318	gt014307	0.026218	29.8457007754	-374567.92
000110	51553	gt014336	gt014337	gt014330	0.026218	29.8457007754	-374567.92
000113	51556	gt014379	gt014380	gt014381	0.026218	29.8457007754	-374567.92
000126	51569	gt014407	gt014408	gt014402	0.026218	29.8457007754	-374567.92
000127	51570	gt014416	gt014417	gt014413	0.026218	29.8457007754	-374567.92
000128	51571	gt014424	gt014425	gt014421	0.026218	29.8457007754	-374567.92
000128	51571	gt014426	gt014427	gt014421	0.026218	29.8457007754	-374567.92
000128	51571	gt014428	gt014429	gt014421	0.026218	29.8457007754	-374567.92
000202	51576	gt014472	gt014473	gt014471	0.01135	29.8446975585	-374545.55
000202	51576	gt014474	gt014475	gt014471	0.01135	29.8446975585	-374545.55
000203	51577	gt014493	gt014494	gt014492	0.01135	29.8446975585	-374545.55
000207	51581	gt014555	gt014556	gt014549	0.01135	29.8446975585	-374545.55
000928	51815	gt015772		gt015759	0.001922	29.8378063425	-374389.59
000928	51815	gt015773		gt015759	0.001922	29.8378063425	-374389.59
000929	51816	gt015815	gt015816	gt015794	0.001922	29.8378063425	-374389.59
001001	51818	gt015855		gt015837	0.020611	29.8368359484	-374379.64
001002	51819	gt015873	gt015872	gt015858	0.020611	29.8368359484	-374379.64
001004	51821	gt015907	gt015906	gt015899	0.020611	29.8368359484	-374379.64
001005	51822	gt015918	gt015917	gt015908	0.020611	29.8368359484	-374379.64
001006	51823	gt015934	gt015935	gt015921	0.020611	29.8368359484	-374379.64
001007	51824	gt015945		gt015937	0.020611	29.8368359484	-374379.64
001026	51843	gt016015		gt015994	0.020611	29.8368359484	-374379.64
001030	51847	gt016040	gt016041	gt016023	0.020611	29.8368359484	-374379.64
001030	51847	gt016042	gt016043	gt016023	0.020611	29.8368359484	-374379.64
001101	51849	gt016059	gt016060	gt016045	0.001004	29.8358332658	-374340.27
001101	51849	gt016061	gt016062	gt016045	0.001004	29.8358332658	-374340.27
001105	51853	gt016091	gt016092	gt016090	0.001004	29.8358332658	-374340.27
001123	51871	gt016211	gt016212	gt016192	0.001004	29.8358332658	-374340.27
001123	51871	gt016213		gt016192	0.001004	29.8358332658	-374340.27
001124	51872	gt016235	gt016236	gt016215	0.001004	29.8358332658	-374340.27
001127	51875	gt016332	gt016333	gt016325	0.001004	29.8358332658	-374340.27
001128	51876	gt016382	gt016383	gt016364	0.001004	29.8358332658	-374340.27
001129	51877	gt016409	gt016410	gt016394	0.001004	29.8358332658	-374340.27
001130	51878	gt016432	gt016433	gt016419	0.001004	29.8358332658	-374340.27
001201	51879	gt016449	gt016450	gt016440	0.022104	29.834863023	-374308.34
001201	51879	gt016451	gt016452	gt016440	0.022104	29.834863023	-374308.34
001220	51898	gt016574	gt016575	gt016560	0.022104	29.834863023	-374308.34
001227	51905	gt016708	gt016709	gt016695	0.022104	29.834863023	-374308.34
010126	51935	gt017029	gt017030	gt017025	0.003678	29.8338605155	-374288.11
011015	52197	gt018328	gt018329	gt018313	0.066574	29.8250347341	-374113.09
011016	52198	gt018348		gt018331	0.066574	29.8250347341	-374113.09
011017	52199	gt018368	gt018369	gt018352	0.066574	29.8250347341	-374113.09
011018	52200	gt018388	gt018389	gt018371	0.066574	29.8250347341	-374113.09
011021	52203	gt018448	gt018449	gt018433	0.066574	29.8250347341	-374113.09
011021	52203	gt018450	gt018451	gt018433	0.066574	29.8250347341	-374113.09
011022	52204	gt018468	gt018469	gt018452	0.066574	29.8250347341	-374113.09
011023	52205	gt018488	gt018489	gt018475	0.066574	29.8250347341	-374113.09
011024	52206	gt018502	gt018503	gt018491	0.066574	29.8250347341	-374113.09
011025	52207	gt018517	gt018518	gt018506	0.066574	29.8250347341	-374113.09
011026	52208	gt018526	gt018527	gt018520	0.066574	29.8250347341	-374113.09

UT Date	MJD	ON ID	OFF ID	N2 ID	t_{JPL}	f	$\dot{f}$
011111	52224	gt018584	gt018585	gt018569	0.060946	29.8240327562	-374078.89
011112	52225	gt018603	gt018604	gt018587	0.060946	29.8240327562	-374078.89
011114	52227	gt018642	gt018643	gt018630	0.060946	29.8240327562	-374078.89
011114	52227	gt018644	gt018645	gt018630	0.060946	29.8240327562	-374078.89
011114	52227	gt018646	gt018647	gt018630	0.060946	29.8240327562	-374078.89
011115	52228	gt018670	gt018671	gt018651	0.060946	29.8240327562	-374078.89
011115	52228	gt018672	gt018673	gt018651	0.060946	29.8240327562	-374078.89
011116	52229	gt018695	gt018696	gt018677	0.060946	29.8240327562	-374078.89
011120	52233	gt018786	gt018787	gt018772	0.060946	29.8240327562	-374078.89
011214	52257	gt018858	gt018859	gt018845	0.083361	29.8230631881	-374050.09
011214	52257	gt018860	gt018861	gt018845	0.083361	29.8230631881	-374050.09
011217	52260	gt018896	gt018897	gt018883	0.083361	29.8230631881	-374050.09
011218	52261	gt018920	gt018921	gt018908	0.083361	29.8230631881	-374050.09
011219	52262	gt018940	gt018941	gt018934	0.083361	29.8230631881	-374050.09
011219	52262	gt018942	gt018943	gt018934	0.083361	29.8230631881	-374050.09
011222	52265	gt018989	gt018990	gt018986	0.083361	29.8230631881	-374050.09
020107	52281	gt019041	gt019042	gt019033	0.090366	29.8220613683	-374017.76
020109	52283	gt019077	gt019078	gt019067	0.090366	29.8220613683	-374017.76
020113	52287	gt019127	gt019128	gt019119	0.090366	29.8220613683	-374017.76
020113	52287	gt019129	gt019130	gt019119	0.090366	29.8220613683	-374017.76
020114	52288	gt019149	gt019150	gt019143	0.090366	29.8220613683	-374017.76
020115	52289	gt019173		gt019167	0.090366	29.8220613683	-374017.76
020115	52289	gt019174		gt019167	0.090366	29.8220613683	-374017.76
020115	52289	gt019175	gt019176	gt019167	0.090366	29.8220613683	-374017.76
020115	52289	gt019177	gt019178	gt019167	0.090366	29.8220613683	-374017.76
020201	52306	gt019264	gt019265	gt019260	0.068878	29.8210596457	-373986.6
020207	52312	gt019278	gt019279	gt019272	0.068878	29.8210596457	-373986.6
020208	52313	gt019298	gt019299	gt019296	0.068878	29.8210596457	-373986.6
020208	52313	gt019302	gt019303	gt019296	0.068878	29.8210596457	-373986.6
020208	52313	gt019304	gt019305	gt019296	0.068878	29.8210596457	-373986.6
020209	52314	gt019322	gt019323	gt019320	0.068878	29.8210596457	-373986.6
020210	52315	gt019346	gt019347	gt019342	0.068878	29.8210596457	-373986.6
020212	52317	gt019404	gt019405	gt019384	0.068878	29.8210596457	-373986.6
020213	52318	gt019425		gt019448	0.068878	29.8210596457	-373986.6

Appendix C

Optimised Cut Values

The following two pages present, in tabular form, the results of the Supercuts optimisations performed as part of this work for all size and elevation bands used.

Size Range (d.c.)	Elevation Bands (degrees) 35-50	51-50	61-70	71-80
150-250	$40 < max1$ $32 < max2$ $0.04 < width < 0.09$ $0.08 < length < 0.27$ $0.31 < distance < 0.96$ $alpha < 18$	$2 < max1$ $62 < max2$ $0.00 < width < 0.07$ $0.09 < length < 0.11$ $0.45 < distance < 1.01$ $alpha < 18$	$38 < max1$ $24 < max2$ $0.02 < width < 0.10$ $0.07 < length < 0.32$ $0.15 < distance < 1.00$ $alpha < 20$	$26 < max1$ $20 < max2$ $0.03 < width < 0.09$ $0.07 < length < 0.22$ $0.50 < distance < 1.08$ $alpha < 48$
250-350	$38 < max1$ $32 < max2$ $0.03 < width < 0.09$ $0.06 < length < 0.46$ $0.23 < distance < 1.05$ $alpha < 20$	$2 < max1$ $76 < max2$ $0.04 < width < 0.09$ $0.08 < length < 0.37$ $0.01 < distance < 0.92$ $alpha < 25$	$36 < max1$ $30 < max2$ $0.05 < width < 0.09$ $0.11 < length < 0.27$ $0.04 < distance < 0.82$ $alpha < 20$	$34 < max1$ $24 < max2$ $0.05 < width < 0.16$ $0.08 < length < 0.23$ $0.54 < distance < 1.05$ $alpha < 20$
350-450	$2 < max1$ $46 < max2$ $0.00 < width < 0.11$ $0.08 < length < 0.19$ $0.03 < distance < 0.93$ $alpha < 23$	$44 < max1$ $34 < max2$ $0.06 < width < 0.11$ $0.13 < length < 0.26$ $0.49 < distance < 0.96$ $alpha < 22$	$56 < max1$ $34 < max2$ $0.02 < width < 0.13$ $0.10 < length < 0.20$ $0.19 < distance < 1.06$ $alpha < 14$	$36 < max1$ $30 < max2$ $0.06 < width < 0.11$ $0.12 < length < 0.20$ $0.46 < distance < 1.04$ $alpha < 18$
450-550	$64 < max1$ $46 < max2$ $0.00 < width < 0.08$ $0.11 < length < 0.47$ $0.28 < distance < 0.97$ $alpha < 12$	$68 < max1$ $46 < max2$ $0.04 < width < 0.11$ $0.12 < length < 0.23$ $0.24 < distance < 0.84$ $alpha < 12$	$62 < max1$ $56 < max2$ $0.07 < width < 0.12$ $0.12 < length < 0.27$ $0.02 < distance < 0.92$ $alpha < 12$	$50 < max1$ $44 < max2$ $0.03 < width < 0.11$ $0.12 < length < 0.20$ $0.26 < distance < 1.09$ $alpha < 17$
550-650	$76 < max1$ $58 < max2$ $0.03 < width < 0.11$ $0.15 < length < 0.20$ $0.01 < distance < 0.97$ $alpha < 10$	$60 < max1$ $52 < max2$ $0.00 < width < 0.11$ $0.11 < length < 0.22$ $0.31 < distance < 1.03$ $alpha < 11$	$58 < max1$ $44 < max2$ $0.06 < width < 0.11$ $0.11 < length < 0.22$ $0.09 < distance < 0.89$ $alpha < 11$	$48 < max1$ $44 < max2$ $0.06 < width < 0.10$ $0.12 < length < 0.21$ $0.54 < distance < 1.01$ $alpha < 11$

Size Range (d.c.)	Elevation Bands (degrees) 35-50	51-50	61-70	71-80
650-750	$84 < max1$ $80 < max2$ $0.07 < width < 0.11$ $0.10 < length < 0.39$ $0.22 < distance < 1.05$ $alpha < 22$	$58 < max1$ $2 < max2$ $0.05 < width < 0.11$ $0.12 < length < 0.22$ $0.43 < distance < 0.92$ $alpha < 9$	$52 < max1$ $2 < max2$ $0.00 < width < 0.10$ $0.12 < length < 0.24$ $0.17 < distance < 0.94$ $alpha < 8$	$56 < max1$ $2 < max2$ $0.06 < width < 0.11$ $0.11 < length < 0.23$ $0.45 < distance < 1.03$ $alpha < 13$
750-1000	$130 < max1$ $96 < max2$ $0.01 < width < 0.09$ $0.11 < length < 0.19$ $0.28 < distance < 1.00$ $alpha < 20$	$66 < max1$ $50 < max2$ $0.02 < width < 0.10$ $0.11 < length < 0.23$ $0.57 < distance < 0.93$ $alpha < 9$	$62 < max1$ $64 < max2$ $0.07 < width < 0.11$ $0.11 < length < 0.24$ $0.40 < distance < 0.92$ $alpha < 10$	$74 < max1$ $60 < max2$ $0.06 < width < 0.11$ $0.12 < length < 0.21$ $0.34 < distance < 0.95$ $alpha < 16$
1000-2000	$168 < max1$ $84 < max2$ $0.03 < width < 0.17$ $0.13 < length < 0.48$ $0.24 < distance < 1.05$ $alpha < 20$	$98 < max1$ $78 < max2$ $0.02 < width < 0.11$ $0.13 < length < 0.24$ $0.37 < distance < 1.03$ $alpha < 9$	$2 < max1$ $2 < max2$ $0.04 < width < 0.11$ $0.14 < length < 0.23$ $0.58 < distance < 0.91$ $alpha < 14$	$2 < max1$ $80 < max2$ $0.00 < width < 0.12$ $0.14 < length < 0.24$ $0.35 < distance < 1.01$ $alpha < 11$
> 2000	$2 < max1$ $2 < max2$ $0.00 < width < 0.11$ $0.13 < length < 0.21$ $0.01 < distance < 1.00$ $alpha < 10$	$200 < max1$ $162 < max2$ $0.07 < width < 0.13$ $0.14 < length < 0.23$ $0.28 < distance < 0.99$ $alpha < 8$	$2 < max1$ $142 < max2$ $0.00 < width < 0.13$ $0.14 < length < 0.25$ $0.53 < distance < 0.93$ $alpha < 11$	$138 < max1$ $128 < max2$ $0.00 < width < 0.14$ $0.15 < length < 0.24$ $0.19 < distance < 0.98$ $alpha < 9$

Table C.1: Breakdown of the optimised Supercuts selection criteria, by elevation and *size* bands.

Appendix D

Kernel $\log(R)$ Cut Values

The following $\log(R)$ cut values were obtained in the banded Kernel optmisations:

Size Band	35-50	51-60	61-70	71-80
0-150	4.25	4.30	4.40	4.30
150-250	2.85	0.35	0.20	-0.10
250-350	3.25	2.60	-1.85	0.00
350-450	-3.00	2.85	2.55	2.00
450-550	3.35	0.85	1.35	2.65
550-650	2.50	2.45	2.60	2.90
650-750	3.80	2.05	2.35	2.45
750-1000	4.60	3.10	2.55	2.05
1000-2000	5.40	3.15	3.20	2.90
>2000	5.30	2.55	3.20	3.00
>150	4.25	4.30	4.40	4.30

Table D.1: Breakdown of the optimised Kernel $\log(R)$ cut values by elevation and *size* band.

Bibliography

Acharya, B. S., Bhat, P. N., Gandhi, V. N., Ramana Murthy, P. V., Sathyanarayana, G. P., and Vishwanath, P. R.: 1992, A&A **258**, 412

Aharonian, F., Akhperjanian, A., Barrio, J., Beilicke, M., Bernlöhr, K., Börst, H., Bojahr, H., Bolz, O., Contreras, J., Cornils, R., Cortina, J., Denninghoff, S., Fonseca, V., Girma, M., Gonzalez, J., Götting, N., Heinzelmann, G., Hermann, G., Heusler, A., Hofmann, W., Horns, D., Jung, I., Kankanyan, R., Kestel, M., Kettler, J., Kohnle, A., Konopelko, A., Kornmeyer, H., Kranich, D., Krawczynski, H., Lampeitl, H., Lopez, M., Lorenz, E., Lucarelli, F., Magnussen, N., Mang, O., Meyer, H., Mirzoyan, R., Moralejo, A., Ona, E., Padilla, L., Panter, M., Plaga, R., Plyasheshnikov, A., Pühlhofer, G., Rauterberg, G., Röhring, A., Rhode, W., Robrade, J., Rowell, G., Sahakian, V., Samorski, M., Schilling, M., Schröder, F., Sevilla, I., Siems, M., Stamm, W., Tluczykont, M., Völk, H. J., Wiedner, C. A., and Wittek, W.: 2002, A&A **384**, L23

Aharonian, F., Akhperjanian, A., Barrio, J., Bernlöhr, K., Börst, H., Bojahr, H., Bolz, O., Contreras, J., Cortina, J., Denninghoff, S., Fonseca, V., Gonzalez, J., Götting, N., Heinzelmann, G., Hermann, G., Heusler, A., Hofmann, W., Horns, D., Ibarra, A., Iserlohe, C., Jung, I., Kankanyan, R., Kestel, M., Kettler, J., Kohnle, A., Konopelko, A., Kornmeyer, H., Kranich, D., Krawczynski, H., Lampeitl, H., Lopez, M., Lorenz, E., Lucarelli, F., Magnussen, N., Mang, O., Meyer, H., Mirzoyan, R., Moralejo, A., Ona, E., Padilla, L., Panter, M., Plaga, R., Plyasheshnikov, A., Prahl, J., Pühlhofer, G., Rauterberg, G., Röhring, A., Rhode, W., Rowell, G. P., Sahakian, V., Samorski, M., Schilling, M., Schröder, F., Siems, M., Stamm, W., Tluczykont, M., Völk, H. J., Wiedner, C. A., and Wittek, W.: 2001, A&A **370**, 112

Aharonian, F., Akhperjanian, A. G., Barrio, J. A., Bernlöhr, K., Bojahr, H., Contreras, J. L., Cortina, J., Daum, A., Deckers, T., Denninghoff, S., Fonseca, V., Gonzalez, J. C., Heinzelmann, G., Hemberger, M., Hermann, G., Heß, M., Heusler, A., Hofmann, W., Hohl, H., Horns, D., Ibarra, A., Kankanyan, R., Kestel, M., Kirstein, O., Köhler, C., Konopelko, A., Kornmeyer, H., Kranich, D., Krawczynski, H., Lampeitl, H., Lindner, A., Lorenz, E., Magnussen, N., Meyer, H., Mirzoyan, R., Moralejo, A., Padilla, L., Panter, M., Petry, D., Plaga,

R., Plyasheshnikov, A., Prahl, J., Pühlhofer, G., Rauterberg, G., Renault, C., Rhode, W., Röhring, A., Sahakian, V., Samorski, M., Schmele, D., Schröder, F., Stamm, W., Völk, H., Wiebel-Sooth, B., Wiedner, C., Willmer, M., and Wirth, H.: 1999, A&A **346**, 913

Aharonian, F. and Atoyan, A.: 1995, *Astroparticle Physics* **3**, N3

Aharonian, F. A., Akhperjanian, A. G., Barrio, J. A., Bernlöhr, K., Bojahr, H., Calle, I., Contreras, J. L., Cortina, J., Denninghoff, S., Fonseca, V., Gonzalez, J. C., Götting, N., Heinzelmann, G., Hemberger, M., Hermann, G., Heusler, A., Hofmann, W., Horns, D., Ibarra, A., Kankanyan, R., Kestel, M., Kettler, J., Köhler, C., Kohnle, A., Konopelko, A., Kornmeyer, H., Kranich, D., Krawczynski, H., Lampeitl, H., Lindner, A., Lorenz, E., Lucarelli, F., Magnussen, N., Mang, O., Meyer, H., Mirzoyan, R., Moralejo, A., Padilla, L., Panter, M., Plaga, R., Plyasheshnikov, A., Prahl, J., Pühlhofer, G., Rauterberg, G., Röhring, A., Sahakian, V., Samorski, M., Schilling, M., Schmele, D., Schröder, F., Stamm, W., Tluczykont, M., Völk, H. J., Wiebel-Sooth, B., Wiedner, C., Willmer, M., and Wittek, W.: 2000, ApJ **539**, 317

Albats, P., Frye, G., Zych, A. D., Mace, O. B., Hopper, V. D., and Thomas, J. A.: 1972, *Nature* **240**, 221

Alvarez-Muñiz, J. and Halzen, F.: 2002, ApJ **576**, L33

Arons, J.: 1983, ApJ **266**, 215

Ascoli Balzanelli, A. and Ascoli, R.: 1953, *Nuovo Cim. Series 9* **10**, 1345

Atoyan, A. M. and Aharonian, F. A.: 1996, A&AS **120**, C453

Barbiellini, G., Tavani, M., Argan, A., Auricchio, N., Caraveo, P., Chen, A., Cocco, V., Costa, E., di Cocco, G., Fedel, G., Feroci, M., Fiorini, M., Froysland, T., Galli, M., Gianotti, F., Giuliani, A., Labanti, C., Lapshov, I., Lipari, P., Longo, F., Massaro, E., Mereghetti, S., Morelli, E., Morselli, A., Pellizzoni, A., Perotti, F., Picozza, P., Pittori, C., Pontoni, C., Prest, M., Rapisarda, M., Rossi, E., Rubini, A., Soffitta, P., Trifoglio, M., Vallazza, E., Vercellone, S., and Zanello, D.: 2001, in *AIP Conf. Proc. 587: Gamma 2001: Gamma-Ray Astrophysics*, p. 774

Becker, W. and Truemper, J.: 1997, A&A **326**, 682

Bennett, K., Bignami, G. F., Boella, G., Buccheri, R., Hermsen, W., Kanbach, G. G., Lichti, G. G., Masnou, J. L., Mayer-Hasselwander, H. A., Paul, J. A., Scarsi, L., Swanenburg, B. N., Taylor, B. G., and Wills, R. D.: 1977, A&A **61**, 279

Beran, R. J.: 1969, *Ann. Math. Statist* **40**, 1196

Bhat, P. N., Ramanamurthy, P. V., Sreekantan, B. V., and Vishwanath, P. R.: 1986, *Nature* **319**, 127

Borione, A., Catanese, M. A., Chantell, M. C., Covault, C. E., Cronin, J. W., Fick, B. E., Fortson, L. F., Fowler, J. F., Gibbs, K. G., Glasmacher, M. A. K., Green, K. D., Kieda, D. B., Matthews, J., Newport, B. J., Nitz, D. F., Ong, R. A., Rosenberg, L. J., Sinclair, D., and van der Velde, J. C.: 1997, ApJ **481**, 313

Bradbury, S.: 1997, in *Workshop Towards a Major Cherenkov Detector (Kruger Park)*, p. 365

Browning, R., Ramsden, D., and Wright, P. J.: 1971, *Nature Physical Science* **232**, 99

Buccheri, R.: 1983, *Astronomy and Astrophysics* **128**, 245

Buccheri, R. and Sacco, B.: 1985, in L. Scarsi, V. Di Gesù, P. Crane, J. H. Friedman, and S. Levialdi (eds.), *Data Analysis in Astronomy*, p. 15, New York: Plenum

Buckley, J. H., Akerlof, C. W., Carter-Lewis, D. A., Catanese, M., Cawley, M. F., Connaughton, V., Fegan, D. J., Finley, J. P., Gaidos, J. A., Hillas, A. M., Krennrich, F., Lamb, R. C., Lessard, R. W., McEnery, J. E., Mohanty, G., Quinn, J., Rodgers, A. J., Rose, H. J., Rovero, A. C., Schubnell, M. S., Sembroski, G., Srinivasan, R., Weekes, T. C., and Zweerink, J.: 1998, A&A **329**, 639

Catanese, M., Akerlof, C. W., Badran, H. M., Biller, S. D., Bond, I. H., Boyle, P. J., Bradbury, S. M., Buckley, J. H., Burdett, A. M., Bussons Gordo, J., Carter-Lewis, D. A., Cawley, M. F., Connaughton, V., Fegan, D. J., Finley, J. P., Gaidos, J. A., Hall, T., Hillas, A. M., Krennrich, F., Lamb, R. C., Lessard, R. W., Masterson, C., McEnery, J. E., Mohanty, G., Quinn, J., Rodgers, A. J., Rose, H. J., Samuelson, F. W., Schubnell, M. S., Sembroski, G. H., Srinivasan, R., Weekes, T. C., Wilson, C. W., and Zweerink, J.: 1998, ApJ **501**, 616

Catanese, M. et al.: 1995, in M. Cresti (ed.), *Workshop Towards a Major Cherenkov Detector (Padova)*, p. 335

Catanese, M. and Weekes, T. C.: 1999, PASP **111**, 1193

Catanese, M. and Whipple Collaboration: 1999, in *ASP Conf. Ser. 159: BL Lac Phenomenon*, p. 243

Cawley, M.: 1993, in R. Lamb (ed.), *Workshop Towards a Major Cherenkov Detector (Calgary)*, p. 176

Cawley, M. F.: 1999, Private Communication

Cawley, M. F., Clear, J., Fegan, D. J., Gibbs, K., Gorham, P., Lamb, R. C., MacRae, I., MacKeown, P. K., Porter, N. A., Stenger, V. S., Turver, K. E., and Weekes, T. C.: 1983, in N. Durgaprasad (ed.), *Proceedings of the 18th International Cosmic Ray Conference (Bangalore)*, p. 118

Cawley, M. F., Fegan, D. J., Harris, K., Kwok, P. W., Hillas, A. M., Lamb, R. C., Lang, M. J., Lewis, D. A., Macomb, D., Reynolds, P. T., Schmid, D. J., Vacanti, G., and Weekes, T. C.: 1990, *Experimental Astronomy* **1**, 173

Cawley, M. F. and Weekes, T. C.: 1995, *Experimental Astronomy* **6**, 7

Chadwick, P., Lyons, K., McComb, T., Orford, K., Osborne, J., Rayner, S., Shaw, S., and Turver, K.: 1999, in *Proceedings of the 26th International Cosmic Ray Conference (Salt Lake City)*, Vol. 4, p. 72

Chadwick, P. M., Dickinson, M. R., Dipper, N. A., Kendall, T. R., McComb, T. J. L., Orford, K. J., Osborne, J. L., Rayner, S. M., Roberts, I. D., Shaw, S. E., and Turver, K. E.: 1998, ApJ **503**, 391

Cheng, K.: 1994, in T. Kifune (ed.), *Workshop Towards a Major Cherenkov Detector (Toyko)*, p. 25

Cheng, Ho and Ruderman: 1986a, ApJ **300**, 500

Cheng, Ho and Ruderman: 1986b, ApJ **300**, 522

Clark, D. H. and Stephenson, R. F.: 1977, *The historical supernovae*, Pergamon International Library of Science, Technology, Engineering and Social Studies, Oxford: Pergamon Press, 1977

Clear, J., Bennett, K., Buccheri, R., Grenier, I. A., Hermsen, W., Mayer-Hasselwander, H. A., and Sacco, B.: 1987, A&A **174**, 85

Cranshaw, T. E.: 1963, *Cosmic Rays*, Clarendon Press

Daugherty, J. K. and Harding, A. K.: 1982, ApJ **252**, 337

Daugherty, J. K. and Harding, A. K.: 1994, ApJ **429**, 325

Daugherty, J. K. and Harding, A. K.: 1996, ApJ **458**, 278

Davies, J. and Cotton, E.: 1957, *Journal of Solar Energy* **1**, 16

de Jager, O. C.: 2002, *Pulsars and Plerions from a Multiwavelength Perspective*, Online proceedings of: The Universe viewed in gamma-rays —The University of Tokyo Workshop 2002. http://icrgate.icrr.u-tokyo.ac.jp/can/Symp2002/Presentations.htm

de Jager, O. C. and Harding, A. K.: 1992, ApJ **396**, 161

de Jager, O. C., Harding, A. K., Michelson, P. F., Nel, H. I., Nolan, P. L., Sreekumar, P., and Thompson, D. J.: 1996, ApJ **457**, 253

de Jager, O. C., Konopelko, A., Raubenheimer, B. C., and Visser, B.: 2001, in *Proceedings of the 27th International Cosmic Ray Conference (Hamburg)*, Vol. 6, p. 2432

de Jager, O. C., Oña-Wilhelmi, E., Konopelko, A., Fonseca, F., and Lopez-Moya, M.: 2002, *African Skies* **7**, 21

de Jager, O. C., Raubenheimer, B. C., and Swanepoel, J. W. H.: 1989, A&A **221**, 180

de Naurois, M., Holder, J., Bazer-Bachi, R., Bergeret, H., Bruel, P., Cordier, A., Debiais, G., Dezalay, J.-P., Dumora, D., Durand, E., Eschstruth, P., Espigat, P., Fabre, B., Fleury, P., Hérault, N., Hrabovsky, M., Incerti, S., Le Gallou, R., Münz, F., Musquère, A., Olive, J.-F., Paré, E., Québert, J., Rannot, R. C., Reposeur, T., Rob, L., Roy, P., Sako, T., Schovanek, P., Smith, D. A., Snabre, P., and Volte, A.: 2002, ApJ **566**, 343

Dorfi, E. A.: 1991, A&A **251**, 597

Dowdall, C.: 2002, *M.Sc thesis in preparation*, National University of Ireland

Dowthwaite, J. et al.: 1984, ApJ **286**, L35

Drury, L. O., Aharonian, F. A., and Voelk, H. J.: 1994, A&A **287**, 959

Dunlea, S.: 2001, *Ph.D. thesis*, National University of Ireland

Dunlea, S., Moriarty, P., and Fegan, D. J.: 2001, in *Proceedings of the 27th International Cosmic Ray Conference (Hamburg)*, Vol. 7, p. 2939

Enomoto, R., Tanimori, T., Naito, T., Yoshida, T., Yanagita, S., Mori, M., Edwards, P. G., Asahara, A., Bicknell, G. V., Gunji, S., Hara, S., Hara, T., Hayashi, S., Itoh, C., Kabuki, S., Kajino, F., Katagiri, H., Kataoka, J., Kawachi, A., Kifune, T., Kubo, H., Kushida, J., Maeda, S., Maeshiro, A., Matsubara, Y., Mizumoto, Y., Moriya, M., Muraishi, H., Muraki, Y., Nakase, T., Nishijima, K., Ohishi, M., Okumura, K., Patterson, J. R., Sakurazawa, K., Suzuki, R., Swaby, D. L., Takano, K., Takano, T., Tokanai, F., Tsuchiya, K., Tsunoo, H., Uruma, K., Watanabe, A., and Yoshikoshi, T.: 2002, Nature **416**, 823

Erickson, R. A., Fickle, R. K., and Lamb, R. C.: 1976, ApJ **210**, 539

Esposito, J. A., Hunter, S. D., Kanbach, G., and Sreekumar, P.: 1996, ApJ **461**, 820

Fegan, D. J.: 1996, *Space Science Reviews* **75**, 137

Fegan, D. J.: 1997, *J. Phys. G: Nucl. Part. Phys.* **23**, 1013

Fegan, D. J.: 2002a, Private Communication

Fegan, D. J.: 2002b, *The Outer Limits*, Internal Whipple collaboration memo

Fierro, J. M.: 1995, *Ph.D. thesis*, Stanford University

Fierro, J. M., Michelson, P. F., Nolan, P. L., and Thompson, D. J.: 1998, ApJ **494**, 734

Finley, J. P. and the VERITAS collaboration: 2001, in *Proceedings of the 27th International Cosmic Ray Conference (Hamburg)*, Vol. 7, p. 2827

Frank, I. and Tamm, I.: 1937, *Dokl. Akad, SSSR* **14**, 109

Gehrels, N. and Michelson, P.: 1999, *Astroparticle Physics* **11**, 277

Gehrels, N. and The GLAST Collaboration: 2001, in *AIP Conf. Proc. 220: High Energy Gamma-Ray Astronomy*, p. 3

Gibson, A. et al.: 1982, in *Proc. International Workshop on VHE Gamma-Ray Astronomy (Ootacumund, India)*, p. 97

Gillanders, G.: 2000, *Pulsar analysis algorithm and programmes used at NUI, Galway*, Private Communication

Gillanders, G. G., Boyle, P. J., Buckley, J. H., Burdett, A. M., Bussons Gordo, J., Carter-Lewis, D. A., Catanese, M., Cawley, M. F., Fegan, D. J., Finley, J. P., Gaidos, J. A., Hillas, A. M., Krennrich, F., Lamb, R. C., Lang, M. J., Lessard, R., Masterson, C., McEnery, J. E., Mohanty, G., Moriarty, P., Quinn, J., Rodgers, A. J., Rose, H. J., Samuelson, F. W., Sembroski, G. H., Srinivasan, R., Weekes, T. C., and Zweerink, J.: 1997, *Proceedings of the 25th International Cosmic Ray Conference (Durban, South Africa)* **25**, 185

Gold, T.: 1968, *Nature* **218**, 731

Goldreich, P. and Julian, W. H.: 1969, ApJ **157**, 869

Goret, P. et al.: 1993, *Astronomy and Astrophysics* **270**, 401

Gould, R. J.: 1965, *Physics Review Letters* **15**, 577

Grindlay, J. E.: 1972, ApJ **174**, L9

Grindlay, J. E., Helmken, H. F., and Weekes, T. C.: 1976, ApJ **209**, 592

Hall, T. A., Bond, I. H., Bradbury, S. M., Buckley, J. H., , Carson, M. J., Carter-Lewis, D. A., Catanese, M., Dunlea, S., d'Vali, M., Fegan, D. J., Fegan, S. J., Finley, J. P., Gaidos, J. A., Gillanders, G. H., Hillas, A. M., Horan, D., Kertzman, M., Kieda, D., Kildea, J., Knapp, J., Krennrich, F., Lang, M. J., LeBohec, S., Lessard, R., Llyod-Evans, J., McKernan, B., Moriarty, P., Müller, D., Ong, R., Quinn, J., Reynolds, P. T., Rose, H. J., Sembroski, G. H., Swordy, S. P., Vassiliev, V. V., and Weekes, T. C.: 2002, *Search for TeV emissions from Pulsars in Binary Systems*, Submitted to Ap.J.

Hall, T. A. et al.: 2001, in *Proceedings of the 27h International Cosmic Ray Conference (Hamburg)*, Vol. 1, p. 2485

Hanbury-Brown, R.: 1966, *Philips Tech Rev* **27**, 141

Hand, D.: 1982, *Kernel Discriminant Analysis*, John Wiley & Sons, Inc., Chichester

Harding, A. K.: 1981, ApJ **245**, 267

Harding, A. K.: 2001, in *AIP Conf. Proc. 220: High Energy Gamma Ray Astronomy*, p. 115

Hartman, R. C., Bertsch, D. L., Bloom, S. D., Chen, A. W., Deines-Jones, P., Esposito, J. A., Fichtel, C. E., Friedlander, D. P., Hunter, S. D., McDonald, L. M., Sreekumar, P., Thompson, D. J., Jones, B. B., Lin, Y. C., Michelson, P. F., Nolan, P. L., Tompkins, W. F., Kanbach, G., Mayer-Hasselwander, H. A., Mücke, A., Pohl, M., Reimer, O., Kniffen, D. A., Schneid, E. J., Von Montigny, C., Mukherjee, R., and Dingus, B. L.: 1999, ApJS **123**, 79

Heiles, C., Campbell, D., and Rankin, J.: 1970, *Nature* **226**, 529

Helene, O.: 1983, *Nuclear Instruments and Methods* **212**, 319

Helmken, H. F., Fazio, G. G., O'Mongain, E., and Weekes, T. C.: 1973, ApJ **184**, 245

Hermsen, W.: 1980, *PhD Thesis*, University of Leiden

Hermsen W. et al.: 1977, *Nature* **269**, 494

Hewish, A., Bell, S. J., Pilkington, J. D., Scott, P. F., and Collins, R. A.: 1968, *Nature* **217**, 709

Higgins, M. G. and Henriksen, R. N.: 1997, MNRAS **292**, 934

Hill, D. and Porter, N.: 1961, *Nature* **191**, 690

Hillas, A.: 1985, in *Proc. 19nd I.C.R.C. (La Jolla)*, Vol. 3, p. 445

Hillas, A.: 1996, *Space Science Reviews* **75**, 17

Hillas, A.: 1997, *Limited Angular acceptance of lightcones*, Internal Whipple Memo

Hillas, A. M., Akerlof, C. W., Biller, S. D., Buckley, J. H., Carter-Lewis, D. A., Catanese, M., Cawley, M. F., Fegan, D. J., Finley, J. P., Gaidos, J. A., Krennrich, F., Lamb, R. C., Lang, M. J., Mohanty, G., Punch, M., Reynolds, P. T., Rodgers, A. J., Rose, H. J., Rovero, A. C., Schubnell, M. S., Sembroski, G. H., Vacanti, G., Weekes, T. C., West, M., and Zweerink, J.: 1998, ApJ **503**, 744

Hirotani, K.: 2001, ApJ **549**, 495

Hoffman, C. M., Sinnis, C., Fleury, P., and Punch, M.: 1999, *Reviews of Modern Physics* **71**, 897

Holder, J., Bond, I. H., Bradbury, S. M., Buckley, J. H., Carter-Lewis, D. A., Cui, W., Duke, C., de la Calle Perez, I., Falcone, A., Fegan, D. J., Fegan, S. J., Finley, J. P., Gaidos, J. A., Gibbs, K., Gammell, S., Hall, J., Hall, T. A., Hillas, A. M., Horan, D., Jordan, M., Kertzman, M., Kieda, D., Kildea, J., Knapp, J., Kosack, K., Krennrich, F., LeBohec, S., Moriarty, P., Müller, D., Nagai, T. N., Ong, R., Page, M., Pallassini, R., Petry, D., Power-Mooney, B., Quinn, J., Reay, N. W., Reynolds, P. T., Rose, H. J., Schroedter, M., Sembroski, G. H., Sidwell, R., Stanton, N., Swordy, S. P., Vassiliev, V. V., Wakely, S. P., Walker, G., and Weekes, T. C.: 2002, *Detection of TeV Gamma Rays from 1es1959+650 with the Whipple 10m Telescope*, Submitted to Ap.J.

Horan, D.: 2001, *Ph.D. thesis*, National University of Ireland

Horan, D., Badran, H. M., Bond, I. H., Bradbury, S. M., Buckley, J. H., Carson, M. J., Carter-Lewis, D. A., Catanese, M., Cui, W., Dunlea, S., Das, D., de la Calle Perez, I., D'Vali, M., Fegan, D. J., Fegan, S. J., Finley, J. P., Gaidos, J. A., Gibbs, K., Gillanders, G. H., Hall, T. A., Hillas, A. M., Holder, J., Jordan, M., Kertzman, M., Kieda, D., Kildea, J., Knapp, J., Kosack, K., Krennrich, F., Lang, M. J., LeBohec, S., Lessard, R., Lloyd-Evans, J., McKernan, B., Moriarty, P., Muller, D., Ong, R., Pallassini, R., Petry, D., Quinn, J., Reay, N. W., Reynolds, P. T., Rose, H. J., Sembroski, G. H., Sidwell, R., Stanton, N., Swordy, S. P., Vassiliev, V. V., Wakely, S. P., and Weekes, T. C.: 2002, ApJ **571**, 753

Hughes, P.: 2001, *Ph.D. thesis*, National University of Ireland

Iyudin, A. and Kanbach, G.: 2001, in V. Schoenfelder (ed.), *The Universe in Gamma Rays*, p. 185

Jelley, J. and Galbraith, W.: 1955, *Part II. J. Atmosph. Terr. Phys.* **6**, 304

Jelley, J. and Porter, N.: 1963, *Quarterly J. of the R.A.S.* **4**, 275

Jennings, D. M., White, G., A., P. N., O'Mongain, E., Fegan, D. J., and White, J.: 1974, *Nuovo Cimento* **20**, 71

Jones, B. B., Lin, Y. C., Michelson, P. F., Nolan, P. L., Roberts, M. S. E., and Tompkins, W. F.: 1997, in *AIP Conf. Proc. 410: Proceedings of the Fourth Compton Symposium*, p. 783

Jones, P. B.: 1981, MNRAS **197**, 1103

Jones, P. B.: 1985, MNRAS **216**, 503

Kanbach, G.: 2002, in W. Becker, H. Lesch, and J. Truemper (eds.), *Neutron Stars, Pulsars, and Supernova Remnants*, pp 91–99

Kerrick, A. D., Akerlof, C. W., Biller, S. D., Buckley, J. H., Cawley, M. F., Chantell, M., Connaughton, V., Fegan, D. J., Fennell, S., Gaidos, J. A., Hillas, A. M., Lamb, R. C., Lewis, D. A., Meyer, D. I., McEnery, J., Mohanty, G., Quinn, J., Rovero, A. C., Rose, H. J., Schubnell, M. S., Sembroski, G., Urban, M., Watson, A. A., Weekes, T. C., West, M., Wilson, C., and Zweerink, J.: 1995, ApJ **438**, L59

Kertzman, M. and Sembroski, G.: 1994, *Nuclear Instruments and Methods A* **343**, 629

Kifune, T., Tanimori, T., Ogio, S., Tamura, T., Fujii, H., Fujimoto, M., Hara, T., Hayashida, N., Kabe, S., Kakimoto, F., Matsubara, Y., Mizumoto, Y., Muraki, Y., Suda, T., Teshima, M., Tsukagoshi, T., Watase, Y., Yoshikoshi, T., Edwards, P. G., Patterson, J. R., Roberts, M. D., Rowell, G. P., and Thornton, G. J.: 1995, ApJ **438**, L91

Kildea, J.: 2000, *Mirror Alignment for the Whipple 10m Telescope*, Internal Whipple Collaboration memo

Kinzer, R. L., Share, G. H., and Seeman, N.: 1973, ApJ **180**, 547

Kirk, J. G., Skjæraasen, O., and Gallant, Y. A.: 2002, A&A **388**, L29

Klages, H. et al.: 1997, *Nucl. Phys. B. Proc. Suppl.* **52B**, 92

Kniffen, D. A., Hartman, R., Thompson, D., Bignami, G. F., Fichtel, C. E., T., T., and H., O.: 1974, *Nature* **251**, 397

Konopelko, A.: 2002, in *Proc. 270. WE-Heraeus Seminar on Neutron Stars, Pulsars and Supernova Remnants, January 21-25, 2002, Physikzentrum Bad Honnef, Germany, Editors: W. Becker, H. Lesch and J. Truemper; MPE-Report 27*, p. 105

Konopelko, A. and Plyasheshnikov, A.: 2000, *Nuclear Instruments and Methods A* **450**, 419

Konopelko et al.: 2002, *April APS/HEAD Meeting, Albuquerque, Session B17*

Krennrich, F., Badran, H. M., Bond, I. H., Bradbury, S. M., Buckley, J. H., Carter-Lewis, D. A., Catanese, M., Cui, W., Dunlea, S., Das, D., de la Calle Perez, I., Fegan, D. J., Fegan, S. J., Finley, J. P., Gaidos, J. A., Gibbs, K., Gillanders, G. H., Hall, T. A., Hillas, A. M., Holder, J., Horan, D., Jordan, M., Kertzman, M., Kieda, D., Kildea, J., Knapp, J., Kosack, K., Lang, M. J., LeBohec, S., McKernan, B., Moriarty, P., Müller, D., Ong, R., Pallassini, R., Petry, D., Quinn, J., Reay, N. W., Reynolds, P. T., Rose, H. J., Sembroski, G. H., Sidwell, R., Stanton, N., Swordy, S. P., Vassiliev, V. V., Wakely, S. P., and Weekes, T. C.: 2001a, ApJ **560**, L45

Krennrich, F., LeBohec, S., Petry, D., and Carter-Lweis, D.: 2001b, *Peak Response Energy of the Whipple Telescope in 2000 and 2001*, Internal Whipple collaboration communication

Kuiper, L., Hermsen, W., Cusumano, G., Diehl, R., Schönfelder, V., Strong, A., Bennett, K., and McConnell, M. L.: 2001, A&A **378**, 918

Kundt, W.: 2001, *Astrophysics*, Springer, Bonn

Lang, M.: 1991, *Ph.D. thesis*, National University of Ireland

Lang, M.: 2001, *SAS: Semi-automated Alignment System*, Whipple Telescope Alignment Manual

LeBohec, S.: 1999, *Mirror Tuning*, Internal Whipple Collaboration memo

Lessard, R. W.: 1999, *Supercuts 2000*, Internal Whipple collaboration communication

Lessard, R. W., Bond, I. H., Boyle, P. J., Bradbury, S. M., Buckley, J. H., Burdett, A. C., Carter-Lewis, D. A., Catanese, M., Cawley, M. F., Dunlea, S., D'Vali, M., Fegan, D. J., Fegan, S. J., Finley, J. P., Gaidos, J. A., Hall, T. A., Hillas, A. M., Horan, D., Knapp, J., Krennrich, F., Le Bohec, S., Masterson, C., Quinn, J., Rose, H. J., Samuelson, F. W., sembroski, G. h., and Vassiliev, V. V.: 1999, in *Proceedings of the 26th International Cosmic Ray Conference (Salt Lake City)*, Vol. 3, p. 488

Lessard, R. W., Bond, I. H., Bradbury, S. M., Buckley, J. H., Burdett, A. M., Carter-Lewis, D. A., Catanese, M., Cawley, M. F., D'Vali, M., Fegan, D. J., Finley, J. P., Gaidos, J. A., Gillanders, G. H., Hall, T., Hillas, A. M., Krennrich, F., Lang, M. J., Masterson, C., Moriarty, P., Quinn, J., Rose, H. J., Samuelson,

F. W., Sembroski, G. H., Srinivasan, R., Vassiliev, V. V., and Weekes, T. C.: 2000, ApJ **531**, 942

Lessard, R. W., Buckley, J. H., Connaughton, V., and Le Bohec, S.: 2001, *Astroparticle Physics* **15**, 1

Lewis, D.: 1990, *Experimental Astronomy* **1**, 213

Lewis, D. A., Biller, S., Buckley, J., Cawley, M. F., Fishman, J., Kaaret, P., and Mattox, J.: 1998, *Notes on Reflector Design*, Internal Whipple collaboration communication

Lorimer, D. R.: 2001, *Living Rev. Relativity [Online article]: cited on 28 Nov 2002 (http://www.livingreviews.org/Articles/Volume4/2001-5lorimer/)* **4**, 5

Lyne, A. G., Jordan, C., and Roberts, M. E., *Jodrell Bank Crab Pulsar Timing Results, Monthly Ephemeris*

Lyubarskii, Y. E.: 1996, A&A **311**, 172

MacKeown, P. K., Cawley, M. F., Clear, J., Fegan, D. J., Lamb, R. C., Turver, K. E., and Weekes, T. C.: 1983, in N. Durgaprasad (ed.), *Proceedings of the 18th International Cosmic Ray Conference (Bangalore)*

Mallet, L.: 1926, *Acad. Sci. (Paris)* **183**, 274

Mallet, L.: 1928, *Acad. Sci. (Paris)* **187**, 222

Mallet, L.: 1929, *Acad. Sci. (Paris)* **188**, 445

Masterson, C. P.: 1999, *Ph.D. thesis*, National University of Ireland

Mayer-Hasselwander, H. A. and Simpson, G.: 1990, in *The Energetic Gamma-Ray Experiment Telescope (EGRET) Science Symposium*, pp 153–159

McBreen, B., Ball, S. E., Campbell, M., Greisen, K., and Koch, D.: 1973, ApJ **184**, 571

Melzer, D. W. and Thorne, K. S.: 1966, ApJ **145**, 514

Michel, F. C.: 1979, ApJ **227**, 579

Moffett, D. A. and Hankins, T. H.: 1996, ApJ **468**, 779

Mohanty, G., Biller, S., Carter-Lewis, D. A., Fegan, D. J., Hillas, A. M., Lamb, R. C., Weekes, T. C., West, M., and Zweerink, J.: 1998, *Astroparticle Physics* **9**, 15

Moriarty, P., Masterson, C., Fegan, D. J., Buckley, J. H., Catanese, M., Quinn, J., Reynolds, P. T., and Krennrich, F.: 1997, *Astroparticle Physics* **7**, 315

Moriarty, P. and Samuelson, F. W.: 2000, in *GeV-TeV Gamma Ray Astrophysics Workshop : towards a major atmospheric Cherenkov detector*, p. 338

Morrison, P.: 1958, *Nuovo Cimento* **7**, 858

Muraishi, H., Tanimori, T., Yanagita, S., Yoshida, T., Kifune, T., Dazeley, S. A., Edwards, P. E., Gunji, S., Hara, S., Hara, T., Jinbo, J., Kawachi, A., Kubo, H., Kushida, J., Matsubara, Y., Mizumoto, Y., Mori, M., Moriya, M., Muraki, Y., Naito, T., Nishijima, K., Patterson, J. R., Roberts, M. D., Rowell, G. P., Sako, T., Sakurazawa, K., Sato, Y., Susukita, R., Tamura, T., Yoshikoshi, T., and Yuki, A.: 1999, in *Proceedings of the 26th International Cosmic Ray Conference (Salt Lake City)*, Vol. 3, p. 500

Muslimov, A. G. and Tsygan, A. I.: 1992, MNRAS **255**, 61

Musqère, A.: 1999, in *Proceedings of the 26th International Cosmic Ray Conference (Salt Lake City)*

Nel, H. and de Jager, O.: 1995, *Astrophysics and Space Science* **320**, 299

Nel, H. I., de Jager, O. C., Raubenheimer, B. C., Brink, C., Meintjes, P. J., and North, A. R.: 1993, ApJ **418**, 836

Neshpor, Y. I., Stepanyan, A. A., Kalekin, O. P., Fomin, V. P., Chalenko, N. N., and Shitov, V. G.: 1998, *Astronomy Letters* **24**, 134

Nishiyama, T., Chikawa, M., Hayashi, Y., Hibino, K., Honda, K., Inoue, N., Ito, N., Kajino, F., Kakizawa, S., Kawasaki, Y., Kitamura, H., Kusano, E., Loh, E. C., Matsuyama, T., Morizane, Y., Nishikawa, D., Nishizawa, M., Ohoka, H., Osone, S., Sakaki, N., Sasano, M., Shiomi, A., Takahashi, T., Taylor, F., Teshima, M., Tsukiji, M., Yamamoto, T., Yasui, K., Yoshii, H., and Yuda, Y.: 1999, in *Proceedings of the 26th International Cosmic Ray Conference (Salt Lake City)*, Vol. 3, p. 370

Nolan, P. L., Arzoumanian, Z., Bertsch, D. L., Chiang, J., Fichtel, C. E., Fierro, J. M., Hartman, R. C., Hunter, S. D., Kanbach, G., Kniffen, D. A., Kwok, P. W., Lin, Y. C., Mattox, J. R., Mayer-Hasselwander, H. A., Michelson, P. F., von Montigny, C., Nel, H. I., Nice, D., Pinkau, K., Rothermel, H., Schneid, E., Sommer, M., Sreekumar, P., Taylor, J. H., and Thompson, D. J.: 1993, ApJ **409**, 697

Ong, R. A.: 1998, Phys. Rep. **305**, 93

Ong, R. A.: 2002, in *Online proceedings of: The Universe viewed in gamma-rays —The University of Tokyo Workshop 2002. http://icrgate.icrr.u-tokyo.ac.jp/can/Symp2002/Presentations.htm*

Oser, S., Bhattacharya, D., Boone, L. M., Chantell, M. C., Conner, Z., Covault, C. E., Dragovan, M., Fortin, P., Gregorich, D. T., Hanna, D. S., Mukherjee, R., Ong, R. A., Ragan, K., Scalzo, R. A., Schuette, D. R., Théoret, C. G., Tümer, T. O., Williams, D. A., and Zweerink, J. A.: 2001, ApJ **547**, 949

Ostriker, J. P. and Gunn, J. E.: 1969, ApJ **157**, 1395

Paciesas, W. S., Meegan, C. A., Pendleton, G. N., Briggs, M. S., Kouveliotou, C., Koshut, T. M., Lestrade, J. P., McCollough, M. L., Brainerd, J. J., Hakkila, J., Henze, W., Preece, R. D., Connaughton, V., Kippen, R. M., Mallozzi, R. S., Fishman, G. J., Richardson, G. A., and Sahi, M.: 1999, ApJS **122**, 465

Pacini, F.: 1967, *Nature* **216**, 567

Pacini, F. and Salpeter, E. E.: 1968, *Nature* **218**, 733

Pacini, F. and Salvati, M.: 1973, ApJ **186**, 249

Parlier, B., Agrinier, B., Forichon, M., Leray, J. P., Boella, G., Maraschi, L., Buccheri, B., Robba, N. R., and Scarsi, L.: 1973, *Nature Physical Science* **242**, 117

Porter, N. A., Delaney, T., Helmken, H. F., and Weekes, T. C.: 1976, *Nuovo Cimento B Serie* **32**, 514

Press, W. H., Teukolsky, S. A., Vetterling, W. T., and Flannery, B. P.: 1988, *Numerical Recipes in C, the Art of Scientific Computing*, Cambridge University Press

Puehlhofer, G. et al.: 1999, in *Proceedings of the 26th International Cosmic Ray Conference (Salt Lake City)*, Vol. 3, p. 492

Punch, M., Akerlof, C. W., Cawley, M. F., Chantell, M., Fegan, D. J., Fennell, S., Gaidos, J. A., Hagan, J., Hillas, A. M., Jiang, Y. K., A. D., Lamb, R. C., Lawrence, M. A., Lewis, D. A., Meyer, D. I., Mohanty, G., O'Flaherty, K. S., Reynolds, P. T., Rovero, A. C., Schubnell, M. S., Sembroski, G., Weekes, T. C., and Wilson, C.: 1992, Nature **358**, 477

Punch, M., Akerlof, C. W., Cawley, M. F., Fegan, D. J., Lamb, R. C., Lawrence, M. A., Lang, M. J., Lewis, D. A., Meyer, D. I., O' Flaherty, K. S. O., Reynolds, P. T., and Schubnell, M. S.: 1991, in *Proc. 22nd I.C.R.C. (Dublin)*, Vol. 1, p. 464

Quinn, J.: 1997, *Ph.D. thesis*, National University of Ireland

Quinn, J., Akerlof, C. W., Biller, S., Buckley, J., Carter-Lewis, D. A., Cawley, M. F., Catanese, M., Connaughton, V., Fegan, D. J., Finley, J. P., Gaidos, J., Hillas, A. M., Lamb, R. C., Krennrich, F., Lessard, R., McEnery, J. E., Meyer, D. I., Mohanty, G., Rodgers, A. J., Rose, H. J., Sembroski, G., Schubnell, M. S., Weekes, T. C., Wilson, C., and Zweerink, J.: 1996, ApJ **456**, L83

Quinn, J., Bond, I. H., Boyle, P. J., Buckley, J. H., Bradbury, S. M., Breslin, A. C., Burdett, A. M., Bussons Gordo, J., Carter-Lewis, D. A., Catanese, M., Cawley, M. F., Fegan, D. J., Finley, J. P., Gaidos, J. A., Hall, A., Hillas, A. M., Krennrich, F., Lamb, R. C., Lessard, R., Masterson, C., McEnery, J. E., Mohanty, G., Moriarty, P., Rodgers, A. J., Rose, H. J., Samuelson, F. W., Sembroski, G. H., Srinivasan, R., Weekes, T. C., and Zweerink, J.: 1997, *Proceedings of the 25th International Cosmic Ray Conference (Durban, South Africa)* **25**, 249

Quinn, J., Buckley, J., Weekes, T. C., Catanese, M., Carter-Lewis, D. A., Krennrich, F., Lamb, R. C., Zweerink, J., Akerlof, C. W., Meyer, D., Schubnell, M., Gaidos, J., Sembroski, G., Wilson, C., Fegan, D. J., Lessard, R., McEnery, J., Cawley, M. F., Biller, S., Hillas, A. M., Rodgers, A., and Rose, J.: 1995, IAU Circ. **6178**, 1

Ramanamurthy, P. V., Bertsch, D. L., Fichtel, C. E., Kanbach, G., Kniffen, D. A., Mayer-Hasselwander, H. A., Nolan, P. L., Sreekumar, P., and Thompson, D. J.: 1995, ApJ **450**, 791

Reimer, O. and Pohl, M.: 2002, A&A **390**, L43

Reynolds, P. T., Akerlof, C. W., Cawley, M. F., Chantell, M., Fegan, D. J., Hillas, A. M., Lamb, R. C., Lang, M. J., Lawrence, M. A., Lewis, D. A., Macomb, D., Meyer, D. I., Mohanty, G., O'Flaherty, K. S., Punch, M., Schubnell, M. S., Vacanti, G., Weekes, T. C., and Whitaker, T.: 1993, ApJ **404**, 206

Richards, D. W. and Comella, J. M.: 1969, *Nature* **222**, 551

Rieke, G. H. and Weekes, T. C.: 1969, Technical Report 301, Smithsonian Astrophysical Observatory

Romani, R. W.: 1996, ApJ **470**, 469

Romani, R. W. and Yadigaroglu, I.-A.: 1995, ApJ **438**, 314

Ruderman, M. A. and Sutherland, P. G.: 1975, ApJ **196**, 51

Sapru, M. L., Kaul, R. K., Bhat, C. L., Dhar, V. K., Rannot, R. C., and Tickoo, A. K.: 1996, *Bulletin of the Astronomical Society of India* **24**, 59

Scott, D.: 1992, *Multivariate Density Estimation*, p. 125, John Wiley & Sons, Inc., New York

Shklovsky, I. S.: 1953, *Dok. Akad. Nauk USSR [Sov. Phys. Dokl.]* **90**, 983

Srinivasan, R.: 1996, Internal Whipple collaboration communication

Srinivasan, R., Finley, J. P., Sembroski, G. H., Weekes, T. C., and Wilson, C.: 1997, in *Workshop Towards a Major Cherenkov Detector (Kruger Park)*, p. 51

Staelin, D. H. and Reifenstein, E. C.: 1968, *Science* **162**, 1481

Staelin, D. H. and Sutton, J. M.: 1970, *Nature* **228**, 69

Standish, E. M.: 1982, A&A **114**, 297

Standish, E. M.: 1997, *The JPL Planetary and Lunar Ephemerides*, ftp://navigator.jpl.nasa.gov/pub/ephem/

Sturner, S. J. and Dermer, C. D.: 1994, ApJ **420**, L79

Sturner, S. J. and Dermer, C. D.: 1995, A&A **293**, L17

Sturrock, P. A.: 1971, ApJ **164**, 529

Swanenburg, B. N., Bennett, K., Bignami, G. F., Buccheri, R., Caraveo, P., Hermsen, W., Kanbach, G., Lichti, G. G., Masnou, J. L., Mayer-Hasselwander, H. A., Paul, J. A., Sacco, B., Scarsi, L., and Wills, R. D.: 1981, ApJ **243**, L69

Tanimori, T., Hayami, Y., Kamei, S., Dazeley, S. A., Edwards, P. G., Gunji, S., Hara, S., Hara, T., Holder, J., Kawachi, A., Kifune, T., Kita, R., Konishi, T., Masaike, A., Matsubara, Y., Matsuoka, T., Mizumoto, Y., Mori, M., Moriya, M., Muraishi, H., Muraki, Y., Naito, T., Nishijima, K., Oda, S., Ogio, S., Patterson, J. R., Roberts, M. D., Rowell, G. P., Sakurazawa, K., Sako, T., Sato, Y., Susukita, R., Suzuki, A., Suzuki, R., Tamura, T., Thornton, G. J., Yanagita, S., Yoshida, T., and Yoshikoshi, T.: 1998, ApJ **497**, L25

Tavani, M., Barbiellini, G., Argan, A., Auricchio, N., Caraveo, P., Chen, A., Cocco, V., Costa, E., di Cocco, G., Fedel, G., Feroci, M., Fiorini, M., Froysland, T., Galli, M., Gianotti, F., Giuliani, A., Labanti, C., Lapshov, I., Lipari, P., Longo, F., Massaro, E., Mereghetti, S., Morelli, E., Morselli, A., Pellizzoni, A., Perotti, F., Picozza, P., Pittori, C., Pontoni, C., Prest, M., Rapisarda, M., Rossi, E., Rubini, A., Soffitta, P., Trifoglio, M., Vallazza, E., Vercellone, S., and Zanello, D.: 2001, in *AIP Conf. Proc. 587: Gamma 2001: Gamma-Ray Astrophysics*, p. 729

Thompson, D. J.: 2001, in *AIP Conf. Proc. 220: High Energy Gamma-Ray Astronomy*, p. 103

Thompson, D. J., Bertsch, D. L., Dingus, B. L., Esposito, J. A., Etienne, A., Fichtel, C. E., Friedlander, D. P., Hartman, R. C., Hunter, S. D., Kendig, D. J., Mattox, J. R., McDonald, L. M., von Montigny, C., Mukherjee, R., Ramanamurthy, P. V., Sreekumar, P., Fierro, J. M., Lin, Y. C., Michelson, P. F., Nolan, P. L., Shriver, S. K., Willis, T. D., Kanbach, G., Mayer-Hasselwander, H. A., Merck, M., Radecke, H.-D., Kniffen, D. A., and Schneid, E. J.: 1995, ApJS **101**, 259

Thompson, D. J., Fichtel, C. E., Hartman, R. C., Kniffen, D. A., and Lamb, R. C.: 1977, ApJ **213**, 252

Thompson, D. J., Fichtel, C. E., Kniffen, D. A., and Ogelman, H. B.: 1975, ApJ **200**, L79

Tumer, O. T., Wheaton, W. A., Godfrey, C. P., and Lamb, R. C.: 1985, in *Proceedings of the 19th International Cosmic Ray Conference (La jolla)*, Vol. 1, p. 139

Urry, C. M. and Padovani, P.: 1995, PASP **107**, 803

Vacanti, G., Cawley, M. F., Colombo, E., Fegan, D. J., Hillas, A. M., Kwok, P. W., Lang, M. J., Lamb, R. C., Lewis, D. A., Macomb, D. J., O'Flaherty, K. S., Reynolds, P. T., and Weekes, T. C.: 1991, ApJ **377**, 467

Vacanti, G., Fleury, P., Jiang, Y., Pare, E., Rovero, A. C., Sarazin, X., Urban, M., and Weekes, T. C.: 1994, *Astroparticle Physics* **2**, 1

Vishwanath, P. R.: 1982, in *Proceedings of the International Workshop on Very High Energy Astronomy, ed. P. V. Ramanamurthy and T. C. Weekes (Bombay: Tata Institute)*, Vol. 1, p. 21

Vishwanath, P. R. et al.: 2001, in *Proceedings of the 27h International Cosmic Ray Conference (Hamburg)*, p. 2392

Weekes, T.: 1999, in B. Dingus (ed.), *Proceedings of the 6th International Workshop 'Towards a Major Cherenkov Detector' (Snowbird) - In Press*, American Institute of Physics

Weekes, T. and Turver, K.: 1977, in *Proceedings of the 12th Eslab Symposium (Frascati)*, Vol. ESA SP-124, p. 279

Weekes, T. C.: 1981, in *Proceedings of the 17th International Cosmic Ray Conference (Paris)*, Vol. 8, p. 34

Weekes, T. C., Cawley, M. F., Fegan, D. J., Gibbs, K. G., Hillas, A. M., Kowk, P. W., Lamb, R. C., Lewis, D. A., Macomb, D., Porter, N. A., Reynolds, P. T., and Vacanti, G.: 1989, ApJ **342**, 379

Weekes, T. C., Fazio, G. G., Helmken, H. F., O'Mongain, E., and Ricke, G. H.: 1972, ApJ **174**, 165

Weiler, K. W.: 1978, *Memorie della Societa Astronomica Italiana* **49**, 545

Wilson, J. G.: 1976, *Cosmic Rays*, p. 20, Wykeham

Yoshikoshi, T., Kifune, T., Dazeley, S. A., Edwards, P. G., Hara, T., Hayami, Y., Kakimoto, F., Konishi, T., Masaike, A., Matsubara, Y., Matsuoka, T., Mizumoto, Y., Mori, M., Muraishi, H., Muraki, Y., Naito, T., Nishijima, K., Oda, S., Ogio, S., Ohsaki, T., Patterson, J. R., Roberts, M. D., Rowell, G. P., Sako, T., Sakurazawa, K., Susukita, R., Suzuki, A., Tamura, T., Tanimori, T., Thornton, G. J., Yanagita, S., and Yoshida, T.: 1997, ApJ **487**, L65